

State-Selective Attachment of Helium to Molecular Ions in a New Cryogenic Ion Trap

In a u g u r a l - D i s s e r t a t i o n

zur

Erlangung des Doktorgrades

der Mathematisch-Naturwissenschaftlichen Fakultät

der Universität zu Köln

vorgelegt von

LARS ALEXANDER KLUGE

aus Leverkusen

Köln 2016

I. Berichterstatter:
II. Berichterstatter:

Professor Dr. Stephan Schlemmer
Professor Dr. Thomas Michely

Tag der mündlichen Prüfung:

16.06.2015

If you thought that science was certain - well, that is just an error on your part.

Richard P. Feynman (1918-1988)

Abstract

Light is the main information about the interstellar medium accessible on Earth. Based on this information one can conclude on the composition of the region where the light originates from, as well as on its history. The requirement for this is that it is possible to identify the different absorption and emission features in the spectrum and assign them to certain molecules, atoms or ions. To enable the identification of the different species, precise spectroscopic investigations of the species in the laboratory are necessary.

In this work a new spectroscopic method is presented, which can be used to record pure rotational spectra of mass selected, cold, stored molecular ions. It is based on the idea of state specific attachment of helium atoms to the stored molecular ions. The new technique has been made possible through the development and recent completion of two new 22-pole ion trap instruments in the work group of Laboratory Astrophysics at the University of Cologne. These new instruments have the advantage to reach temperatures as low as 4K compared to the 10 K of the predecessor instrument. These low temperatures enable the ternary attachment of helium atoms to the stored molecular ions and by this make it possible to develop this new method for pure rotational spectroscopy.

According to this, this work is divided into two parts. The first part deals with the new FELion experiment that was build and characterized in the first part of the thesis. FELion is a cryogenic 22-pole ion trap apparatus, allowing to generate, mass select, store and cool down, and analyze molecular ions. The different components of the instrument, e.g. the Storage Ion Source for generating the ions or the first quadrupole mass filter, are described and characterized in this part. Besides this also the newly developed control and data acquisitions system is introduced. With this instrument the measurements presented in the second part of the work were performed.

The second part deals with the new action spectroscopic method of state-selective helium attachment to the stored molecular ions. For a deeper analysis of the new technique the systems of CD^+ and helium and HCO^+ and helium are investigated in detail. Analytical and numerical models of the process are presented and compared to experimental results. The results of these investigations point to a seemingly very general applicability of the new method to a wide class of molecular ions.

In the final part of the thesis measurements of the rotational spectrum of $l\text{-C}_3\text{H}^+$ are presented. These measurements have to be high-lighted, since it was possible for the first time in the laboratory to unambiguously measure four low-lying rotational transitions of $l\text{-C}_3\text{H}^+$. These measurements ([1]) enabled the reliable identification of so far unidentified emission lines observed in several regions of the interstellar medium([2], [3], [4]).

Kurzzusammenfassung

Licht ist die Hauptquelle, aus der wir auf der Erde Informationen aus dem interstellaren Raum erhalten. Anhand dieser Informationen kann man sowohl auf die Zusammensetzung der Region zurückschließen, aus der das Licht zur Erde gelangte, als auch auf dessen Entwicklungsgeschichte. Voraussetzung dafür ist, dass man die aufgezeichneten Spektren interpretieren und die Absorptions- und Emissionslinien gewissen Molekülen, Atomen oder Ionen zuordnen kann. Um die Identifikation zu ermöglichen, sind spektroskopische Untersuchungen der verschiedenen Spezies im Labor nötig.

In der vorgelegten Arbeit wird ein neues Verfahren vorgestellt, mit dem es möglich ist, reine Rotationsspektren von massenselektierten, gespeicherten und kalten Ionen aufzunehmen. Dieses Verfahren basiert auf der Idee der zustandsabhängigen Anlagerung von Heliumatomen an die gespeicherten Ionen. Möglich wurde die Entwicklung dieser Methode erst durch die Fertigstellung zweier neuer kalter Ionenspeicherapparaturen in der Arbeitsgruppe Laborastrophysik an der Universität zu Köln. Diese neuen Speicherapparaturen haben im Vergleich zu der vorherigen Generation unter anderem den Vorteil, dass sie tiefere Temperaturen von 4 K erreichen können; bei dem vorherigen Experimenten waren nur Temperaturen von 10 K möglich. Diese niedrigeren Temperaturen ermöglichen überhaupt erst die ternäre Anlagerung der Heliumatome an die gespeicherten Ionen und damit die Entwicklung der neuen Messmethode für reine Rotationsspektroskopie an gespeicherten Ionen.

Dementsprechend gliedert sich die Arbeit in zwei Teile. Der erste Teil befasst sich mit dem neuen Speicherexperiment FELion, das im ersten Teil der Promotion aufgebaut und charakterisiert wurde. FELion ist ein kryogener 22-Pol Ionenspeicher, mit dem Ionen erzeugt, massenselektiert, gespeichert und gekühlt, sowie analysiert werden können. Die unterschiedlichen Komponenten des Instrumentes, z.B. die Ionenquelle oder der erste Quadrupol-Massenfilter, werden in diesem Teil der Arbeit beschrieben und charakterisiert. Außerdem wird auf das neu entwickelte Kontroll- und Datenaufnahmesystem eingegangen. Mit diesem neuen Experiment wurden die Messungen durchgeführt, die im zweiten Teil der Arbeit präsentiert werden.

Der zweite Teil behandelt das neue action spectroscopy Verfahren, das auf der zustandsspezifischen Anlagerung von Heliumatomen an gespeicherten Ionen basiert. Für eine genauere Analyse der Methode werden die Systeme von CD^+ und Helium sowie HCO^+ und Helium genauer untersucht. Es werden analytische und numerische Modelle vorgestellt und mit experimentellen Daten verglichen. Die Ergebnisse dieser Untersuchungen deuten daraufhin, dass das neue Verfahren einen breiten Anwendungsbereich besitzt und auf eine große Klasse von Ionen anwendbar ist.

Im abschließenden Teil der Arbeit wird das Rotationsspektrum von $1\text{-C}_3\text{H}^+$ gezeigt. Diese Messungen sind deshalb hervorzuheben, da es hier zum ersten Mal zweifelsfrei im Labor gelungen ist, vier niedrig liegende Rotationsübergänge von $1\text{-C}_3\text{H}^+$ zu messen. Die Messungen ([1]) ermöglichten die verlässliche Zuordnung von bis dahin nicht identifizierten Emissionslinien, die in verschiedenen Regionen des interstellaren Mediums beobachtet worden waren ([2], [3], [4]).

Contents

Abstract	i
Kurzzusammenfassung	iii
Preface	1
I FELion	3
1 Introduction	5
2 Design FELion & Test Measurements	9
2.1 Vacuum System	9
2.2 The Storage Ion Source	9
2.2.1 Technical Design	10
2.2.2 Test Measurements	11
2.3 The First Quadrupole Mass Filter	16
2.3.1 Technical Design	19
2.3.2 Test Measurements	20
2.4 The Quadrupole Bender	23
2.4.1 Technical Design	24
2.5 The 22-pole Ion Trap	24
2.5.1 Technical Design	27
2.5.2 Test Measurements	28
2.6 The Second Quadrupole Mass Filter	31
2.6.1 Technical Design	32

2.6.2	Test Measurements	33
2.7	The Daly-type Detector	34
2.7.1	Technical Design	36
2.8	The NI CompactRIO System	36
3	Control Software for FELion	39
3.1	The FPGA Module	40
3.1.1	FPGA VI	40
3.1.2	ORTEC FPGA ONE CYCLE	41
3.2	The Graphical User Interface	43
3.3	Measurement Modes	45
3.3.1	Counter Mode	45
3.3.2	Continuous Mass Scan Mode	47
3.3.3	Discrete Mass Scan Mode	48
3.3.4	Time Scan Mode - Storage Time	49
3.3.5	Time Scan Mode - Piezo Valve	51
3.3.6	Pressure Calibration Mode	51
3.3.7	THz Scan Mode	53
3.3.8	THz Stability Mode	56
II	Rotational Spectroscopy of Cold Molecular Ions by State Specific Helium Attachment	59
4	Introduction to Rotational Spectroscopy	61
5	Rotational Spectroscopy with FELion	63
5.1	Experimental Setup	63
5.1.1	Ion Production	63
5.1.2	Helium Number Density Calculation	64
5.1.3	Calibration of the mm-Wave Source	67
5.1.4	Determination of the collisional ion temperature	70
5.1.5	Measurement Modes	71
5.2	Kinetic Measurements of CD ⁺ and Helium	73
5.2.1	Theory of Ternary Reactions	73

5.2.2	Time Evolution of the CD^+ + Helium System	75
5.3	Rotational Spectroscopy of CD^+	81
5.3.1	The Analytical Model	82
5.3.2	Numerical Simulation with Python	89
5.3.3	Comparison of the Measurements with the Two Models	92
5.4	Rotational Spectroscopy of HCO^+	111
5.4.1	Motivation	111
5.4.2	Experimental Setup	111
5.4.3	Experimental Data	111
5.4.4	Conclusion & Discussion	119
6	Rotational Spectroscopy of C_3H^+	121
6.1	C_3H^+	121
6.1.1	Astronomical Interest	121
6.1.2	Experimental Setup	122
6.1.3	Experimental Data & Results	123
6.1.4	Discussion & Conclusion	127
7	Conclusion & Outlook	129
III	Appendix	133
8	Appendix - Design FELion	135

List of Tables

2.1	Measured RF characteristic of the Storage Ion Source	12
2.2	Calibration of the first quadrupole	21
2.3	Comparison between theoretical and experimental settings for the first quadrupole.	22
2.4	Calibration 22-pole trap-heater	29
2.5	Calibration spinning rotor gauge	31
2.6	Differential pumping	32
2.7	Typical operational values for the Daly-detector at FELion	35
2.8	Indicators for the Daly-detector at FELion	35
5.1	Experimental setup for source and first quadrupole for CD^+	64
5.2	Calculated collisional temperatures of the CD^+ ions	71
5.3	Overview of the obtained ternary rate-coefficients for different temperatures	79
5.4	Overview of the obtained collision induced dissociation rate-coefficients for different temperatures	79
5.5	Calculated binding energies for the helium atom	81
5.6	Thermal rate-coefficients $k_{JJ'}$ for rotational collisional de-excitation of CH^+ in collision with 4He	83
5.7	Extrapolated rate-coefficients $k_{JJ'}$ for collisional de-excitation rates of CH^+ in collision with 4He	83
5.8	Parameters for the numerical simulation	91
5.9	Parameters for the simulations - helium number density dependency . . .	93
5.10	Relative number of $He\bullet CD^+$ ions and cluster depletion signal as a function of helium number density	94
5.11	Observed cluster depletion signals in the experiment for different helium number densities	97

5.12	Parameters for the simulations - mm wave power dependency	97
5.13	Parameters for the simulations - temperature dependency	101
5.14	Results for the temperature dependence of the analytical model & the numerical simulation	101
5.15	Summarized experimental values for the cluster depletion signal at different temperatures	103
5.16	Parameters for the simulations - storage time dependency	104
5.17	Results for the storage time dependence of the numerical simulation . . .	104
5.18	Observed cluster depletion signals for different storage times	106
5.19	Parameters for the simulations - estimation of a for CD^+	106
5.20	Results for a for CD^+ obtained with the analytical model	107
5.21	Fit results for a for CD^+ with the numerical model	109
5.22	Calculated strength of the cluster depletion signal varying the collisional rate-coefficients for CD^+ and helium and ratio a	110
5.23	Overview of the obtained ternary rate-coefficients for different temperatures for HCO^+	115
5.24	Overview of the obtained collision induced dissociation rate-coefficients for different temperatures for HCO^+	116
5.25	Rate-coefficients $k_{JJ'}$ for rotational collisional excitation of HCO^+ in collision with 4He	117
5.26	Parameters for the simulations - estimation of a for CD^+	117
5.27	Calculated strength of the cluster depletion signal varying the collisional rate-coefficients for HCO^+ and helium and ratio a	118
6.1	Measured rotational transition frequencies of $I-C_3H^+$	127
6.2	Spectroscopic constants $I-C_3H^+$	127

List of Figures

1.1	Technical drawing of FELion	7
2.1	Mass spectrum from the SIS with CD_3H	10
2.2	Technical drawings of the Storage Ion Source	11
2.3	Wiring concept of the SIS	12
2.4	Photos of the Storage Ion Source	13
2.5	Ion current as a function of RF-amplitude	14
2.6	Ion current as a function of <i>repeller</i> voltage	15
2.7	Ion pulse as a function of <i>B0</i> opening time	17
2.8	Stability diagram of a quadrupole mass filter	19
2.9	Technical drawing of the first quadrupole	20
2.10	Calibration measurement of the first quadrupole	21
2.11	Cut-off behavior of the first quadrupole	23
2.12	Technical drawing and photo of the bender.	24
2.13	Effective potentials for different geometries	27
2.14	Technical drawing and photo of the 22-pole trap.	28
2.15	Cooldown and warmup characteristic FELion	29
2.16	Calibration of the antenna and resonance curve of the 22-pole trap	30
2.17	Technical drawing of the second quadrupole	33
2.18	Mass-calibration measurement for the second quadrupole	34
2.19	Principle of the Daly-detector	35
2.20	Technical drawing of the Daly-detector	36
3.1	Scheme of the general setup	39

3.2	Scheme of the pulsed sequence on the Compact Rio FPGA	42
3.3	Typical pulsed sequence	42
3.4	Scheme of the interface between the control software on the PC and the Compact RIO system at the experiment	43
3.5	Screenshot of the General Settings section on the GUI	44
3.6	Screenshot of the Voltage Control Section for the experiment	45
3.7	Screenshot of the Counter Mode	46
3.8	Scheme of the Counter Mode source code	46
3.9	Screenshot of the Continuous Mass Scan Mode	47
3.10	Scheme of the Countinuous Mass Scan source code	48
3.11	Screenshot of the Discrete Mass Scan Mode	49
3.12	Scheme of the Discrete Mass Scan source code	49
3.13	Screenshot of the Time Scan Mode	50
3.14	Scheme of the Time Scan source code	51
3.15	Screenshot of the Piezo Valve Time Scan Mode	52
3.16	Scheme of the Pressure Calibration source code	52
3.17	Screenshot of the THz Scan Mode	53
3.18	Scheme of the THz Scan Mode source code	55
3.19	Screenshot of the THz Stability Mode	56
3.20	Scheme of the THz Stability Mode source code	58
4.1	LIR Schemes	61
5.1	Unfiltered mass spectrum from the ion source	65
5.2	Filtered mass spectrum from the ion source	66
5.3	Mass spectrum of the content of the 22 pole ion trap at 4 K and after a storage time of 600 ms	66
5.4	Technical drawing of the 22-pole trap section	68
5.5	Picture of the 22-pole ion trap apparatus together with the VDI WR9.0 Starterkit and the focussing mirror	68
5.6	Relative calibration measurement of the VDI WR9.0 THz Starter Kit at 453 GHz	69
5.7	Cluster depletion signals of CD ⁺ at 4 K	70
5.8	Time scan of the trapped CD ⁺ and cluster ions at 4K and $1.7 \cdot 10^{14} \text{ cm}^{-3}$ helium number density	77

5.9	Time scan of the trapped CD^+ and cluster ions at 4 K and $9 \cdot 10^{14} \text{ cm}^{-3}$ helium number density	77
5.10	Effective binary rate-coefficient for CD^+ and He at 4 K	78
5.11	Typical rotational line of CD^+ at 4 K	82
5.12	Simplified scheme of the kinetics for the CD^+ and helium system	83
5.13	Simulated dependency of the cluster depletion signal for the $J=1 \leftarrow 0$ transition of CD^+ on the helium number density in the trap with the analytical model	93
5.14	Simulated level populations for CD^+ at a helium number density of $1 \cdot 10^{13} \text{ cm}^{-3}$ with and without radiation	95
5.15	Simulated level populations for CD^+ at a helium number density of $1 \cdot 10^{15} \text{ cm}^{-3}$ with and without radiation	95
5.16	Simulated level populations for CD^+ at a helium number density of $5 \cdot 10^{15} \text{ cm}^{-3}$ with and without radiation	96
5.17	Simulated dependency of the cluster depletion signal for the $J=1 \leftarrow 0$ transition of CD^+ on the power of the mm-wave source with the analytical model	98
5.18	Simulated level populations for CD^+ for different radiation power level	99
5.19	Measured power dependence curves for the cluster depletion signal for $2.94 \cdot 10^{14} \text{ cm}^{-3}$ and $4.87 \cdot 10^{14} \text{ cm}^{-3}$ helium number density	100
5.20	Measurement of the power dependence of the cluster depletion signal for CD^+ with focussing optic	101
5.21	Simulated level populations for CD^+ for nominal temperatures of 4 K and 12 K with and without radiation	102
5.22	Simulated level populations for CD^+ for storage times of 100 ms and 2000 ms with and without radiation	105
5.23	Fits for CD^+ with the analytical model	107
5.24	Fits for CD^+ with the numerical model	108
5.26	Time evolution of the HCO^+ and He system	113
5.27	Dependence of the helium-cluster formation rate-coefficient on the helium number density for HCO^+	114
5.28	Temperature dependence of the ternary rate-coefficient and the collision induced dissociation rate-coefficient for HCO^+	115
5.29	Cluster depletion signal of HCO^+	116
5.30	Simulated level populations for HCO^+ at a helium number density of $5 \cdot 10^{14} \text{ cm}^{-3}$ with and without radiation	119
6.1	Mass scan of trapped C_3H^+ at 4 K	123

6.2	Time scan for a long storage time of C_3H^+ and helium	124
6.3	Time scan for a short storage time of C_3H^+ and helium	125
6.4	Rotational transitions of $I-C_3H^+$	126
8.1	Circuit diagramm of the 10 MHz RF-generator for the Storage Ion Source .	136
8.2	Circuit diagramm of the 1.5 MHz RF-generator for the first quadrupole mass filter	137
8.3	Technical drawing of the feedthrough-flange for the SIS	138
8.4	Schematic of the Connection Box for the Storage Ion Source	138
8.5	3D-view of the Einzel-lense of the first quadrupole with designations . . .	139
8.6	Schematic of the Connection Box for the first quadrupol	139
8.7	Designation of the bender-parts	140
8.8	Technical drawing of the feedthrough-flange for the 22-pole trap	140
8.9	Schematic of the Connection Box for the 22-pole trap	141
8.10	Schematic of the Connection Box for the 22-pole trap	141

Preface

Light is the most important information we can use to investigate and understand different processes like star formation and the chemical composition of our Earth or other objects in our solar system and beyond. In order to understand the processes, the observed light has first to be assigned to matter (atoms, molecules, ions or grains). After the identification, the information can be used to obtain physical properties of the absorbing or emitting particles, for example their density in the observed region or their temperature. In addition, the development history of the observed region can be studied. For this, a detailed knowledge of the astrophysical chemistry and chemical inventory is needed. The more reaction mechanisms and reaction rates are known, the better one can use this knowledge to retrieve the chemical evolution based on the current composition of the observed region.

In the laboratory astrophysics group at the University of Cologne investigations of both spectroscopy as well as astrochemistry are conducted. By using temperature variable ion trap experiments, especially the investigation of ions is possible.

Ions play a minor role for the chemistry on Earth, but in space ions are much more important. This is due to the fact that the conditions in the interstellar medium are very different from the conditions on Earth. The interstellar medium is typically very thin (number densities of 10^2 - 10^6 cm^{-3} are typical for molecular clouds compared to) and cold (6-100 K) compared to the Earth ($\sim 10^{19}$ cm^{-3} and 300 K respectively). Thus, highly endothermic reactions are hindered since they have to overcome high energetic barriers. The barriers for reactions between ions and neutrals are typically much smaller than barriers for neutral-neutral reactions or zero. Therefore, ion-neutral reactions can be expected to dominate at temperatures of a few Kelvin. Hence, it is very important to study these types of reactions in the laboratory. Moreover, in order to identify the molecular ions in space it is equally important to record the rovibrational and rotational spectra of the ions in the laboratory.

For the investigation of such reactions and the spectroscopy of ions several ion trap experiments are available in the Cologne laboratories. One of these experiments is the LIRTRAP apparatus, which is used since a number of years in Cologne to investigate ion-molecule reactions and high resolution spectra of ions in the temperature range between 10 K and 300 K. Two improved instruments based on the LIRTRAP design, COLTRAP and FELion, were recently finished. With these new trap experiments, the investigation of ion-molecule reactions and spectroscopy experiments down to a nominal temperature of 4 K are possible. This lower temperature enabled us to develop a new experimental technique for pure rotational spectroscopy of ions. The FELion apparatus, which has now been moved to the "Free Electron Lasers for Infrared experiments"(FELIX) in Nijmegen, The Netherlands, is described and characterized in

chapter 2 of this work. Besides the experiment itself also the newly developed software for controlling the experiments in the trap is presented in chapter 3.

As mentioned above, it is also possible to record high resolution spectra of ions in the trap experiments. In the past, the main method for recording spectra in the cold trap experiments was the technique of Laser Induced Reactions (LIR). This method is based on the idea that in the trap experiments the equilibrium of an ion-neutral reaction can be shifted via resonant laser irradiation. With the new generation of traps, which can reach temperatures of 4 K, new experimental schemes for the spectroscopy of ions are possible. The new technique of cluster depletion is based on the idea of state specific helium attachment to molecular ions and therefore it can be viewed as a special case of LIR. By this it is possible to record pure rotational transitions of the stored cold molecular ions. In chapter 5, the technique and an underlying kinetic model are introduced. An analytical and a numerical implementation of this model is tested for CD^+ and HCO^+ . With the new technique it was also possible in the laboratory to record four low-lying transitions of $l\text{-C}_3\text{H}^+$. These data, presented in chapter 6, were used to confirm the detection of $l\text{-C}_3\text{H}^+$ in space.

Part I

FELIX Ion Trap,
FELion

Introduction

The origin of trap experiments is the quadrupole ion trap (or Paul trap) invented by Wolfgang Paul ([5], [6]). The Paul trap and the quadrupole mass filter (also invented by Wolfgang Paul) are still relevant for today's experiments in ion physics, astrochemistry or biochemistry. The Paul trap for example is still in use for experiments with laser-cooled stored ions. This technique can be used to investigate single atomic ions ([7]), Coulomb crystals ([8]) or for optical clocks ([9]).

It turned out that trap experiments are a suitable tool for the laboratory investigation of ion-molecule reactions relevant for astrochemistry. The disadvantage of the use of Paul traps for astrochemistry is that it is difficult to reach low temperatures of only a few Kelvin with these experiments, but for astrochemistry it is very important to investigate the reaction at temperatures below 10 K, since many astronomical objects (for example dark molecular clouds) have temperatures as low as 6 K ([10]). The extrapolation of the results obtained at temperatures close to room temperature down to a few Kelvin is not possible in a satisfying way. Therefore, for astrochemical experiments higher order multi-pole traps with large field-free regions allowing effective buffer gas cooling are needed. Dieter Gerlich pioneered experiments with low temperature multi-pole traps ([11]). Today the most used ion trap geometry for experiments in astrochemistry is the 22-pole ion trap ([12], [13]). Experiments with 22-pole traps mounted on a 10 K closed cycle cryogenic cooler were used in the last decade of the 20th century to investigate many different (mostly astrophysically motivated) reactions. Some of these experiments addresses the radiative association ([14]), deuteration processes ([15]) or cluster formation ([16], [17]).

For the investigation of, for example, biologically relevant molecules ([18], [19]) or floppy molecules as CH_5^+ ([20], [21], [22]) even lower temperatures are needed. For this purpose two new 22-pole ion trap instruments COLTRAP and FELion were build in the Cologne Laboratories.

FELion is a dedicated cryogenic 22-pole ion trap apparatus, developed and built in the Cologne Laboratory Astrophysics group, to be installed permanently at the "Free Electron Lasers for Infrared eXperiments"(FELIX) in Nijmegen, The Netherlands. FELion is intended for recording gas-phase IR and FIR spectra of mass-selected, internally and kinetically cold molecular ions at temperatures in the range of 4-300 K through a variety of sensitive action spectroscopic methods. The experiment consists of different parts that will be described in chapter 2 in detail. Thus, here will be given only a short

overview of the experimental setup. The ions to be investigated in the experiment are created in a Storage Ion Source (see also figure 1.1 for the different parts of the experiment) and are mass-selected in the first quadrupole mass filter. Due to the angled setup a bender is used in this experiment to guide the ions into the 22-pole trap, which is mounted on a closed cycle 4 K cryostat. The ions can be stored in the trap for a certain time and kinetic or spectroscopic experiments can be performed. Subsequently the ions are extracted into the second quadrupole mass filter. After this second filtering the ions of interest are counted with a Daly-type detector system. To be able to investigate the ions the complete experiments must be operated under ultra high vacuum (UHV) conditions.

The first part of my thesis focuses on the new design of FELion compared to the predecessor LIRTRAP, which is still in service in our laboratory in Cologne and is upgraded at the moment. In addition, characterization-measurements of the different parts, e.g. the Storage Ion Source, the first quadrupole, and the Daly-type detector will be presented. One of the main improvements of the new setup/new machine is the use of a more powerful coldhead. This closed-cycle helium cryostat enables to reach temperatures of 4 K in the experiment. Compared to LIRTRAP also the construction of FELion is changed, to an angled setup allowing a better in coupling of the different radiation sources into the experiment. Compared to the linear setup of LIRTRAP, this reduces the minimum distance between the optical port and the 22-pole trap. The new construction of FELion is shown in figure 1.1. The reduced distance combined with the new more powerful 4 K-coldhead enables to perform THz spectroscopy of cold molecular ions. These measurements are presented in chapters 5 and 6.

The angled setup of FELion not only allows an easier in coupling of the radiation used or the use of a molecular beam, but it also makes two photon experiments possible ([23]). For such experiments the second color photon can be in coupled into the trap through the second quadrupole. The design itself is modular, which results in an easy exchange of different parts of the experiment, e.g. the ion source or the detector. As sources for the experiment a Storage Ion Source (SIS) and an ElectroSpray Ionization source (ESI) are designated. The Storage Ion Source is described in the following chapter in more detail, and performance test measurements are presented. The ESI source is still under construction and will be tested in our laboratory soon. The standard detector for the experiments is a Daly-type detector, which is capable of counting single ions. Other possible detector types are for example a Micro-Channel Plate Detector (MCP) or a channeltron.

A further development is the newly designed 22-pole trap. In contrast to older models, the copper housing and the stainless steel RF electrodes are machined and electroformed out of single bulk pieces ([13]). This results in better cryogenic properties, good vacuum performance, and easy maintenance. Furthermore also the concept of the control and data acquisition system was completely changed. Instead of using several different power supplies for the low voltages needed for the experiment a NI Compact RIO system with an FPGA (Field Programmable Gate Array) is used to generate and control these voltages. This system has several advantages compared to the former system. The first main improvement is that the complete voltage pulsing scheme is generated by one single unit, which can be directly controlled by the PC. Moreover, during the measurements the Compact RIO system with the FPGA is completely autonomous from the control PC, which is a big advantage in terms of reliability

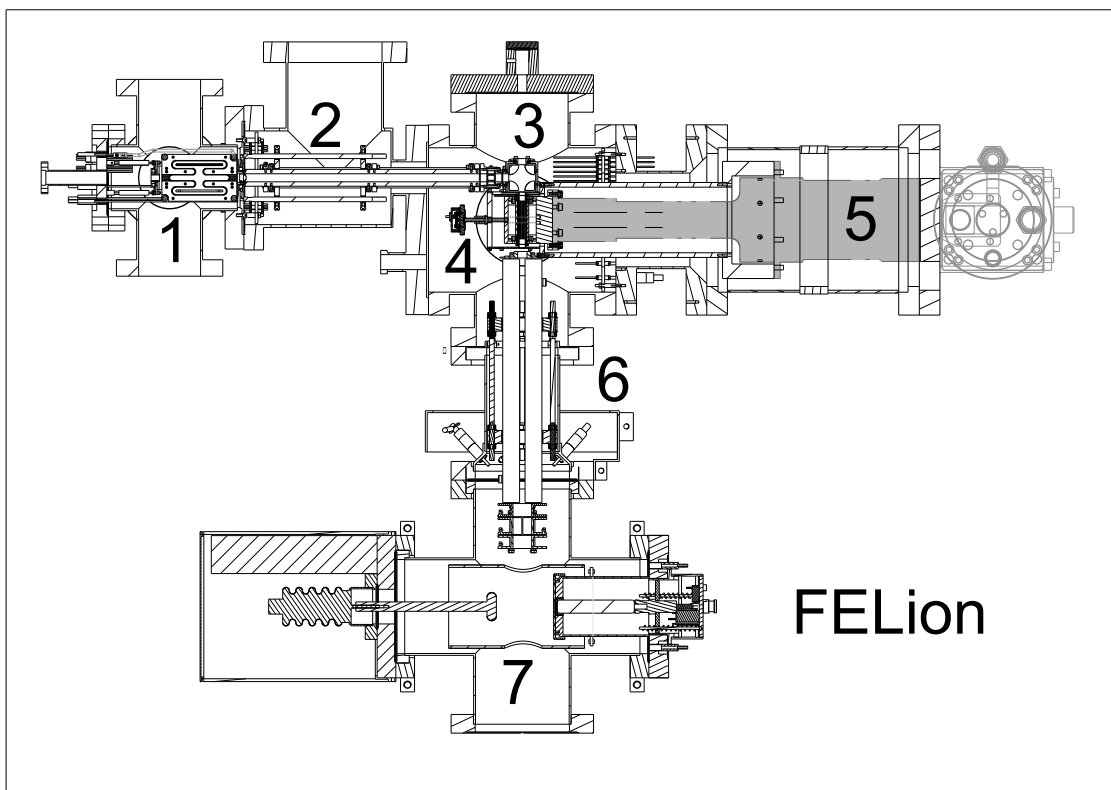


Figure 1.1: Technical Drawing of FELion. In the upper left corner the Storage Ion Source (1) with the newly designed vacuum chamber is visible. The part to the right of the source is the first quadrupole (2), followed by the quadrupole-bender (3), and the 22-pole trap (4) itself. Above the quadrupole bender one of the two optical ports is placed. The trap is mounted on the coldhead (5), shown on the right side of the sketch. Below the trap the second quadrupole (6) is visible, followed by the 4-way-cross that contains the Daly-type detector (7). The second optical port is located at the lower end of the 4-way-cross.

for the timing. The control software for this system is presented briefly in chapter 3. Additionally the Compact RIO system is space-saving compared to the former electronic system. Thus, the new ion trap apparatus is also more compact and easier to transport.

2

Design FELion & Test Measurements

In this chapter the different parts of the new 22-pole ion trap apparatus are described in detail. The sections are introduced in the chronological order of the experiment, starting with the production of the ions in the Storage Ion Source and ending with their detection in the Daly-type ion detector. In each section the corresponding parts are described giving technical details along with test and calibration measurements.

2.1 Vacuum System

For investigations of very reactive ions, ultra-high vacuum (UHV) conditions are needed. Due to this FELion is equipped with different oil-free magnetically levitated turbo pumps from Pfeiffer Vacuum GmbH. On the main chamber a Pfeiffer HiPace 700 (up to $685 \ell/s$ for N_2 , with TC 400 electronic unit and DCU control unit) is mounted and on the chamber of the first quadrupole a Pfeiffer TMU 200MP (up to $180 \ell/s$ for N_2 , with TCM 1601 electronic and control unit). The HiPace 700 has an extra backing pump Pfeiffer TPD 011-N (up to $10 \ell/s$ for N_2). The first backing pump for the complete vacuum system is a Varian IDP-3 scroll pump (up to $60 \ell/min$ for N_2). For measuring the pressure inside the vacuum chambers the FELion experiment is equipped with a Pfeiffer Compact Cold Cathode Gauge IKR-251 at the chamber of the first quadrupole and with a Pfeiffer Compact Full Range Gauge PKR-251. Both gauges are controlled and read out with a Dual Gauge Controller TPG262 from Pfeiffer. To protect the experiment a home-made interlock system is used, which switches off all high voltages in case of vacuum failure. Without baking typical base pressures of 10^{-8} mbar are reached.¹

2.2 The Storage Ion Source

One challenge for experiments with molecular ions is that they are highly reactive. Thus, the ions have to be generated during the experiments. For FELion one possible

¹Measured with the Pfeiffer PKR-251. These values are used in this thesis. In the meantime the PKR-251 is replaced by a Arun Microelectronics P003-025 UHV pressure gauge. The measured base pressure with this setup is in the range of 10^{-9} mbar.

type of ion source is the Storage Ion Source, which was invented by Dieter Gerlich ([11]). The main advantage of this design is that the ions are not only generated in the source, but they are also stored. Since the primary ions created by electron impact ionization (typical electron energy 20-40 eV, depending on the target ion) are hot and excited, the benefit of storing the ions in the source is that they can undergo collisions with the present neutral gas (typical density 10^{13} cm^{-3} , mean free path few ten mm), and thereby they will leave the source with a narrow energy distribution and in the electronic ground state. In addition, also reactions with the neutral gas are possible. By this, more complex molecular ions can be formed in the source, which are not accessible with other methods. Figure 2.1 shows a typical unfiltered mass scan from the source with CD_3H as a precursor gas.

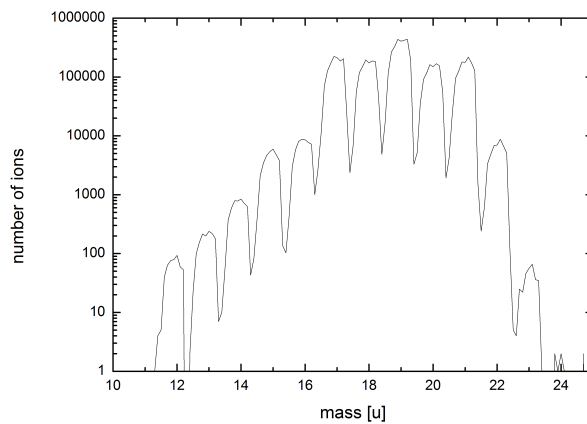


Figure 2.1: Unfiltered mass scan from the storage ion source operated with CD_3H as precursor gas at a pressure of $\sim 9 \cdot 10^{-6}$ mbar. The mass spectrum was recorded in the range of 10-25 u. The maximum electron energy for the ionization was ~ 37 eV. The recorded spectrum shows a variety of different ionic species CH_nD_m ($n, m = 0-5$).

The operating principle of the Storage Ion Source is quite simple. The ions are produced by electron impact ionization of neutral precursor gas in the source. The ions are then stored for some time in the source by using an inhomogeneous RF field and DC potentials. At a certain time the ions are extracted into the first quadrupole by applying an adjustable pulse on the exit electrode (called B0 in the following).

2.2.1 Technical Design

The Storage Ion Source is made of 1 mm thick molybdenum plates. The plates themselves are formed in a "double-H-shape" (see figure 2.2(b)). The central stack for the source is built of eight of these plates, which are electrically insulated by ruby-balls of 1 mm diameter. Four of the eight plates are connected to each other alternately. To these group of plates the RF-voltage, typical amplitudes are in a range between 50 V and 200 V, is applied. On the top and bottom of the source the filament units are mounted on the endplates, which are held on a positive DC-potential (typically 1-2 V) to confine the ions inside the source together with the applied RF-fields. The filament units (see figure 2.4(a)) consist of a filament (rhenium 99.97 %, diameter 0.2 mm)

which is clamped between two springs made of 0.5 mm thick molybdenum. Typical operational values for the filaments are ~ 7 V and 2.8 A. The filament is covered by the repeller and the focus, both are made of 0.5 mm thick molybdenum plates (unalloyed vacuum arc-cast molybdenum from WHS Sondermetalle) as well. The repeller is connected to the negative end of the corresponding filament. During the experiment DC-voltages are applied to these two components to focus and accelerate the electrons into the source. A scheme of this wiring concept is shown in figure 2.3. From this scheme the maximum electron energy can be estimated by the difference between the source float and the repeller voltage plus the negative voltage of the filament (typically ~ -7 V). A test-measurements for the repeller is shown in figure 2.6. At the front and back of the source the apertures B0 and B-1 are mounted. They are used to confine the ions in the axial direction of the source by applying positive DC-potentials and B0 to extract a short ion pulse for the experiments. Two test measurements of the functionality of B0 are shown in the figures 2.7(a) and 2.7(b) in the next subsection.

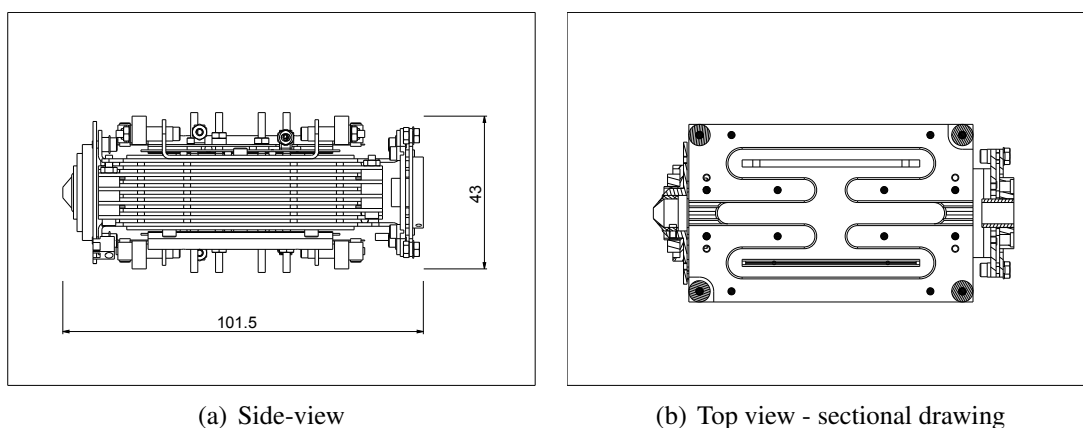


Figure 2.2: Technical drawings of the Storage Ion Source. (a) shows a side view of the ion source. The source mainly consists of eight plates, which are connected to the RF voltages. On top and bottom the endplates together with the filaments are placed. The endplates are set to a positive potential to confine the positively charged ions inside the source together with the applied RF fields. On the left side *B0* is visible. By applying a short negative voltage pulse to this electrode the ions are extracted out of the source. (b) is a sectional drawing of the source viewed from top. The double-H structure is clearly visible. By producing the ions in the left or right channel, but extracting them out of the source from the middle one, it is ensured that the ions undergo enough collisions with the neutral gas to de-excite.

The Storage Ion Source of FELion is driven by a self-made RF-generator with a frequency of ~ 6.3 MHz of the push-pull type ([24], [25]), using QQE06/40 double tetrode tubes. The circuit diagrams of both RF-generators (for the Storage Ion Source and the first quadrupole mass filter) can be found in the appendix (figures 8.1 and 8.2).

2.2.2 Test Measurements

To check the performance of the newly built Storage Ion Source for FELion some test measurements were carried out. On one hand, these measurements are used to ensure the functional capability of the source. On the other hand, it is possible to obtain some operational benchmarks, which can be used as a reference to check the performance of

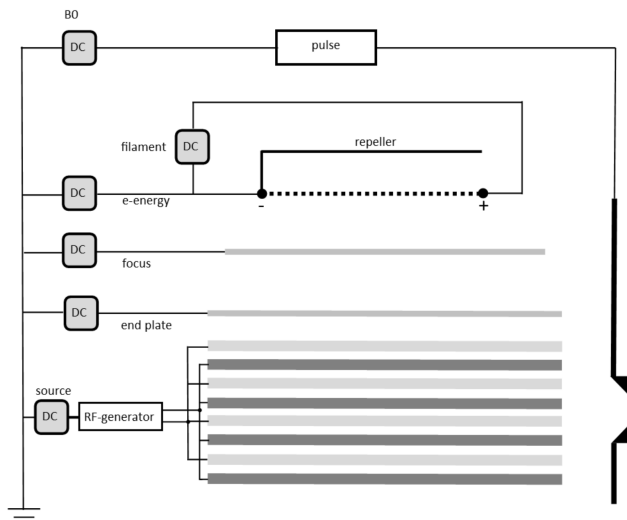


Figure 2.3: Wiring concept of the SIS. The eight plates of the SIS are connected alternately with the RF source. A DC potential can be added to the RF field (source float, normally near to ground). The endplates are on a positive DC potential, as well as the focus. The repeller is on a negative DC potential and is in addition connected to the negative end of the filament. By this, the maximum electron energy is given by the difference between the source float and the negative potential of the repeller. Due to the voltage drop over the filament of usually ~ 7 V, the electron energy is smeared. B0 is on positive potential and for extracting the ions into the first quadrupole mass spectrometer a negative pulse can be applied.

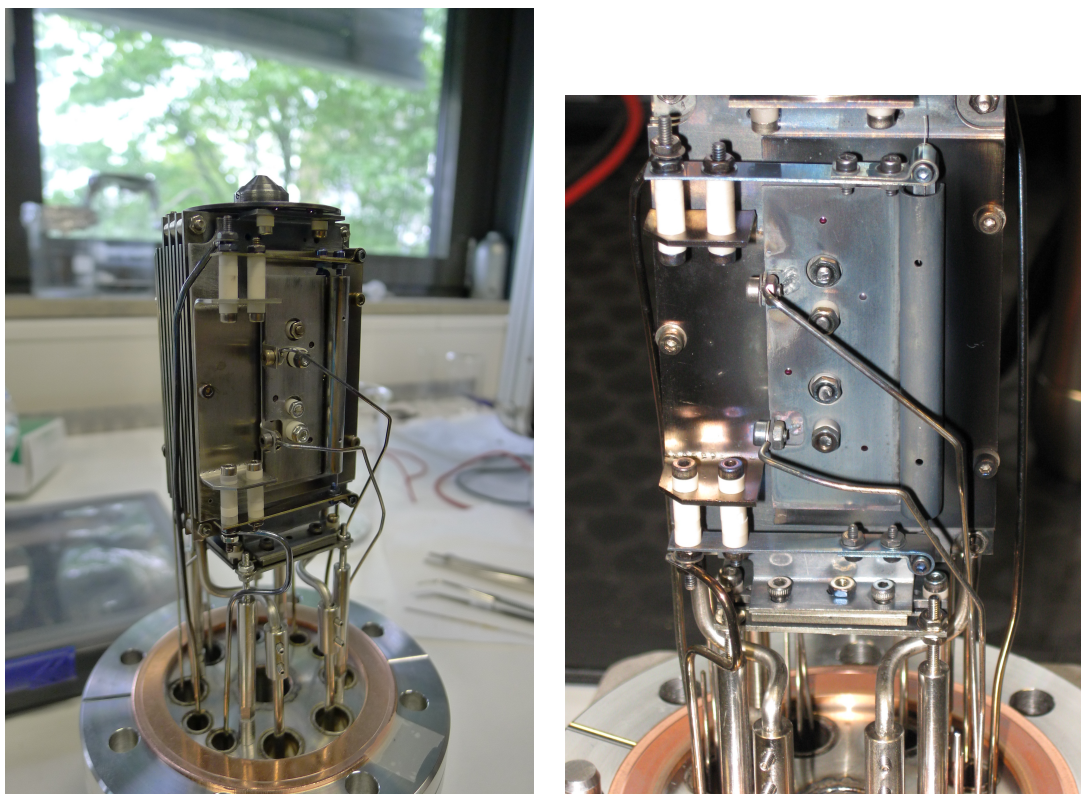
the source in case of problems during operation.

One reference value for the source is the capacitance of the Storage Ion Source, when it is mounted in the 6-way-CF63-cross. The capacitance between the RF plates is ~ 200 pF measured directly at the BNC-connectors at the source connection box. Together with the 1.5 m long BNC-cables the overall capacitance is 300 pF. The first test measurement is to check if the source oscillates. For this test different nominal voltages (read out from the RF-generator) were applied and the peak-to-peak value from the RF-plates of the source was measured. The results of this test are given in table 2.1 together with some values measured with the LIRTRAP source. The values for the

Table 2.1: Measured RF characteristic of the Storage Ion Source. For this measurement the applied voltage at the RF-generator (U_{set}) was tuned in the range of 100-250 V and the amplitude at the RF-plates (U_1 and U_2) was recorded. For this, 1 M Ω -probes with a capacity of 12 pF were used. The RF-frequency of the Storage Ion Source was 6.04 MHz. The values measured at the plates were peak-to-peak values.

$U_{\text{set}}[\text{V}]$	$U_1[\text{V}]$	$U_2[\text{V}]$	$U_{\text{LIRTRAP}}[\text{V}]$
100	57.5 ± 1.0	61.5 ± 1.0	74
150	93 ± 2	100 ± 2	-
200	129 ± 2	138 ± 2	165
250	173 ± 5	189 ± 5	-

new source are a little lower than for the source used in LIRTRAP, but the deviation is acceptable and probably due to the higher overall capacitance of the new source



(a) SIS mounted on feedthrough-flange

(b) Close-up of one filament unit

Figure 2.4: Photos of the Storage Ion Source. The left picture shows the complete ion source mounted on the CF63 feedthrough-flange. The cone-shaped electrode on top is $B0$ (made of 99.95% molybdenum). The inlet of $B0$ can be exchanged. The one currently used in the experiment has an opening of 3 mm. (b) Close-up of one filament unit. On the right side part of the rhenium wire filament (diameter 0.2 mm; 99.97% rhenium) is visible. The filament unit is made of 99.95% molybdenum-plates (thickness 0.5 mm; Unalloyed vacuum arc-cast)

(mostly because of the longer BNC cables).

To investigate the storage capability of the source we measured the ion current as a function of the applied RF-amplitude. For this test the ion source was operated with air as a precursor at a pressure of $5 \cdot 10^{-5}$ mbar. The maximum electron energy for these measurements was 27 eV. The ion current was measured with the Keithley 6485 Picoammeter on the shorted rod-pairs of the first quadrupole. They were held on a negative potential of -20 V and the aperture $B0$ was held on -10 V to accelerate the ions in the direction of the first quadrupole. The endplates and $B-1$ were on a positive potential of 5 V to confine the ions in the trap. The set value for the applied RF-voltage was varied in the range of 0-250 V. For the measurement, which is shown in figure 2.5, the first filament was used and operated at 7 V and 2.8 A. The ion current as a function of the RF amplitude shows the expected behavior. For too small RF amplitudes it is not possible to store the ions in the source. This results in a vanishing ion current on the first quadrupole. For nominal RF-amplitudes larger than 100 V the ions are stored and the measured ion current increases. At ~ 230 V there is a maximum in the detected ion current of approx 10.5 nA. For larger RF amplitudes the ion current decreases again, which is expected, because the applied voltages at the endplates and at $B-1$ are too small to confine the ions in the source.

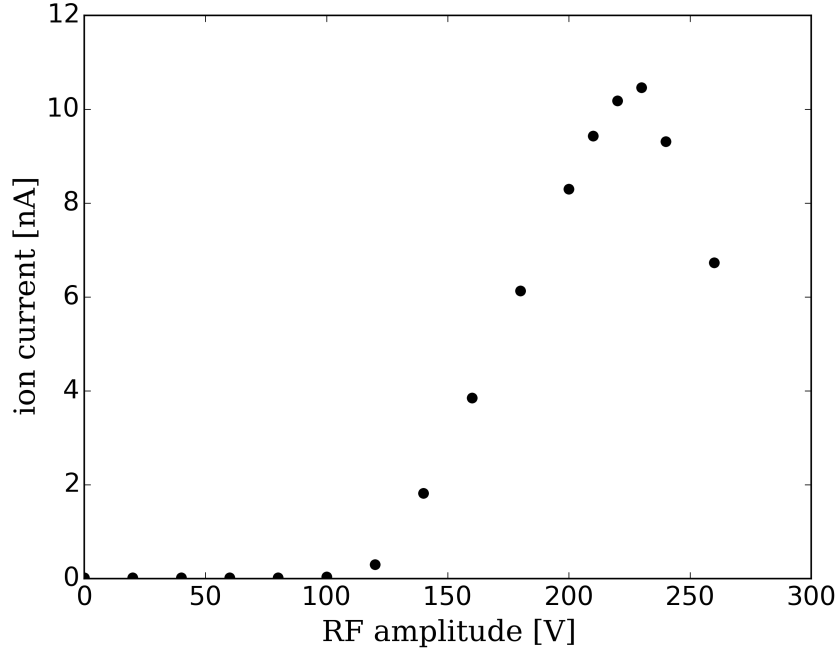


Figure 2.5: Ion current as a function of RF-amplitude. For this measurement the RF-amplitude of the source was varied. The ion current is measured on the first quadrupole with the Keithley 6485 Picoammeter, and the two pairs of rods were connected with each other. The potentials were -20 V for *quad1*, and -10 V for *B0*. The source was operated with air at a pressure of $5 \cdot 10^{-5}$ mbar and with an maximum electron energy of 27 eV.

The maximum value of the ion current of ~ 23 nA ($\sim 2 \cdot 10^9$ ions), measured on Blende 0 at a pressure of $8 \cdot 10^{-5}$ mbar and an electron energy of ~ 23 eV, is in principle satisfying, but to get an idea of the efficiency of the source this value must be connected to the electron current and the pressure of the precursor gas in the source. With this values the efficiency s can be calculated:

$$s = \frac{I_{\text{ion}}}{I_{\text{electron}} \cdot p} \quad (2.1)$$

I_{ion} and I_{electron} are the ion current and the electron current, respectively, and p is the pressure of the precursor gas in the source. The electron current was measured on the focus, using the Keithley 6485 Picoammeter. This test was performed for both filaments operated at 7.5 V and 3 A. The focus was set to 14 V and the voltage on the repeller was tuned in the range of 0-16 V. From these measurements one could estimate a maximum electron current of (1.3 ± 0.1) mA for both filaments. With these values s can be derived.

$$s = \frac{23 \text{ nA}}{1.3 \text{ mA} \cdot 8 \cdot 10^{-5} \text{ mbar}} = 0.22 \text{ mbar}^{-1} \quad (2.2)$$

This value for s is relatively small compared to the efficiency of 19 mbar^{-1} (for nitrogen) of a commercial Bayard-Alpert Ion Gauge from AML. However, the calculated

value for s is only a lower limit, since only a maximum repeller voltage of -16 V (corresponding to the maximum electron energy of ~ 23 eV) could be used for the test. The maximum electron energy is high enough to ionize the nitrogen (ionization energy ~ 14.5 eV) and oxygen (13.6 eV) molecules in the source, but the electron energy used in Bayard-Alpert Ion Gauge from AML (electron energy ~ 200 eV) is at approximately a factor of 10 higher. The distinct effect of the applied repeller voltage on the measured ion current is shown in figure 2.6. For this measurement the filament was operated at slightly lower settings of 6.8 V and 2.7 A and the ion current was measured on the rods of the first quadrupole and not on B0 in comparison to the measurements discussed above. This results in the overall lower maximum ion current of ~ 7 nA instead of 23 nA, but nevertheless the influence of the repeller voltage, i.e. the electron energy, on the measured ion current is clearly visible.

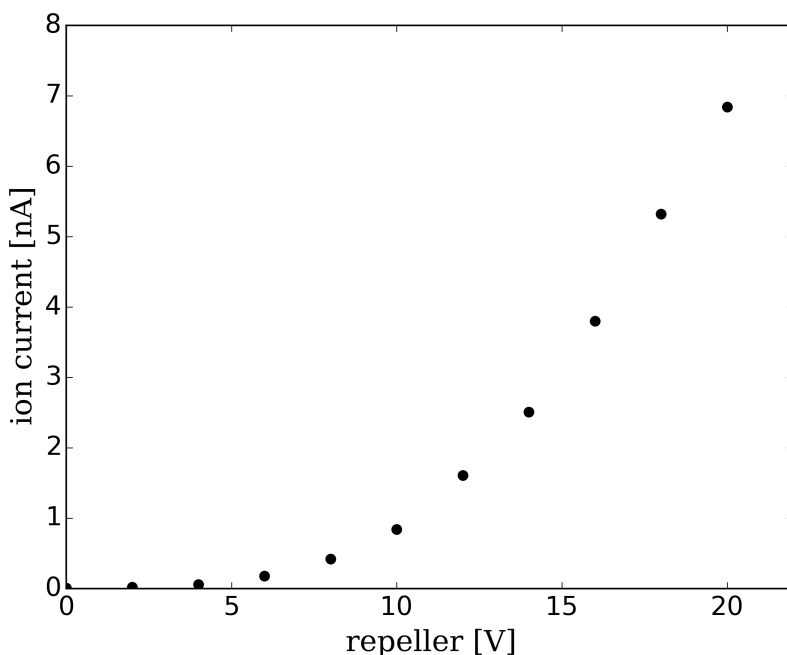


Figure 2.6: Ion current as a function of *repeller* voltage measured on the rods of the first quadrupole. The maximum electron energy is ~ 27 eV. The onset for the measured ion current at a *repeller* voltage of 6 V corresponds to an maximum electron energy of ~ 13 eV, which is close to the ionization energy of oxygen. Since the measurement was not performed with the dedicated power supply, it is limited to low voltages.

The measurements shown in figure 2.6 demonstrates also that the transmission through B0 is working and the ions can be extracted out of the source in the direction of the first quadrupole.

The last two test measurements that are presented here address the functionality of B0. Since the idea of the ion source is to store the produced ions in the source and extract them at a certain time into the experiment, one would expect at the beginning of a long (a few milliseconds) pulse that the density of the ions is higher than in the end. Another interesting aspect is the shape of the ion pulse. The main difficulty for this is that if the applied pulse on B0 is not fast enough the pulse flank might be blurred. In the best case the detected ion pulse has a rectangular shape with the same length as the pulse applied to B0. For these measurements the strategy has to be changed, since

only static measurements are possible with the Picoammeter. The basic idea for the measurements presented here is to use the Daly-detector and the Ortec 996 counter in combination with a gate signal. For the measurements, the gate-width was set to $5\ \mu\text{s}$ and the position relative to B0 was shifted in time. Thus, time-resolved measurements of the ion pulse from the source were possible. The disadvantage of this method is of course, that the ion pulse has to pass through the whole experiment, which can influence the ion pulse. The measurements recorded with this method are shown in the figures 2.7(a), and 2.7(b).

The first test (figure 2.7(a)) addresses the shape of the pulse. For this, the pulse length of B0 was varied between $10\ \mu\text{s}$ and $400\ \mu\text{s}$. First of all, it is apparent that the first edge of the ion pulse is steep. This means that the applied pulse on B0 is fast enough to extract the ions in the right way out of the source. For all pulse-lengths the first ions arrive $\sim 100\ \mu\text{s}$ after the start of the pulse for B0. Together with the path length of $\sim 870\ \text{mm}$ through the experiment one can derive a velocity of $8700\ \frac{\text{m}}{\text{s}}$ for the ions. This is equal to the energy the ions would gain by an acceleration voltage of $\sim 6\ \text{V}$, which is a reasonable value for the experiment. For all settings the ion pulse is broadened by a constant value of $\sim 50\ \mu\text{s}$. This is due to the fact that the ions have different start velocities in the source, when they are extracted, leading to a dispersion in the arrival time. Another interesting aspect is the dip in the ion pulse, which is visible for the three longer pulse lengths. The reason for this is that the detector system is not fast enough and is blacked out if too many ions hit the detector. From the experiments a maximum count rate of $30\ \text{MHz}$ for the detector system was calculated (for the detector system see section 2.7).

The second test is shown in figure 2.7(b). For these measurements, the pulse length for B0 was $1500\ \mu\text{s}$ and $2000\ \mu\text{s}$, respectively. If the source works correctly the ion density per $5\ \mu\text{s}$ -bin should be higher for the beginning of the pulse than for the end. This can be explained as follows: if the storage in the source works accurately, the source is completely filled with ions in the beginning. By applying the extraction pulse on B0, the ions can leave the source and the source is emptied. During the time the pulse is applied the source still produces ions, but they are extracted immediately and so the density of the ions decreases with time. From figure 2.7(b) one can derive a half-life period of $\tau = \frac{1}{700\ \mu\text{s}}$.

This is exactly what can be seen in figure 2.7(b). At the beginning of the pulse, the number of ions counted in a bin is much higher than in the end. In the second measurement the number of ions per bin is roughly constant in the end. The value of 20 ions/bin corresponds to approximately $1.6 \cdot 10^6$ ions per second on the detector. This value is comparable to the typical number of ions obtained in the cw mode of the Storage Ion Source. This number can be also compared to the maximum value of 160 ions/bin, which results in a superelevation factor of ~ 8 . Since it is possible that the detector is already saturated with the 160 ions/bin this number is a lower limit for this value.

2.3 The First Quadrupole Mass Filter

The function of the first quadrupole is to ensure that only one mass-to-charge ratio $\frac{m}{q}$ is guided from the source into the 22-pole ion trap for the experiments. This is necessary,

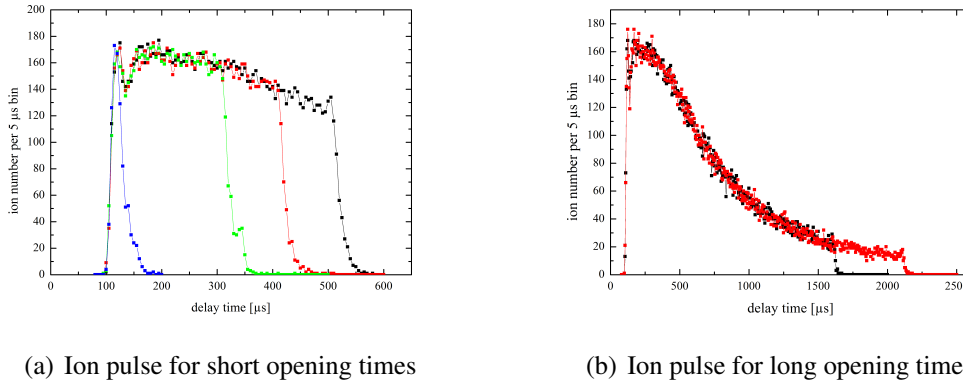


Figure 2.7: Ion pulses as a function of time. For these measurements the opening times for $B0$ were varied. The Ortec 996 counter was controlled with a $5\mu\text{s}$ gate, which was shifted in time with respect to $B0$. By this the time resolution of the pulse was recorded. (a) shows the result for opening times between $10\mu\text{s}$ (blue), $300\mu\text{s}$ (green), $400\mu\text{s}$ (red), and $500\mu\text{s}$ (black). (b) shows the same measurements for opening times of $1500\mu\text{s}$ (black), and $2000\mu\text{s}$ (red). The maximum value of 160 ions/bin is possibly limited by saturation effects of the detector system

since a lot of different ions are produced in the Storage Ion Source (see section 2.2). Under standard conditions in the source only singly charged ions are produced. Thus, in our experiments the ratio is only given by the mass of the selected ion. The selection is achieved by applying a combination of AC- and DC-difference-voltages to the two pairs of rods of the quadrupole. A comparison between the theoretical values and the experimental values for the quadrupole can be found in subsection 2.3.2. Before the technical design and the test measurements are presented, a short summary of the theory for quadrupoles is given. For a more detailed discussion see ([26]).

The field of a quadrupole in Cartesian coordinates is given as:

$$\vec{E} = E_0 \cdot (\lambda \vec{x} + \sigma \vec{y} + \gamma \vec{z}) \quad (2.3)$$

The field of the quadrupole has to fulfill the Laplace equation, therefore:

$$\vec{\nabla} \vec{E} = 0 \quad (2.4)$$

A commonly used solution for this condition is

$$\lambda = -\sigma; \gamma = 0 \quad (2.5)$$

To determine the potential of the quadrupole, the field, given in 2.3, has to be integrated under the conditions defined in 2.5. Thus, for the potential one can write:

$$\phi = \frac{\phi_0 \cdot (x^2 - y^2)}{2 \cdot r_0^2} \quad (2.6)$$

with $\lambda = -\frac{1}{r_0^2}$ and ϕ_0 the applied voltage at the rods. In order to derive the time dependency of ϕ_0 the equations of motion have to be investigated. In Cartesian coordinates they can be written as:

$$\ddot{x} + \left(\frac{e}{m \cdot r_0^2} \right) \cdot \phi_0 \cdot x = 0 \quad (2.7)$$

$$\ddot{y} - \left(\frac{e}{m \cdot r_0^2} \right) \cdot \phi_0 \cdot y = 0 \quad (2.8)$$

$$m \cdot \ddot{z} = 0 \quad (2.9)$$

if the longitudinal axis is oriented in the z-direction. By using a superposition of time depended part and a constant part for ϕ_0 the quadrupole works as a high pass mass filter in x-direction and as a low pass mass filter in y-direction. Through a combination of these features it is possible to use the quadrupole as a mass filter. For the potential ϕ_0 one choose

$$\phi_0(t) = U - V \cdot \cos(\omega t) \quad (2.10)$$

where U is constant and V is the amplitude of the sinusoidal part of the potential. By applying this to the equations 2.7 and 2.8 one can write

$$\ddot{x} + \left(\frac{e}{m \cdot r_0^2} \right) \cdot (U - V \cdot \cos \omega t) \cdot x = 0 \quad (2.11)$$

$$\ddot{y} - \left(\frac{e}{m \cdot r_0^2} \right) \cdot (U - V \cdot \cos \omega t) \cdot y = 0 \quad (2.12)$$

$$(2.13)$$

Defining the parameters

$$a_u = a_x = -a_y = \frac{8 \cdot e \cdot U}{m \cdot \omega^2 \cdot r_0^2} \quad (2.14)$$

$$q_u = q_x = -q_y = \frac{4 \cdot e \cdot V}{m \cdot \omega^2 \cdot r_0^2} \quad (2.15)$$

$$(2.16)$$

and using the parameter ξ :

$$\xi = \frac{\omega \cdot t}{2} \quad (2.17)$$

for the time dependence, the equations of motion 2.11 and 2.12 can be written as

$$\frac{d^2u}{d\xi^2} + (a_u - 2 \cdot q_u \cdot \cos 2 \cdot \xi)u = 0 \quad (2.18)$$

where u is either x or y . Equation 2.18 is called Mathieu equation and can be used to describe the trajectories of the ions in the quadrupole. This results in a so called stability diagram. A scheme this diagram is shown in figure 2.8.

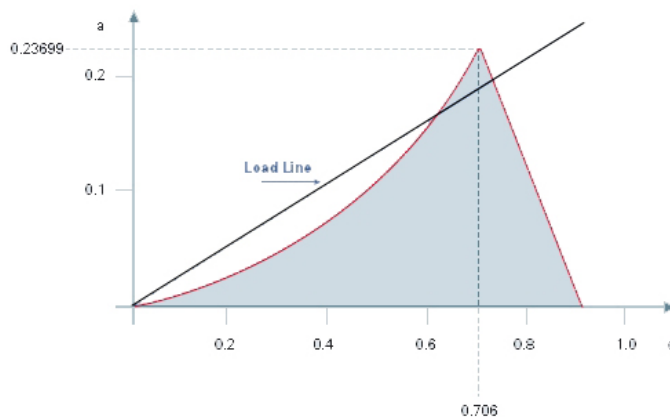


Figure 2.8: Stability diagram of a quadrupole mass filter. For $a = 0$ the load line is on the y -axis. This means that the quadrupole is working as an ion guide and in principle all masses are transmitted. To achieve the best mass resolution of the quadrupole the load line has to hit the tip of the triangle at $(a=0.237, q=0.706)$. Picture based on [27].

The tip of the triangle is located at $(a=0.237; q=0.706)$. If the quadrupole is operated under these conditions for a given mass m of an ionic species the mass filter behavior of the quadrupole is best. This is used to derive the theoretical values in table 2.3 in section 2.3.2.

2.3.1 Technical Design

The first quadrupole (for a technical drawing see figure 2.9) consists of four rods with a length of 250 mm. The rods themselves are manufactured out of stainless steel rods with two different radii. The relevant radius for the quadrupole is the radius on the inner side of 5 mm. The four rods are positioned on a circle in a way that the enclosed radius is 4.3 mm, giving a ratio of $\frac{r}{r_0} = 1.163$, which is close to the optimum ratio of 1.1468 ([26]). However, due to difficulties with the production of the rods, this enclosed radius is in reality only 4.275 mm, which results in a ratio of 1.1696, and it is not perfectly constant over the whole length. The two pairs of rods are mounted on a support part, which is attached to the vacuum chamber of the source. The electrical supply lines for the quadrupole are installed at the 6-way-cross of the source as well. Thus, the vacuum chamber of the source and the first quadrupole are one unit, which can be removed or attached to the experiment in one part. At the end of the quadrupole an Einzel-lens is mounted, consisting of a four-fold electrode in the middle framed by two electrodes to focus and steer the ions. A 3D-view of the lens together with the designations for the different electrodes is given in the appendix (see figure 8.5).

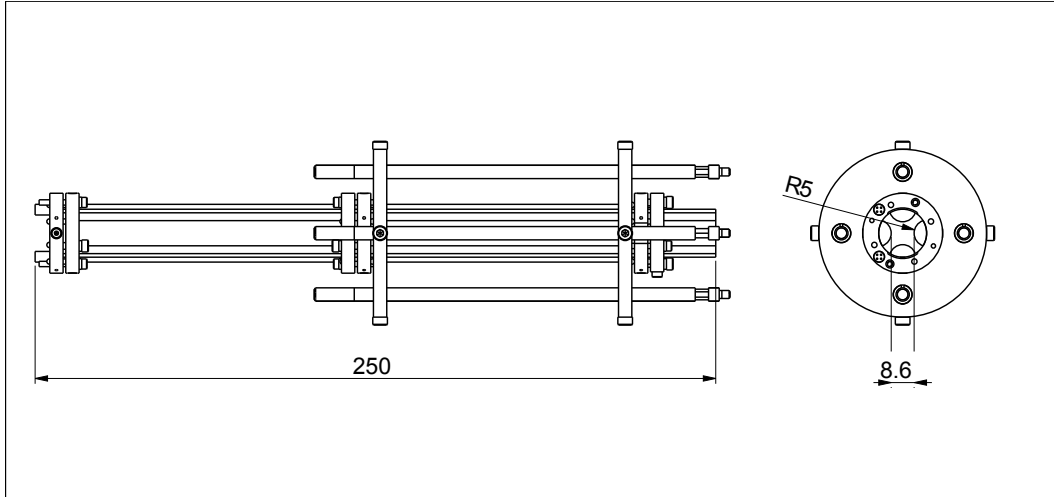


Figure 2.9: Technical drawing of the first quadrupole. Its length is 250 mm and the minimal distance between the rods is 8.6 mm. The rods themselves are manufactured out of stainless steel rods with a radius on the inner side of 5 mm. This results in a ratio of $\frac{r}{r_0} = 1.163$, which is close to the optimum value of 1.1468. ([26])

The first quadrupole of FELion is driven by a self-made RF generator of the push-pull type ([24], [25]). For the mass range of 1-100 u the frequency of the quadrupole is around 1.5 MHz.

2.3.2 Test Measurements

The first reference value for the quadrupole is again the capacitance. In this case a capacitance of 101 pF was measured including the BNC-connectors at the connection panel for the first quadrupole as well as the 30 cm long BNC-cables from the panel to the feedthroughs in the 6-way cross. The overall capacitance including the BNC-cables from the panel to the RF-generator is ~ 201 pF.

In the next step, the first quadrupole is connected to the 1.5 MHz-RF-generator and the amplitudes of the AC-voltage at the rods is recorded as a function of the set-voltage at the RF-generator (see table 2.2) The measured RF-frequency was 1.47 MHz.

The plot of the calibration measurement is shown in figure 2.10, and the amplitude was fitted with a linear function to

$$V_0[\text{V}] = -12.31 \text{ V} + 0.925 \cdot U_{\text{set}} \quad (2.19)$$

With these values, the maximum mass range of the first quadrupole can be derived as well as theoretical settings for the filtering of different masses, and be compared to experimental values. For the calculation of the theoretical values, we use the two parameters a and q :

Table 2.2: Calibration of the first quadrupole. For this measurement the amplitude (V_0) of the AC-voltage at the rods of the first quadrupole were recorded as a function of the set-voltage ($V_{0,\text{set}}$) at the RF-generator. The measured RF-frequency was 1.47 MHz.

$V_{0,\text{set}}$ [V]	V_0 [V]
25	7.2
30	14.0
40	23.6
50	33.0
60	44.0
70	55.0
80	64.5
90	74.0
100	81.0
150	126
200	170

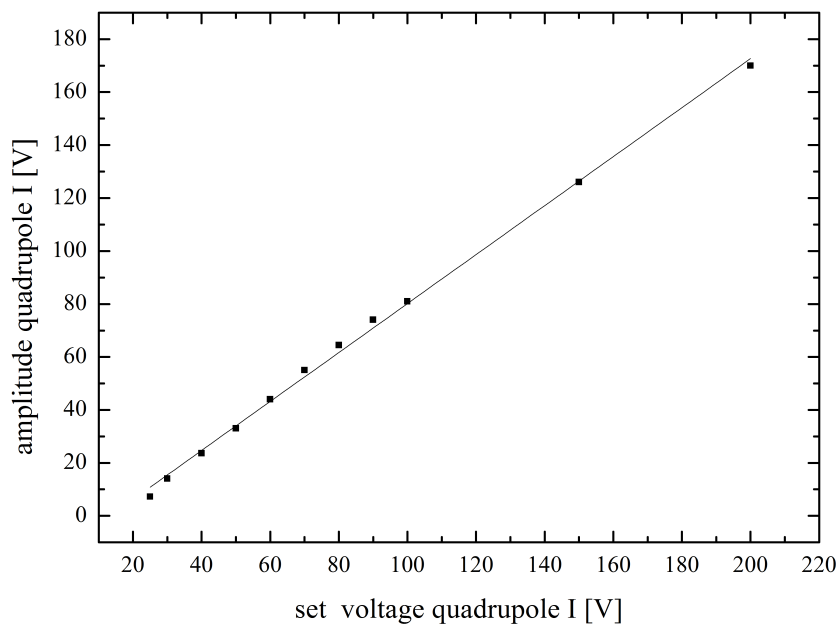


Figure 2.10: Calibration measurement of the first quadrupole. The amplitude V_0 recorded at the rods of the first quadrupole is plotted as a function of the set voltage at the RF-generator for the first quadrupole. The solid line is a linear fit to the data. The result of this fit is given in equation (2.19).

$$a = \frac{8 \cdot e \cdot U_0}{m \cdot \omega^2 \cdot r_0^2} \quad (2.20)$$

$$q = \frac{4 \cdot e \cdot V_0}{m \cdot \omega^2 \cdot r_0^2} \quad (2.21)$$

$$(2.22)$$

where U_0 is the applied DC-difference voltage, V_0 the amplitude of the AC-voltage, e the charge of the selected ion, m the mass, ω the angular frequency of the oscillation, and r_0 the enclosed radius of the quadrupole. For the mass selecting mode the values for a and q can be obtained from the stability diagram for a quadrupole (for a complete description of the theory for quadrupoles see [26]). For $a = 0.237$ and $q = 0.706$, and a given mass m one can now calculate the theoretically required voltages. For these calculations, summarized in table 2.3, the measured frequency of 1.47 MHz and the measured enclosed radius of 4.275 mm were used.

Table 2.3: Comparison between theoretical (index t) and experimental (index e) settings for the first quadrupole to select different ionic species.

ion	mass [u]	$V_{0,t}$ [V]	$U_{0,t}$ [V]	$V_{0,e}$ [V]	$U_{0,e}$ [V]
H_3^+	3	8.55	1.44	7.88	1.50
CD^+	14	39.92	6.70	39.49	6.05
CH_2D^+	16	45.62	7.66	45.04	7.35
CD_2H^+	17	48.47	8.14	47.82	7.45
NH_2D^+	19	54.18	9.09	54.29	8.50
C_2H^+	25	71.28	11.96	70.94	11.25
$C_2H_3^+$	27	76.99	12.92	76.49	12.05
CO^+	28	79.84	13.40	80.19	12.65
HCO^+	29	82.69	13.88	83.43	13.35
C_3H^+	37	105.50	17.71	107.02	16.70
$C_3H_2^+$	38	108.85	18.19	109.79	17.00
$C_3H_3^+$	39	111.20	18.67	112.57	18.10
$C_6H_5^+$	77	219.56	36.85	220.79	35.35

In table 2.3 the theoretically calculated values (with an index t) for V_0 and U_0 are listed for different ionic species together with the values obtained from the experiment (with an index e). A comparison of these pairs reveals that the experimental values are in very good agreement with the calculated ones.

With the current RF power supply (fug HCE35-350) a maximum $V_{set,max} = 350 \text{ V} \hat{=} V_{0,max} = 311.44 \text{ V}$ is possible, which results in a maximum selectable mass of

$$m_{max} = \frac{4 \cdot V_0 \cdot e}{q \cdot \omega^2 \cdot r_0^2 \cdot u} = 109 \text{ u}$$

For the experiments in Cologne this mass range is sufficient, but for the planned experiments with biomolecules at the FELIX facility it is probably too limited. Besides installing a power supply for higher voltages, there is also the possibility to reduce the frequency of the first quadrupole by changing the tubes in the RF-generator for the first quadrupole. If one assumes that the rest of the system does not change, the maximum mass for a frequency of 1.2 MHz is $m_{max} = 164 \text{ u}$ or $m_{max} = 236 \text{ u}$ for a frequency of 1 MHz. This is maybe a way to be considered, if there is the requirement for a wider mass range in the future.

The two measurements shown in figure 2.11 demonstrate the effect of different settings for the mass resolution. In both measurements the voltage V_0 of the quadrupole was $\sim 32 \text{ V}$ and U_0 was tuned from 5.0 V (black) to 5.5 V (red). The source was operated

with air at a pressure of $1 \cdot 10^{-4}$ mbar. Figure 2.11 shows that in case of the DC-voltage of 5.5 V the masses larger than 14 u are completely suppressed, whereas for 5.0 V they are clearly visible in the spectrum. Another interesting fact is that the number of ions on mass 14 u is nearly constant for the two different DC-voltages. This means that the transition losses are minimal, which is favorable for the experiments. The best measured mass resolution with the FELion setup was $\frac{m}{\Delta m} = 77$ (measurement of $C_6H_5^+$ with a resolution of <1 u). This value is a lower limit for the mass resolution of the first quadrupole.

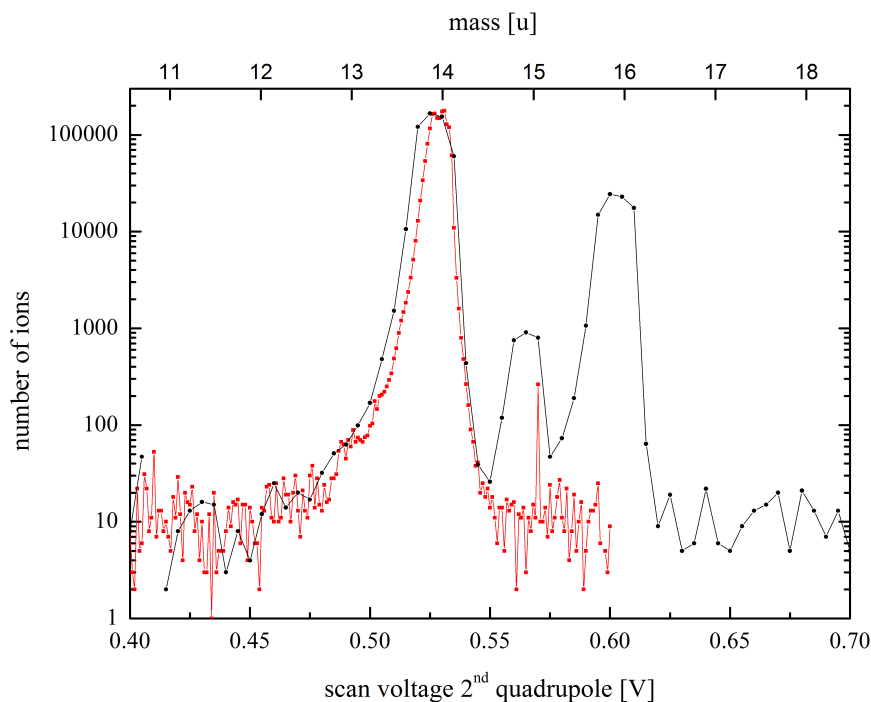


Figure 2.11: Cut-off behavior of the first quadrupole. The plot shows two different mass-spectra recorded with different U_0 voltages applied to the first quadrupole with the same V_0 voltage of ~ 32 V. The black curve was recorded with a U_0 voltage of 5.0 V and the red one with 5.5 V.

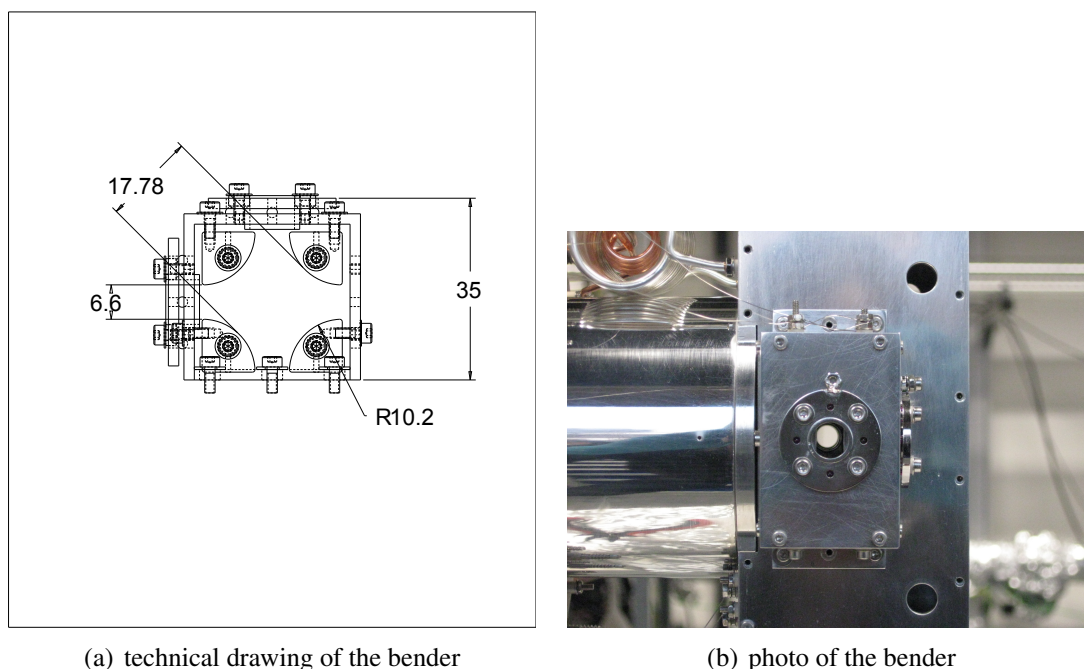
The measurements presented in this section demonstrate that the first quadrupole of FELion works properly. In addition, table 2.3 can be used in the experiment to find start settings for the selection of a special ionic species. Of course, the values given in the table have to be fine tuned for the experiment.

2.4 The Quadrupole Bender

The next part of the apparatus is the quadrupole bender. It is needed due to the angled design of FELion. After the ions leave the Einzel-lens of the first quadrupole, they enter the quadrupole bender and are deflected by 90° into the 22-pole ion trap.

2.4.1 Technical Design

The quadrupole bender (technical drawing see figure 2.12(a)) consists of four quarter rods with a radius of 10.2 mm. The inscribed radius of the quadrupole bender is 8.9 mm. Thus, the ratio $\frac{r}{r_0} = 1.146$ for the quadrupole bender. Like for a quadrupole the two opposite rods are connected to each other, but in case of the bender only a DC-voltage between +10 V and -10 V is applied to the rods. On the side to the first quadrupole and on the side to the optical port, there are two apertures installed to achieve an additional focussing effect for the ions. The bender itself is directly mounted on the housing of the 22-pole ion trap. A 3D view of the bender together with the designation of the different electrodes is shown in the appendix (figure 8.7).



(a) technical drawing of the bender

(b) photo of the bender

Figure 2.12: Technical drawing and photo of the bender. (a) In principle the bender is a small quadrupole rotated by 90°. The mass selected ions coming from the first quadrupole enter the bender on the left side through an entrance and focussing lens. The entrance to the 22-pole trap is on the bottom at the lower end of the bender. As for a quadrupole, the diagonal opposite rods are on the same electrical potential. At the top side of the bender there is a second focussing lens, which is normally not used in the experiments. (b) shows the bender mounted on the trap housing. The viewing direction is from the optical port to the 22-pole trap. In the assembled experiment, the first quadrupole is attached to the right side. The cylindrical part of the left side is the coldhead. In the left upper corner the two coils for the in coupling of the RF in the trap are visible.

For a more detailed description of the theory and the functionality of the bender see [28] and [29].

2.5 The 22-pole Ion Trap

The 22-pole ion trap is the central part of the instrument. A detailed description of the 22-pole ion trap design is given in [13]. The mass selected ions coming from

the source are stored in the trap with a reaction gas, and usually together with a buffer-gas (for example helium) in order to cool down the injected ions by collisions with the cold buffer gas. Most of the experiments are performed at low temperatures. To cool down the 22-pole trap it is mounted on a closed-cycle helium cryostat from Sumitomo Heavy Industries, Ltd. (RDK-408D2 coldhead in combination with a F50H compressor unit). The coldhead reaches a minimum temperature of ~ 3.9 K and the cooldown process from room temperature down to the minimum temperature takes only one hour (see figure 2.15(a)). Since the cryostat is not temperature controllable, a heating tape (Telemeter Electronic GmbH, HK5230R18.8L12A) is installed to enable experiments at higher and controllable temperatures. A characterization of the heater is given in table 2.4.

The construction of the ion trap allows two possibilities for the injection of the reaction- and the buffer-gas, either in a continuous way by a leak valve, or via a piezo-valve operated in "tickling" mode (typical pulse resolution $5\mu\text{s}$, typical pulse lengths 50 - $2000\mu\text{s}$ given by the resonance frequency of the piezo-valve). Commonly the reaction- and the buffer-gas are different, but for the experiments presented in this thesis (see chapters 5 and 6) helium is used for the buffer-gas as well as for the reaction-gas.

The cooldown process for the ions is a multi-stage process. First the neutral buffer-gas atoms are precooled before they enter the trap. By collisions with the cold walls of the trap-housing and the rods, they are finally cooled down to the ambient temperature. When the ions enter the trap, they will run into this cold bath of helium atoms and by collisions with them, they also cool down. The final temperature of the ions is typically higher than the temperature of the helium atoms. For more details see section 5.1.4 in chapter 5.

The functional principle of the 22-pole ion trap is similar to the one for the source. The ions are confined inside the trap by the RF-fields created by the 22 rods of the trap. Since the construction of the trap is rotationally symmetric around the optical axis, only two electrostatic electrodes, at the entrance and at the exit of the trap, are needed to store the ions in the trap. Both electrodes are usually held on a small positive potential of less than 1 V to minimize effects on the RF-fields. To open the entrance and the exit of the trap, negative pulses are applied at the electrodes. An overview of the different experimental methods, which can be realized with this setup, is given in chapter 3. Before the technical design and the different test measurements are presented, a short summary of the theory of motion of charged particles in oscillating fields is given. A substantially more detailed description of the function principle of the trap as well as a discussion of the potentials and the motion of the stored ions in the trap is given for example in [11].

The movement of a charged particle with the mass m and the charge q in an external electromagnetic field (\vec{E}, \vec{B}) can be described classically by

$$m \cdot \ddot{\vec{r}} = q \cdot \vec{E}(\vec{r}, t) + q \cdot \dot{\vec{r}} \times \vec{B}(\vec{r}, t) \quad (2.23)$$

For the movements of ions in 22-pole traps the second summand in equation 2.23 can be neglected. If one assumes in addition that the quasi-stationary field $\vec{E}(\vec{r}, t)$ can be written as a superposition of a static field $\vec{E}_s(\vec{r})$ and a time depended field $\vec{E}_0(\vec{r}) \cdot \cos(\Omega t)$ equation 2.23 can be simplified to:

$$m \cdot \ddot{\vec{r}} = q \cdot \vec{E}_s(\vec{r}) + q \cdot \vec{E}_0(\vec{r}) \cdot \cos(\Omega t) \quad (2.24)$$

If one neglects the static field and uses a homogenous field for \vec{E}_0 , equation 2.24 can be solved. As a special solution one obtains

$$\vec{r}(t) = \vec{r}(0) - \vec{a} \cos(\Omega t) \quad (2.25)$$

with

$$\vec{a} = \frac{q \cdot \vec{E}_0}{m \cdot \Omega^2} \quad (2.26)$$

To describe the motion of the ion a few assumptions are made. One assumption is that the field is more or less constant as a function of \vec{r} and the amplitude \vec{a} of the applied field is small, due to high enough frequencies of the field. It is also assumed that the solution \vec{r} can be written as a combination of a slow drift part $\vec{R}_0(t)$ and a fast oscillating movement $\vec{R}_1(t)$. This means

$$\vec{r}(t) = \vec{R}_0(t) + \vec{R}_1(t) \quad (2.27)$$

with \vec{R}_1

$$\vec{R}_1(t) = -\vec{a}(t) \cdot \cos(\Omega t) \quad (2.28)$$

By expansion of $\vec{E}_0(\vec{r})$ around \vec{R}_0 one obtains a time-independent mechanical potential, which can be used to calculate the force that affects the charged particles.

$$V^*(\vec{R}_0) = \frac{q^2 \cdot E_0^2(\vec{R}_0)}{4 \cdot m \cdot \Omega^2} + q\Phi_s \quad (2.29)$$

The equation of motion for the drift part of the solution can now be written as

$$m\ddot{\vec{R}}_0 = -\nabla V^*(\vec{R}_0) \quad (2.30)$$

V^* is called effective potential. The shape of the potential is determined by the given field geometries. In figure 2.13 the effective potential for a Paul-trap and a 22-pole ion trap are shown. The effective potential of the 22-pole trap is remarkable steeper than for the Paul-trap, resulting in larger field free region inside the trap.

For storing ions in such a potential the value of the stability factor η

$$\eta = 2n(n-1) \cdot \frac{q \cdot V_0}{m\Omega^2 r_0^2} \cdot \hat{r}^{n-2} \quad (2.31)$$

with $n=11$ for the used 22-pole ion trap, V_0 amplitude of the applied AC-field, $\hat{r} = \frac{r}{r_0}$, and r_0 inner radius of the trap, must be less than 0.3.

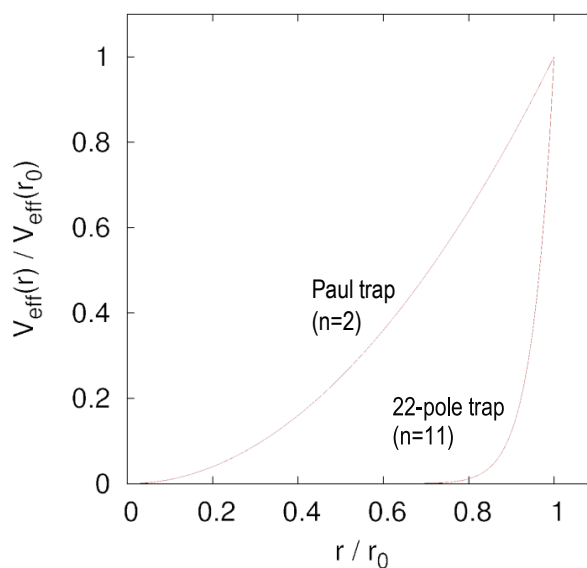


Figure 2.13: Comparison of the effective potentials of a Paul-trap and a 22-pole ion trap. The effective potential of the 22-pole trap is considerably steeper than the potential of the Paul-trap. This results in a larger field free region inside the trap for the 22-pole trap geometry.

2.5.1 Technical Design

In figure 2.14(a) two views of a technical drawing of the 22-pole trap are shown. The trap has an overall length of 59.4 mm including the entrance and the exit electrode. The radius inside the trap is 5 mm, whereas the inner radius of the two electrodes is 3.3 mm. The trap is made of two pieces with 11 rods each. The rods have a circular shape with a radius of 0.5 mm. In contrast to the predecessor version, these pieces are manufactured out of one chunk of stainless steel for better conductance. The rods are installed in a copper housing, which is directly mounted on the second stage of the coldhead. The different teflon supply lines, with an inner diameter of 3 mm, for the buffer- and the reaction-gases are reaching directly into the copper housing. The feedthroughs for the electrical connections for the 22-pole trap as well as for the bender are mounted on the CF-160 flange that also includes the coldhead. The configuration of the feedthroughs and of the two connection panels for the source and the bender are shown in the appendix (figures 8.8 - 8.10).

The LC-circuit of the trap is excited by a home-made RF power supply (based on a DDS followed by an amplifier). The required output power is a few Watt. As oscillator a 20 MHz direct digital synthesis (DDS) board is used. The output signal of the system can be tuned in 1 Hz steps and the needed output power is achieved by amplifying the signal with a broadband amplifier (QRP-PA-2008). For the inductive coupling 2 coils are used. The primary coil has 1.5 windings and the secondary coil has 11 windings. In the middle of the secondary coil also the contact for the trap float is mounted. In the upper left part of figure 2.12(b) the coils are visible. The primary coil is the inner one (Note: The photo shows an older configuration with a larger primary coil with three windings).

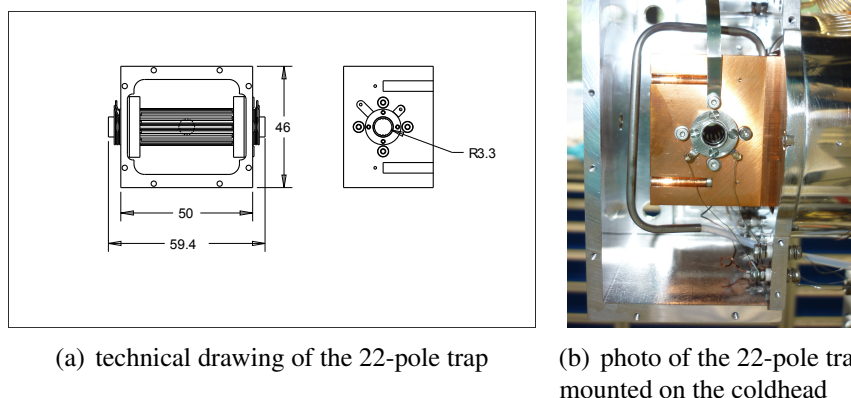


Figure 2.14: Technical drawing and photo of the 22-pole trap. (a) The two elements with the 11 rods each are mounted in a copper housing. The overall length of the trap, including the entrance and the exit electrode, is 59.4 mm. The inner radius of the entrance and the exit electrode of the trap is 3.3 mm. The copper housing is mounted on a copper plate, which is directly fixed to the coldhead, to achieve an optimum thermal conductivity. (b) The photo shows the copper housing with the 22-pole inside and the aluminum heat shield. On the right side the coldhead is visible and parts of the coils for the in coupling of the RF-voltage for the trap. The combination of the metal tube with the teflon tube is one of the continuous gas inlets.

2.5.2 Test Measurements

One characteristic of the apparatus is the cooldown and warmup behavior of the trap. To document this behavior, the trap temperature (measured with a Lakeshore DT-470-CU-13 diode attached to the trap housing) together with the pressure (measure with the installed cold cathode gauges from Pfeiffer Vacuum GmbH) in the trap chamber was recorded as a function of time. This was done for the cooldown phase as well as for the warm-up phase. The measurements are shown in the figures 2.15(b) and 2.15(a). The cooldown process is fast and it takes approximately only one hour to cool down the trap from room temperature to 4 K. Typical background pressures in the main chamber are around $6 - 7 \cdot 10^{-8}$ mbar and this pressure usually drops to approx. $4 \cdot 10^{-8}$ mbar during the cooldown phase, due to freeze out effects at temperatures below 100 K. The warmup phase is much slower than the cooldown, and it takes normally more than 10 hours to warm up without using the heater. In the warmup phase shown in figure 2.15(b) the heater was switched on after approx. 7000 s to speed up the warmup process. The accompanying pressure measurements show an interesting characteristic in the shape of a double peak. The significant pressure increase is due to frozen out gas (likely N_2 , O_2 , and CO) that evaporates from the walls of the trap and the coldhead. The double peak structure can always be observed. A possible reason for this is that the housing of the trap is likely a few K warmer than the trap itself, and due to this the frozen out gas evaporates in quick succession from these two places.

The heater is not only useful to speed up the time consuming warm-up process, but it is also used to warm up the trap during the experiment if measurements at higher temperatures than 4 K are performed. For this the calibration table 2.4 is useful to find the right settings for the heater.

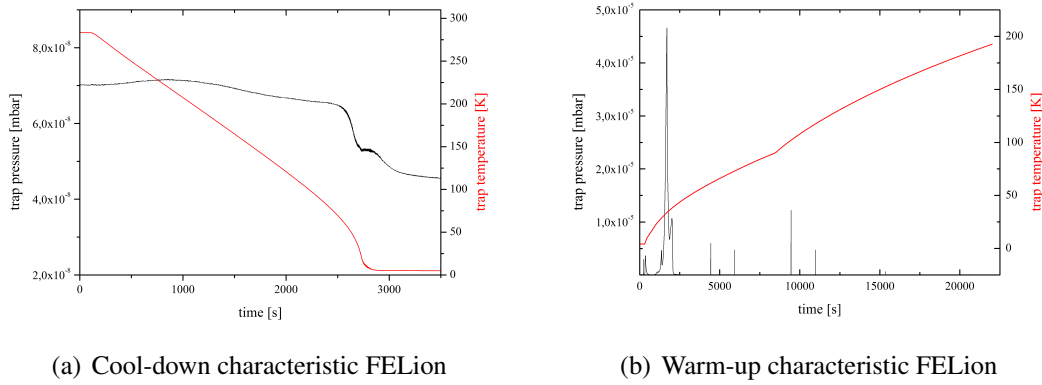
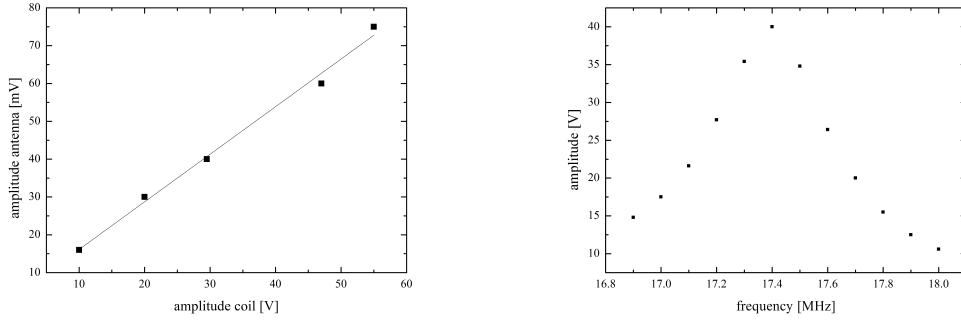


Figure 2.15: (a) shows the cooldown behavior of FELion. The red line is the trap temperature recorded as a function of time. In black the pressure in the main chamber is shown. The cooldown process from room temperature down to 4 K usually takes less than one hour. Standard background pressures are in the range of 10^{-8} mbar. (b) shows the warmup behavior of FELion. Again in red the temperature and in black the pressure in the main chamber are plotted as functions of time. The first part of the warmup phase is without heating and the second part with using the heater. At a trap temperature of around 30 K N_2 , O_2 , and CO evaporate. The double-peak structure in the pressure curve is typical.

Table 2.4: Calibration of the 22-pole trap-heater. For this measurement the voltage U_{heater} applied at the power supply of the heater was tuned between 4 V and 25 V. For all settings the corresponding current I_{heater} and the trap temperature T_{trap} was recorded. The heating power P_{heater} is calculated from U_{heater} and I_{heater}

$U_{\text{heater}}[\text{V}]$	$I_{\text{heater}}[\text{A}]$	$P_{\text{heater}} [\text{W}]$	$T_{\text{trap}} [\text{K}]$
4	0.105	0.4	4.3
6	0.154	0.9	4.8
8	0.207	1.6	5.4
10	0.255	2.5	6.0
12	0.307	3.7	6.8
14	0.355	5.0	8.0
16	0.405	6.5	9.0
18	0.454	8.2	10.0
20	0.502	10.0	11.0
22	0.550	12.1	15.0
24	0.600	14.4	20.0
25	0.620	15.5	22.3

For estimating η and V_{eff} the real RF amplitudes V_0 , which are used to store the ions in the trap, have to be known. Since it is impossible to measure these amplitudes directly at the rods during the experiment, a small antenna is installed inside the vacuum chamber as a probe. This antenna is aligned perpendicular to the windings of the two coils used for the inductive in coupling of the AC-voltage into the 22-pole trap. The calibration measurement is shown in figure 2.16(a). For this measurement, the voltage at the secondary coil, which is directly connected to the rods, was varied and at the same time the amplitude of the signal in coupled at the antenna was recorded.



(a) calibration of the antenna for the 22-pole trap

(b) resonance curve of the 22-pole trap

Figure 2.16: Calibration of the antenna and resonance curve of the 22-pole trap. (a) shows the calibration measurement of the antenna installed inside the vacuum chamber. The antenna is aligned perpendicular to the windings of the coil. For the measurement the applied voltage at the secondary coil was varied and the corresponding amplitude at the antenna was recorded. The black line in the plot is a linear fit to the data. (b) shows the resonance curve of the 22-pole trap. For this measurement the applied frequency was varied and the amplitude at the secondary coil was measured.

This measurement was performed at 291 K and at a frequency of 17.73 MHz for the open trap. In figure 2.16(a), a linear fit to the data is shown. The best fit straight line is given by:

$$V_{\text{antenna}}[\text{mV}] = (1.26 \pm 0.06) \cdot V_{\text{coil}}[\text{V}] + 4 \pm 2 \text{ V}$$

The second measurement shown in figure 2.16(b) is the resonance curve of the L-C circuit of the 22-pole trap and coil. For this measurement the frequency of the RF-generator was changed, and the amplitude of the AC-voltage at the secondary coil was recorded. From the plot shown in 2.16(b), the resonance frequency can be determined to be 17.39 MHz.

The last calibration measurements presented in this subsection are not directly linked to the 22-pole trap itself. These measurements deal with different pressure calibrations. The first measurement, summarized in table 2.5, deals with the pressure difference between the inside of the housing of the 22-pole trap and the measured pressure outside in the main-chamber. The factor between these two values depends on the construction of the 22-pole and the used gas. It is important to know this factor, because for kinetic measurements one needs to know the number density inside the trap. This is obtained from the pressure inside the trap, but normally the pressure is only measured in the main chamber. For the calibration measurement a spinning rotor gauge (MKS SRG 2CE/O) was used to measure the pressure directly inside the trap and the pressure in the main chamber was recorded with the installed Pfeiffer cold cathode gauges. In table 2.5 the calibration factors for three different gases are listed. With the calibration factors from table 2.5 the number density inside the trap can be calculated by

$$n_{\text{trap}} = 4.18 \cdot 10^{17} \cdot \frac{C \cdot p_{\text{main chamber}}}{\sqrt{T_{\text{trap}}}} \quad (2.32)$$

Equation 2.32 takes the calibration factor into account, as well as the effect that if the trap is operated under cold conditions, the measured pressures have to be corrected to obtain the real number density. For a more detailed discussion see [30].

Table 2.5: Calibration of the pressure in the main chamber against the pressure inside the trap. The pressure inside the trap was measured with a MKS SRG 2CE/O spinning rotor gauge and the pressure in the main chamber with the Pfeiffer cold cathode gauges at room temperature. With these calibration factors, the pressure inside the trap can be calculated from the pressures measured outside.

molecule	calibration factor C
H ₂	92
He	103
O ₂	112

The second pressure measurement is used to check the differential pumping of the experiment. In table 2.6, the calibration of the different pressure gauges used in the experiment is shown. For this measurement, a hot cathode gauge (Huntington TK-150 with AML PGC-2 controller) was mounted on the 6-way-cross of the source in order to measure the pressure in the source chamber directly. For the calibration, the air pressure was varied between $1.1 \cdot 10^{-6}$ mbar and $9.6 \cdot 10^{-5}$ mbar. The pressures in the vacuum chamber of the first quadrupole and the main chamber were measured with the installed cold cathode gauges (Pfeiffer Cold Cathode Gauge IKR-251 and Pfeiffer Full Range Gauge PKR-251). The measurements were performed at room temperature and all gauges were calibrated to N₂. The result of this measurement is summarized in table 2.6.

An interesting correlation in this context is the pressure increase in the main chamber as a function of the pressure in the source, because in the experiment the precursor gas from the source can influence the chemistry in the trap, and in the worst case can disturb the experiments. Hence, it is desirable that the pressure increase in the main chamber is much smaller than in the source chamber. In this case the pressure in the source was increased by a factor of ~ 100 , and the pressure in the main chamber increased only by a factor of three. The connection between the two pressures (for air) can be described by a linear function

$$p_{\text{trap}}[\text{mbar}] = 0.0017 \cdot p_{\text{source}}[\text{mbar}] + 6.3 \cdot 10^{-8} \text{ mbar}$$

This means at a pressure of 10^{-5} mbar in the source, the pressure in the main chamber is approximately $1.2 \cdot 10^{-7}$ mbar, which corresponds to a background gas number density of $\sim 10^8 \text{ cm}^{-3}$.

2.6 The Second Quadrupole Mass Filter

The purpose of the second quadrupole is similar to the first quadrupole. While the ions are stored in the 22-pole trap, they can undergo chemical reactions with the reaction gas, the buffer gas or with residual gases or impurities. Thus, at the end

Table 2.6: Pressure measurement of the pressure gauges in the vacuum chamber of the first quadrupole and in the trap chamber as a function of the pressure in the source chamber. The pressure in the source chamber was measured with a hot cathode ion gauge. In the chamber of the first quadrupole and in the main chamber the installed cold cathode gauges were used. The trap temperature was 295 K and the gauges were calibrated to N_2 , which was also the used gas.

p_{source} [mbar]	$p_{\text{quad I}}$ [mbar]	p_{trap} [mbar]
$1.1 \cdot 10^{-6}$	$2.6 \cdot 10^{-8}$	$6.5 \cdot 10^{-8}$
$1.3 \cdot 10^{-6}$	$2.8 \cdot 10^{-8}$	$6.5 \cdot 10^{-8}$
$1.6 \cdot 10^{-6}$	$2.9 \cdot 10^{-8}$	$6.5 \cdot 10^{-8}$
$1.9 \cdot 10^{-6}$	$3.1 \cdot 10^{-8}$	$6.6 \cdot 10^{-8}$
$2.2 \cdot 10^{-6}$	$3.2 \cdot 10^{-8}$	$6.6 \cdot 10^{-8}$
$2.5 \cdot 10^{-6}$	$3.3 \cdot 10^{-8}$	$6.7 \cdot 10^{-8}$
$3.1 \cdot 10^{-6}$	$3.6 \cdot 10^{-8}$	$6.8 \cdot 10^{-8}$
$3.6 \cdot 10^{-6}$	$3.8 \cdot 10^{-8}$	$6.9 \cdot 10^{-8}$
$4.0 \cdot 10^{-6}$	$4.3 \cdot 10^{-8}$	$7.0 \cdot 10^{-8}$
$4.2 \cdot 10^{-6}$	$4.2 \cdot 10^{-8}$	$7.0 \cdot 10^{-8}$
$5.7 \cdot 10^{-6}$	$5.0 \cdot 10^{-8}$	$7.2 \cdot 10^{-8}$
$6.6 \cdot 10^{-6}$	$5.5 \cdot 10^{-8}$	$7.4 \cdot 10^{-8}$
$8.7 \cdot 10^{-6}$	$6.5 \cdot 10^{-8}$	$7.7 \cdot 10^{-8}$
$1.1 \cdot 10^{-5}$	$7.8 \cdot 10^{-8}$	$8.1 \cdot 10^{-8}$
$1.2 \cdot 10^{-5}$	$8.4 \cdot 10^{-8}$	$8.4 \cdot 10^{-8}$
$1.4 \cdot 10^{-5}$	$9.3 \cdot 10^{-8}$	$8.8 \cdot 10^{-8}$
$1.9 \cdot 10^{-5}$	$1.1 \cdot 10^{-7}$	$9.5 \cdot 10^{-8}$
$2.4 \cdot 10^{-5}$	$1.4 \cdot 10^{-7}$	$1.0 \cdot 10^{-7}$
$3.3 \cdot 10^{-5}$	$1.8 \cdot 10^{-7}$	$1.2 \cdot 10^{-7}$
$4.5 \cdot 10^{-5}$	$2.3 \cdot 10^{-7}$	$1.4 \cdot 10^{-7}$
$5.9 \cdot 10^{-5}$	$2.9 \cdot 10^{-7}$	$1.6 \cdot 10^{-7}$
$7.1 \cdot 10^{-5}$	$3.4 \cdot 10^{-7}$	$1.8 \cdot 10^{-7}$
$8.1 \cdot 10^{-5}$	$3.9 \cdot 10^{-7}$	$2.0 \cdot 10^{-7}$
$9.6 \cdot 10^{-5}$	$4.5 \cdot 10^{-7}$	$2.2 \cdot 10^{-7}$

of the storage time normally different ionic species are present in the trap. However, the Daly-type detector (see subsection 2.7) cannot distinguish between these different masses. Nevertheless, for the experiments information on the number of the different species is crucial. To achieve this, the second quadrupole is used to select only one type of ion coming from the source and to guide it into the detector. The disadvantage of this method is of course that for every different type of ion a new experimental cycle is needed, since during one cycle only one type of ion can be counted.

2.6.1 Technical Design

The construction of the second quadrupole (technical drawing see figure 2.17) differs a bit to the first one. The length of the quadrupole is with 260 mm comparable to the first quadrupole, but in contrast to the first one the second quadrupole is build of cylindrical rods with a radius of 9 mm and the enclosed radius is with 7.84 mm considerably larger than the one for the first quadrupole ($\frac{r}{r_0} = 1.1479$). Together with the maximum RF-

voltage from the QMH 410-3 RF-generator of $V_0 = 2486$ V at 1.44 MHz, this results in a maximum mass of ~ 270 u that can be selected with the second quadrupole. At the end of the second quadrupole there is also an Einzel-lens mounted, but in contrast to the Einzel-lens of the first quadrupole, the middle electrode is only divided into two parts. The lens is orientated in a way that the impact point of the ions on the Daly-stamp can be tuned horizontally forward or backward. As for the first quadrupole the ions are also focussed by the lens.

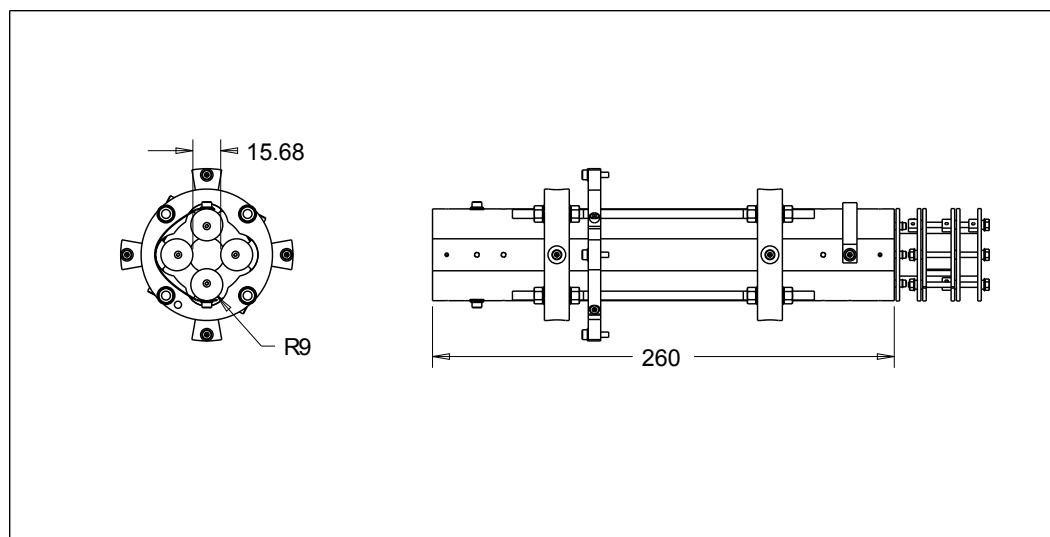


Figure 2.17: Technical drawing of the second quadrupole. The length of the second quadrupole is 260 mm. It is manufactured of cylindrical rods of stainless steel with a radius of 9 mm. The enclosed radius of the four rods is 7.84 mm. At the right end of the quadrupole an Einzel-lens is mounted. The middle electrode of the lens is divided into two parts and it is used to tune the point of impact of the ions on the stamp of the Daly-detector.

2.6.2 Test Measurements

To use the second quadrupole in the experiment it is necessary to calibrate the applied control voltage first. The control voltage for the second quadrupole is in the range of 0 V to 10 V corresponding to a V_0 between 0 V and 2486 V. For the calibration measurement the source was operated with air at a pressure of $\sim 1 \cdot 10^{-4}$ mbar and the control voltage was varied between 0 V and 2 V. The three most prominent peaks in the recorded spectrum (see figure 2.18) can be assigned to H_2O^+ , N_2^+ , and O_2^+ . The idea for the calibration is to determine the corresponding voltages to these three masses for calibration. The voltage values are 0.685 V for H_2O^+ , 1.065 V for N_2^+ , and 1.217 V for O_2^+ . From these three values one can derive a conversion-factor between the mass and the corresponding control voltage for the second quadrupole, which results in

$$1 \text{ V} \cong 26.3 \text{ u}$$

This calibration value is implemented in the control software (see chapter 3) in the different modes, whenever the user can choose the masses of the ions in a sub-program.

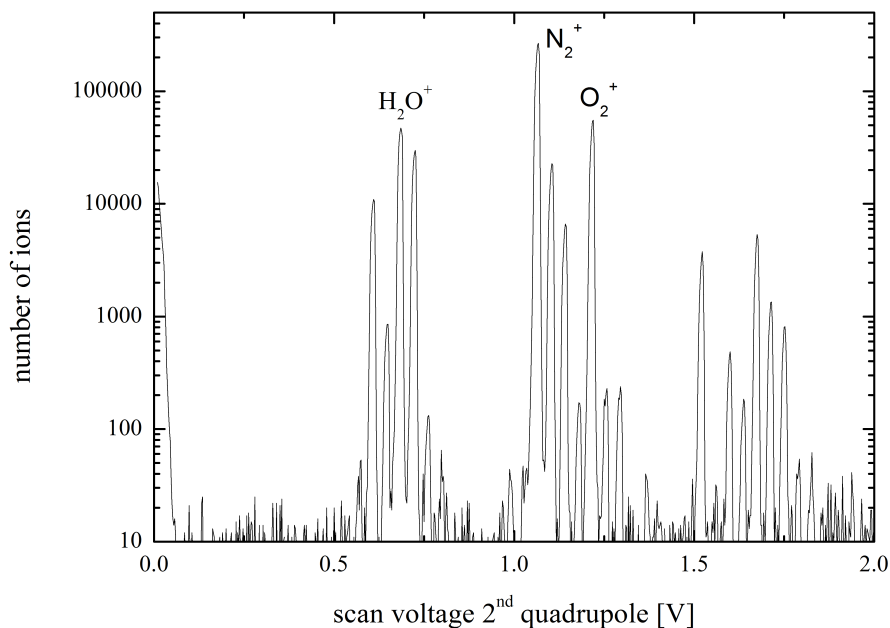


Figure 2.18: Mass-calibration measurement for the second quadrupole. For this measurement air was used as a precursor-gas in the source. The first quadrupole was used as an ion-guide and the ions were not stored. By scanning the second quadrupole, the shown spectrum was recorded. The three most prominent peaks were designated to H_2O^+ , N_2^+ , and O_2^+ . From the corresponding voltages a calibration of the second quadrupole was performed.

As for the first quadrupole the highest mass, selected with the second quadrupole, was 77 u. So also for the second quadrupole the lower limit for the mass resolution is $\frac{m}{\Delta m} = 77$.

2.7 The Daly-type Detector

The standard detector used in the FELion experiment is a Daly-type detector ([31]). The detector system is mounted in a 4-way-CF100-cross and it consists of an aluminum stamp, which is held on a potential of ~ -30 kV (Spellman UM8-40 NY), a plastic-scintillator (BC 400, Saint Gobain, coated with 200 nm aluminum on one side), and a photomultiplier tube (Hamamatsu R647 Series). For the analysis of the signals produced by the photomultiplier tube, a discriminator unit (Phillips Scientific Model 6908, 300 MHz Discriminator) is used and the signals are counted with an Ortec 996 Counter & Timer unit, which is read out by the control software (see chapter 3). The principle of the detector system is that the mass-selected ions, which come from the second quadrupole filter, are accelerated by the negative voltage of 37 kV applied to the aluminum knob. When the ions hit the aluminum they release electrons out of the material, which are accelerated in the other direction onto the scintillator. By hitting the scintillator material they cause light flashes. These light signals are converted into electron signals and the signal is intensified by the photomultiplier tube (PMT). The current signal produced by the PMT is then converted to a voltage pulse, amplified,

and processed by the discriminator unit and finally the signals are counted by the Ortec 996 Counter & Timer unit. A scheme of this sequence is shown in figure 2.19. There are two advantages of this detector type. First only the aluminum knob and the scintillator are inside the vacuum. The rest of the detector is outside. Due to this, the maintenance of the detector system is relatively easy. Second, the detector system is extremely sensitive and capable to count single ions. Disadvantages of the system are that it is not mass selective (see section 2.6) and only works for positive ions.

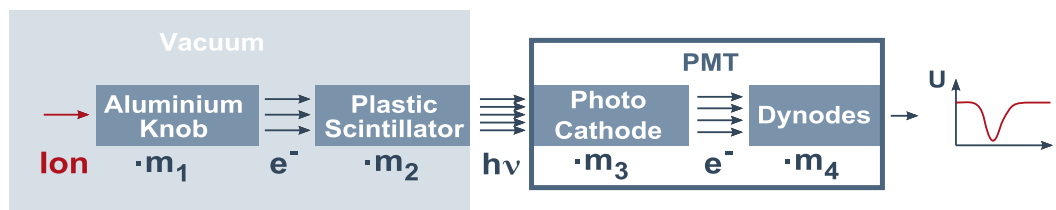


Figure 2.19: Principle of the Daly-detector. The ions are converted into electrons when they hit the aluminum knob. The electrons are then converted via the plastic scintillator into light flashes, which are processed by the PMT. In table 2.8 the given multiplication factor $M = m_2 \cdot m_3$. The scheme is taken from [32].

A much more detailed description of the Daly-detector together with a lot of test-measurements for different settings can be found in the Staatsexamensarbeit of Sven Fanghänel ([33]). In this work, also the limitations of the used detector system on FELion are discussed in a detailed way. Nevertheless, one limitation of the system should be repeated here again. From the test measurements of the source (see subsection 2.2.2) it turned out that the limitation of the count rate is ~ 30 MHz. Hence, especially for the kinetic experiments it is crucial to ensure that the number of ions is not exceeding this limit. In table 2.7 typical values for the different voltages are listed for the operation of the Daly-detector. Table 2.8 lists some characteristic values, if the detector system is operated under the settings listed in table 2.7.

Table 2.7: Typical operational values for the different voltages for the Daly-detector at FELion. Taken from [33].

Setting	value
U_{PMT}	800 V
U_{Daly}	37 kV
$U_{\text{Discriminator}}$	6 mV

Table 2.8: Indicators for the Daly-detector at FELion. Taken from [33].

parameter	value
detection losses	$\sim 0.5\%$
average peak height	30 - 40 mV
typical conversion m_1	7
typical amplification M	9

2.7.1 Technical Design

Figure 2.20 shows a technical drawing of the Daly-detector system mounted in the 4-way-cross. The ions enter the detector from the top side and on the bottom side the second optical port for the in coupling of radiation is located. In the drawing a shield is visible, which covers the scintillator and partly also the knob. Due to some difficulties with leakage currents in the detector, this shield was removed for operating the experiment.

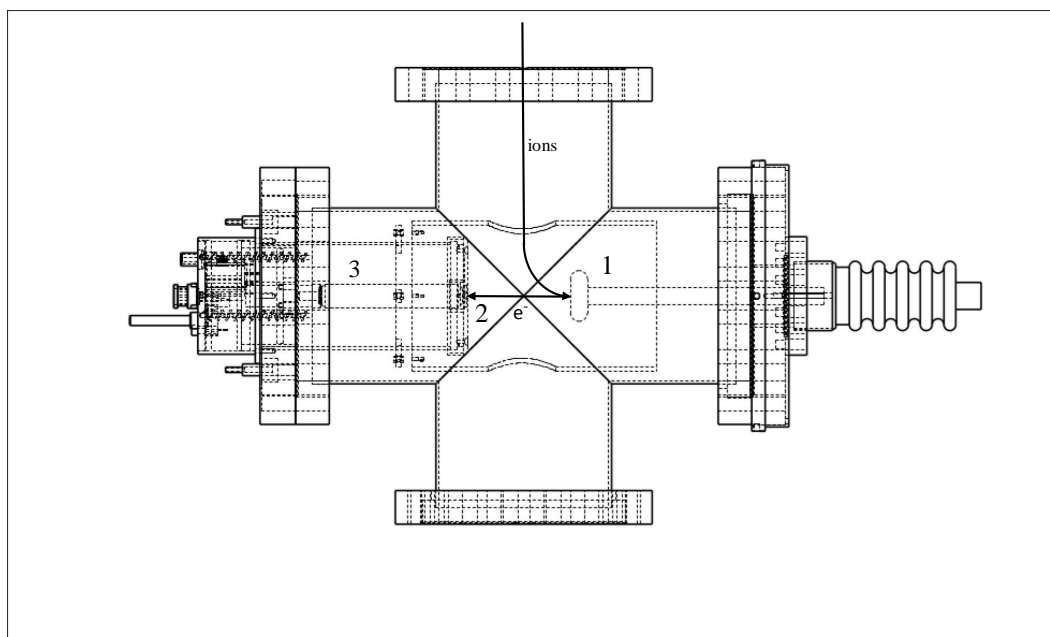


Figure 2.20: Technical drawing of the Daly-detector. On the right side the aluminum knob (1) for converting the ions into electrons is visible. The electrons are accelerated to the scintillator (2), which is shown on the left side together with the PMT (3). The shield, which is visible in the middle of the 4-way-cross, was dismantled due to some difficulties with leakage currents.

2.8 The NI CompactRIO System

For the predecessor experiment LIRTRAP many different analog power supplies and delay generators were used to generate the ion guiding and pulsing voltages. For the new experiment FELion this concept of individual power supplies was replaced partly by a new approach. The idea is to use one power supply unit for the low control voltages (between -10 V and 10 V) for the different parts of the experiment, such as the pulsed voltage for B0 (see section 2.2) or the voltages for the Einzel-lens of the first quadrupole (see section 2.3). In addition, this unit should also be capable to provide pulsed sequences for the voltages with a high time resolution as well as TTL-pulses to gate the Ortec 996 Counter & Timer as a part of the detector system (see section 2.7). In contrast to the LIRTRAP experiment it should also be possible to control this unit via the control and measurement PC, in order to improve the usability of the experiment. An ideal candidate to fulfill these requirements is the CompactRIO system from National Instruments. In principle this system is a stand-alone system,

which uses a Field Programmable Gate Array (FPGA) to create the required voltages and pulse sequences. The advantages of this system are the modular concept, i.e. the system can be configured for the specific requirements and it can easily be extended with new modules if needed, it can run independently from the control PC, and due to the embedded FPGA it can be reprogrammed easily. This means in case of a new measurement procedure, the system can be adapted easily simply by defining a new sequence in the software, which is then rewritten on the FPGA. This control software for the experiment is described in chapter 3.

For FELion the CompactRIO system consists of the following components. As a control unit the CompactRIO NI cRIO-9022 Intelligent Real-Time Embedded Controller is used. This controller is combined with the CompactRIO Reconfigurable Embedded Chassis cRIO-9114, which hosts the FPGA mentioned above, and which can be equipped with up to eight different modules, providing the voltages needed for the experiment. In the current configuration, four of the eight slots of the chassis are in use. The used modules are one NI 9263 module (4-channel, ± 10 V, 16-bit analog voltage output, time resolution 3 - 9.5 μ s for 1-4 channels in use, slew rate 4 V/ μ s), two NI 9264 (16-channel, ± 10 V, 16-bit analog voltage output, time resolution 3.1 - 37 μ s for 1-16 channels in use, slew rate 4 V/ μ s), and one NI 9401 module (8-channel, 5 V TTL, digital input output, time resolution 100 ns). In total this system has 36 analog output channels and 8 digital I/O channels. In case that more channels are needed in the future, there are still four idle slots to extend the number of channels. Their integration in the control software would as well be uncomplicated.

The complete machine cycle is synchronized with the coldhead of the experiment (1 Hz) by using one of the digital I/O channels of the CompactRIO system to increase the stability of the experiment. The software solution for the synchronization is described in the next chapter in section 3.1.

3

Control Software for FELion

In this chapter, the newly developed control software for FELion is introduced. The software is written with LabVIEW (National Instruments), which is a graphical programming language. There are two big advantages of this programming language. First, the easy communication with any hardware component of the experiment and second the integrated graphical user interface (GUI) (see section 3.2).

The overall idea for this new control software was to use one control program for all measurement modes of the instrument in order to standardize the routines and to improve the usability of the program. The user-friendliness of the software was an important issue during the development, since FELion will be located at the FELIX Facility, Radboud University Nijmegen, and the control software will be used also by scientists who are not familiar with this program. Figure 3.1 shows the hierarchy of the setup.

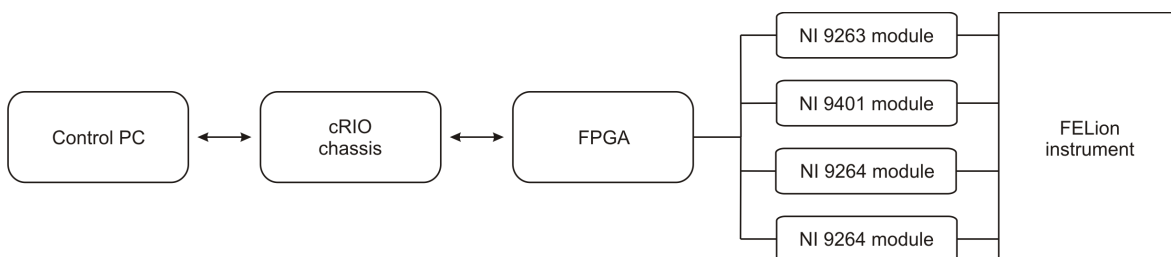


Figure 3.1: Scheme of the general setup. The highest instance in the setup is the PC with the control software. The computer controls the cRIO chassis with the embedded FPGA on it. Via the FPGA the different modules are controlled, which provide the voltages for the FELion instrument.

The highest instance in the setup is the measurement PC with the software, which will be described in this chapter. The software communicates with the cRIO chassis with the embedded FPGA. The FPGA itself controls the four different modules, which deliver the voltages for the experiment. For programming the FPGA in LabVIEW a special subVI is needed. This subVI is described in the following section.

3.1 The FPGA Module

3.1.1 FPGA VI

The FPGA module is the central part of the software. It is used as the interface between the control elements in the software and the different modules that provide the voltages for the instrument. This VI allows to program the Field Programmable Gate Array (FPGA) on the Compact RIO in the way the user needs it for the application. In our case this means that we can get access to the different modules of our Compact RIO system. It consists of one NI 9263 module, one NI 9401 and two NI 9264 modules. For more technical details of the different modules refer to section 2.8 in chapter 2. With the FPGA one can operate these modules in any necessary way for the experiment and this is defined by the FPGA VI. Here, it is important that any software solution, which is developed with the FPGA VI is compiled on the FPGA. This means that the software part is translated into a hardware code on the FPGA. As a result, the Compact RIO together with the FPGA and the different modules are independent from the control PC. Hence, for an experimental cycle only the values for the different voltages and the delays are submitted to the Compact RIO system at the beginning of the measurement. After this, the measurement runs independently from the PC. Only after the measurement is finished, the result, i.e. the number of counts, is transmitted back to the PC. This feature is crucial, because the timing for the experiment is autonomous from the PC and so it cannot be disturbed by background applications on the control PC.

The FPGA VI for controlling the Compact RIO system is divided into two parts which corresponds to the two different operating modes of the ion trap apparatus. The first - not so often used - mode is the continuous mode and the second one is the pulsed mode. In the VI they are distinguished by a case selector structure. In case of the continuous mode, one voltage is set to a constant value for every channel in use. This value is maintained until the user changes it or the program is stopped. The realization of this mode is quite simple. For every module used in this mode, there is one read/write module, and every channel is connected with the corresponding control unit. The control elements for the user are the low voltage control-elements on the graphical user interface.

The implementation of the pulsed mode is more complex. A scheme of the pulsed sequence is shown in figure 3.2. Besides the values for the voltages, also values for the different delays for the pulsed voltages are needed, and has to be implemented in a timing structure for the different voltages. To realize the timing structure, a flat sequence is used in the code. In the first step, the low values for the pulsed voltages are set. This is the same as for the continuous mode. The next step is to synchronize the pulsed voltages sequence with the experiment. The synchronization is realized by reading out one of the digital channels from the module 2 that is connected to the synchronizer. The output of the synchronizer is a TTL (Transistor-Transistor Logic) pulse which is used as a trigger-signal. In the While Loop, the digital in/out module is checked if a TTL pulse is applied. In this case, the While Loop is aborted and the pulsed sequence starts. The While Loop is permanently checking for a trigger pulse. If a trigger-pulse is received, the software uses a boolean variable to submit this information into the next frame. This procedure is necessary to ensure that the timed sequences

on the different modules of the Compact RIO use the same reference time. Using this boolean variable and embedding the pulse sequences for the different modules in Case structures is an easy way to define a common start time for all sequences on the FPGA. At the moment there are five pulsed sequences defined on the FPGA. The first sequence is used for the source and provides the pulse for the Blende 0. The second sequence is intended for a test channel. This channel is not permanently connected to the experiment and can be used if another pulsed voltage is needed. The third sequence is used for the trap entrance electrode (Speichereingang/SE) and trap exit electrode (Speicherausgang/SA) sequence. This sequence is the most complex one and will be described in more detail below. The remaining two sequences are used for the gate and for the piezo-valve. Their construction is in principle identical to the first two sequences, but in this case no voltage is set but the digital output is changed in terms of the Transistor-Transistor Logic. The organization of the pulsed sequences is always similar. The first step is a delay which is used to shift the pulse sequence with respect to the reference time defined by the trigger-pulse. After this delay time the voltage is set to the high value or in case of the digital channels to the true value. After another delay time defined by the pulse length (width), the value is again set back to the low/false value, which causes the pulse to switch off. This sequence is schematically shown in figure 3.2 on the top-right side. The sequence for the SE and SA is different to the pulsed sequence described above. In this sequence the two voltages for SE and SA are combined, and in the case of the SA voltage also a voltage-ramp is included. The beginning of the sequence is identical to the ones described above. The sequence starts with a delay, then the high value for the SE is set and after a certain width it is set back to the low value. The delay is equal to the opening time for the SE. After a second delay, which corresponds to the storage time for the ions, the ramp sequence for the SA starts. The ramp starts at the low value for the SA and a While Loop is used to reduce the voltage on the channel with every iteration by a given value. Between two steps of the loop, a waiting time of $10 \mu\text{s}$ is implemented. By this, the user can define the slope for the ramp in volts per $10 \mu\text{s}$. The loop is repeated until the value reaches the high level for the pulse. This is the exit condition for the loop and the high value is set. This value is hold for a certain time which corresponds to the opening time of the SA. After this time the value for the SA is switched back to the low level. A pattern of this sequence is also given in figure 3.2 on the right side and figure 3.3 shows a typical pulse sequence used in the experiment.

3.1.2 ORTEC FPGA ONE CYCLE

This subVI is used to integrate the FPGA cycle and the counter in the experimental sequence. For a better overview, the sequence of this subVI is shown in figure 3.4. The first step is to activate the counter with the start command. For the communication with the counter the subVI ORTEC 996 Write Read is used. With this subVI one can submit a command to the Ortec counter and check if the counter responds in the right way. The next step is to start the FPGA cycle with the Run command. The option Wait Until Done is activated to ensure that the FPGA really carries out the whole sequence. In the same frame, there is also a Wait command implemented, which is controlled by the cycle time value set by the user. This is an important feature, because it guarantees that every cycle of the experiment takes the same time. For time

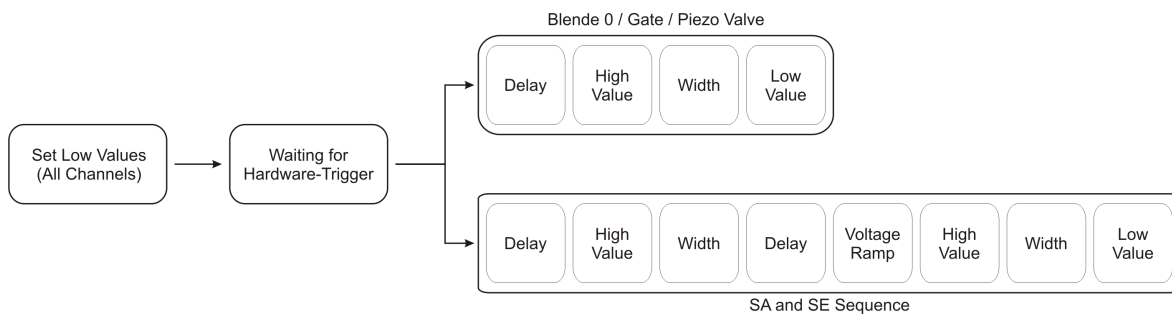


Figure 3.2: Scheme of the pulsed sequence on the Compact Rio FPGA. High Values denote the voltage level during the pulse and Low Level for the remaining time. The hardware trigger is used to ensure that all pulsed channels refer to the same reference time. Since the sequences for Blende 0, Gate and piezo-valve are identical there are shown as one sequence. The sequence for the trap entrance electrode (SE) and the exit electrode (SA) is programmed in a different way. The second delay in this sequence corresponds to the storage time of the ions.

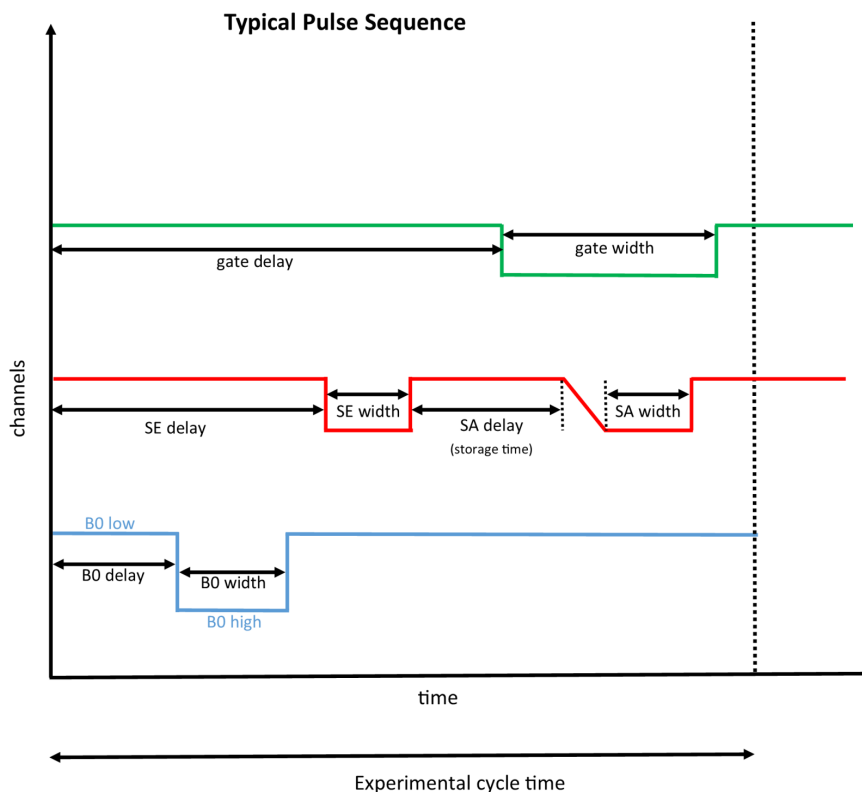


Figure 3.3: Diagram of a typical pulsed sequence generated by the FPGA. All channels are referenced to the same reference time.

scans (see 3.3.4) this feature is essential. In this case, the trap time is varied over a wide range, which causes the length of the FPGA cycle to change with every measurement. Using the cycle time controller, this effect can be avoided. By selecting a cycle time longer than the longest FPGA cycle time the cycle time will dictate the length of the sequence. For example, using the Time Scan Mode with trap times between 50 milliseconds and 700 milliseconds and choosing a cycle time of 1000 milliseconds the whole experimental cycle is dominated by the 1000 milliseconds cycle time. Hence, the

cycle time is the same for each experimental cycle irrespective of the individual storage times. If the user chooses a cycle time of only 500 milliseconds, the cycle times are equal for storage times up to 500 milliseconds, but for longer storage times the cycle time will vary.

After the FPGA cycle is completed the counter is stopped. The counts are read out after a short waiting time of 10 milliseconds. This is necessary to guarantee a correct communication time with the Ortec counter. The last step is to clear the counter for the next cycle.

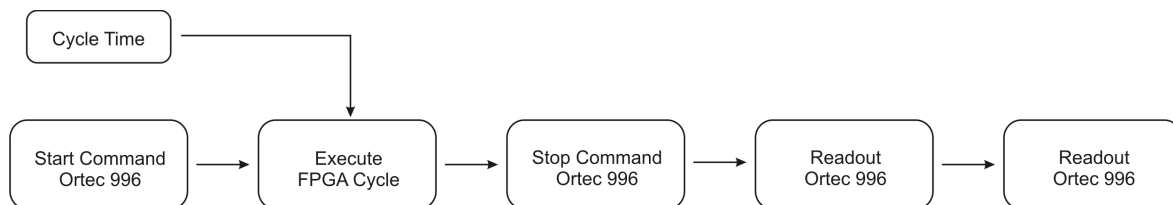


Figure 3.4: Scheme of the interface between the control software on the PC and the Compact RIO system at the experiment. This sequence is used in every measurement mode of the control software. In the following schemes is it denoted as Start Measurement Cycle.

3.2 The Graphical User Interface

The graphical user interface (GUI) is mainly divided into three different parts. One part is to control general settings for the software like the cycle time or piezo and gate settings (see 3.5). In addition, information about the status of the experiment are displayed here. The next section (see 3.6) contains the control panels for the different voltages of the experiment and is divided into different groups for the various parts of the 22-pole ion trap apparatus (e.g. for the Storage Ion Source, the quadrupole bender, the 22-pole trap,...). The control panels for the general settings and for the voltage settings are equal for all sub-modes of the program. The third part is different for every sub-mode. It contains the individual control elements for every mode as well as the charts. The different sub-modes can be selected by clicking on a tab. By default, the program starts in the counter mode (see section 3.3.1).

General Settings

The topmost part of the GUI is the General Settings section. It is divided into six sub-parts called Settings, Start/Stop Measurement & Program, File Management, Pressure & Temperature, Piezo Valve & Gate and Test Channel. Figure 3.5 shows a screenshot of the general settings part from the graphic user interface. In this section the user can set the cycle time of the experiment and choose between a continuous and a pulsed mode (see 3.2). In the pulsed mode, pulsed sequences can be selected for some voltages like SE trap or SA trap. In the continuous mode the pulsed sequences are disabled. The second part of the Start/Stop Measurement & Program consists of four buttons. One for starting the measurement, one for aborting the current measurement, one for closing the complete program, and the last one for restarting the ViscoVac VM210

Spinning Rotor Gauge. In case of closing the program, all voltages for the experiment are set to 0 V and also all open connections for example to the pressure gauges and the Compact RIO system are closed. The File Management part displays the directories, in which the measured data is saved. If connected to the AFS (Andrew File System, network file system of the I. Physikalisches Institut), the software will create one backup copy on the AFS and one local copy on the control PC. The program always displays the name of the latest measurement data file that has been stored. The last component in this section is a button that can be used to open the two directories (the local one and the one on the AFS) in the Windows explorer. The paths of the directories can only be changed by editing the source code in the subVI Data_CreateFileName. The Pressure & Temperature section contains indicators for the pressure gauges in the vacuum chamber of quadrupole I and in the main chamber. Next to the indicators there are two lamps which display the status (OK (green) oder Error (red)) of the pressure gauges. Also the trap temperature is displayed there. In addition, the sample rate for measuring the pressure and the temperature can be set. This part of the program is always running, and is independent from all other measurement modes. In the section Piezo Valve & Gate the pulsed voltage for the piezo-valve and the gate are controlled (see 3.2). For the counter, there is also the option to decide whether the program calculates the delay time for the gate or if the user chooses a delay time. The last part is the test channel section. The test channel is a normal pulsed voltage channel that is not permanently connected to the experiment. As for all other pulsed channels, the user can define the delay relative to the common reference time and the width of the pulse as well as the low and high voltage value for the pulse.

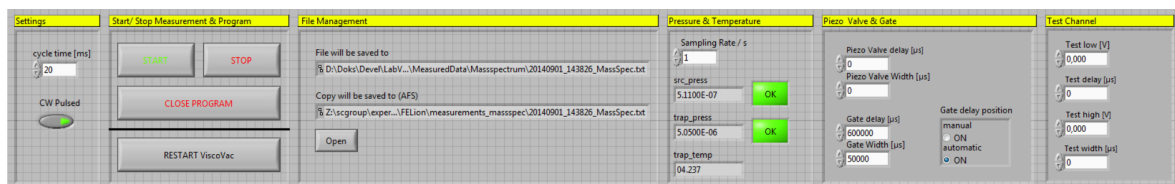


Figure 3.5: Screenshot of the General Settings section on the GUI. In addition to the main feature of starting/stopping the measurement, the user can define the cycle time of the experiment (left), see the file storage location (middle), check the status of the experiment (e.g. pressure and trap temperature), and choose settings for the piezo-valve and the gate channel controlling the Ortec 996 Counter & Timer (right).

Voltage Control

The Voltage Control section is divided into the same sections as the 22-pole ion trap apparatus. The first part is the Storage Ion Source. The user can control the voltages for Blende 0, Blende -1, Endplates and Source Float. The last three ones are continuous voltages while Blende 0 is pulsed. The second part contains the controller for the voltages for the first quadrupole. The user can set the voltage for the DC float of the quadrupole and can control the Einzel-lens at the end of quadrupole I. The six voltages for this are labeled Bq0 to Bq5. The names correspond to the ones of the different segments of the Einzel-lens shown in the appendix 8.5. The next part serves to control the DC voltages for the quadrupole bender (see appendix 8.7). The next section is for the 22-pole ion trap. The user can control Blende 4 & Blende 5 as well as the

trap entrance (SE) and trap exit (SA) electrodes. Also the DC float of the 22-pole ion trap can be set here. The voltages for the entrance and the exit of the 22-pole trap are combined in one pulsed sequence so that the controller trap time defines the delay time of the trap exit electrode relative to the pulse-end of the entrance electrode (see figure 3.2). In case of the trap exit, the user has also two additional options called SA jump and SA slope. With these two settings, the ramp for SA is controlled. In case this option is not needed, the SA jump value must be equal to the difference between SA Trap out and SA high. The last part is used for controlling the values for the second quadrupole. The two options for this part are the resolution and the DC float voltage.

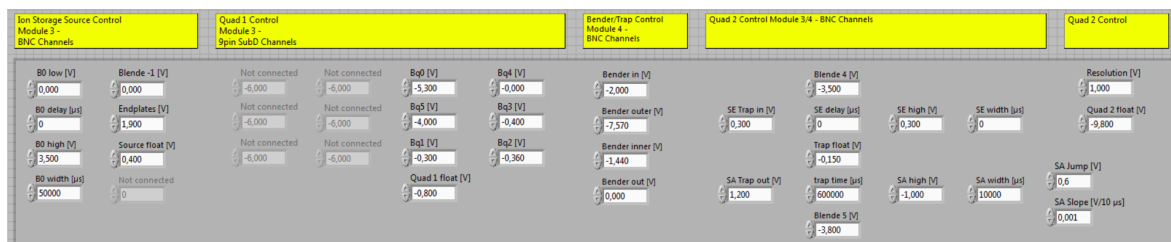


Figure 3.6: Screenshot of the Voltage Control Section for the experiment. The controllers are used to define most of the potentials in the experiment as well as the timing for the different pulsed channels.

Measurement Mode

The different measurement modes will be described below in 3.3. The user can choose between the different modes by clicking on the named tabs below the voltage control section.

3.3 Measurement Modes

In this section, the functions of the different sub-modes for operating the experiment will be described as well as the source code.

3.3.1 Counter Mode

The user interface for this mode consists of a time plot with the number of ions shown as a function of time and the number of measurement cycles, respectively. The user can select the ion displayed by entering its mass in atomic units. This value is used to determine the control voltage for the second quadrupole. For additional user information, this control voltage is shown in an indicating element as well as the actual number of counts on the selected ion mass. The main application for this mode is to optimize the settings of the experiment. Figure 3.7 shows a screenshot of the Counter Mode.

The source code for the Counter Mode is mainly divided into three parts. In the first step the values from the GUI for the gate settings, the control voltages, and the ion mass

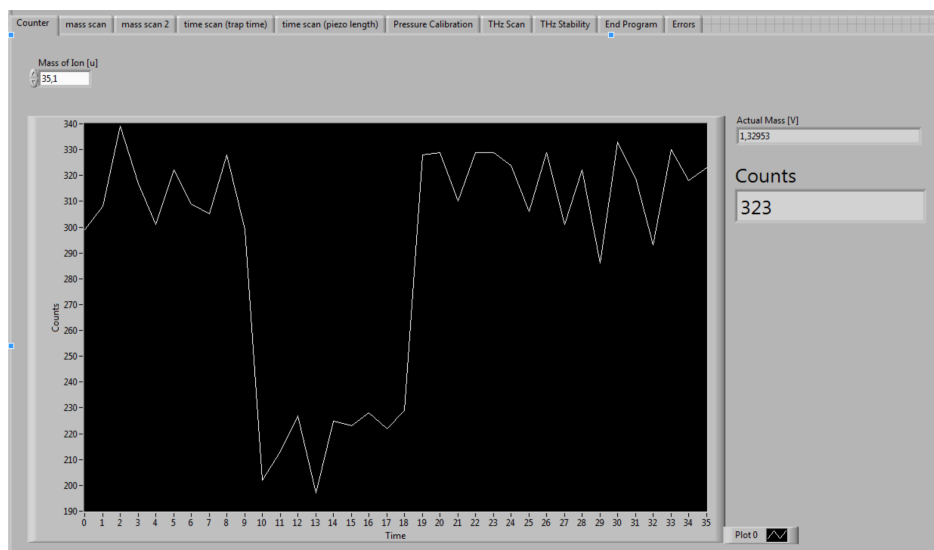


Figure 3.7: Screenshot of the Counter Mode. The mode can be activated by clicking on the counter tab. The user can define the mass of the ion with the controller in the upper left corner. On the chart the number of ions on the selected mass is plotted against time. On the right side there are two indicating elements for the number of counts and the control voltage for the second quadrupole corresponding to the selected ion mass.

are read in and processed. In the next step the values are sent to the FPGA module via the subVI `Fpga_SendData` and afterwards the `Fpga_Ortec996_OneCycle` subVI is accessed. After completing this cycle, the current number of counts is displayed and the chart is updated. A scheme of this is shown in figure 3.8. In the subVI `Chart_CreateData2`, the user can adjust the maximum number of measurement cycles that are displayed on the screen. Using a While Loop, this cycle is repeated until the user stops the program by pressing the STOP button on the GUI. The data collected during the counter mode operation is not saved directly, but it can be copied to Excel by a right click on the chart and choosing the Export Clipboard to Excel option. Another feature of the software is that it creates an ini-file every time the counter mode is stopped. This ini file contains all relevant values from the Counter Mode. However, at the moment, it is not possible to read in these files automatically.

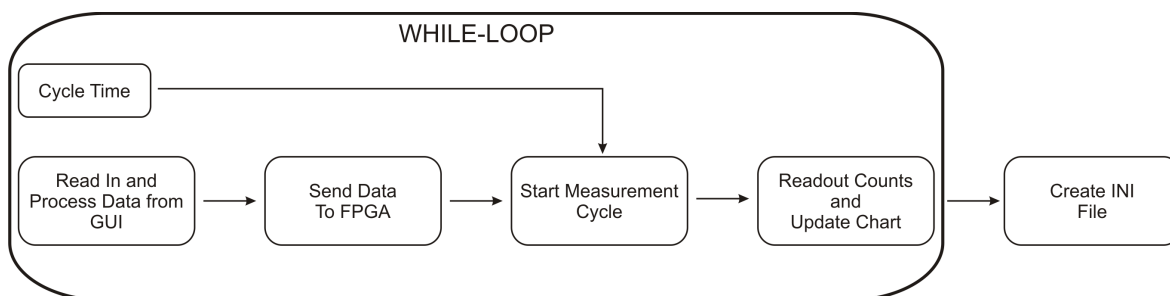


Figure 3.8: Schematic illustration of the source code of the counter mode. The complete mode is controlled by a While Loop, i.e. the counter program runs (executes) until the user stops the measurement.

3.3.2 Continuous Mass Scan Mode

In this mode, the user can choose the mass range for a mass scan by defining the start mass and the end mass in atomic mass units. The number of steps between these two masses is set by entering a step value (again in atomic units). For normal operation a value of 0.1 u seems to be suitable. Finally, the user can define the number of iterations for the mass scans by the Iterations control panel. Like in the counter mode described above, the GUI (see figure 3.9) of the mass scan mode is dominated by a big chart. In this case, the number of ions is plotted against the ion mass. If the number of iterations is larger than one, the different iterations are shown separately. At the right side of the chart, there is a control panel where actual information is shown, such as the number of counts, the ion mass (in atomic units as well as the corresponding control voltage for the second quadrupole), and the number of the current iteration is shown.

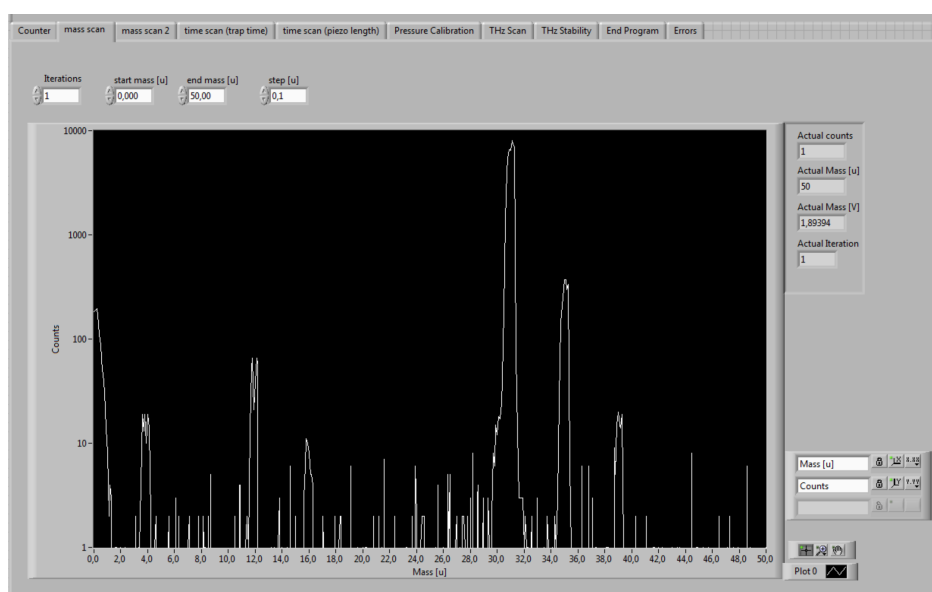


Figure 3.9: Screenshot of the Continuous Mass Scan Mode. The GUI is dominated by the chart where the counts are plotted in dependence on the mass. With the controllers at the top, the user can select the number of iterations for the measurement, the mass range, and the step size (all in atomic mass units). On the right side, there are indicating elements for the actual status of the executing measurement.

Figure 3.10 shows the structure of the source code for the Continuous Mass Scan Mode. The first step is to initialize an array of the right length to store the measured number of ions temporarily. In the next step, the values from the GUI are read in, processed, and sent to the FPGA. Then the `Fpga_Ortec996_OneCycle` subVI is accessed and the chart is updated when the measurement cycle is completed. The counts from the last cycle are stored in the array by adding up the counts for the corresponding mass. This sequence is embedded in a While Loop which automatically stops when the actual control voltage is higher than the one corresponding to the end mass. The next higher entity is a For Loop and the number of loops is defined by the number of iterations. After the For Loop is processed, the number of ions for every mass is averaged and stored into a file. The filename is created automatically and consists of the actual date, the time, and the ending `MassSpec.txt`.

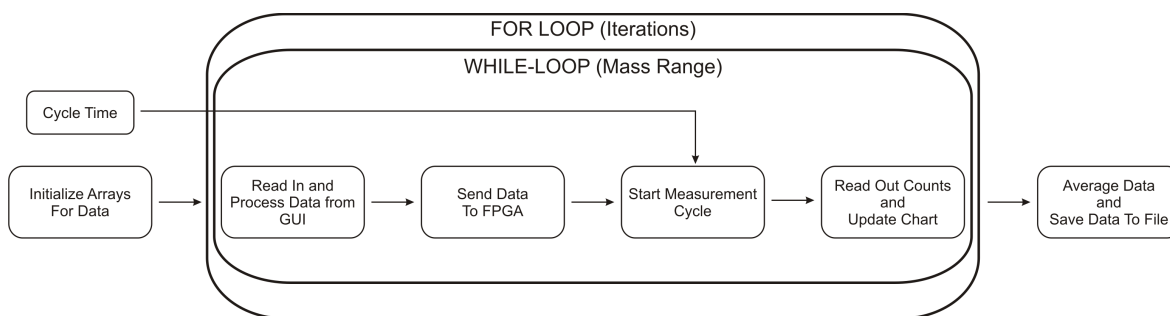


Figure 3.10: Structure of the code for the Continuous Mass Scan Mode. This mode is controlled by two loops. The inner loop is a While Loop that terminates if the scanned mass is at the end of the defined mass range. The outer loop is a For Loop which is controlled by the number of iterations. After processing both loops the data is stored in a txt-file.

3.3.3 Discrete Mass Scan Mode

This mode is very similar to the Continuous Mass Scan Mode described above (screenshot see figure 3.11). The main difference is that the user can define a list of masses and the program will only scan these masses by jumping from one mass to the one next in the list. The user has an input box for the number of iterations. In addition, the user has to define the number of masses to be scanned. Irrespective of the number of entries in the list, the program will only scan the first elements of the list corresponding to the number of masses (to be scanned) that has been set by the controller. A chart displays the number of ions counted for the different masses as a function of the number of iterations. This way, the user can check whether the number of ions on the different masses are stable. Furthermore, there is a list showing the corresponding control voltages for the masses, and again there are indicators for the actual status of the measurement, such as the iteration, the current mass in atomic mass units and the corresponding control voltage for the second quadrupole.

The source code (scheme is shown in figure 3.12) is similar to the Continuous Mass Scan Mode. An array is used to store the recorded data temporarily. The outermost loop is a For Loop defined by the number of iterations, but now the second loop is also a For Loop instead of a While Loop, which is controlled by the defined number of masses. The sequence in the inner loop is equal to the two modes explained above. The data for the different masses and iterations is stored separately in an array. The chart is updated after every iteration so that the user can see changes in the number of ions on a short timescale. With this, the Discrete Mass Scan Mode can be used to search for drifts on different masses. One possible reason for drifting is the change of the pressure in the trap. For this reason, a sub-mode records the pressure with the VM210 ViscoVac Spinning Rotor Gauge. The pressure is always recorded after the end of every iteration. To communicate with the VM210 the `Command_ViscoVac210` subVI is used. In this case, the communication is easy: the ViscoVac is started at the beginning of the measurement and after each iteration the pressure is read out. After the last iteration, the ViscoVac is stopped and the remote control mode is switched off. Since the ViscoVac can only be operated by remote control if it is set manually to the F6 mode by the user (by pressing the F and the 6 button on the key panel of the ViscoVac), there is a security query in the code. After starting the measurement, the user has to confirm that the ViscoVac is in the remote control mode. In addition,

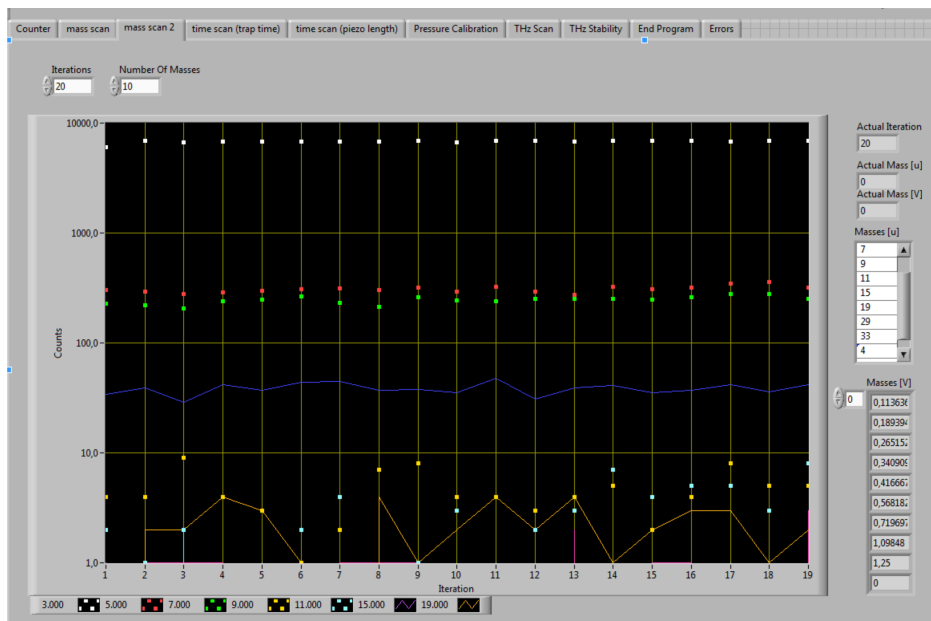


Figure 3.11: The GUI of the Discrete Mass Scan Mode. On the right side, the user can define a list of masses to be scanned as well as the number of iterations. The history of the different masses is shown in the chart. Note: The number of the scanned masses is set with the controller at the top and not by the number of entries in the list.

there is also a waiting time of 60 seconds included in the program. This is the time the ViscoVac with standard settings needs to measure the first pressure value after the Run command.

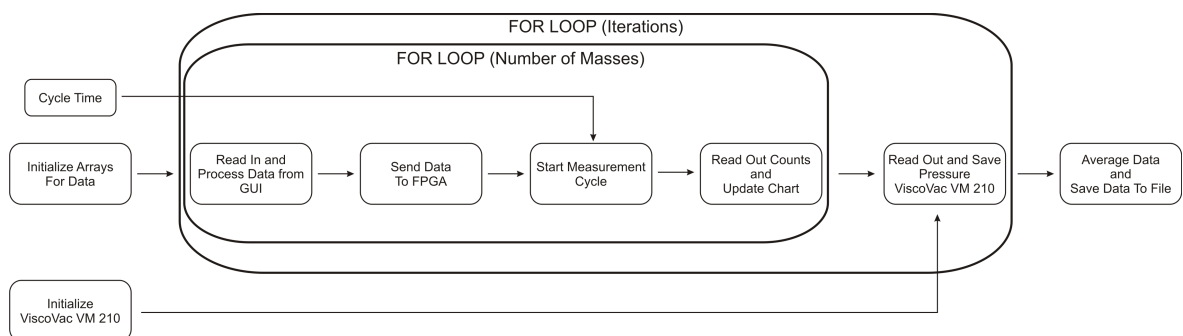


Figure 3.12: The source code of this mode is comparable to the one for the Continuous Mode. The difference is that the inner loop in this case is also a For Loop controlled by the number of masses instead of a While Loop, and in addition the pressure inside the trap is monitored. One pressure value is recorded after each iteration.

3.3.4 Time Scan Mode - Storage Time

To enable kinetic measurements, this mode provides the opportunity to record different masses and to vary the storage time. Like in the Continuous Mass Scan Mode, the user can set a starting and ending trap time in milliseconds and decides into how many steps the program divides this span. The user also defines a list of masses to be measured. A special feature of this mode is that for every mass the number of iterations can be set

independently. Note: The number of masses to be scanned is defined by the regulator Number of Masses and not by the amount of entries or lines in the list. Like in the other modes, a big chart shows the counts on the different masses plotted as a function of the storage time. The chart is updated after every iteration. In addition, there are again the familiar indicators for the actual values of iteration, mass, number of counts, and storage time.

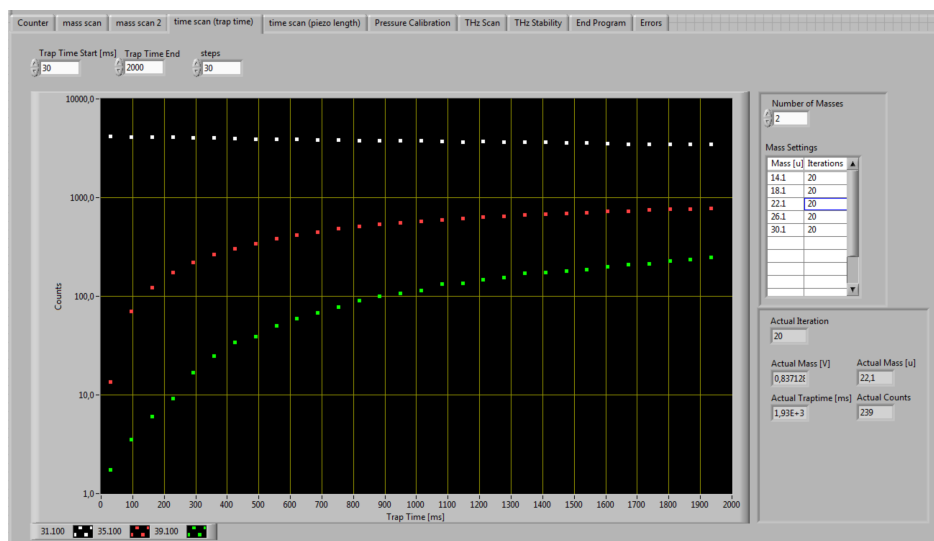


Figure 3.13: Screenshot of the Time Scan Mode. At the top there are controllers for the storage time (starting and ending time and number of steps). On the right the different masses to be scanned can be defined. For each mass a separate number of iterations can be chosen. The chart is used to display the time evolution of the different ions.

The source code (see figure 3.14) for this mode differs to the other modes. One big difference is the order of the loops in the code. Since the user can choose a different number of iterations for each mass, it is not useful to control the outer For Loop with the number of iterations. Instead, the number of ions is used. This changes the logic of the program and as a result, the program will first measure one mass with all the iterations requested before turning to the next mass. Another difference is that two arrays were used in this mode for saving the data. In one array the total number of ions is stored - like in the modes explained above - and in the second array, the actual averaged number of ions is stored. This is necessary to be able to update the chart after every iteration. The next For Loop in the code is controlled by the number of iterations belonging to the actual mass. The different iteration numbers are also stored in an array. The last and innermost For Loop is controlled by the number of steps. The structure in this loop is identical to the structures in the other modes and consists of a sequence to read in the values from the GUI, send the data to the FPGA, run the FPGA and the counter, and to update the chart. After processing all loops, the averaged data is written to a file with the ending timescan.txt. In the header of the file the different masses and the number of iterations per mass are listed.

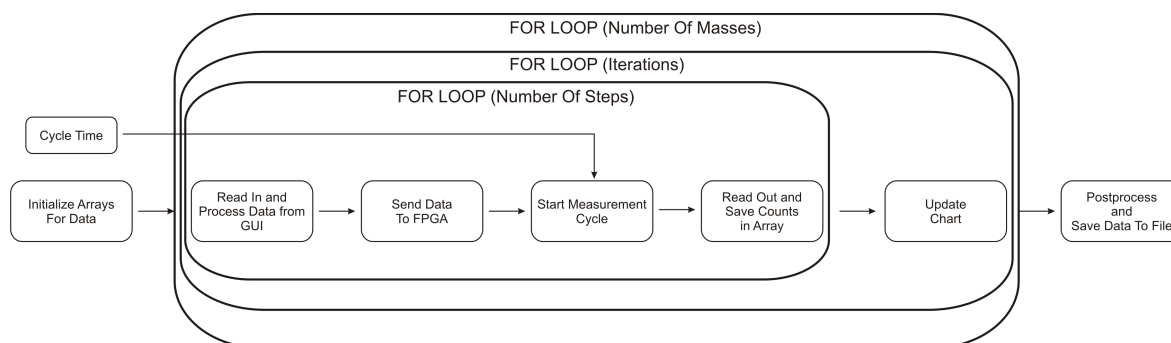


Figure 3.14: Block diagram of the code for the Time Scan Mode. The mode is controlled by three loops. The most outer one is a For Loop for the number of masses. The middle one is a For Loop controlled by the number of iterations for the active mass and the inner For Loop is set by the number of steps for scanning the storage time range. Due to the order of the loops, first all iterations for the first mass in the list are processed and then the next mass is scanned. After every iteration the chart is updated. The principle of the code for the Piezo Scan Mode (see 3.3.5) is identical to this code. The only difference is that instead of the storage time, the pulse length of the piezo-valve is varied.

3.3.5 Time Scan Mode - Piezo Valve

The basic idea of this mode is that it may be favorable to define the reaction time not by storing the ions for a certain time together with the reactants in the trap, but to inject the reactants into the trap only for a certain time period. Thus, instead of varying the storage time, the opening time of the piezo-valve is varied. The interface (figure 3.15) of the second Time Scan Mode is more or less identical to the first one, but instead of defining the range for the trap time, the user defines the length of the piezo pulses. For this, there are three control elements called Piezo Start Length, Piezo End Length and Steps. The latter is identical to the Steps control element in the Time Scan Mode for the trap time while the other two elements correspond to the Trap Time Start and Trap Time End controls.

Since the two modes are very similar to each other, also the source code is in principal identical. Again there are three For Loops controlled by the number of masses, the iterations per mass, and the number of the steps. The chart is updated after every finished iteration with the new averaged number of ions. The data is written to a file, which is equally constructed as the one for the other Time Scan Mode. The filename suffix for this type of measurements is TimeScan2.txt. For a schematic diagram of this mode refer to figure 3.14

3.3.6 Pressure Calibration Mode

This mode can be used to calibrate the two Pfeiffer vacuum gauges and the ViscoVac VM 210 Spinning Rotor Gauge against each other. The interface for this mode is very simple. There are only two indicators for this mode. One shows the number of iterations (in this mode called time) and the other one is a text box, which is used to list the measured values. Each set of measured data consists of three pressure values (one value for each gauge).

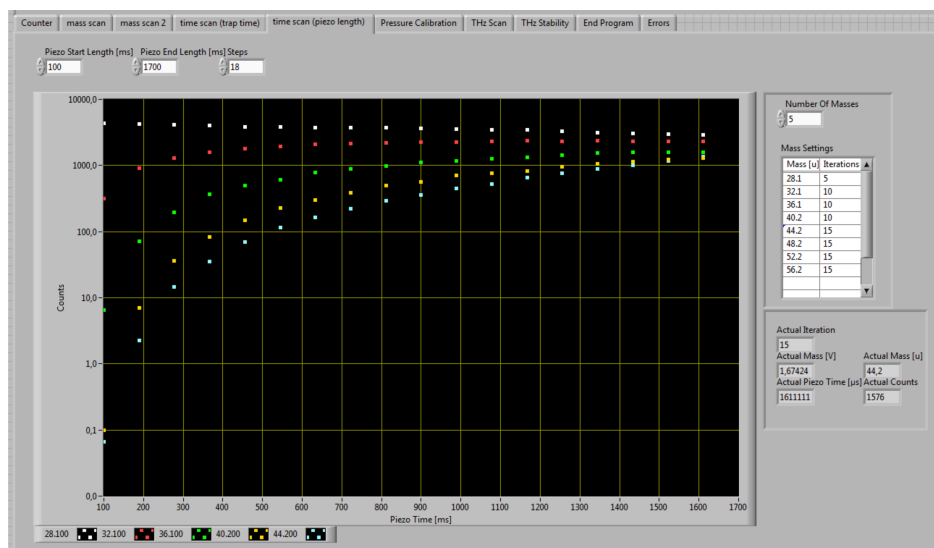


Figure 3.15: The GUI for the Piezo Valve Time Scan Mode. The interface is more or less equal to the one for the storage time (see figure 3.13). The only difference is that the user defines the range for the piezo valve pulse-length instead of the storage time.

In the source code, the first step is a control sequence. The user is asked to confirm that the ViscoVac is in the remote control mode. After confirmation, the connection to the ViscoVac is initialized and the gauge is started. The waiting time of 60 seconds afterwards is needed to ensure that the ViscoVac really measured the first pressure before the software tries to readout the value. The measurement sequence is embedded into a While Loop so the user can stop the measurement at any time. In this mode the complete communication and data transfer to the FPGA is included although it is actually not used in this mode. Therefore it is advisable to set the cycle time to zero for this mode. In the next step, the values from the ViscoVac are read out and processed. After this the two pressures from the Pfeiffer gauges are recorded and combined with the VisoVac pressure in a string. When the user stops the measurement, the string containing the measured pressure values is written into a file with the ending Calibration.txt and the VisoVac is stopped and switched back to local mode.

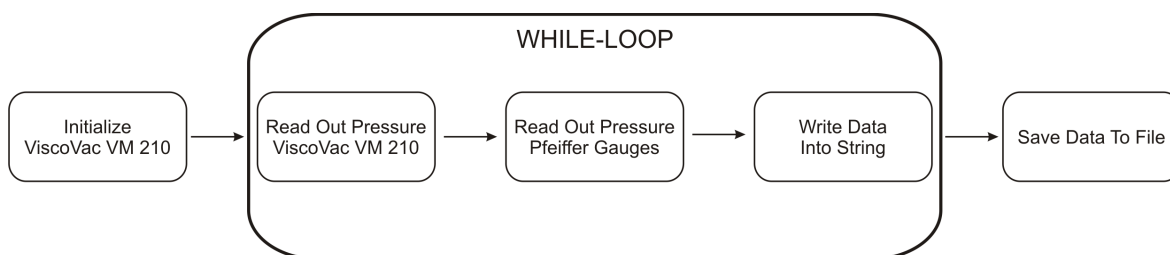


Figure 3.16: Scheme of the Pressure Calibration source code. In this code the Compact RIO system is not needed. The While Loop can be aborted by the user and while its running the software records the pressure values from the different pressure gauges.

One important point is that the read out of the different pressures does not happen exactly at the same time. Hence, this mode is only usable for static measurements. For dynamic measurements, a better time resolution is needed.

3.3.7 THz Scan Mode

This mode is used for recording THz spectra of trapped ions. The interface is divided into two main parts (see figure 3.17). In the upper part there are two areas with control elements and one with indicators. The bottom part contains the chart for displaying the recorded spectrum. In the upper left corner the user can define the start frequency in GHz, the end frequency in GHz and the step frequency in kHz (!) for the measurement. There are control elements for the number of iterations and the Off Resonant Frequency, which is used for on-off measurements. During long-time scans, this mode allows to suppress slow drifts in the measurement by taking an additional data point at an off resonant frequency position for each resonant frequency scanned. The corresponding number of ions measured at these frequencies are subtracted and this difference is displayed in the chart. In the middle section, the user can choose the mass of the ion in atomic units. The right panel includes only indicator elements, such as the actual frequency of the scan, the actual iteration number, and the number of ion counts.

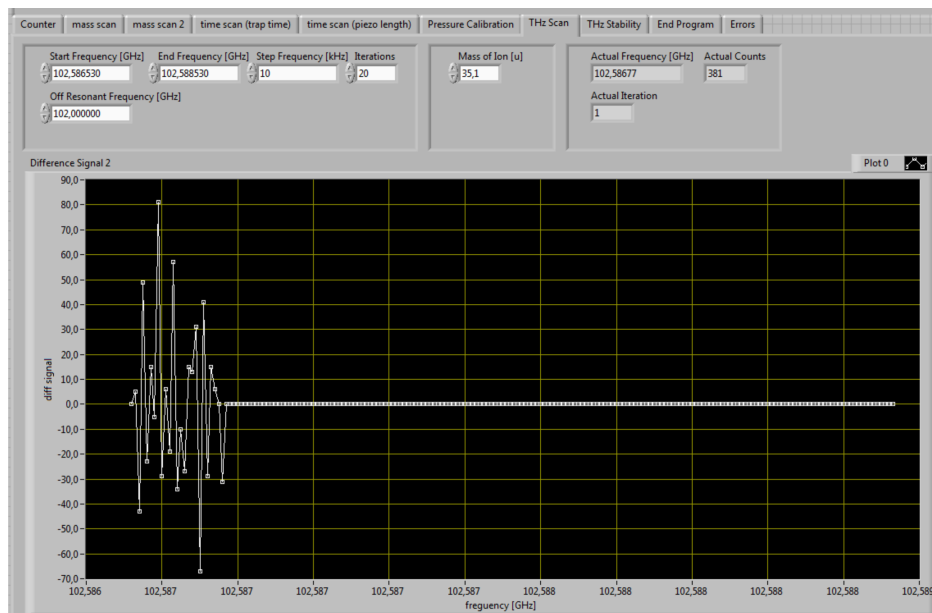


Figure 3.17: GUI of the THz Scan Mode. In the upper part some parameters for the scan such as the start- and stop-frequency of the scan, the frequency step, the number of iterations and the off-resonant frequency. Also the mass of the ion can be selected. The right panel on the upper part provides some information on the running scan. The lower part displays the chart where the difference signal is plotted as a function of the frequency. After every measurement cycle the chart is updated.

The source code (for the scheme see figure 3.18) of this part is costlier than for the other modes. This is partly due to the necessity to communicate not only with the FPGA and the ViscoVac, but also with the synthesizer used as a radiation source for the measurements. The first step is again a security query. The user is asked to confirm whether the ViscoVac and the synthesizer are configured correctly. After this, the connections to the ViscoVac and to the synthesizer are initialized, the values for the frequencies are read in and processed, and the start-frequency is submitted to the synthesizer. To store the data, two arrays are initialized for the on- and the off-

measurements. Before the measurement sequence starts, a 60 seconds waiting time is implemented due to the measuring delay of the ViscoVac. The measurement sequence itself is embedded into a For Loop, which is controlled by the number of iterations. The next inner structure is a Case Selector that is used to switch the direction of scanning after each iteration. The condition for the program to decide the direction of scanning is whether the last frequency is lower than the end frequency. If this is the case, the software scans from lower frequencies to higher frequencies. The first iteration is finished when the scanned frequency is higher than the stop frequency. The next evaluation of the Case Selector is now false, thus the software will scan from higher to lower frequencies for the second iteration. The next inner loop in the Case Selector is a While Loop and as described above, the exit condition for this loop is the comparison of the actual frequency with the start or stop frequency (depending on the direction of the scan). The measurement sequence itself contains the read in and processing of data from the GUI and the submission of the frequency to the synthesizer. In parallel, the ViscoVac pressure is read out. Since it is normally not necessary to read out the pressure for each measurement cycle the readout is restricted to every fifth cycle. If needed, the condition for the readout can be changed in the source code easily. Afterwards, the values are transmitted to the FPGA and the measurement cycle starts. With completion, the number of ions is written into the array at the position for the on-frequency value. With this step, the on-measurement is completed and the frequency is switched to the off-value. The next steps are again sending the data to the FPGA, processing the FPGA cycle, and writing the number of ions in the array for the off-values. For a live update of the chart, the values for the on- and off-measurements have to be subtracted and averaged. This is done in the next step and then the chart is updated. After all iterations are completed, the data for the measurements are written into a file. This is organized in the following way: The first part of the file consists of the on-measurement values. They are listed in a table, where the first column contains the frequency and the following columns hold the different iterations. The next block of the file is the same for the off-measurements. The last part of the file comprises the measured pressure values. The pressure values can be matched to a frequency data point by using the corresponding iteration and frequency listed in the first two columns. The last steps of the program are to set back the ViscoVac and the synthesizer to local mode and to close the connections.

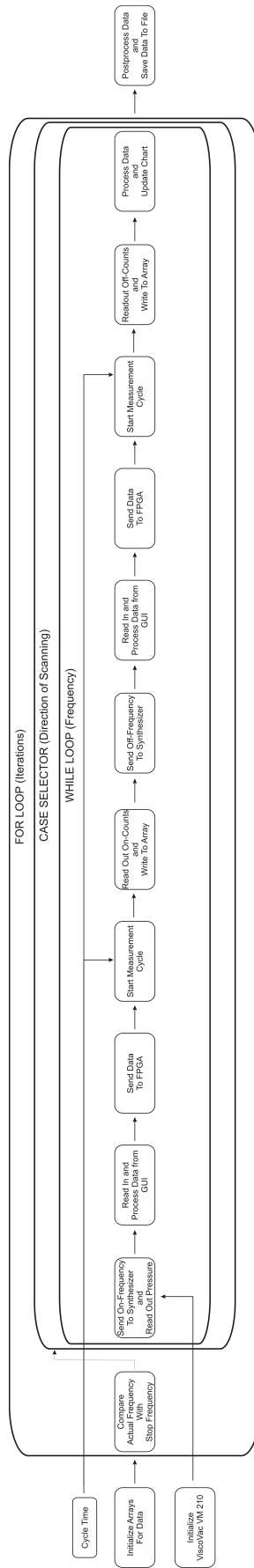


Figure 3.18: Block diagram of the THz Scan Mode. The code bases on two loops and includes a case structure. The inner loop is a While Loop that is defined by the frequency range, i.e. it terminates if the actual scanned frequency is out of the frequency range. In this loop two measurements (at the on- and off-frequencies) are performed. The case structure is used to decide whether the frequency range is scanned from low to high or from high to low frequencies. The outer For Loop is defined by the number of iterations.

3.3.8 THz Stability Mode

For some tests or experiments the THz Scan mode is too slow since for some applications it is not preferable to scan a frequency range, but to switch only between two frequencies. This opportunity is provided by the THz Stability Mode. The interface of this mode is different to the THz Scan Mode introduced above, since it contains multiple charts with different experimental parameters. In the upper part there are three boxes. In the left one, the user can set the two frequencies for the on- and off-resonant measurements. The middle one contains control elements to define two masses (in atomic mass units). The right panel includes indicators for the iteration, the ion mass, the scanned frequency and the ion counts. On the lower part of the GUI six small charts are placed. They display different experimental properties as the number of cluster ions at on- and off-frequency, the difference signal, the number of parent ions, the trap temperature, and the pressure measured with the ViscoVac all given as a function of time.

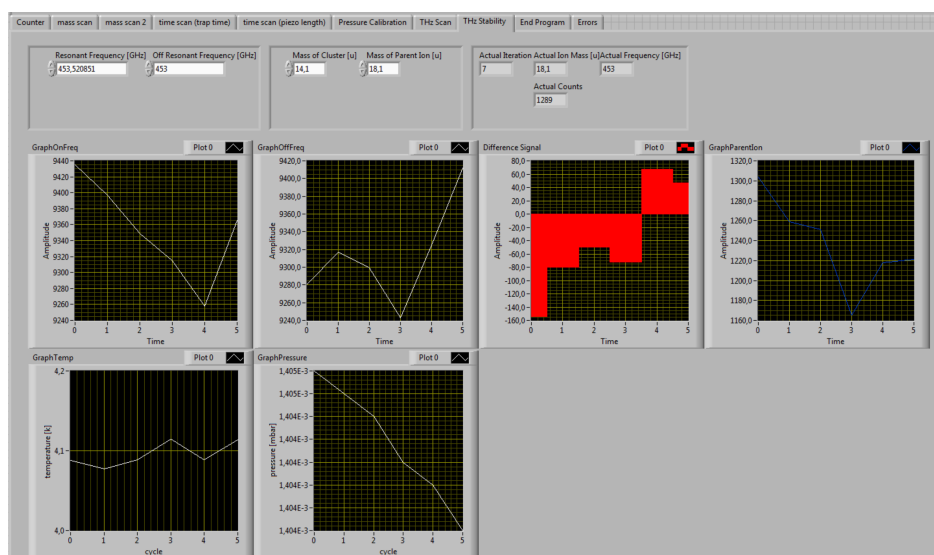


Figure 3.19: Screenshot of the GUI for the THz Stability mode. The user defines an on- and an off-frequency with the controllers at the top-left panel and the two mass to be measured in the top-middle section. The top-right panel includes different status elements. The lower part of the GUI is used for displaying different parameters of the experiment such as the cluster counts on the on- and off-frequency, the difference signal between those signals, the number of parent ions, and the temperature and pressure in the trap.

Like the other modes using the ViscoVac and/or a synthesizer, the first step in the code is a security query to ensure that the external hardware is configured correctly. The next steps are the set up of the connections to the ViscoVac and the synthesizer as well as the initialization of the arrays for the different data. After the usual time delay of 60 seconds to wait for the ViscoVac's first pressure value, the main part of this mode starts. The code is embedded in a While Loop and the user can abort the loop by clicking on the Stop Measurement button. In this loop, first the data from the GUI are read in, the on-frequency is transmitted to the synthesizer, and the ViscoVac is read out together with the trap temperature. In the next step the FPGA cycle is processed for the first time and the counts on the cluster ion mass are measured. Following is the measurement of the cluster ions at the off-resonant frequency. In

order to do this, the value for the off-frequency is submitted to the synthesizer and the FPGA cycle is processed for the second time. The new number of ion counts is stored in the corresponding array for the cluster ions at the off-frequency. The third and last FPGA cycle is processed for the parent ions. For this, the frequency of the synthesizer is not changed. Before starting this cycle, the control voltage for the second quadrupole is changed to the mass of the parent ion. After processing the FPGA cycle, the number of counts for the parent ion is stored in another array. Now the different charts for the measured values are updated and a new cycle starts. After stopping the measurement, the connections to the synthesizer and to the ViscoVac are closed, and the values from the arrays are written to file with the ending THzStability.txt. The file is organized as a list, i.e. the values for every iteration are written in one line with each line corresponding to a new iteration.

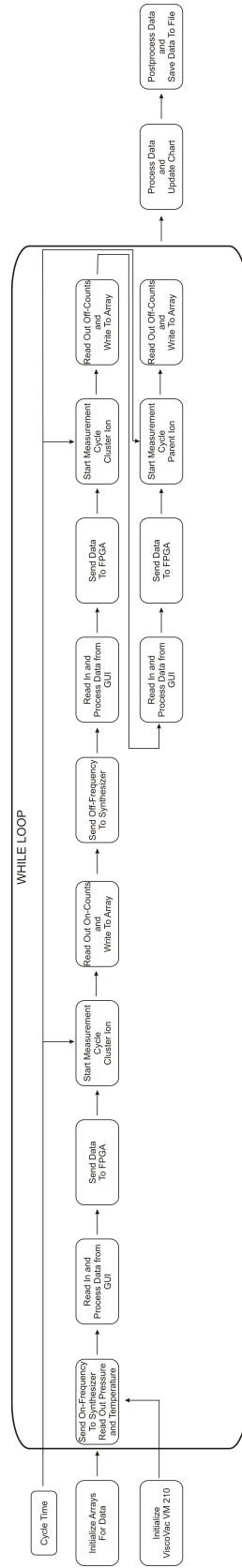


Figure 3.20: Scheme of the source code for the THz Stability Mode. This mode is controlled by one While Loop that can be terminated by the user. During one iteration the measurements at the on- and off-frequency are performed and also the pressure and temperature are recorded. At the end of each iteration, the six charts on the GUI are updated.

Part II

Rotational Spectroscopy of Cold Molecular Ions by State Specific Helium Attachment

4

Introduction to Rotational Spectroscopy

The second part of the work deals with the description of a newly developed method for rotational spectroscopy of mass selected cold molecular ions in a 22-pole ion trap, which can be used for recording pure rotational transitions. Normally, direct absorption spectroscopy is used for recording rotational transitions. Due to the low number of only a few thousand ions stored in the 22-pole trap during the experiment, this method is not applicable, since it is impossible to detect the light absorption directly with any detector. Therefore, action spectroscopy is applied. The idea is that light influences the number of product ions of a chemical reaction.

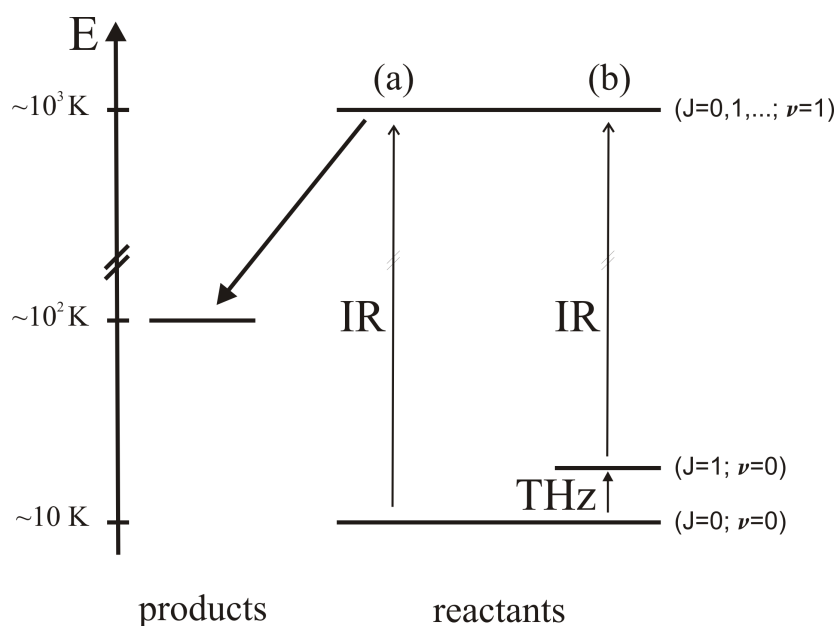


Figure 4.1: Laser Induced Reactions (LIR) Schemes. The figure shows two different types of the LIR scheme. The left scheme (a) is for ro-vibrational spectroscopy using an IR-photon. The reactants have not enough energy to form the products, if they are cooled down in the trap. By absorption of an IR-photon the stored ions are excited and by this the reaction becomes possible. The second scheme (b) shows a two photon scheme. In this case the IR-laser is set to a known ro-vibrational transition and the THz-photon is used to probe the rotational transition. The THz-photon itself does generally not provide enough energy to enable the reaction.

Figure 4.1 shows an example for the Laser Induced Reactions (LIR) method, which

was developed in the Cologne Laboratory Astrophysics group. A slightly endothermic chemical reaction between an ion and a neutral molecule does not happen at low temperatures, since the two reactants do not have enough energy to enable the reaction. By applying energy in form of light at the resonant frequency, the reaction is enabled and the product ion is formed. The number of the product ions can be recorded as a function of the frequency of light and by this, for example, a ro-vibrational spectrum of the reactant ion can be recorded. This spectroscopy method is called Laser Induced Reactions (LIR). It is used in the Cologne Laboratory Astrophysics group regularly for the investigation of different ions of astrophysical or astrochemical relevance ([34], [21], [35], [36], [37], [38]). This method can be extended to a two photon experiment ([23]). In this case an IR-photon and a THz-photon are used to enable the reaction at low temperatures. For example the IR-laser is tuned to a known ro-vibrational transition of the investigated ion, which starts from a rotational excited level. The second THz-photon is used to pump the ions from a lower lying rotational level into the higher rotational level. By scanning the THz frequency the pure-rotational spectrum can be recorded. The disadvantage of the LIR-method is that for both schemes an appropriate endothermic reaction is needed to perform this method. This fact restricts the LIR method to a limited number of ions.

To overcome the limitation caused by this, one idea is to use the mechanism of helium cluster formation at low temperatures. This method is based on an observed rotational-state dependent attachment of He atoms to cold stored molecular ions. It can be regarded as a variant of action spectroscopy, which was so far, with a few exceptions, limited to ro-vibrational or electronic spectroscopy. The difficulty is the necessity of low temperatures for the formation of the helium clusters, which were not reachable with the LIRTRAP experiment in the past. However, with the newly constructed experiments FELion (see part I) and COLTRAP ([39]) this limit is no more relevant. The advantage of this new approach is that it is applicable to a lot of different ionic species and at a wide frequency range. With this technique it is possible to record electronic spectra (for example of N_2 [40]), and it can also be used to record IR-spectra, which was also done in the Cologne Laboratory ([39]). Since the photons are highly energetic in these two cases, it is reasonable that the attachment of the helium is inhibited. Besides, it is also possible to use a THz-photon to excite the ion. This results in a sufficient change of the attachment process of the helium, which can be recorded ([1]). This introduces the possibility for direct rotational spectroscopy with mass selected ions in a cold 22-pole trap, which was possible before only in very special cases, as for example H_2D^+ and D_2H^+ ([41]), where the usual LIR technique can be applied.

5

Rotational Spectroscopy with FELion

In this chapter the systems of CD^+ and helium and HCO^+ and helium will be investigated. The main part of this chapter will deal with the measurements of CD^+ and helium. There are several reasons why CD^+ was chosen for the investigation of the process. First of all CD^+ is a simple closed shell diatomic, whose ground state transition is well known due to investigations of Amano ([42]). The rotational ground state transition at 453 GHz is also in a range accessible with available radiation sources with sufficient power. Last but not least it appeared that the strength of the cluster depletion signal in this case is much stronger than for any other ions we tested so far. These three features qualify CD^+ as a good candidate for test measurements to obtain a better assessment of the method and the involved processes.

5.1 Experimental Setup

In this section the experimental conditions for the different measurements are summarized. Besides the settings for the Storage Ion Source and the first quadrupole mass filter this includes also the calibration measurements for the used mm-wave source as well as the calculation of the helium number densities, which are needed for the analysis of the measurements. Another critical number is the temperature of the ions. Since this temperature cannot be measured directly in this section a procedure for estimating the ion temperature is presented. Finally a short description of the used measurement modes is given.

5.1.1 Ion Production

For the experiments on the CD^+ and helium system the Storage Ion Source (see 2.2) was driven with CD_4 as a precursor gas. Some typical settings for the Storage Ion Source and the first quadrupole (see 2.3) are summarized in table 5.1.

In the figures 5.1 and 5.2 two typical mass scans (for more information about the Mass Scan Mode see chapter 3.3.2) from the source are shown. Figure 5.1 shows the unfiltered mass spectrum from the source with no DC voltage applied to the first

Table 5.1: Experimental setup for the source and the first quadrupole for CD^+ with typical parameters.

parameter	value
precursor gas	CD_4
pressure (source chamber)	$\sim 5 \cdot 10^{-6}$ mbar
electron energy	31.1 eV
focus	28.7 V
endplates	1.5 V
source float	0.1 V
endplates	1.5 V
B0 opening time	15 ms
quad I AC, U_{set}	54 V / 9.9 mA
quad I DC, V_{set}	11.8 V

quadrupole. In this spectrum two different bands are visible. The first one is CD_n^+ containing the required CD^+ at mass 14 u and the second band is C_2D_n^+ . Figure 5.2 shows the remaining CD^+ , when selecting $\frac{m}{q} = 14 \frac{u}{e}$ in the first quadrupole. For the kinetic measurements (see 5.2.2) the number of transmitted CD^+ ions per source opening is usually below 10000, while for the rotational measurements (see 5.3) the number of CD^+ ions is around 15000. The variation for the different measurements can easily be controlled by the pressure in the Storage Ion Source, the extraction pulse length of the source, and by the filter settings of the first quadrupole.

For the kinetic measurements as well as for the rotational spectroscopy measurements the CD^+ ions were stored in the 22-pole ion trap with helium at high number densities and at low nominal trap temperatures between 4 K to 12 K. Typical helium pressures were in the range between $5 \cdot 10^{-4}$ mbar and $4 \cdot 10^{-3}$ mbar. These pressure values were directly measured inside the trap housing via the connected spinning rotor gauge. These pressures correspond to number densities inside the trap between $1.2 \cdot 10^{14} \text{ cm}^{-3}$ and $1.4 \cdot 10^{15} \text{ cm}^{-3}$ at 4 K. The procedure for calculating the number density based on the measured pressure is described in the next subsection. A typical mass spectrum of stored CD^+ together with helium at 4 K is shown in figure 5.3.

The first peak at mass 14 u on the left side is the initial CD^+ , which was injected into the 22-pole trap. Figure 5.3 shows that under the typical conditions in the trap up to four helium atoms can be attached to the CD^+ ion. The ratio between the initial CD^+ and the $\text{He}\bullet\text{CD}^+$ cluster ion after a storage time of 600 ms is (at 4 K and a helium number density of $5 \cdot 10^{14} \text{ cm}^{-3}$) $\sim 15\%$. This ratio is larger than for C_3H^+ for example. This is a helpful fact for the rotational measurements described in chapter 5.3, since more cluster ions are available for the measurement.

5.1.2 Helium Number Density Calculation

In the experiment only the helium pressure inside the trap is measured with a spinning rotor gauge. To determine absolute rate-coefficients from the observed time evolution measurements (see chapter 5.2.2) it is necessary to know the helium number density in the trap. Since the pressure is measured directly in the trap it is not necessary to

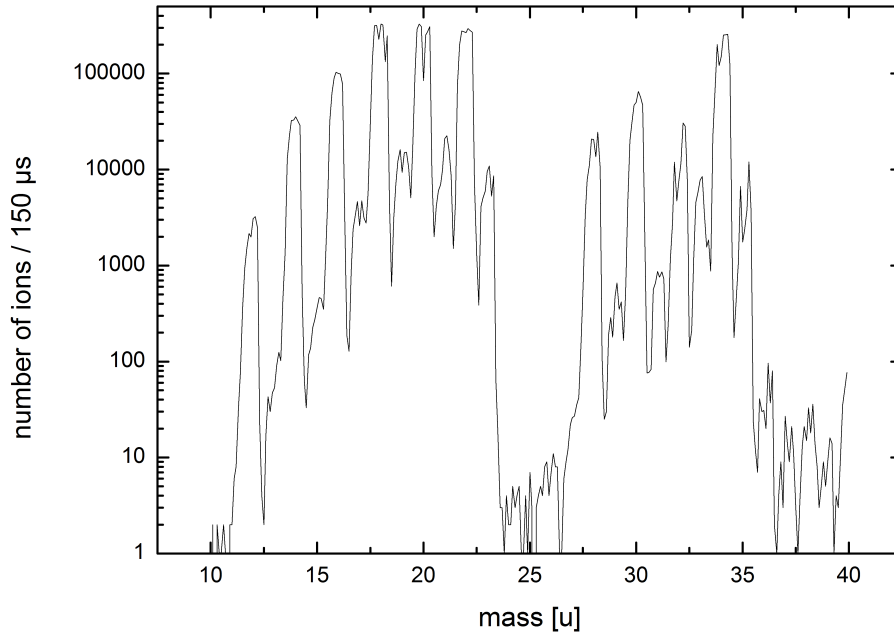


Figure 5.1: Unfiltered mass spectrum from the ion source. For this scan the first quadrupole was used in transmission mode (no DC voltage and AC voltage was set to 55 V). The ions were not trapped in the 22 pole trap and no helium was admitted to the trap. The other settings were equal to the values given in table 5.1.

use a calibration factor as given in table 2.5 in chapter 2.5.2. However, in this case the thermal transpiration effect has to be taken into account, which occurs at the low temperatures in the trap. This effect was discovered first by Reynolds in 1879. When a large temperature difference between two vessels, filled with rarefied pure gas and connected with a pipe, exists, the thermal transpiration effect describes the significant pressure difference obtained in the two reservoirs. In order to describe this effect several different theoretical and empirical equations have been proposed (e.g. [43], [44]). In our experiment this effect occurs since the 22-pole ion trap is at 4 K and the ViscoVac VM210 Spinning Rotor Gauge is at room temperature and both are connected by a tube with a diameter d of 3 mm. A critical parameter for this effect is the ratio $\frac{d}{\lambda}$ where λ is the mean free path of the gas particles. In the case that λ is much larger than d the low density approximation can be used.

$$\frac{p_{\text{trap}}}{p_{\text{Visco}}} = \sqrt{\frac{T_{\text{trap}}}{T_{\text{Visco}}}} \quad (5.1)$$

Where the index trap denote the values for the 22-pole ion trap and Visco the ones for the ViscoVac VM210 Spinning Rotor Gauge. To calculate the number density in the trap region the equation

$$n_{\text{trap}} [\text{cm}^{-3}] = 4.2 \cdot 10^{17} \frac{p_{\text{Visco}} [\text{mbar}]}{\sqrt{T_{\text{trap}} [\text{K}]}} \quad (5.2)$$

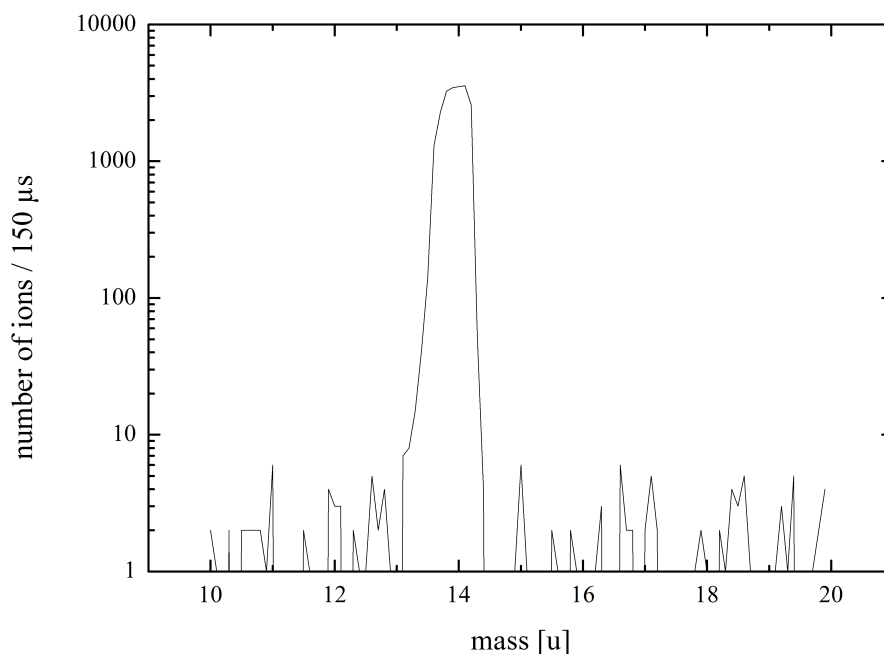


Figure 5.2: Example for a mass spectrum coming from the source with the first quadrupole in the mass selecting mode, tuned for CD^+ . The ions are again not trapped and no helium was admitted into the trap.

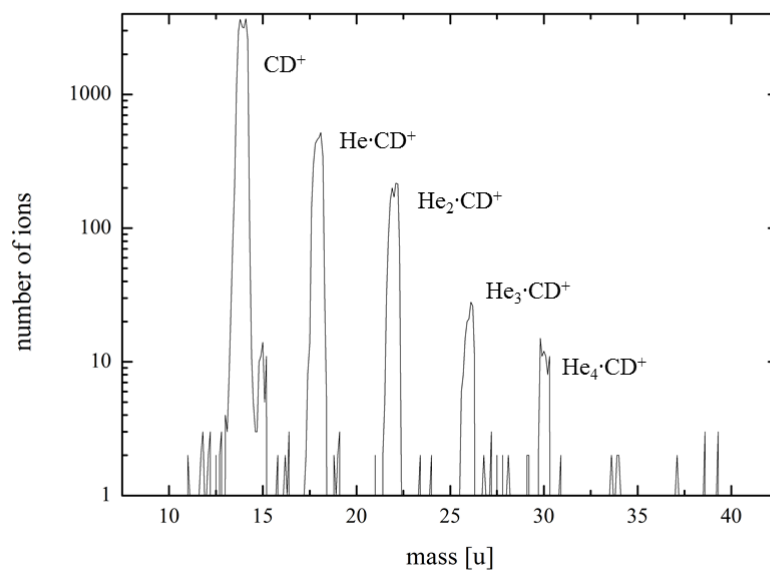


Figure 5.3: Mass spectrum of the content of the 22 pole ion trap at a nominal temperature of 4 K and after a storage time of 600 ms. The used helium number density in this experiment was $5 \cdot 10^{14} \text{ cm}^{-3}$. On the left hand the first mass peak is the initial CD^+ .

is used ($T_{\text{Visco}} = 300 \text{ K}$ included in the prefactor). If the trap is operated at higher pressures like for these experiments the formula from Takaishi and Sensui ([45]), i.e. the empirically determined approximation given by Tanuma et al. ([44]) is used

$$\frac{p_{\text{trap}}}{p_{\text{Visco}}} = 1 + \frac{\left(\frac{T_{\text{trap}}}{T_{\text{Visco}}}\right)^{0.5} - 1}{6.11 \cdot x^2 + 4.26 \cdot x + 0.52 \cdot x^{0.5} + 1} \quad (5.3)$$

where the dimensionless parameter x is specified as

$$x = 2 \cdot \frac{d [\text{mm}] p_{\text{Visco}} [\text{Pa}]}{T_{\text{trap}} [\text{K}] + T_{\text{Visco}} [\text{K}]} \quad (5.4)$$

The correct number density can then be calculated by

$$n_{\text{trap}} = n_0 \frac{p_{\text{trap}}}{p_0} \sqrt{\frac{T_0}{T_{\text{trap}}}} \quad (5.5)$$

with p_0 the standard pressure of 1 bar, $T_0 = 273.15 \text{ K}$, and $n_0 = 2.651 \cdot 10^{19} \text{ cm}^{-3}$. By using this formalism the helium number densities corresponding to the different pressures are calculated.

5.1.3 Calibration of the mm-Wave Source

For the measurement of the pure rotational transitions of CD^+ presented in chapter 5.3 two different setups to couple radiation into the trap were used. As a radiation source we used the Virginia Diodes, Inc. (VDI) WR9.0 THz Starter Kit in the WR2.2 band configuration. In this configuration the VDI W9.0AMC was combined with two doubler elements, the WR4.3X2 and the WR2.2X2. As an RF-source the narrowband ($\ll 1 \text{ Hz}$), rubidium-clock referenced microwave synthesizer Rhode und Schwarz SMF100A was used. In the first configuration the VDI WR9.0AMC was placed directly in front of a 0.8 mm thick CVD diamond window (Diamond Materials GmbH) (see figure 5.4 for a technical drawing including relevant dimensions) and the radiation was coupled into the trap without any other optical elements. To get an idea of the total power available in the trap region, which is important to know for the numerical and analytical simulations (see chapters 5.3.1 and 5.3.2), a geometrical estimation was done. As a starting point the maximum output power of $8 \cdot 10^{-5} \text{ W}$ of the VDI WR9.0 THz Starterkit at 453 GHz (VDI User Guide) was used. From the VDI Waveguide Feedhorn Specifications the full 3 dB bandwidth angle of 10° for the WR-2.2 configuration was used to estimate the available power at the trap entrance at a distance of 140 mm. Besides the geometrical aspect also the transmittance of the diamond was taken into account, which is 70 % for radiation at this wavelength. Overall the estimated THz power in the trap region is

$$P_{\text{Trap}} \approx 0.06 \cdot P_0 = 3.5 \cdot 10^{-6} \text{ W} \quad (5.6)$$

This value for the THz power is only a geometrical approximation and does not take any other effects, e.g. standing waves, into account.

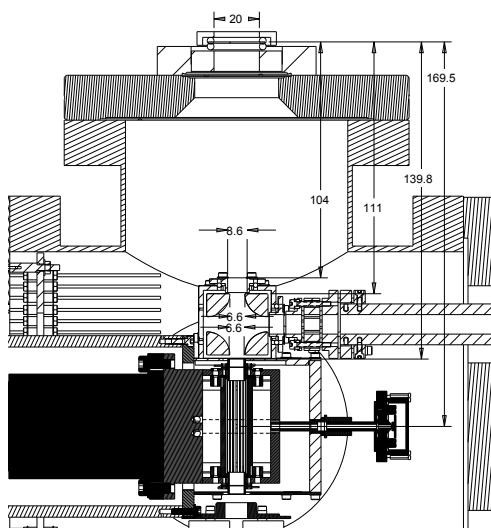


Figure 5.4: Technical drawing with relevant dimensions for in coupling the mm-wave radiation. The diamond window is shown in the upper part of the figure.

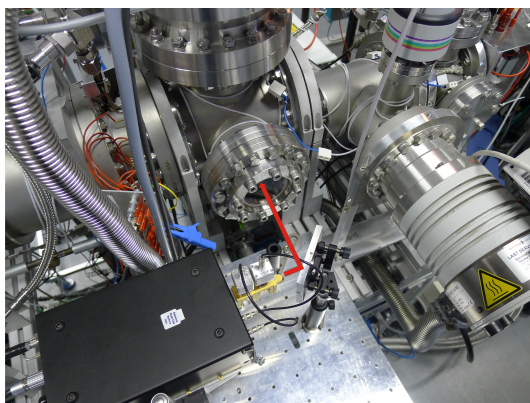


Figure 5.5: This picture shows the 22-pole ion trap apparatus together with the VDI WR9.0 THz Starterkit. In the center of the picture the focussing mirror for the in coupling of the THz radiation into the trap is shown. The black box on the left hand side is the VDI Starterkit and in red the beam path is schematically shown.

For the second configuration the VDI WR9.0 THz Starterkit was used in combination with an elliptical focussing mirror (focus point $f = 43.7$ mm). The setup is shown in the picture 5.5.

For this setup the VDI WR9.0 THz Starterkit is no longer positioned directly in front of the window but it is rotated by 90° . To focus the THz-radiation into the trap an elliptical mirror is used. Since the focus of the beam is positioned in the trap region the beam waist at the window is very broad and due to this the small diamond window has to be replaced by a larger quartz window (Z-cut quartz, Torr Scientific Ltd., BVPZ64NQZ, $\sim 80\%$ transmission coefficient) in order not to lose too much of the beam. To optimize the maximum available power in the trap region the VDI WR9.0 THz Starterkit can be moved with a x-y-z table from Thorlabs. The position and the angle of the mirror can also be fine tuned. Since it is not possible to measure the power directly inside the trap the whole setting is mounted on an optical plate, so it can easily be removed from the machine for calibration. For calibration and alignment a pyro

detector is positioned at the place of the 22-pole trap, the quartz window and the trap entrance electrode are simulated with two iris diaphragms. With this configuration it is possible to measure an approximate value for the maximum THz power at the trap region, which is five times higher than the value for the unfocussed setup. Taking the higher transmissivity of the quartz window into account, the power for the focussed setup can be estimated with

$$P_{\text{Trap, focussed}} \approx 2 \cdot 10^{-5} \text{ W} \quad (5.7)$$

at 453 GHz. This setup was also used to record a relative power calibration curve for the VDI WR9.0 THz Starterkit. By applying an attenuation voltage between 0-5 V it is possible to reduce the output power of the VDI Starterkit. By using this setup the relative power in dependence of the attenuation voltage amplitude was measured.

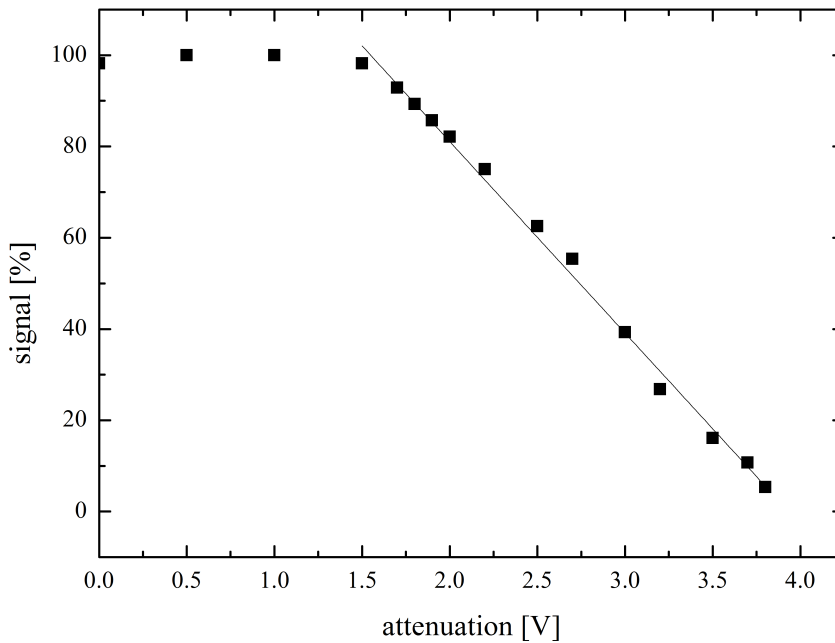


Figure 5.6: Relative calibration measurement of the VDI WR9.0 THz Starter Kit at 453 GHz. The relative output power is plotted as a function of the applied attenuation voltage. For the focussed setup 100% = $2 \cdot 10^{-5} \text{ W}$ and for the unfocussed setup 100% = $3.5 \cdot 10^{-6} \text{ W}$

Figure 5.6 shows the calibration measurement for the relative output power. Below a value of 1.5 V of the attenuation voltage there is no effect visible. For higher attenuation voltages the behavior of the output power was fitted with a linear function and can be described in the range of 1.5 V to 4.0 V with the equation

$$P_{\text{rel}}[\%] = 165\% - x[\text{V}] \cdot 42 \frac{\%}{\text{V}} \quad (5.8)$$

This calibration is used for the measurements presented in section 5.3.3.2 for the conversion of the applied attenuation voltage to relative power (see figures 5.19 and 5.20).

5.1.4 Determination of the collisional ion temperature

One important parameter in the models presented in the chapters 5.3.1 and 5.3.2 is the collisional temperature of the stored ions. This temperature cannot be measured directly in comparison to the trap temperature. In order to get an estimation for the translational temperature of the ions the equation

$$T_{\text{coll}} = \frac{m_{\text{He}} \cdot T_{\text{ion}} + m_{\text{ion}} \cdot T_{\text{He}}}{m_{\text{He}} + m_{\text{ion}}} \quad (5.9)$$

is used. The temperature of the helium is assumed to be 4 K as the nominal trap temperature. The temperature of the ions is estimated from the width of the recorded rotational lines of CD^+ . Figure 5.7 shows a typical rotational transition of CD^+ at a nominal temperature of 4 K. Since the lines are power broadened the observed line profile is a Voigt profile. The Voigt profile is a convolution of the Doppler profile caused by the temperature of the ions and a Lorentzian profile due to the power broadening of the lines. To get an estimation for the ion temperature only the Doppler profile has to be separated from the observed Voigt profile.

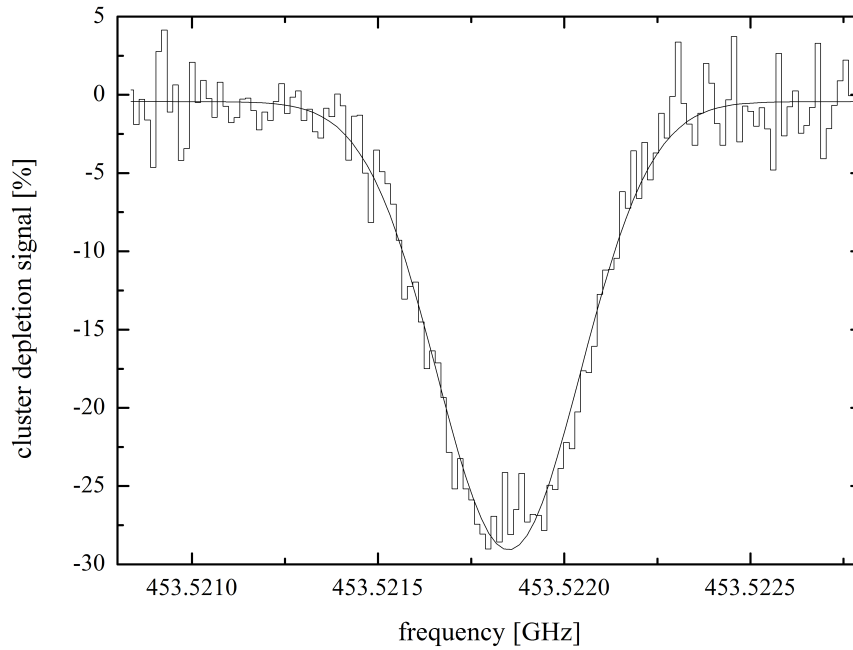


Figure 5.7: Cluster depletion signal of CD^+ at a nominal trap temperature of 4 K. The black lines is the averaged signal of 20 measurements and the black solid curve shows a fitted Voigt profile. From the FWHM of 453 kHz of the fit the temperature of the ions is calculated. The corresponding Doppler temperature is 12.3 K. The signal was recorded with the focussed setup and a power of $2 \cdot 10^{-5}$ W. Note: The signal is multiplied with a factor of -1.

For the FWHM of the Doppler broadening one can write

$$\Delta\nu_G = 2\nu_C \cdot \sqrt{\frac{2kT_D \ln(2)}{mc^2}} = c_G \sqrt{T_{\text{ion}}} \quad (5.10)$$

where $\Delta\nu_G$ is the FWHM of the Gauss profile, ν_C the center frequency, k the Boltzmann constant, T_{ion} the ion temperature, m the mass of the ion, and c the speed of light. c_G is constant factor for a certain transition of one ion. For the Lorentzian profile one can also write down the FWHM maximum, which depends on the applied power

$$\Delta\nu_L = 2 \cdot \sqrt{\frac{3c^2 A}{4\pi^2 \nu_C h}} \cdot \sqrt{I} = 2 \cdot c_L \cdot \sqrt{P} \quad (5.11)$$

where $\Delta\nu_L$ is the FWHM of the Lorentzian profile, A is the Einstein A coefficient for the transition, and h the Planck constant. I and P are the intensity of the light and the power, respectively. c_L is again a constant for one transition of a certain ion in the 22-pole ion trap. The convolution of the Voigt profile can be described by the approximation from Olivero and Longbothum ([46])

$$\Delta\nu_V = 0.5346\Delta\nu_L + \sqrt{0.2166\Delta\nu_L^2 + \Delta\nu_G^2} = 0.5346\Delta\nu_L + \sqrt{0.2166\Delta\nu_L^2 + c_G^2 T_{\text{ion}}} \quad (5.12)$$

This function was fitted to the different observed FWHM, which were observed at a nominal trap temperature of 4 K at different power levels. From this fit the ion temperature at a nominal trap temperature of 4 K was derived with 12.3 K and the value of c_L was fitted to $(5.5 \pm 0.6) \cdot 10^7$. With the values for c_G and c_L and equation 5.12 the ion temperatures for the other nominal trap temperatures could be calculated. In table 5.2 the calculated ion temperatures are listed together with the corresponding collisional temperatures for different nominal trap temperatures.

Table 5.2: Calculated collisional temperatures of the CD^+ ions. From the recorded rotational lines at different nominal temperatures a Doppler temperature was derived by applying the described procedure. The temperatures T_{coll} were calculated by using formula 5.9. The helium temperature is assumed to be equal to the nominal temperature.

T_{nom}	T_{ion}	T_{coll}
4 K	12.3 K	5.7 K
7 K	15.5 K	8.9 K
8 K	17.8 K	10.2 K
13 K	30.6 K	16.9 K

5.1.5 Measurement Modes

For the measurements presented in this chapter primarily three different measurement modes were used. These modes are explained in this section in a short way. A more detailed description of the measurement modes and their implementation is given in chapter 3.3.

5.1.5.1 Mass Scan Mode

This mode is used to record mass spectra as shown in figure 5.3. The setup of FELion allows to record mass spectra of either the content of the Storage Ion Source without storage time (see figure 5.1) or of the content of the 22-pole ion trap after a certain storage time (see figure 5.3). In both cases the cycle time of the experiment and the storage time are fixed and for every measurement cycle the mass setting for the second quadrupole is changed. The mass range to be scanned, the step size and the number of iterations can be chosen.

This method allows to figure out which ion species are produced in the source or in the trap under the chosen conditions. For the experiments described below this is useful to check whether it is possible to grow helium cluster ions under the given settings (temperature and helium number density). This mode does not provide any information about the rate and by this about the rate-coefficients of the "system". For this the Time Scan Mode is used, which is described in the next paragraph.

5.1.5.2 Time Scan Mode

The Time Scan Mode is used for the investigation of the reaction kinetics in the trap. This is one of two main applications of the 22-pole experiments. The other main application is spectroscopy of ions.

The time evolution of a reaction system can be investigated by varying the storage time. For this measurement mode usually one mass is selected by the first quadrupole coming from the source. The ions are stored together with the reaction and buffer gas, both are helium for these experiments, and the trap is kept at the temperature of interest. To measure the time evolution all expected product masses have to be recorded as a function of storage time. In order to do this, the experimental cycle has to be repeated with different settings for the storage time and the second quadrupole mass filter. To improve the statistics the measurements are repeated several times. The software for this mode (see chapter 3.3.4) allows to selected the number of iterations for each mass separately. Optionally the time for helium admittance can be varied instead of the storage time. (see chapter 3.3.5).

5.1.5.3 THz Scan Mode & THz Stability Mode

The last modes used for the measurements, presented in this chapter, are the THz Scan Mode and the THz Stability Mode. The THz Scan Mode is used to record the rotational spectra as shown for example in figure 5.7. For this mode one type of ion is selected by the first quadrupole and the second quadrupole mass filter is set to the mass of the corresponding helium cluster ion. For the spectroscopy measurements the storage time is fixed and the frequency of the mm-wave source is scanned in a defined range. For each frequency point two measurements are performed. For the first measurement the frequency of the mm radiation is tuned to the actual frequency of the scan and for the second measurement the frequency is shifted to a so called off-frequency. This frequency should not hit any rotational transition of the investigated ion or the corresponding cluster-ion. The cluster depletion signal s is then calculated with these data as follows:

$$s = \frac{N_{\text{off}} - N_{\text{on}}}{N_{\text{off}}}$$

Since the number of formed helium cluster-ions is lower if a transition of the bare molecular ion is hit, the cluster depletion signal is positive. The spectra shown in this work are multiplied with a factor of -1 to obtain "normal" absorption lines. In most cases the signal to noise ratio is not sufficient after a single iteration, so a higher number of iterations can be set. The direction of scanning is changed after each iteration in order to compensate for drifts.

For some measurements, as for example the power dependence measurements shown in figures 5.19 and 5.20, the use of the THz Scan Mode would be too time consuming and it is not necessary to record for every setting the whole rotational line. For this purpose the THz Stability Mode was developed (see section 3.3.8). In this mode the signal is basically obtained in the same way as in the THz Scan Mode, but instead of scanning a frequency range the mode uses only the center frequency of the line and the off frequency to record the cluster depletion signal. The number of iterations can again be chosen.

5.2 Kinetic Measurements of CD⁺ and Helium

In this section the kinetic measurements for the CD⁺ and helium system are presented. The section starts with a short overview of the theory of ternary reactions ([14]). Afterwards the kinetic measurements itself together with a numerical simulation, used for fitting the measurements, are shown.

5.2.1 Theory of Ternary Reactions

In this section some of the fundamental assumptions used to describe association processes are summarized. It is commonly assumed that in such a reaction two different species come together and form an excited intermediate, which is then stabilized by an emission of a photon ("two-step" process). While in interstellar space this is usually the only association process, due to the low number densities, in the laboratory the intermediate can also be stabilized by a collision with a third body. For the experiments in this thesis the neutral reaction partner is always a helium atom. Hence, the overall association reaction can be written as:



where k^* is a second-order rate-coefficient. The given empirical description is a simple approximation, which uses some elementary processes, stabilizing the intermediate or dissociating it. In most theoretical descriptions the process described in equation (5.13) is assumed to be a process of two independent stages. The first step is the two species A⁺ and He collide and form a collision complex. This reaction can be described with a bimolecular capture rate-coefficient k_c



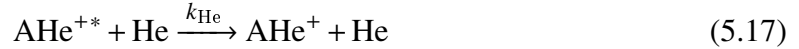
AHe^{+*} means that the complex is excited and the internal energy of the complex is above its dissociation limit. To describe the lifetime of the complex a mean value τ_{dis} is used



where $k_{\text{dis}} = \frac{1}{\tau_{\text{dis}}}$. Under most conditions in the laboratory the back-dissociation process will dominate and only a few complexes are stabilized. For the stabilization different processes can occur. The first process is the stabilization via emission of a photon



where $k_{\text{rad}} = \frac{1}{\tau_{\text{rad}}}$. The second process is the stabilization by a collision with a neutral third body. Normally the experiment is performed with a reaction gas and a buffer gas, so in principle there are two different collisions possible. For the experiments presented here the reaction gas and the buffer gas are both helium. Thus, only one process has to be taken into account:



again with $k_{\text{He}} \cdot [\text{He}] = \frac{1}{\tau_{\text{He}}}$ (with k_{He} is a binary rate-coefficient). Besides these two processes in general it can also occur that the excited intermediate can dissociate into two new reaction products. For the discussion here this process is neglected. With the elementary processes (5.13) to (5.17) the overall second-order rate-coefficient k^* can be written as:

$$k^* = k_c \cdot \frac{k_{\text{He}} \cdot [\text{He}] + k_{\text{rad}}}{k_{\text{dis}} + k_{\text{He}} \cdot [\text{He}] + k_{\text{rad}}} \quad (5.18)$$

where $[\text{He}]$ is the helium number density in the experiment and k_c and k_{He} can be rewritten by using the Langevin rate-coefficient k_L and a stabilization efficiency factor f

$$k_c = k_L \cdot f_c \quad (5.19)$$

$$k_{\text{He}} = k_L \cdot f_{\text{He}} \quad (5.20)$$

$$(5.21)$$

For the system of CD^+ and He investigated in this chapter $k_L = 6 \cdot 10^{-10} \text{ cm}^3 \text{ s}^{-1}$. Of course the two stabilization efficiency factors can be quite different. Depending on the experimental conditions equation 5.18 can be simplified. For example at low

helium number densities and if $k_{\text{dis}} \gg k_{\text{He}} \cdot [\text{He}] + k_{\text{rad}}$ all terms in the denominator besides k_{dis} can be neglected. By this a bimolecular radiative rate-coefficient

$$k_r = k_c \cdot \frac{k_{\text{rad}}}{k_{\text{dis}}} = k_c \cdot \frac{\tau_{\text{dis}}}{\tau_{\text{rad}}} \quad (5.22)$$

and a ternary association rate-coefficient

$$k_3 = k_c \cdot \frac{k_{\text{He}}}{k_{\text{dis}}} \quad (5.23)$$

can be introduced. By this the overall second-order rate-coefficient can be written as

$$k^* = k_3 \cdot [\text{He}] + k_{\text{rad}} \quad (5.24)$$

The overall second-order rate-coefficient k^* is observed in the experiment and by this also k_3 and k_r are accessible.

In the experiment the temperature dependence of the ternary rate-coefficient is of special interest, since the dependence can be validated. To derive the temperature dependence for example RRKM-like approaches (named after the inventors Rice-Ramsperger-Kassel-Marcus) are used, which bases on the density of states in the intermediate complex and in the transition state. The modified thermal treatment developed by Bates and Herbst ([47], [48]) predicts that the temperature dependence is

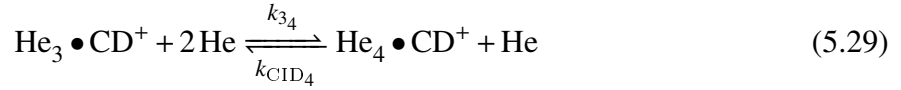
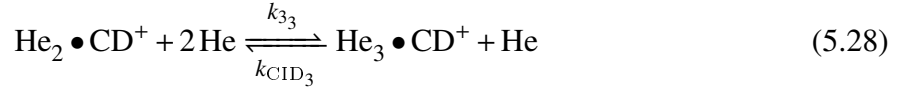
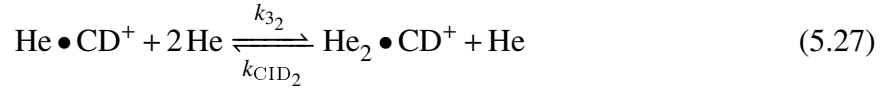
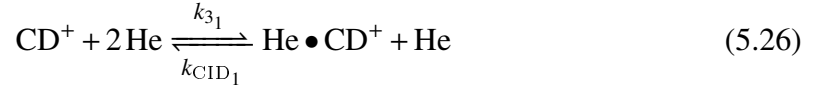
$$k_3 \sim T^{-\frac{l}{2} + \delta} \sim T^{-\frac{1}{2}} \quad (5.25)$$

where l is the number of rotational degrees of freedom and δ is used to take the temperature dependence of the stabilization into account (e.g. $l = 2$ for CD⁺ + He). The difficulties to derive the temperature dependence for the ternary rate-coefficients are mainly due to the difficulties to obtain the internal energies of the intermediate complex, the bare ion, and the neutral reaction partner as a function of energy or temperature.

5.2.2 Time Evolution of the CD⁺ + Helium System

Beside the spectroscopy of the $J = 0-1$ rotational transition of CD⁺ and the understanding and the modeling of the new spectroscopic method also the underlying kinetics of the CD⁺ + He system is important, since the obtained rate-coefficients are needed for the numerical simulation presented in section 5.3.2.

The formation of the different He_{*n*} • CD⁺ ($n = 0, \dots, 4$) ions is described by the reaction chain (if k_r is neglected for the moment):



$$(5.30)$$

The formation of the cluster ions is a three body process (see discussion above), this means for the formation of the cluster ions always two helium atoms are necessary. In contrast to this we assume that the destruction process is a binary process, so the cluster ion is eventually destroyed by a collision with a single helium atom. For the investigation of this system the temporal evolution of the different $\text{He}_n \bullet \text{CD}^+$ ($n = 0, \dots, 4$) was studied when CD^+ and helium at high number densities are stored together in the cold 22-pole ion trap. These measurements were performed at nominal temperatures in the range of 4 K to 10 K and at different helium number densities. The injected ions were cooled down by collisions with helium buffer- and reaction gas. The helium was let in continuously into the trap. For this experiments it is important to ensure that the sum of all involved ion species is constant over the storage time (i.e. that no additional reaction products are missing). The figures 5.8 and 5.9 show two different examples of such measurements. The total number of ions (black dots) is constant over the storage time and thus the measurements can be described by numerical simulations of the forward and backward reactions given in 5.26 to 5.29. The results of the simulations are shown in the figures 5.8 and 5.9 as solid lines.

The numerical simulation is based on the rate equation system, where N_x is the number of ions of type x.

$$\begin{aligned} \frac{dN_{\text{CD}^+}}{dt} &= -R_{3_1} \cdot N_{\text{CD}^+} + R_{\text{CID}_1} \cdot N_{\text{He} \bullet \text{CD}^+} \\ \frac{dN_{\text{He} \bullet \text{CD}^+}}{dt} &= +R_{3_1} \cdot N_{\text{CD}^+} - R_{\text{CID}_1} \cdot N_{\text{He} \bullet \text{CD}^+} - R_{3_2} \cdot N_{\text{He} \bullet \text{CD}^+} + R_{\text{CID}_2} \cdot N_{\text{He}_2 \bullet \text{CD}^+} \\ \frac{dN_{\text{He}_2 \bullet \text{CD}^+}}{dt} &= +R_{3_2} \cdot N_{\text{He} \bullet \text{CD}^+} - R_{\text{CID}_2} \cdot N_{\text{He}_2 \bullet \text{CD}^+} - R_{3_3} \cdot N_{\text{He}_2 \bullet \text{CD}^+} + R_{\text{CID}_3} \cdot N_{\text{He}_3 \bullet \text{CD}^+} \\ \frac{dN_{\text{He}_3 \bullet \text{CD}^+}}{dt} &= +R_{3_3} \cdot N_{\text{He}_2 \bullet \text{CD}^+} - R_{\text{CID}_3} \cdot N_{\text{He}_3 \bullet \text{CD}^+} - R_{3_4} \cdot N_{\text{He}_3 \bullet \text{CD}^+} + R_{\text{CID}_4} \cdot N_{\text{He}_4 \bullet \text{CD}^+} \\ \frac{dN_{\text{He}_4 \bullet \text{CD}^+}}{dt} &= +R_{3_4} \cdot N_{\text{He}_3 \bullet \text{CD}^+} - R_{\text{CID}_4} \cdot N_{\text{He}_4 \bullet \text{CD}^+} \end{aligned}$$

The $\text{He}_4 \bullet \text{CD}^+$ ions are in this system a reservoir for all cluster ions with $n \geq 4$. In the experiment, by using the Time Scan mode (see chapter 5.1.5), the different

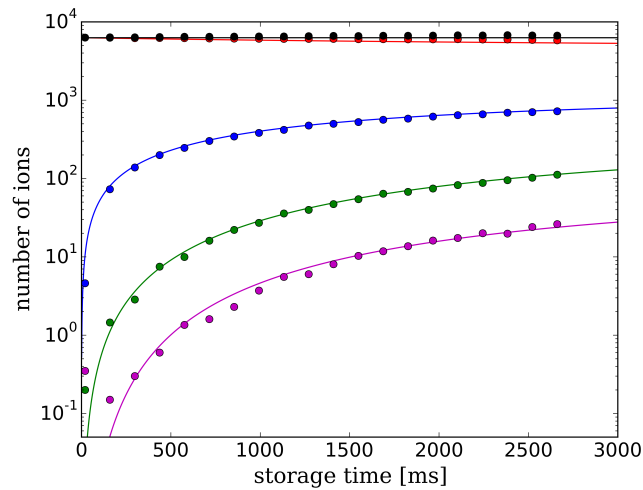


Figure 5.8: Time scan of the trapped CD^+ and cluster ions at 4K. The helium number density during this measurement was $1.7 \cdot 10^{14} \text{ cm}^{-3}$. The dots represent the measured ion numbers at different storage time while the solid lines represent the output of the numerical model. The black lines and dots represents the total number of ions measured, CD^+ is shown in red, $\text{He}\bullet\text{CD}^+$ in blue, $\text{He}_2\bullet\text{CD}^+$ in green and $\text{He}_3\bullet\text{CD}^+$ in magenta. Under these conditions higher order cluster does not appear in the measurement.

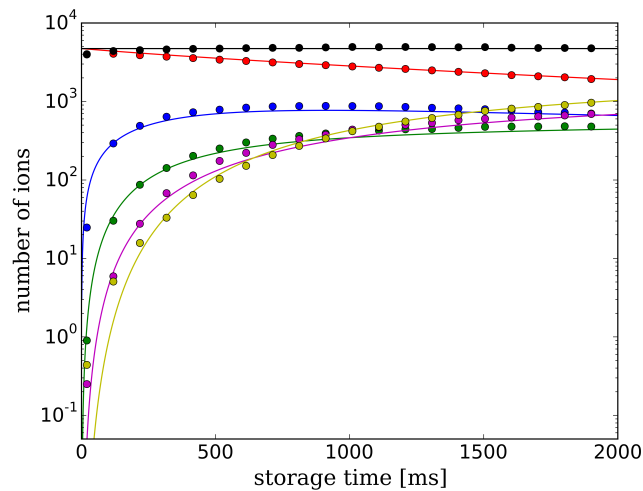


Figure 5.9: Time scan of the trapped CD^+ and cluster ions at 4K. The helium number density during this measurement was $9 \cdot 10^{14} \text{ cm}^{-3}$. The dots represent the measured ion numbers at different storage time while the solid lines represent the output of the numerical model. The black lines and dots represents the total number of ions measured, CD^+ is shown in red, $\text{He}\bullet\text{CD}^+$ in blue, $\text{He}_2\bullet\text{CD}^+$ in green, $\text{He}_3\bullet\text{CD}^+$ in magenta and $\text{He}_4\bullet\text{CD}^+$ in yellow. In comparison to figure 5.8 the number density is a factor of \sim five higher. Under these conditions the cluster growth is faster and also $\text{He}_4\bullet\text{CD}^+$ can be observed.

rates for the cluster formation (denoted as R_{3_x} in the rate equations) and the binary collision induced dissociation rates (denoted as R_{CID_x}) are observed and can be fitted in the numerical model. To derive the ternary rate-coefficients and the collision induced dissociation rate-coefficients the derived rates have to be scaled with the helium number density n_{He} . A description how the helium number densities are calculated from the

measured pressure values is given in section 5.1.2. To obtain the corresponding rate coefficients the relations

$$k_{3_x} = \frac{R_{3_x}}{n_{\text{He}} \cdot n_{\text{He}}} \quad (5.31)$$

$$k_{\text{CID}_x} = \frac{R_{\text{CID}_x}}{n_{\text{He}}} \quad (5.32)$$

$$(5.33)$$

are used.

In the first step the pressure dependence of the ternary rate-coefficients was investigated at a nominal temperature of 4 K. Concerning equation 5.24 in the theory section these measurements can be used to estimate k_r for the CD^+ and helium system. For this the effective binary rate-coefficient k^* is plotted as a function of the helium number density. The plot should be a linear function. The slope of this linear function should equal to the ternary rate-coefficient for the same temperature and the intercept of the function is equal to k_r . Figure 5.10 shows the dependence of the effective binary rate-coefficient as a function of the helium number density.

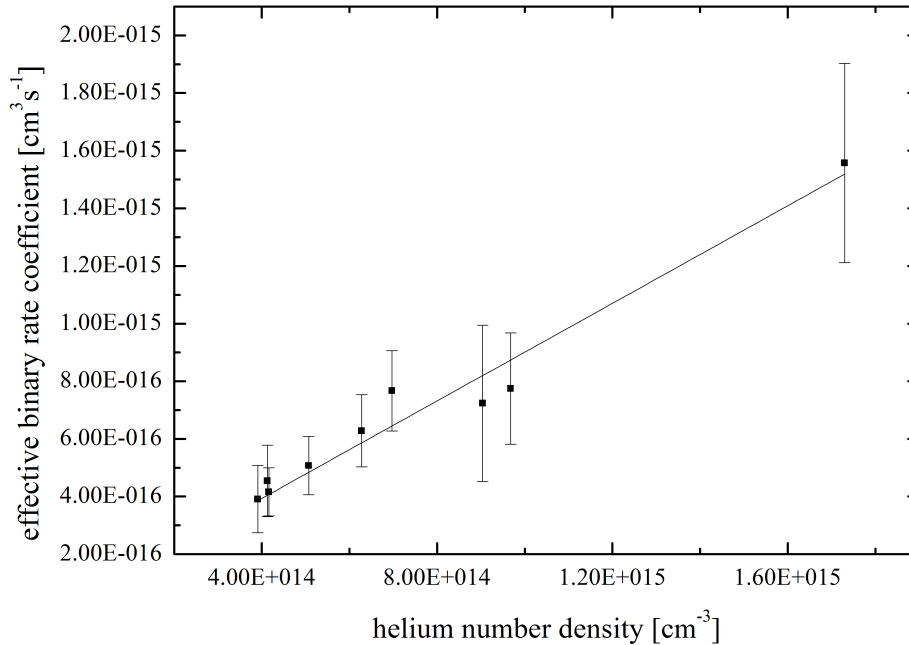


Figure 5.10: Effective binary rate-coefficient for CD^+ and He at a nominal temperature of 4 K. The solid line shows a linear fit to the data. The slope of $(8.3 \pm 0.8) \cdot 10^{-31} \text{ cm}^6 \text{ s}^{-1}$ of the fit corresponds to the ternary rate-coefficient k_{3_1} of the CD^+ and He system. The intercept of $(9 \pm 5) \cdot 10^{-17} \text{ cm}^3 \text{ s}^{-1}$ is equal to k_r for this system.

From the linear fit the obtained value for the slope is $(8.3 \pm 0.8) \cdot 10^{-31} \text{ cm}^6 \text{ s}^{-1}$, which matches within the errors with the calculated values for k_{3_1} given in table 5.3. The value for k_r , derived from the intercept of the linear function, is $(9 \pm 5) \cdot 10^{-17} \text{ cm}^3$

s⁻¹, which is not zero, but \sim a factor of 10 smaller than $k_{31} \cdot n_{\text{He}}$ and therefore, k_r is neglected in the formation process of the cluster ion and a pure ternary formation is assumed.

Based on this assumption the numerical simulation can be used to fit the observed time scans for different nominal temperatures. The results for the derived rate-coefficients for the different temperatures are summarized in table 5.3 for the ternary rate-coefficients and in table 5.4 for the binary collision induced dissociation rate-coefficients.

Table 5.3: Overview of the obtained ternary rate-coefficients for different temperatures. The rate-coefficients for the ternary processes are given in cm⁶ s⁻¹. In case of the values for 4 K the errors given are statistical errors of the performed measurements. For the higher temperatures only one measurement was performed per temperature and the given errors are the fitting errors.

T _{nom} [K]	k ₃₁	k ₃₂	k ₃₃	k ₃₄
4	$(9.6 \pm 1.1) \cdot 10^{-31}$	$(2.9 \pm 0.5) \cdot 10^{-30}$	$(7.6 \pm 1.5) \cdot 10^{-30}$	$(1.1 \pm 0.3) \cdot 10^{-29}$
5	$(1.2 \pm 0.1) \cdot 10^{-30}$	$(3.7 \pm 0.3) \cdot 10^{-30}$	$(1.3 \pm 0.2) \cdot 10^{-29}$	$(1.9 \pm 0.2) \cdot 10^{-29}$
7	$(1.7 \pm 0.2) \cdot 10^{-30}$	$(5.1 \pm 0.3) \cdot 10^{-30}$	$(1.5 \pm 0.1) \cdot 10^{-29}$	$(2.4 \pm 0.2) \cdot 10^{-29}$
10	$(1.7 \pm 0.2) \cdot 10^{-30}$	$(5.0 \pm 0.2) \cdot 10^{-30}$	$(1.1 \pm 0.2) \cdot 10^{-29}$	$(2.4 \pm 0.3) \cdot 10^{-29}$

Table 5.4: Overview of the obtained collision induced dissociation rate-coefficients for different temperatures. The rate-coefficients for the collision induced dissociation processes are given in cm³ s⁻¹. In case of the values for 4 K the errors given are statistical errors of the performed measurements. For the higher temperatures only one measurement was performed per temperature and the given errors are the fitting errors.

T _{nom} [K]	k _{CID1}	k _{CID2}	k _{CID3}	k _{CID4}
4	$(6.7 \pm 1.6) \cdot 10^{-16}$	$(1.9 \pm 0.5) \cdot 10^{-15}$	$(2.7 \pm 1.3) \cdot 10^{-15}$	$(5.5 \pm 1.4) \cdot 10^{-15}$
5	$(9 \pm 2) \cdot 10^{-16}$	$(1.9 \pm 0.2) \cdot 10^{-15}$	$(6.5 \pm 0.9) \cdot 10^{-15}$	$(1.1 \pm 0.3) \cdot 10^{-14}$
7	$(9 \pm 3) \cdot 10^{-16}$	$(2.5 \pm 0.4) \cdot 10^{-15}$	$(6.5 \pm 0.7) \cdot 10^{-15}$	$(1.2 \pm 0.4) \cdot 10^{-14}$
10	$(1.5 \pm 0.4) \cdot 10^{-15}$	$(3.0 \pm 0.5) \cdot 10^{-15}$	$(5.0 \pm 0.8) \cdot 10^{-15}$	$(1.5 \pm 0.3) \cdot 10^{-14}$

The results for the obtained ternary rate-coefficients are somewhat surprising. The first finding is that the ternary rate-coefficients for the larger cluster ions are higher than the ones for the smaller cluster ions. For example the formation rate-coefficients for the He₃•CD⁺ is more than a factor 10 higher than the rate-coefficient for the formation of the He•CD⁺ out of the parent CD⁺ ion. Another interesting and unexpected finding is that the ternary rates increase for higher temperatures. That is in contradiction to the theory presented in 5.2.1 since there the predicted temperature dependence is T^{-0.5} so for higher temperatures the ternary rate-coefficients should be smaller. A possible reason for this is may be due to experimental problems with the pressure measurements. At low temperatures around 4 K even helium starts to freeze out at the walls and since the temperature is not constant over the coldhead cycle of one second one can observe the effect that the pressure fluctuates approximately by a factor of two in the main chamber during a coldhead cycle. The used ViscoVac VM210 spinning rotor gauge only shows an averaged pressure over \sim 30 seconds and this pressure is used in the calculations for deriving the rate-coefficients. For the measurements at \sim 10 K this effect is not so prominent since the freeze out of helium does not occur. Due to this the pressure measurement for the 4 K and 5 K measurements are not as reliable as the measurements for the higher temperatures. If one assume that the variation in the

helium pressure inside the trap is in the same range than this result in an additional uncertainty for the calculated number densities by a factor of two. For the calculation of the ternary rate-coefficients the calculated number densities are squared so the additional factor is here four. If one takes this into account it is realistic to say that we do not observe a temperature dependence in our experiment for the ternary rate-coefficients. Another possible effect, one could imagine, is that some of the cluster ions dissociate during the extraction out of the trap into the second quadrupole. This would result in a smaller number of detected cluster ions (and a larger number of detected CD^+ ions) and this could also lead to a misinterpretation of the experimental resulting in wrong ternary and collision induced dissociation rate-coefficients. Otherwise if the observed temperature dependence is true this can maybe explained with an onset of resonances. Xie et al. for example claimed that the effective ternary rate-coefficient for the system $\text{He}^+ + 2\text{He}$ has a maximum around 25 K and decreases again for lower temperatures ([49]).

The derived rate-coefficients for the binary cluster induced dissociation show a moderate temperature dependence in the observed temperature range. The value for k_{CID_1} increases by a factor of \sim two from $(6.7 \pm 1.6) \cdot 10^{-16} \text{ cm}^3 \text{ s}^{-1}$ at 4 K to $(1.5 \pm 0.4) \cdot 10^{-15} \text{ cm}^3 \text{ s}^{-1}$ at 10 K, for example. This dependence can be explained with the higher kinetic energy of the helium atoms at higher temperatures. Thus, the helium atoms are able to destroy the helium cluster ions more effectively at higher temperatures.

The derived dissociation rate-coefficients can also be used to get an approximation for the binding energy of the helium atom to the CD^+ ion. The relation between collision induced dissociation rate-coefficient and the binding energy T_{D} of the helium atom (in K) can be estimated with

$$k_{\text{CID}} = k_L \cdot \exp\left(-\frac{T_{\text{D}}}{T}\right) \quad (5.34)$$

where $k_L = 6 \cdot 10^{-10} \text{ cm}^3 \text{ s}^{-1}$ is the Langevin rate-coefficient for the reaction. The used collisional temperature T_{coll} is calculated as explained in section 5.1.4 for the different nominal temperatures. With the calculated collisional temperature and the values for the collision induced dissociation rate-coefficients given in table 5.4 the binding energies can be calculated. This was done for the measurements at a nominal temperature of 4 K, and 7 K. The results for this are summarized in table 5.5.

The calculated binding energies for the two different temperatures match within their errors, but they are markedly lower as for other ionic species ([50]). For example the binding energy for H_3^+ is 139 K and for N_2^+ it is 197 K. So maybe the very simple model, which is used for the calculation of T_{D} failed. The obtained values for the binding energy can also be compared to the theoretically calculated value for the minimum of the potential by Stoecklin and Voronin ([51]). The calculated value for CH^+ is \sim 743 K, which is a factor of 10 larger than the values calculated here. The main difference between these two values is that the theoretical values corresponds to the minimum of the potential D_e , whereas the derived values here in the best case correspond to the lowest energy level D_0 . For CH^+ Meuwly et al. ([52]) state that the difference between the minimum of the potential and the lowest energy level is \sim 348 K. This reduces the gap between the theoretical values and the calculated value from our experiment. Nevertheless, the derived values are still too low. A possible reason for this is maybe that not all cluster ions are in the rotational ground state, but several

Table 5.5: Calculated binding energies for the helium atom. The binding energies are calculated based on the calculated collision induced dissociation rate-coefficients obtained from kinetic measurements at two different nominal trap temperatures and the corresponding collisional temperatures T_{coll} (see table 5.2).

Ion	T_{nom} [K]	k_{CID_1} [$\text{cm}^3 \text{s}^{-1}$]	T_{coll} [K]	T_{D} [K]
He•CD ⁺	4	$(6.7 \pm 1.6) \cdot 10^{-16}$	(5.5 ± 1.4)	(78 ± 21)
He ₂ •CD ⁺	4	$(1.9 \pm 0.5) \cdot 10^{-15}$	(5.3 ± 1.5)	(70 ± 20)
He ₃ •CD ⁺	4	$(2.7 \pm 1.3) \cdot 10^{-15}$	(5.1 ± 1.6)	(65 ± 20)
He ₄ •CD ⁺	4	$(5.5 \pm 1.4) \cdot 10^{-15}$	(5.0 ± 1.6)	(60 ± 19)
He•CD ⁺	7	$(9 \pm 3) \cdot 10^{-16}$	(6.1 ± 1.1)	(85 ± 16)
He ₂ •CD ⁺	7	$(2.5 \pm 0.4) \cdot 10^{-15}$	(5.7 ± 1.2)	(74 ± 15)
He ₃ •CD ⁺	7	$(6.5 \pm 0.7) \cdot 10^{-15}$	(5.5 ± 1.2)	(66 ± 15)
He ₄ •CD ⁺	7	$(1.2 \pm 0.4) \cdot 10^{-14}$	(5.4 ± 1.2)	(60 ± 14)

rotational states are populated. This would result in a smaller effective T_{D} , which is observed in the experiment. The population of higher rotational states is possibly caused by collisions with helium atoms during the extraction of the cluster-ions out of the 22-pole ion trap.

5.3 Rotational Spectroscopy of CD⁺

In this section a new technique that we developed in our group will be described. With this new method it is possible to measure directly rotational transitions of stored cold molecular ions in a 22-pole ion trap apparatus. This method is based on the idea that helium-attachment to cold stored molecular ion is inhibited when a molecular vibration or electronic state is excited. This fact has been used for measuring high resolution electronic ([40]) and ro-vibrational spectra of cold molecular ions ([39]). The effect of rotational excitation is less obvious but also leads to a change of the cluster signal as a function of excitation frequency. We used this fact for example to record pure rotational transitions of C₃H⁺ ([1]). In this section the rotational spectroscopy of CD⁺ (¹Σ⁺) is presented. For the spectroscopy the ions were stored together with helium in the cold 22-pole ion trap and were then exposed to tunable cw mm-wave radiation. The spectra were recorded by using the THz Scan Mode described at the beginning of this chapter (see 5.1.5). A typical spectrum of the rotational transition J=1←0 of CD⁺, at 453.521851 GHz ([42]) recorded with the new method, at a nominal trap temperature of 4K is shown in figure 5.11.

The aim of this section is to introduce a simple analytical kinetic model, including the interaction of the stored ions with light and helium, which is able to quantify some of the key processes involved. Besides this a numerical description of the model is presented in this section, which is implemented in Python. In the last part of this section the experimental results, e.g. the dependence of the signal strength of the rotational transitions on the helium number density, are explained by the models.

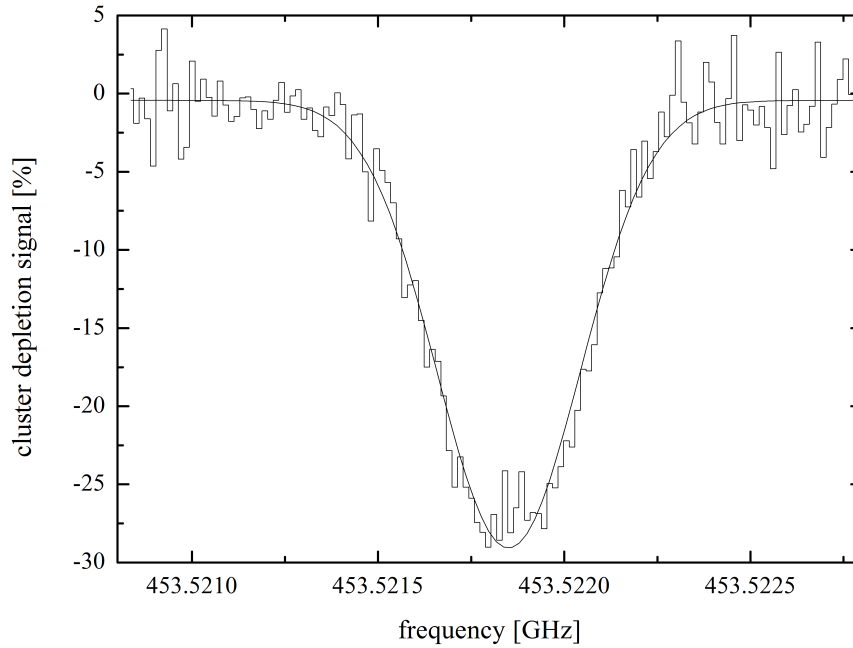


Figure 5.11: Typical rotational line of CD^+ at 4 K. The black histogram shows the averaged cluster depletion signal after 20 iterations together with a Voigt profile fit (solid black line). For this measurements the CD^+ ions were stored for 600 ms in the trap together with helium at a number density of $3.5 \cdot 10^{10} \text{ cm}^{-3}$. The applied power for this measurement was $2 \cdot 10^{-5} \text{ W}$.

5.3.1 The Analytical Model

The observed cluster depletion signal strength up to 28 % for the rotational transition $J=1 \leftarrow 0$ of CD^+ requires a detailed modeling of the underlying processes. A likely simplified scheme of the kinetics for the helium and CD^+ system is shown in figure 5.12. The involved processes in the scheme can be divided into different classes. The first class of processes are the cluster formation and cluster destruction processes, which are investigated in chapter 5.2.2. For the model it is assumed that the cluster formation process is state selective. This means that the rate-coefficients $k_3(J, T)$ (with $J \leq 1$), which describe the formation of the cluster ion from the bare CD^+ ion, depends on the initial rotational state of the CD^+ ion, but not on the final rotational state in the cluster ion. The second class includes the inelastic collisions with the helium atoms that change the rotational population of the initial CD^+ ions. The third class includes the radiative excitation and de-excitation processes, as well as spontaneous emission.

For the first approach we will neglect the influence of the mm-wave radiative excitation and de-excitation. After entering the trap the CD^+ ions will undergo collisions with the helium atoms present in the trap. Since the helium atoms are neutral they are not influenced by the radio-frequency fields in the trap regions and they can collide with the rods of the cold 22-pole ion trap. By this collisions the helium atoms cool down to the nominal trap temperature of 4 K. Beside the translationally cooling effect the CD^+ ions can also be rotational excited or de-excited by collisions with helium. Since there are no experimental or theoretical values available for the collisions of CD^+ ions with

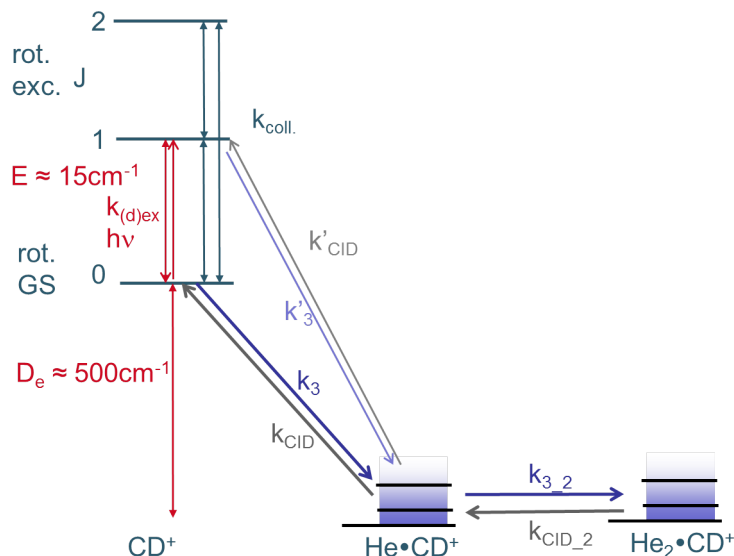


Figure 5.12: Simplified scheme of the kinetics for the helium and CD^+ system. The involved processes in this scheme are the ternary Helium-cluster formation, the collision induced cluster dissociation, the (de-) excitation of the CD^+ ions by collisions with Helium and the radiative (de-) excitation of CD^+

helium we use for our model and calculations the calculated collisional rate-coefficients $k_{JJ'}$ from Turpin et al. ([53]) for collisions of CH^+ with helium. The rate-coefficients for 1 K and 10 K are given in table 5.6.

Table 5.6: Thermal rate-coefficients $k_{JJ'}$ for rotational collisional de-excitation of CH^+ in collision with 4 He between the lowest rotational levels ($J < 3$). The rate-coefficients are given in units of $\text{cm}^3 \text{ molecule}^{-1} \text{ s}^{-1}$. The notation $a(b)$ means $a \times 10^{-b}$. Values are taken from Turpin et al. ([53])

$k_{JJ'}$	1 K	10 K
k_{10}	3.2579(11)	6.4569(11)
k_{20}	3.5955(11)	3.2011(11)
k_{21}	1.4211(10)	1.0617(10)
k_{30}	1.3521(11)	9.1738(12)
k_{31}	8.0492(11)	5.9896(11)
k_{32}	6.6780(11)	5.8912(11)

Since there are only calculated values available for 1 K, 10 K and much higher temperatures up to 200 K, the rate-coefficient values for the temperatures of 4 K, 7 K, and 12 K are derived by linear approximation. They are given in table 5.7.

Table 5.7: Extrapolated rate-coefficients $k_{JJ'}$ for collisional de-excitation rates of CH^+ in collision with ^4He at 4 K, 7 K, and 12 K. The collisional rate-coefficients are given in units of $\text{cm}^3 \text{ molecule}^{-1} \text{ s}^{-1}$. The notation $a(b)$ means $a \times 10^{-b}$.

$k_{JJ'}$	4 K	7 K	12 K
k_{10}	4.3242(11)	5.3845(11)	7.5232(11)
k_{20}	3.4640(11)	3.3326(11)	3.0696(11)
k_{21}	1.3013(10)	1.1815(10)	0.9419(10)

The corresponding rotational excitation rate-coefficients $k_{J'J}$ can be obtained from these values by applying the detailed balance relationship:

$$k_{J'J} = k_{JJ'} \cdot \frac{g_J}{g_{J'}} \cdot \frac{\exp\left(\frac{E_J}{k_B \cdot T_{\text{coll}}}\right)}{\exp\left(\frac{E_{J'}}{k_B \cdot T_{\text{coll}}}\right)} = k_{JJ'} \cdot \frac{g_J}{g_{J'}} \cdot \exp\left(\frac{h\nu}{kT}\right) \quad (5.35)$$

Where T_{coll} is the collisional temperature, k_B the Boltzmann constant, g_J and $g_{J'}$ the statistical weight of the rotational levels, and E_J , and $E_{J'}$ the corresponding energy levels.

Based on these number we can make some estimates for the speed of the different processes mentioned in the beginning. Assuming a helium number density $[\text{He}]$ of around 10^{15} cm^{-3} during the experiments we can calculate the (de-)excitation rates with

$$R_{\text{coll}_{J'J}} = k_{J'J} \cdot [\text{He}] \quad (5.36)$$

These rates are in the order of 10^4 s^{-1} in the temperature range between 4 K and 10 K. In comparison to this the ternary reaction rates are significantly slower. The measured rate-coefficients for the ternary rate-coefficients k_3 are of the order of $10^{-30} \text{ cm}^6 \text{ s}^{-1}$ (5.2.2) and the rate-coefficients for the collision induced dissociation are of the order of $10^{-15} \text{ cm}^3 \text{ s}^{-1}$. The corresponding rates can be calculated with

$$R_3 = k_3 \cdot [\text{He}]^2 \quad (5.37)$$

$$R_{\text{CID}} = k_{\text{CID}} \cdot [\text{He}] \quad (5.38)$$

to be of the order of 1 s^{-1} at the same helium number density. With $R_3 \approx R_{\text{CID}} \ll R_{\text{coll}}$ it can be assumed for the model that the reactions always see the same level population, even if the process of collision induced dissociation leads initially to rotationally excited CD^+ . The same holds for the cluster ions. If the created cluster ions are rotationally excited it is likely that they de-excited by collisions with helium atoms on a very short timescale. In this way it can be assumed that the system is in Local Thermal Equilibrium (LTE). The thermal rotational level populations for a given collisional temperature T_{coll} can be calculated by

$$\frac{N_J}{N} = \frac{g_J}{Z(T_{\text{coll}})} \cdot \exp\left(-\frac{E}{k_B T_{\text{coll}}}\right) \quad (5.39)$$

where $Z(T_{\text{coll}})$ is the total rotational partition function at a given collisional temperature, $g_J = 2J+1$ is the statistical weight of the rotational level J and E is the level-energy. The values for $Z(T_{\text{coll}})$ and E for CD^+ were calculated based on parameters from the Cologne Database for Molecular Spectroscopy (CDMS) ([54]) and Amano ([42]). For the calculations it is assumed that all CD^+ ions are in the vibrational ground state. The measured total ternary rate-coefficient k_3 for the Helium attachment to CD^+ is in this model thought of as a population weighted sum of rotational state specific

coefficients $k_3(J, T)$. If we for now ignore successive reactions to form larger clusters we will obtain an equilibrium ratio of

$$\frac{N_{\text{He}\bullet\text{CD}^+}}{N_{\text{CD}^+}} = \frac{[\text{He}] \sum_J k_3(J, T) N_{\text{CD}^+, J}(T)}{k_{\text{CID}}(T) N_{\text{CD}^+}} \quad (5.40)$$

where $[\text{He}]$ is the helium number density, $N_{\text{CD}^+, J}$ the number of CD⁺ ions in a rotational state J , and N_{CD^+} and $N_{\text{He}\bullet\text{CD}^+}$ the number of CD⁺ and He •CD⁺ ions. For the observed cluster depletion signal we assume that this is due to a redistribution out of LTE caused by the mm-wave radiation. A simple approach is to assume a two level system (with $E_1 > E_0$). The radiative excitation and de-excitation rates can be calculated from the Einstein coefficient A_{10} for the spontaneous emission and the coefficients for the stimulated emission and absorption

$$B_{10} = \frac{c^3}{8\pi h \nu^3} A_{10} \quad (5.41)$$

$$B_{01} = \frac{g_1}{g_0} B_{10} \quad (5.42)$$

$$(5.43)$$

The values for the transition between the rotational ground state and the first excited state for CD⁺ are:

$$A_{10} = 6.24 \cdot 10^{-4} \text{ s}^{-1} \quad (5.44)$$

$$B_{10} = 1.086 \cdot 10^{19} \text{ m}^3 \text{ J}^{-1} \text{ s}^{-2} \quad (5.45)$$

$$B_{01} = 3.258 \cdot 10^{19} \text{ m}^3 \text{ J}^{-1} \text{ s}^{-2} \quad (5.46)$$

$$(5.47)$$

To calculate the transition rates due to the influence of the mm-wave radiation we have to make a few assumptions about the radiation field. The spectral energy density of a narrow bandwidth mm-wave source can be expressed by a δ - function around the center frequency ν_c with the total power P_c at the center frequency and light cross section A_c

$$\rho(\nu - \nu_c) = \delta(\nu_c) \cdot \frac{P_c}{A_c c} \quad (5.48)$$

The next step is to calculate the fraction f of ions in the two rotational states $J=0$ and $J=1$ that interact with the light at frequency ν . Assuming a Voigt profile V (as discussed in section 5.1.4) the fraction for the transition frequency ν_{01} is given by

$$f_{0/1}(\nu) = \frac{A_c}{A_{\text{trap}}} \cdot V(\nu - \nu_{01}, \Delta\nu_G, \Delta\nu_L) \quad (5.49)$$

where A_{trap} is the trap area and $V(\nu - \nu_{01}, \Delta\nu_G, \Delta\nu_L)$ is the Voigt profile. The Voigt profile depends on the FWHM of the Doppler profile $\Delta\nu_G$ and the FWHM of the Lorentzian profile $\Delta\nu_L$. At the resonance frequency ν_{01} equation 5.49 is simplified to

$$f_{0/1}(\nu_{01}) = \frac{A_c}{A_{\text{trap}}} \cdot V(0, \Delta\nu_G, \Delta\nu_L) \quad (5.50)$$

The value for $V(0, \Delta\nu_G, \Delta\nu_G)$ can be derived with

$$V(0, \Delta\nu_G, \Delta\nu_G) = \frac{\text{Re}[\omega(z)]}{\Delta\nu_G \sqrt{2\pi}} \quad (5.51)$$

where $\text{Re}[\omega(z)]$ is the real part of the Faddeeva function evaluated for

$$z = \frac{i\Delta\nu_L}{\Delta\nu_G \sqrt{2}} \quad (5.52)$$

Based on this the respective zero-order stimulated rates at the resonance frequency ν_{01} can be written as

$$f_{0/1}(\nu_{01}) \cdot B_{ij} \cdot \rho = B_{ij} \cdot \frac{P_L}{A_{\text{trap}} \cdot c} \cdot V(0, \Delta\nu_G, \Delta\nu_G) \quad (5.53)$$

By using equation 5.53 the rates for the CD^+ transition from $J = 0$ to $J = 1$ at a frequency of 453 GHz can be calculated. For this we assume a microwave radiation power of $2 \cdot 10^{-5}$ W at the transition frequency (see section 5.1.3), a Doppler width corresponding the ion temperature of 12.3 K, and a trap area of 50 mm^2 . With this assumptions we obtain the following rates for the stimulated processes

$$A_{10} = 6.24 \cdot 10^{-4} \text{ s}^{-1} \quad (5.54)$$

$$f_{0/1}(\nu_{01}) \cdot B_{10} \cdot \rho = 1.08 \cdot 10^4 \text{ s}^{-1} \quad (5.55)$$

$$f_{0/1}(\nu_{01}) \cdot B_{01} \cdot \rho = 3.24 \cdot 10^4 \text{ s}^{-1} \quad (5.56)$$

$$(5.57)$$

The value for A_{10} is given here again for comparison. The rates for the stimulated emission and absorption are orders of magnitude larger than the rates for the spontaneous emission in this system. Therefore, in the further discussion we will neglect the influence of the spontaneous emission. The values for the stimulated emission and absorption rates are roughly in the same order of magnitude as the collisional (de-)excitation rates. However, if we disregard collisions in the system for the moment, the relative population of the two rotational CD^+ states $J=1$ and $J=0$ in (radiative) equilibrium is simply calculated by the statistical weights of the two states

$$\frac{N_{J=1}}{N_{J=0}} = \frac{g_1}{g_0} = 3 \quad (5.58)$$

We can use this simple ratio to get an idea of the maximal achievable cluster depletion signal for CD⁺. For this we assume that the first rotational excited state J=1 does not form any Helium-clusters. So this means in terms of formula (5.40) $k_3(J,T) = 0$ with $J > 0$. With this assumptions and a nominal temperature of 4 K we obtain from (5.40) a maximal signal strength s of

$$s = \frac{N_{\text{He}\bullet\text{CD}^+, \text{on}} - N_{\text{He}\bullet\text{CD}^+, \text{off}}}{N_{\text{He}\bullet\text{CD}^+, \text{off}}} = \frac{N_{\text{CD}^+, 0, \text{off}} - N_{\text{CD}^+, 0, \text{on}}}{N_{\text{CD}^+, 0, \text{off}}} = 73.4\% \quad (5.59)$$

Of course the obtained signal in the experiment will be smaller than calculated in 5.59 due to the collisions with helium. The signal strength will also decrease if the temperature is higher and if not only the rotational ground state can form clusters ($k_3(J,T) \neq 0$ for $J > 0$).

So the first step to improve the expression 5.59 is to take collisions with helium atoms into account. If a two level system is assumed the improved expression for (5.58) is:

$$\frac{N_1}{N_0} = \frac{g_1}{g_0} \cdot \frac{f \cdot B_{10} \cdot \rho + k_{\text{coll}(10)} \cdot [\text{He}] \cdot \exp\left(-\frac{h\nu}{k_B T}\right)}{f \cdot B_{10} \cdot \rho + k_{\text{coll}(10)} \cdot [\text{He}]} \quad (5.60)$$

Equation (5.60) can be rewritten by using P instead of ρ as follows:

$$\frac{N_1}{N_0} = \frac{g_1}{g_0} \cdot \frac{\frac{P}{[\text{He}]} + \frac{k_{\text{coll}(10)}}{B_{10}c_0} \exp\left(-\frac{h\nu}{k_B T}\right)}{\frac{P}{[\text{He}]} + \frac{k_{\text{coll}(10)}}{B_{10}c_0}} \quad (5.61)$$

where the constant $c_0 = \frac{1}{A_{\text{trap}} \cdot c} \cdot V(0, \Delta\nu_G, \Delta\nu_L)$. This equation is interesting, because at a fixed temperature the relative population of the two levels is set by the parameters P and $[\text{He}]$, which can be both controlled in the experiment. The results of this relatively simple formula can also be compared to the results of the more complex numerical simulation (see chapter 5.3.2. Equation (5.61) can also be rewritten since many terms of the sum are constant for a certain temperature and a certain type of ion. So the ratio between the two rotational levels is:

$$\frac{N_1}{N_0} = c_1 \cdot \frac{x + c_2 c_3}{x + c_2} \quad (5.62)$$

with the constants $c_1 = \frac{g_1}{g_0}$, $c_2 = \frac{k_{\text{coll}(10)}}{B_{10} \cdot c_0}$, $c_3 = \exp\left(-\frac{h\nu}{k_B T}\right)$ and the variable $x = \frac{P}{[\text{He}]}$. Equation (5.62) can be used to derive an expression for the cluster depletion signal, which then can be compared with the experimental data. For this first the definition of the relative cluster depletion signal s is needed:

$$s = \frac{N_{\text{off}}(\text{He}\bullet\text{CD}^+) - N_{\text{on}}(\text{He}\bullet\text{CD}^+)}{N_{\text{off}}(\text{He}\bullet\text{CD}^+)} \quad (5.63)$$

$$= 1 - \frac{N_{\text{on}}(\text{He}\bullet\text{CD}^+)}{N_{\text{off}}(\text{He}\bullet\text{CD}^+)} \quad (5.64)$$

$$(5.65)$$

where the indices on and off indicates whether the radiation is switched on or off. If we again assume an equilibrium situation we can write for the cluster depletion signal

$$s = 1 - \frac{\sum_J k_3(J, T) N_{\text{on}}(J, T)}{\sum_J k_3(J, T) N_{\text{off}}(J, T)} \quad (5.66)$$

This general equation is reduced if we again assume only a two level system at a temperature T

$$s = 1 - \frac{k_3(0, T) N_{\text{on}}(0, T) + k_3(1, T) N_{\text{on}}(1, T)}{k_3(0, T) N_{\text{off}}(0, T) + k_3(1, T) N_{\text{off}}(1, T)} \quad (5.67)$$

By plugging in the the ratio of $\frac{N_1}{N_0}$ given by 5.62 we obtain for the cluster depletion signal

$$s = \frac{c_1(1 - c_3)(k_3(0, T) - k_3(1, T))}{k_3(0, T)(1 + c_1) + k_3(1, T)(1 + c_1)c_1c_3 + \frac{1}{x}(k_3(0, T)c_2(1 + c_1c_3) + k_3(1, T)c_1c_2c_3(1c_1c_3))} \quad (5.68)$$

If one can calculate the constants, this formula can be used to calculate for example the dependency of the cluster depletion signal on the radiation power at a given helium number density in the experiment. This is a nice result since you can compare the output of this formula with the experimental data and with the output of the numerical simulation. But there are still many uncertainties in this formula. The first problem is that the constant c_2 contains the collisional de-excitation rate-coefficient for collisions of CD^+ with helium. Since this number is not known very well this is still a serious problem. The second problem of course is that expression 5.68 uses the different ternary rate-coefficients $k_3(0, T)$ and $k_3(1, T)$ which cannot be measured separately in the experiment. One aim of this investigation is to derive a value for the ratio of $k_3(0, T)$ and $k_3(1, T)$. To find an expression for this ratio one can start at 5.68 with a gedankenexperiment. In this experiment it is assumed that it is possible to increase the radiation power up to a very high level. By doing this the Voigt profile will change into a Lorentzian profile and instead of using $V(0, \Delta\nu_G, \Delta\nu_L)$ one can directly write $\frac{1}{\Delta\nu_L\pi}$. Thus, equation 5.68 is simplified since $x = \frac{\sqrt{P}}{[\text{He}]}$ (for the Lorentzian profile) becomes infinity and $\frac{1}{x}$ becomes zero. This means 5.68 is now reduced to

$$s = \frac{c_1(1 - c_3)(k_3(0, T) - k_3(1, T))}{k_3(0, T)(1 + c_1) + k_3(1, T)(1 + c_1)c_1c_3} \quad (5.69)$$

Inspection of 5.69 gives that the cluster depletion signal is no longer dependent on the constant c_2 . This is a nice fact, because the unknown collisional rate-coefficients for CD^+ and helium are no longer of interest. In the gedankenexperiment one can measure the cluster depletion signal, and by using 5.69 a simple expression for the ratio between the two ternary rate-coefficients $k_3(0, T)$ and $k_3(1, T)$ can be derived. For this the connectivity

$$k_3(1, T) = a \cdot k_3(0, T) \quad (5.70)$$

is used and one obtains as a new expression for the cluster depletion signal

$$s = \frac{c_1(1-c_3)(1-a)}{(1+c_1)+a(1+c_1)c_1c_3} \quad (5.71)$$

In the extreme case of $a=0$, which means that the first rotational state of CD⁺ cannot form the helium cluster ion, equation 5.71 is equal to the estimation for the maximum signal given in 5.59. The expression (5.71) can easily be converted into an expression for the ratio a we are interested in:

$$a = \frac{c_1 - c_1c_3 - s - c_1s}{c_1c_3s + c_1^2c_3s + c_1 - c_1c_3} \quad (5.72)$$

In the gedankenexperiment one can obtain a value for the ratio of the two ternary rate-coefficients. Of course in reality it is technically impossible to increase the radiation power up to infinity but in reality this is not needed. The requirement is only that $f \cdot B_{10} \cdot \rho \gg k_{\text{coll}} \cdot [He]$. If it is possible in the experiment to measure the cluster depletion signal as a function of the radiation power and a maximum value for the cluster depletion signal is obtained, even if the radiation power is not infinity, then equation 5.72 can be used to calculate the value a for the ion species in the experiment. This is discussed in chapter 5.3.3.5.

5.3.2 Numerical Simulation with Python

Besides the analytical model described in (5.3.1) a numerical approach is used to model and understand the cluster depletion signal. An interesting aspect of the numerical simulation is that this approach can be used to check whether the assumptions used for the analytical model are reasonable or not. In the simulation also different parameters as the ratio between the two ternary rate-coefficients $k_3(1, T)$ and $k_3(0, T)$ for building helium-clusters can be tuned. The idea of the simulation is to get an estimation for this value as we derived with the analytical solution and compare these values.

The numerical simulation bases on the following rate equation system, which can be

derived from figure 5.12:

$$\begin{aligned}
\frac{dN_{\text{CD}^+_0}}{dt} &= -R_3 \cdot N_{\text{CD}^+_0} + R_{\text{CID}} \cdot N_{\text{He}\bullet\text{CD}^+} \cdot p \\
&\quad -R_{B_{01}} \cdot N_{\text{CD}^+_0} + R_{B_{10}} \cdot N_{\text{CD}^+_1} + R_{A_{10}} \cdot N_{\text{CD}^+_1} \\
&\quad -R_{\text{coll}_{01}} \cdot N_{\text{CD}^+_0} + R_{\text{coll}_{10}} \cdot N_{\text{CD}^+_1} \\
&\quad -R_{\text{coll}_{02}} \cdot N_{\text{CD}^+_0} + R_{\text{coll}_{20}} \cdot N_{\text{CD}^+_2} \\
\frac{dN_{\text{CD}^+_1}}{dt} &= -R'_3 \cdot N_{\text{CD}^+_1} + R_{\text{CID}} \cdot N_{\text{He}\bullet\text{CD}^+} \cdot (1-p) \\
&\quad +R_{B_{01}} \cdot N_{\text{CD}^+_0} - R_{B_{10}} \cdot N_{\text{CD}^+_1} - R_{A_{10}} \cdot N_{\text{CD}^+_1} \\
&\quad +R_{\text{coll}_{01}} \cdot N_{\text{CD}^+_0} - R_{\text{coll}_{10}} \cdot N_{\text{CD}^+_1} \\
&\quad -R_{\text{coll}_{12}} \cdot N_{\text{CD}^+_1} + R_{\text{coll}_{21}} \cdot N_{\text{CD}^+_2} \\
\frac{dN_{\text{CD}^+_2}}{dt} &= +R_{\text{coll}_{02}} \cdot N_{\text{CD}^+_0} - R_{\text{coll}_{20}} \cdot N_{\text{CD}^+_2} \\
&\quad +R_{\text{coll}_{12}} \cdot N_{\text{CD}^+_1} - R_{\text{coll}_{21}} \cdot N_{\text{CD}^+_2} \\
\frac{dN_{\text{He}\bullet\text{CD}^+}}{dt} &= +R_3 \cdot N_{\text{CD}^+_0} - R_{\text{CID}} \cdot N_{\text{He}\bullet\text{CD}^+} \cdot p \\
&\quad +R'_3 \cdot N_{\text{CD}^+_1} - R_{\text{CID}} \cdot N_{\text{He}\bullet\text{CD}^+} \cdot (1-p) \\
&\quad -R_{3_2} \cdot N_{\text{He}\bullet\text{CD}^+} + R_{\text{CID}_2} \cdot N_{\text{He}_2\bullet\text{CD}^+} \\
\frac{dN_{\text{He}_2\bullet\text{CD}^+}}{dt} &= +R_{3_2} \cdot N_{\text{He}\bullet\text{CD}^+} - R_{\text{CID}_2} \cdot N_{\text{He}_2\bullet\text{CD}^+}
\end{aligned}$$

There are five species included in the numerical simulation. The CD^+ ions are divided into three different classes for the rotational levels $J = 0$, $J = 1$, and $J = 2$ (denoted with the indices 0,1, and 2). In addition, the two cluster ions $\text{He}\bullet\text{CD}^+$ and $\text{He}_2\bullet\text{CD}^+$ are used in the numerical model. These ions are connected via three different classes of process. First the cluster formation and cluster destruction processes (described by the corresponding rates R_3 , R'_3 , and R_{3_2} for the cluster formation and R_{CID} , and R_{CID_2} for the collision induced dissociation of the clusters). The parameter p is used for modeling the collisional induced dissociation of the first helium cluster ion to tune the ratio of produced CD^+ in the rotational ground state and in the first excited state. Second are the radiation processes. In the simulation the spontaneous emission (corresponding rate $R_{A_{10}}$) as well as the stimulated emission (rate $R_{B_{10}}$) and the absorption (rate $R_{B_{01}}$) are included. The rates for the radiation processes are derived as described in equation (5.57). The third class of processes are the inelastic collisions with helium. In the numerical simulation the rotational population of the three lowest rotational levels of CD^+ is changed by collisions with helium. All three rotational levels are connected with each other. The corresponding rates are denoted by $R_{\text{coll}_{JJ'}}$, where J is the initial rotational level and J' is the final rotational level. The values for the collisional rates bases on the collisional rate-coefficients given in tables (5.6) and (5.7) and are calculated as in equation (5.36).

From the given rate equation system it is obvious that some assumption have been made for the numerical simulation. Theses assumptions are summarized in the following part.

The first assumption is that the CD⁺ ions are in the vibrational ground state and all higher rotational levels with $J > 2$ of CD⁺ are neglected. It is also assumed that the cluster formation process of He•CD⁺ is state selective and only the two lowest rotational levels of CD⁺ are able to form the cluster ion. The second assumption concerning the formation and destruction of the clusters is that these two processes are separated from each other and the formation of the cluster ions is a strict ternary process. Furthermore, in the simulation the cluster ions are not excited (only rotational and vibrational ground state), in contrast to the CD⁺ ions. The second cluster He₂•CD⁺ is in addition a reservoir for all higher cluster ions with more than two helium atoms. To calculate the initial distribution of the CD⁺ ions in their rotational states it is assumed that the internal temperature of the CD⁺ ions is equal to the collisional temperature.

In the simulation the cluster depletion signal s is calculated as in the experiment by using the formula:

$$s = \frac{N_{\text{off}}\text{He} \bullet \text{CD}^+ - N_{\text{on}}\text{He} \bullet \text{CD}^+}{N_{\text{off}}\text{He} \bullet \text{CD}^+} \quad (5.73)$$

The index off means for the simulation that the light is switched off. In this case the two rates $R_{B_{10}}$ and $R_{B_{01}}$ are set to zero in the model in order to simulate the system without light. For the system with light the full rate equation system, given in equation (5.73), is used.

To run the simulation, some parameters has to be defined, which are summarized in table 5.8. In the table the name of the input parameter is given together with the name of the parameter in the code and, if it is useful, with a typical value or range for CD⁺.

Table 5.8: List of parameters for the numerical simulation, which have to be defined by the user to run the simulation. For the different parameters the name of the variable in the code is given and for most of the parameters some typical values for the simulation of CD⁺ and helium.

parameter	parameter in the code	value
collisional & internal temperature	CD.temp	4-20 K
storage time	CD.time	100-2000 ms
helium number density	CD.n_He	10 ¹² -10 ¹⁶ cm ⁻³
radiation power	CD.P_THz	2 · 10 ⁻⁵ W
rate-coefficients cluster formation	R.k3_0; R.k3_1; R.k32	~10 ⁻³⁰ cm ⁶ s ⁻¹
rate-coefficients cluster destruction	R.k3_CID; R.k3_CID2	~10 ⁻¹⁵ cm ³ s ⁻¹
branching ratio p	CD.p	0-1
THz frequency & Einstein A coefficient	nu; R.A_10	453 GHz; 6.24 s ⁻¹
collisional rate-coefficients with helium	R.q_JJ'	~ 10 ⁻¹¹ cm ³ s ⁻¹
time resolution	T.step	5 · 10 ⁻⁴ ms

By using the given temperature the first step in the simulation is to compute a weighted Boltzmann distribution based on the rotational energy levels of CD⁺. At the beginning it is assumed in the simulation that only CD⁺ in the different rotational states and helium is present in the trap. So the start number of the two cluster ions is zero. Depending on the chosen storage time and time resolution the simulation computes the time evolution of the system by using the rate equation system given in

equation (5.73). This done for the system with and without light.

After terminating the computation the code provides the results in different output files. The main output is the result for the cluster depletion signal. This consists of the radiation power and the corresponding cluster depletion signal. Besides this file the code generates two more files. They contain the time dependent information about the population of the different ion species and different rotational levels. The columns in the file corresponds to the different ion species and the lines are assigned to the different timesteps. The first column represents the number of ions in the rotational ground state of the bare ion, the second one is the first excited state, the second excited state, first and second cluster ion, and the last column is the sum of all ions in the system. These files are available for the system with and without radiation and they are used in the following section 5.3.3 to analyze the dependencies of the cluster depletion signal on the different experimental parameters.

5.3.3 Comparison of the Measurements with the Two Models

In this section the experimental results are explained by using the analytical and the numerical approach described in the sections 5.3.1 and 5.3.2, respectively. In the experiment the dependency of the cluster depletion signal on the helium number density, the power of the mm-wave source, the trap temperature and the storage time was investigated. Besides this the measurements of the CD^+ and HCO^+ (for the measurements see section 5.4) will be compared and a basic explanation for the different signal strength within the scope of the used model will be given. The last part of the section deals with the estimation of the ratio between the different ternary rate-coefficients of the rotational ground state and the first excited rotational state of CD^+ . In this context also a short discussion of this results will be given.

In general the discussion of the different dependencies are organized as follows. In the beginning a table with the different parameters and their values used in the models is given. In the next step the analytical model is used to discuss the expected behavior of the signal. Afterwards, the result of the corresponding numerical simulation is presented. Finally the results of the measurement are presented (if possible) and a short discussion is given.

5.3.3.1 Dependence on the Helium Number Density

The helium number density in the experiment is a parameter which can be easily changed and which should be a significant factor for the strength of the measured cluster depletion signal, if our model concept is correct. In table 5.9 the values, used for the simulations in this section, are summarized.

To get an idea of the effect of the helium number density on the cluster depletion signal first the analytical model is used. Figure 5.13 shows the result of the analytical model. For this plot the helium number density was varied between $1 \cdot 10^{12} \text{ cm}^{-3}$ and $1 \cdot 10^{18} \text{ cm}^{-3}$.

Based on the simulation the cluster depletion signal is maximum for low helium number densities and decreases for increasing helium number densities. This dependence is obvious regarding equation (5.68). By increasing the helium number density

Table 5.9: Parameters for the simulations - helium number density dependency

parameter	value
nominal temperature	4 K
collisional & internal temperature	5.7 K
storage time	600 ms
helium number density	variable
radiation power	$2 \cdot 10^{-5}$ W
ratio a	0.5
rate-coefficients $k_{3_0} / k_{3_1} / k_{32}$ [$\text{cm}^6 \text{s}^{-1}$]	$9.6 \cdot 10^{-31} / a \cdot 9.6 \cdot 10^{-31} / 2.9 \cdot 10^{-30}$
rate-coefficients $k_{\text{CID}} / k_{\text{CID}2}$ [$\text{cm}^3 \text{s}^{-1}$]	$6.7 \cdot 10^{-16} / 1.9 \cdot 10^{-15}$
branching ratio p	0.5
collisional rate-coefficients	see table 5.6 and 5.7

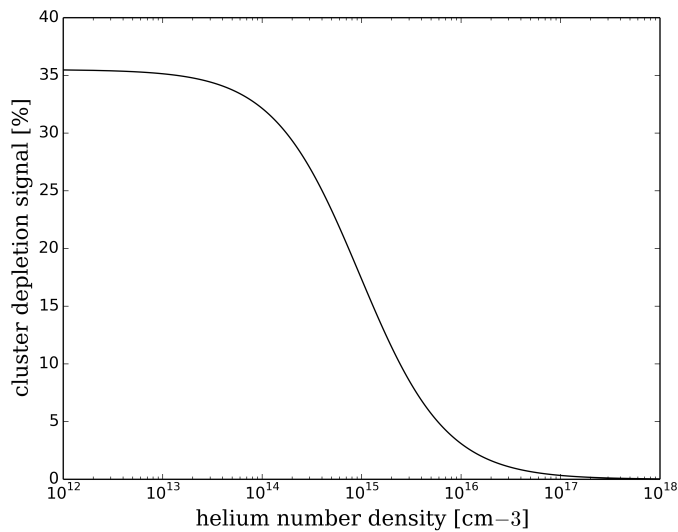


Figure 5.13: Simulated dependency of the cluster depletion signal for the $J=1 \leftarrow 0$ transition of CD⁺ on the helium number density in the trap with the analytical model. The number density was varied between $1 \cdot 10^{12} \text{ cm}^{-3}$ and $1 \cdot 10^{18} \text{ cm}^{-3}$. For the other parameters see table (5.9).

$n_{\text{He}} \propto \frac{P}{[He]}$ (see equation 5.62) decreases. This results in a increasing denominator in equation (5.68) and by this the signals decreases. Physically this can be explained in the model picture by the effect that higher helium number densities reduce the redistribution effect of the radiation, because the number of collisions between the ions and the helium atoms increase linearly with the number of helium atoms. Since the de-exciting collisions are more efficient than the exciting collisions the redistribution of the ions, due to the irradiated light, is reduced in the model. A conclusion from the analytical model would be that is preferable to measure at low number densities to obtain a maximum signal. In the real experiment the number of helium cluster ions is another requirement that has to be fulfilled to measure the cluster depletion signal at a good noise level. At low helium number densities as $1 \cdot 10^{12} \text{ cm}^{-3}$ the number of cluster ions after an acceptable storage time, as for example 600 ms, is negligible and, therefore it is difficult to measure a cluster depletion signal in the experiment. In table 5.10 the relative number of helium cluster ions, formed after 600 ms storage time, for different

helium number densities is listed together with the calculated cluster depletion signal from the numerical approach. The relative number of cluster ions is obtained from the numerical simulation, performed with the values given in table 5.9.

Table 5.10: Relative number of $\text{He}\bullet\text{CD}^+$ ions and strength of the cluster depletion signal (s_{num}) in the numerical simulation as a function of helium number density. To obtain a sufficient number of ions in the experiment helium number densities between $5 \cdot 10^{14} \text{ cm}^{-3}$ and $5 \cdot 10^{15} \text{ cm}^{-3}$ are preferable.

[He] [cm^{-3}]	$\text{He}\bullet\text{CD}^+$ ions [%]	s_{num} [%]
$1 \cdot 10^{12}$	0.0	35.5
$1 \cdot 10^{13}$	0.0	35.2
$1 \cdot 10^{14}$	0.5	32.1
$1 \cdot 10^{15}$	21.5	13.3
$1 \cdot 10^{16}$	6.1	0.1
$1 \cdot 10^{17}$	0.0	0.0

Based on the calculated values given in table 5.10 a helium number density range between $\sim 5 \cdot 10^{14} \text{ cm}^{-3}$ and $\sim 1 \cdot 10^{15} \text{ cm}^{-3}$ should be used in the experiment. An interesting finding is that the relative number of $\text{He}\bullet\text{CD}^+$ ions starts to decrease again for helium number densities higher than $1 \cdot 10^{15} \text{ cm}^{-3}$. To explain this, as well as the decreasing cluster depletion signal, with the numerical model, the level population files can be used. The decrease of the signal for high helium number densities is due to fact that the CD^+ ions are converted into $\text{He}_2\bullet\text{CD}^+$ cluster ions, which are not effected by the applied radiation. Figures 5.14(a) to 5.16(b) shows the level population for three different helium number densities. For each number density the level population is shown with and without radiation. Based on these figures the decrease of the cluster depletion signal is explained in more detail.

At the low helium number density of $1 \cdot 10^{13} \text{ cm}^{-3}$ the collisions with helium play a minor role in comparison to the effect of the light ($K_{\text{coll}} \sim 10^2 \text{ s}^{-1}$ vs. $\sim 10^4 \text{ s}^{-1}$ for the light stimulated processes). The system without radiation is described by a Maxwell Boltzmann distribution at 5.7 K. At this temperature 93.8 % of the ions are in the rotational ground state of CD^+ and approximately 6.2 % are in the first rotational state. By switching the light on the population is inverted and 74.2 % of the ions are in the first excited rotational state and 25.6 % are in the rotational ground state of CD^+ . The ratio between these two states is nearly maximum (the maximum value would be 3 due to the statistical weights). This strong population inversion results in a maximum cluster depletion signal.

As shown in figures 5.14(a) and 5.14(b) the amount of cluster ions in the system after the storage time of 600 ms is below 0.0 % (see also table 5.10). So in the experiment is is not possible to observe a cluster depletion signal.

In case of a helium number density of $1 \cdot 10^{15} \text{ cm}^{-3}$ (shown in figures 5.15(a) and 5.15(b)) the situation is different. On the one hand the collisions with helium reduce the influence of the radiation (both rates are $\sim 10^4 \text{ s}^{-1}$). By switching on the light the population between the lowest two rotational states of CD^+ is still inverted, but the effect is smaller than for a helium number density of $1 \cdot 10^{13} \text{ cm}^{-3}$ (ratio of ~ 1.5 instead of 2.9 between the $J=1$ and $J=0$ for CD^+). On the other hand at this number density a sufficient number of helium cluster ions is created on this timescale. After 600 ms

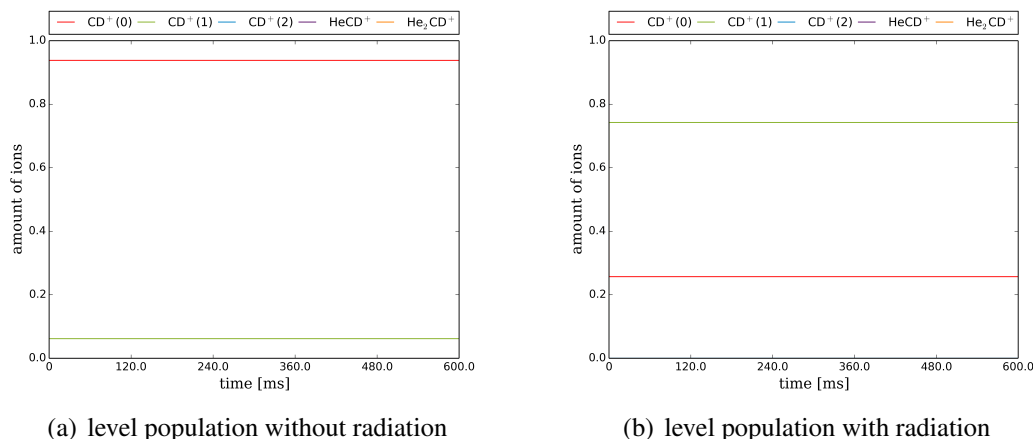


Figure 5.14: The two figures show the different simulated level populations for CD⁺ at a low helium number density of $1 \cdot 10^{13} \text{ cm}^{-3}$. On the timescale of 600 ms there is no cluster growth visible for such a low number density. The only populated states in this case are the rotational ground state of CD⁺ (CD⁺(0)) and the first rotational excited state (CD⁺(1)). Most of the CD⁺ ions are in the rotational ground state (93.8%). The right plot shows the situation with light applied to the system and by this the population is reversed. The ratio in the simulation between $J=1$ and $J=0$ is 2.9, which close to the maximum value of 3 limited by the statistical weights ($2J+1$) of the rotational levels. The amount of ions in the second rotational state of CD⁺ (CD⁺(2)) is in both cases $\sim 0.05\%$.

approximately 21 % of the CD⁺ ions are converted into He•CD⁺ cluster ions. Thus, for the experiment this helium number density is better suited to record a cluster depletion signal, even if the effect of the radiation is reduced by the collisions with helium.

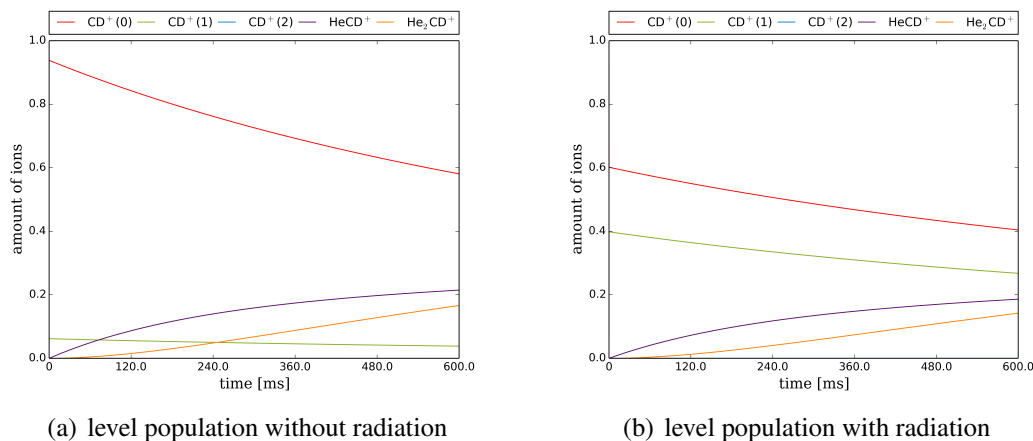


Figure 5.15: For these two figures the helium number density in the simulation was changed to $1 \cdot 10^{15} \text{ cm}^{-3}$. Due to the higher number density in this case a remarkable number of cluster-ions ($\sim 21\%$) (He•CD⁺) is formed after 600 ms of storage time. In the left plot without radiation the He•CD⁺ ions are mostly formed by conversion of CD⁺ ions in the rotational ground state. In (b) the radiation was switched on and the two lowest rotational states are reversed. Due to collisions with helium the ratio between the $J=1$ and $J=0$ state is here only 1.5 instead of 2.9. Since both levels are populated the cluster ions are formed from both rotational levels. This results in a smaller number of cluster-ions after the simulated storage time of 600 ms in comparison to the situation without radiation. The equilibrium for these conditions is reached after ~ 1800 ms.

In the third case the helium number density is increased again by a factor of five to $5 \cdot 10^{15} \text{ cm}^{-3}$. For this helium number density the collisional rates are larger than the stimulated rates. The redistribution of the two lowest rotational states of CD^+ is even more reduced and as shown in figure 5.16(b) the population of the two states is not reversed. This fact leads to a smaller cluster depletion signal. In addition, the cluster formation at such a high number density is so efficient that all CD^+ ions are converted into cluster ions after a storage time of 600 ms. This results in a constant number of $\text{He}\bullet\text{CD}^+$ cluster ions for both systems (with and without radiation). Therefore, the cluster depletion signal will vanish for such high number densities.

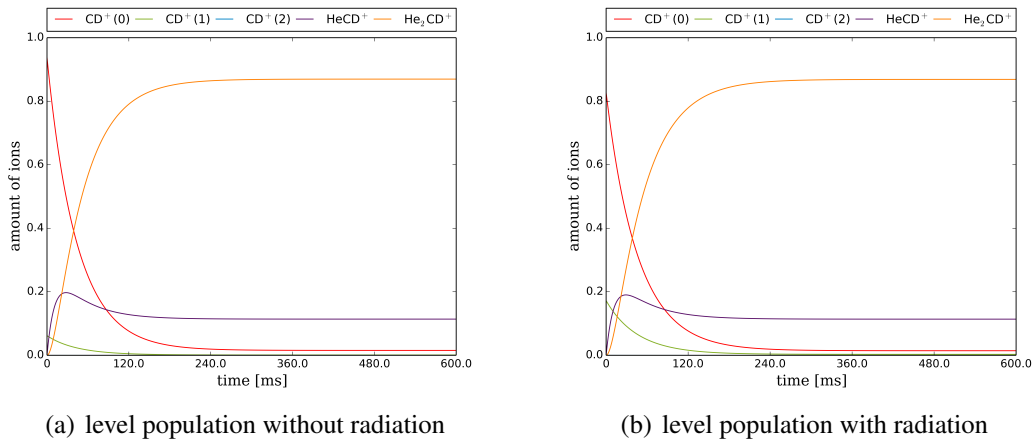


Figure 5.16: For these figures the number density was again increased to $5 \cdot 10^{15} \text{ cm}^{-3}$. The situation is complete different compared to the previous plots. After 300 ms all CD^+ ions are converted into cluster-ions. This effect is independent of the radiation and so both systems reach an equilibrium state after a simulated storage time of approximately 350 ms. This results finally in a disappearance of the cluster depletion signal for such high number densities (see figure 5.13). Another interesting fact is that the influence of the radiation on the initial population of the CD^+ rotational states is suppressed in comparison to lower number densities, since the collisions with helium are so effective.

From the simulations and discussion in this section it is possible to give some boundary conditions for the experiments. The two factors, which have to be taken into account, are the strength of the cluster depletion signal and the number of the $\text{He}\bullet\text{CD}^+$ cluster ions after a reasonable storage time. Without consideration of technical limitations a helium number density between $\sim 5 \cdot 10^{14} \text{ cm}^{-3}$ and $\sim 2 \cdot 10^{15} \text{ cm}^{-3}$ is preferable, since on the one hand in this density range the cluster depletion signal is strong enough (see figure 5.13) and on the other hand the number of $\text{He}\bullet\text{CD}^+$ cluster ions is sufficient (see table 5.10).

In the experiment we varied the helium number density in a range between $2.5 \cdot 10^{14} \text{ cm}^{-3}$ and $8.3 \cdot 10^{14} \text{ cm}^{-3}$. The observed cluster depletion signals are given in table 5.11.

The experimental values shows the same tendency as expected from the simulations. The value of the cluster depletion signal is maximum for the lowest observed helium number density and decreases with the helium number density. Due to technical limitations no measurements at number densities in the range of 10^{15} cm^{-3} are performed.

Table 5.11: Observed cluster depletion signals (s_{exp}) in the experiment for different helium number densities.

$n_{\text{He}} [\text{cm}^{-3}]$	$s_{\text{exp}} [\%]$
$2.5 \cdot 10^{14}$	25.1
$4.6 \cdot 10^{14}$	19.7
$8.3 \cdot 10^{14}$	13.6

5.3.3.2 Dependence on the Power of the mm-Wave Source

The power of the mm-wave radiation is another parameter, which can be varied in the experiment. As the helium number density the radiation power has to influence the observed cluster depletion signal. In table 5.12 the values for the simulations performed for the discussion in this section are summarized.

Table 5.12: Parameters for the simulations -mm wave power dependency

parameter	value
nominal temperature	4 K
collisional & internal temperature	5.7 K
storage time	600 ms
helium number density	$5 \cdot 10^{14} \text{ cm}^{-3}$
radiation power	variable
ratio a	0.5
rate-coefficients $k3_0 / k3_1 / k32 [\text{cm}^6 \text{ s}^{-1}]$	$9.6 \cdot 10^{-31} / a \cdot 9.6 \cdot 10^{-31} / 2.9 \cdot 10^{-30}$
rate-coefficients $k_CID / k_CID2 [\text{cm}^3 \text{ s}^{-1}]$	$6.7 \cdot 10^{-16} / 1.9 \cdot 10^{-15}$
branching ratio p	0.5
collisional-rate coefficients	see table 5.6 and 5.7

For the discussion first the analytical model is used. The expectation from the model is that the cluster depletion signal should increase with increasing power of the radiation source. In equation 5.68 an increasing radiation power results in a increasing factor x . Thus, $\frac{1}{x}$ decreases and so the signal increases. In case of a system that is dominated by the radiation the signal strength is limited and the maximum signal is described by equation 5.71. Figure 5.17 shows the result of the analytical model. The radiation is varied between 0 W and $2 \cdot 10^{-5}$ W, whereas the maximum value corresponds to the estimated maximum value for the setting with the focussing mirror (see section 5.1.3).

The shown cluster depletion signal dependency is as expected. With the used settings for the plot (5.17) also the leveling off of the signal is visible. The maximum value in this case is determined by the chosen value of a .

The physical reason for the increasing cluster depletion signal in the model is quite simple. With increasing radiation power at the same helium number density the rates for the stimulated processes increases and by this the redistribution of the two rotational levels $J=0$ and $J=1$ become more effective. This is shown in the plots 5.18(a) - 5.18(c). These plots are derived with the numerical simulation.

In figure 5.18(a) the situation is shown without radiation applied to the system. The distribution between the two lowest rotational states of CD⁺ is given by a Maxwell

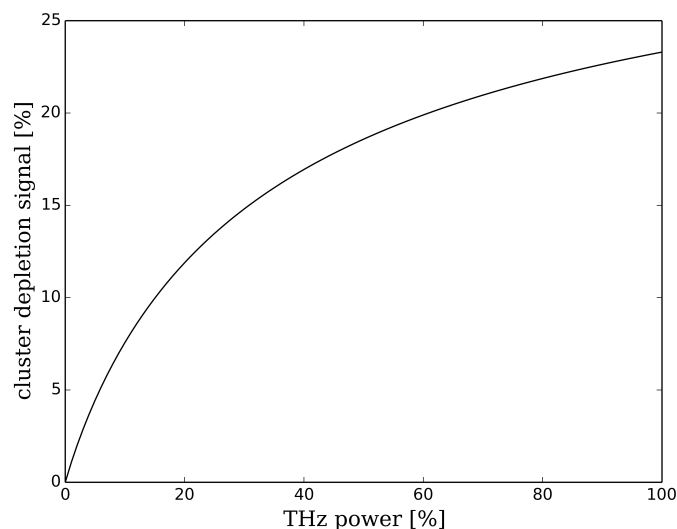


Figure 5.17: Simulated dependency of the cluster depletion signal for the $J=1 \leftarrow 0$ transition of CD^+ on the power of the mm-wave source based on the analytical model. For the simulation $100\% = 2 \cdot 10^{-5} \text{ W}$.

Boltzmann distribution at a temperature of 5.7 K ($J=0$: 93.8 %; $J=1$: 6.2 % at the beginning) In figure 5.18(b) the radiation is switched on, but the system is still dominated by the collisions with helium and so the redistribution of the two $J=0$ and $J=1$ levels of CD^+ is visible, but ineffective ($J=0$: 91.2 %; $J=1$: 8.2 %). This small change in the population of these two states results in a small cluster depletion signal, since the situation is still comparable to the situation without light. The situation in figure 5.18(c) is different. The stimulated rates are now in the same order as the collisional rates and the population of the two lowest rotational levels of CD^+ is inverted ($J=0$: 48.5 %; $J=1$: 51.2 %). The ratio between the two rotational states stays constant with time. Since the cluster ions are formed from the first rotational excited state half as fast in the model as from the rotational ground state this redistribution leads to a large cluster depletion signal.

In the experiment three different measurements are performed. Two of the three measurements are done without the mirror (see section 5.1.3) In this case the maximum available mm-wave power was $\sim 3.5 \cdot 10^{-6} \text{ W}$. This is almost a factor of ten less than the assumed mm-power used for the simulations above. The last measurement was done with the focussing mirror. With this setup the estimated radiation power is a factor of five larger. If the simulations are correct the leveling off of the cluster depletion signal should be visible in this case. Figure 5.19 shows the two measurements with the unfocussed setup.

The measurements were performed at two different helium number densities of $2.94 \cdot 10^{14} \text{ cm}^{-3}$ and $4.87 \cdot 10^{14} \text{ cm}^{-3}$. The recorded curves show the same overall shape as the simulated power dependency curves. This means that the simulation can reproduce the power dependency. Due to the relatively low radiation power the signal does not level off under this conditions. In addition, the effect of a higher helium number density on the cluster depletion signal is visible in figure 5.19. The red curve for the higher helium number density is below the black one for the lower density. This is in accordance with the simulations and the measurements presented in section 5.3.3.1.

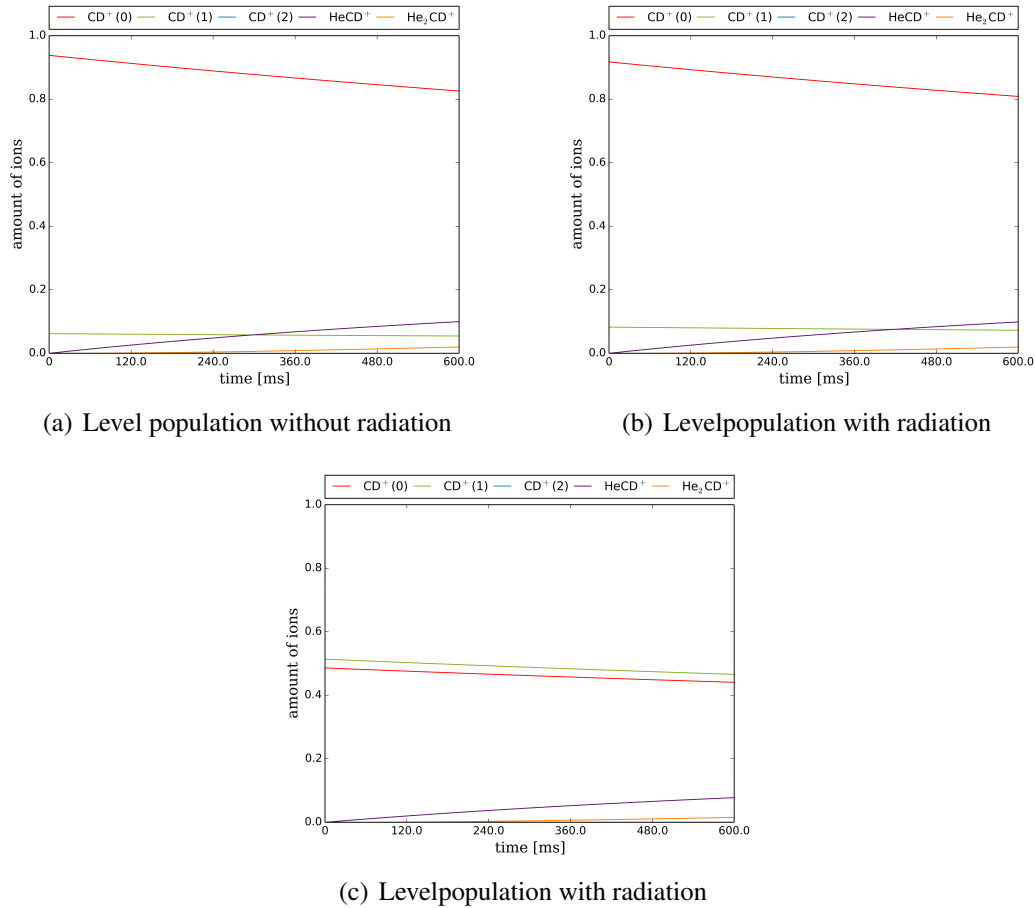


Figure 5.18: Simulated level populations for CD^+ for different radiation power level. In (a) the situation is shown without radiation. In this case 93.8% of the ions are in the rotational ground state at the beginning and 6.2% are in the first rotational state of CD^+ . In (b) the radiation is switched on. The power is $2 \cdot 10^{-7}$ W. By this the population is slightly influenced and 91.2% of the ions are in the rotational ground state at the beginning and 8.2% are in the first rotational state of CD^+ . In (c) the power is increased to $2 \cdot 10^{-5}$ W and by this the the $J=0$ level of CD^+ is populated with 48.5% and 51.2% of the ions are in the first rotational state of CD^+ at the beginning of the simulation. The ratio between the population of the two rotational states is constant with time.

The third measurement with the focussed setup is shown in figure 5.20. The available radiation power is in this case $\sim 2 \cdot 10^{-5}$ W. This is equal to the radiation power used for the simulations in this section. If the simulations are correct, one would expect to observe leveling off of the cluster depletion signal for this measurement.

This effect is visible in figure 5.20. The observed maximum cluster depletion signal for this setting is larger than for the unfocused setting at a comparable helium number density. The maximum values observed in the experiment is also in a good agreement with the value obtained from the simulation. These three measurements will be used in section 5.3.3.5 to estimate the ratio between the ternary rate-coefficients for the two lowest rotational states of CD^+ .

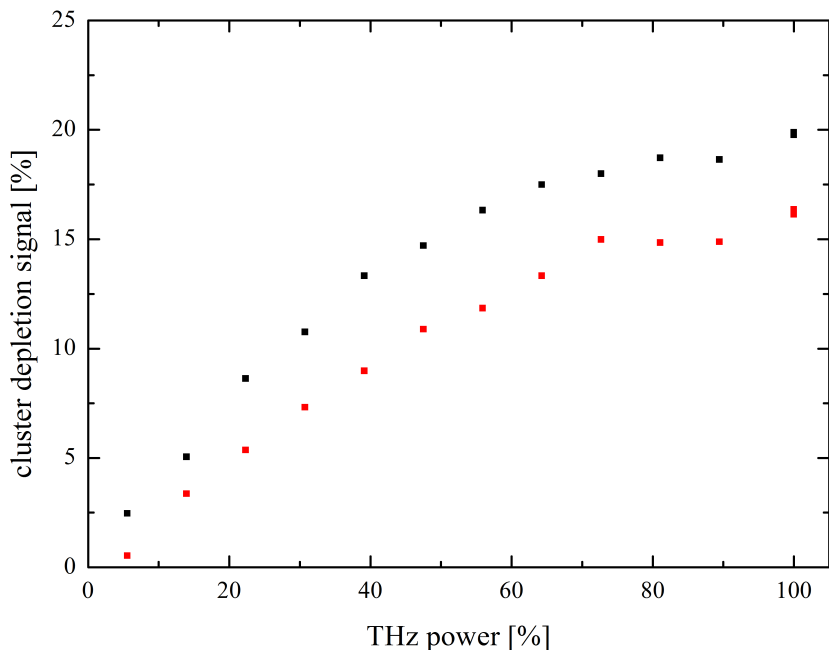


Figure 5.19: Measured power dependence curves for the cluster depletion signal for the two helium number densities of $2.94 \cdot 10^{14} \text{ cm}^{-3}$ (black) and $4.87 \cdot 10^{14} \text{ cm}^{-3}$ (red) with the unfocused setup. The experimental conditions were a nominal trap temperature of 4 K and a storage time of 600 ms. The different power levels were achieved by applying an attenuation voltage at the VDI Starter Kit (see section 5.1.3 for more details). For these measurements $100\% = 3.5 \cdot 10^{-6} \text{ W}$.

5.3.3.3 Dependence on the Trap Temperature

The third parameter that could be varied in the experiments is the temperature of the trap. If the trap is heated up on the one hand the collisional temperature is changed, which influences in our model the rotational population of the CD^+ ions and by this it should influence the cluster depletion signal. On the other hand the collisional rates may change with the temperature (see tables 5.6 and 5.7). Since the collisions with helium are more effective for higher temperatures this should lead to a decrease of the simulated and observed cluster depletion signal. In table 5.13 the values used for the simulations in this section are listed.

The analytical model was performed at three different nominal temperatures of 4 K, 7 K, and 12 K. The results of these calculations are summarized in table 5.14.

For the simulations at the different temperatures the collisional rate-coefficients given in table 5.7, the collisional temperatures given in table 5.2 and the rate-coefficients from the tables 5.3 and 5.4 are used. Since no kinetic measurements for 12 K were performed for this temperature the values for 10 K are used. The simulations predict that the cluster depletion signal decreases for increasing temperature. Physically this can be explained in the model by the different initial populations of the rotational states of CD^+ . At higher temperatures the excited rotational state $J=1$ is already populated without light. This reduces the effect of the redistribution due to the radiation. This results than in a smaller observable cluster depletion signal. In addition,

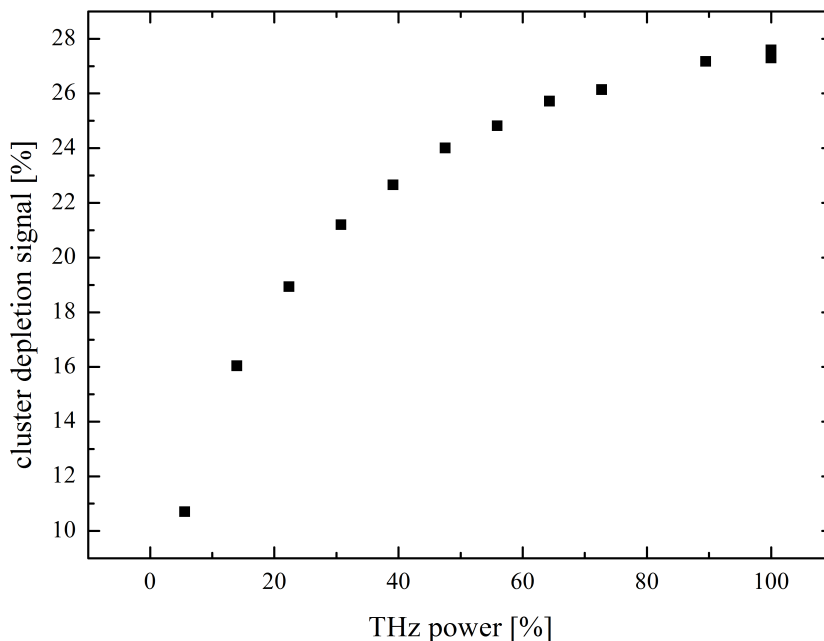


Figure 5.20: Measurement of the power dependence of the cluster depletion signal for CD⁺ with the focussed setup (see section 5.1.3). The measurements were performed at a nominal trap temperature of 4 K and at a storage time of 600 ms. The helium number density in the trap was $3.48 \cdot 10^{14} \text{ cm}^{-3}$. For this measurement 100% = $2 \cdot 10^{-5} \text{ W}$.

Table 5.13: Parameters for the simulations - temperature dependency

parameter	value
nominal temperature	variable
collisional & internal temperature	variable
storage time	600 ms
helium number density	$5 \cdot 10^{14} \text{ cm}^{-3}$
radiation power	$2 \cdot 10^{-5} \text{ W}$
ratio a	0.5
rate-coefficients $k_{3_0} / k_{3_1} / k_{32} [\text{cm}^6 \text{ s}^{-1}]$	variable
rate-coefficients $k_{\text{CID}} / k_{\text{CID}2} [\text{cm}^3 \text{ s}^{-1}]$	variable
branching ratio p	0.5
collisional-rate coefficients	variable; see table 5.6 and 5.7

Table 5.14: Results for the temperature dependence of the analytical model (s_{ana}) and the numerical simulation (s_{num}), assuming a constant helium number density for all temperatures. s_{num} is calculated after a storage time of 600 ms.

T _{nom}	T _{coll}	S _{ana}	S _{num}
4 K	5.3 K	29.8 %	22.1 %
7 K	8.9 K	16.6 %	15.2 %
12 K	16.9 K	6.3 %	6.1 %

the collisional rates for the de-excitation from $J=1$ to $J=0$ is in the model higher for a higher temperature. This effect also reduces the redistribution due to the radiation. Figures 5.21(a) to 5.21(d) show the simulated level population for two different temperatures, derived from the numerical simulation.

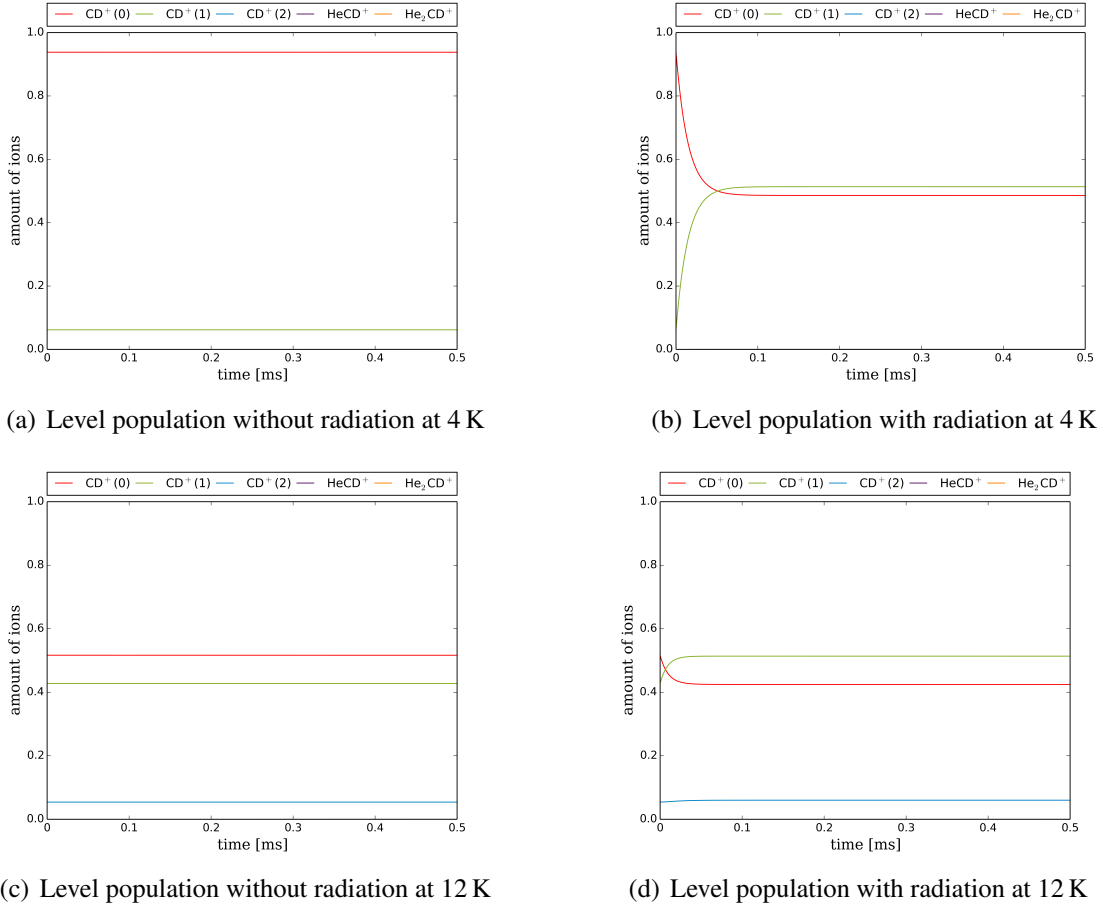


Figure 5.21: These figures show the simulation for the first 0.5 ms storage time for two different nominal temperatures. In the top row the simulation is performed for 4 K and in the bottom row for 12 K. The plots in the left column are without radiation and in the right column with radiation.

For the discussion only the initial distribution of the rotational states of CD^+ is needed. Therefore, only the first 0.5 ms of the storage time are shown in the figures 5.21(a) to 5.21(d). For the nominal trap temperature of 4 K the change in the population of the different rotational levels is more pronounced. Without radiation the distribution in the rotational levels of CD^+ is $J=0$: 93.8 %, $J=1$: 6.2 %, and $J=2$: 0.0 %. By switching the light on the relative populations are $J=0$: 48.4 %, $J=1$: 51.2 %, and $J=2$: 0.0 %. For the higher nominal temperature of 12 K the change in the distributions due to the light is smaller. At this temperature without radiation the distribution in the CD^+ levels is $J=0$: 51.6 %, $J=1$: 42.7 %, and $J=2$: 5.4 %. With radiation the distribution changes to: $J=0$: 42.4 %, $J=1$: 51.3 %, and $J=2$: 6.0 %. The fact that at a nominal temperature of 12 K temperatures the relative population of the first excited rotational state is \sim seven times higher than for 4 K reduces the influence of the radiation on the rotational distribution. This leads to a decreasing cluster depletion signal for increasing temperatures in the model. In addition, in the two plots 5.21(b) and 5.21(d) the timescale for the redistribution due to the influence of the light can be estimated. For

Table 5.15: In this table the experimental values for the cluster depletion signal s_{exp} at different nominal temperatures are summarized. All measurements were performed with the focussing optic. The storage time for the measurement was 600 ms. In addition, the results of the analytical model (s_{ana}) and the numerical (s_{num}) model, using the correct helium number densities, are listed.

T_{nom} [K]	n_{He} cm ⁻³	s_{exp} [%]	s_{ana} [%]	s_{num} [%]
4	$3.5 \cdot 10^{14}$	28.8	26.0	25.4
5	$3.0 \cdot 10^{14}$	27.5	25.2	24.4
7	$2.5 \cdot 10^{14}$	25.9	22.8	21.2
8	$2.3 \cdot 10^{14}$	24.9	20.9	19.7
12	$1.8 \cdot 10^{14}$	21.2	12.1	11.7

this helium number density of $5 \cdot 10^{14}$ cm⁻³ the timescale is below 0.1 ms. This fact confirms the assumption that the reactions always see the same rotational distribution, since the timescale for the reactions is much slower than the redistribution of the ions in the different rotational levels. In figure 5.21(d) it is also visible that the second rotational level of CD⁺ is populated at nominal temperature of 12 K, and the amount of ions in the second rotational level of CD⁺ changes, when the radiation is switched on. Even if the amount of ions in this levels is comparably small the assumption of a two level system for the analytical model is not completely true.

In the experiment measurements in the temperature range between 4 K and 12 K are performed. The results are summarized in table 5.15.

As predicted by the simulations the cluster depletion signal decreases for increasing temperatures in the experiment. The predicted cluster depletion signals given in table 5.14 overestimate the drop of the signal. This is partly because of the assumed constant helium number density for all temperatures in the simulation. Due to the experimental procedure the helium number density decreases with increasing temperature. In the experiment the helium pressure in the trap was set for the experiment at 4 K. For the next experiments at 5 K, 7 K and so on the helium pressure was constant and this leads, due to the higher nominal temperature, to lower helium number densities in the trap (see section 5.1.2). For the results of the simulations listed in table 5.15 this effect is included and by this the simulation can better reproduce the observed decrease of the cluster depletion signal in the experiment.

Based on the simulations it is obvious that it is favorable to measure at the lowest possible temperature to achieve the maximum cluster depletion signal. Of course, this is only true if the ground state transition is measured. For transitions starting at the first excited rotational level it is may be useful to heat up the trap, in order to achieve a sufficient population of this state (see for example figure 5.21(c)).

5.3.3.4 Dependence on the Storage Time

The last parameter that is varied in the experiment is the storage time. The structure of this section is slightly different compared to the previous ones, since the storage time is a parameter, that is not included in the analytical model. In this model one of the assumptions is that the system is in equilibrium. Therefore, the storage does not have an effect on the cluster depletion signal. So in this section only the numerical model is used. In table 5.16 the values used for the simulation are summarized.

Table 5.16: Parameters for the simulations - storage time dependency

parameter	value
nominal temperature	4 K
collisional & internal temperature	5.7 K
storage time	variable
helium number density	$5 \cdot 10^{14} \text{ cm}^{-3}$
radiation power	$2 \cdot 10^{-5} \text{ W}$
ratio a	0.5
rate-coefficients $k3_0 / k3_1 / k32 \text{ [cm}^6 \text{ s}^{-1}\text{]}$	$9.6 \cdot 10^{-31} / a \cdot 9.6 \cdot 10^{-31} / 2.9 \cdot 10^{-30}$
rate-coefficients $k_CID / k_CID2 \text{ [cm}^3 \text{ s}^{-1}\text{]}$	$6.7 \cdot 10^{-16} / 1.9 \cdot 10^{-15}$
branching ratio p	0.5
collisional rate-coefficients	see table 5.6 and 5.7

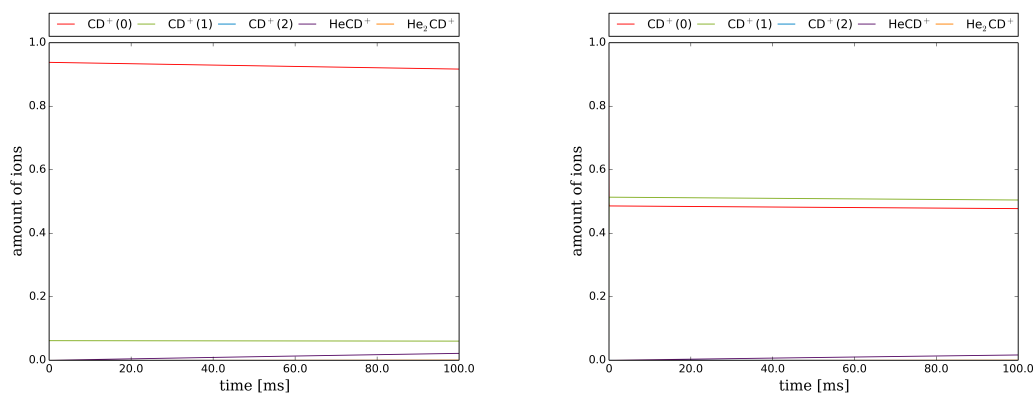
The results for the cluster depletion signal of the numerical simulation are listed in table 5.17.

Table 5.17: Results for the storage time dependence of the cluster depletion signal in the numerical simulation (s_{num}). In the last column the amount of $\text{He}_2 \bullet \text{CD}^+$ ions for the different storage times is listed for the situation without radiation.

storage time [ms]	s_{num} [%]	amount of $\text{He}_2 \bullet \text{CD}^+$ [%]
50	23.2	0.0
100	23.1	0.1
200	22.9	0.3
400	22.5	1.0
600	22.1	2.0
800	21.7	3.1
1000	21.3	4.3
1500	20.3	7.3
2000	19.4	9.9
2500	18.7	12.3
5000	15.8	19.3
10000	13.1	23.1
20000	12.1	23.8

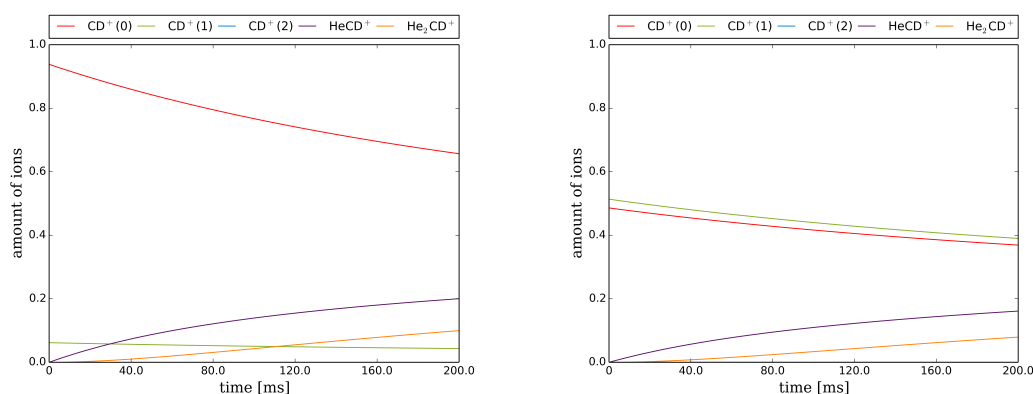
The results of the numerical simulation show that the cluster depletion signal decreases with increasing storage time. In the range of useable storage times in the experiment between 100 ms and 600 ms the calculated cluster depletion signal drops from 23.1% to 22.1%. This is a small decrease, which is probably hard to observe in the experiment. To explain this effect figures 5.22(a) to 5.22(d) show the calculated level populations for a short storage time of 100 ms and a long storage time of 2000 ms.

For longer storage times the number of CD^+ ions in the system is reduced, since they are converted into larger cluster ions (with more than one helium atom). These larger cluster ions are not directly influenced by the applied radiation and by this the cluster depletion signal is reduced in the model. This effect is visible in the figures 5.22(a) to 5.22(d). Especially the amount of ions in the reservoir for the second helium cluster ion increases. For the relatively short storage time of 100 ms the amount of ions



(a) level population for 100 ms without radiation

(b) level population for 100 ms with radiation



(c) level population for 2000 ms without radiation

(d) level population for 2000 ms with radiation

Figure 5.22: Simulated level populations for CD^+ for storage times of 100 ms and 2000 ms with and without radiation. In red the population of the rotational ground state of CD^+ is shown, in green the first rotational state, in dark purple the first helium cluster ion and in light purple the second helium cluster ion. The number of the second helium ions increases with the storage time, which are not effected by the applied radiation. The increasing number of these ions with the storage time results in a decreasing cluster depletion signal for longer storage times.

in this reservoir is 0.1 %, whereas for the storage time of 2000 ms already 9.7 % of the ions are in the reservoir. In table 5.17 in addition to the computed cluster depletion signal the amount of ions in the $\text{He}_2 \bullet \text{CD}^+$ reservoir for the simulation without radiation is listed.

In the experiment three different storage times were realized. The cluster depletion signal was recorded for 200 ms, 400 ms, and 600 ms with the unfocussed setup. The recorded values for the cluster depletion signal are summarized in table 5.18. In the experiment the storage time was only varied in this small range, since for storage times longer than 600 ms the amount of time needed for the measurements increases extremely, due to technical reasons (synchronization with the coldhead).

In the experimental data a small decrease in the signal is visible, but it is difficult to decide, whether this effect is real or due to other drifts in the experiment. The predicted change of the cluster depletion signal by the numerical model for these storage times is also only one percentage point for the conditions given in table 5.16. The predicted change in the signal by the model is even smaller if conditions are used as in the

Table 5.18: Observed cluster depletion signals for different storage times. The measurements are performed at a nominal temperature of 4 K and a helium number density of $\sim 3.7 \cdot 10^{14} \text{ cm}^{-3}$ with the unfocussed setup. Hence, the maximum available power for these measurements was $3.5 \cdot 10^{-6} \text{ W}$. For the calculated signals the helium number density and the radiation power was changed in comparison to table 5.16.

storage time [ms]	S_{exp} [%]	S_{num} [%]
200	20.0	13.3
400	19.5	13.1
600	19.3	12.9

experiment. Based on the available data it is not possible to decide if the prediction of the model is correct or not.

If one assumes that the prediction of the model is correct, than it is favorable to measure at short storage times, since the signal decreases for longer storage times. The disadvantage of short storage times is of course that the number of cluster ions is smaller than for longer storage times and by this the signal to noise ratio increases.

5.3.3.5 Estimation of the Ratio $a = \frac{k_3(1)}{k_3(0)}$ for CD^+

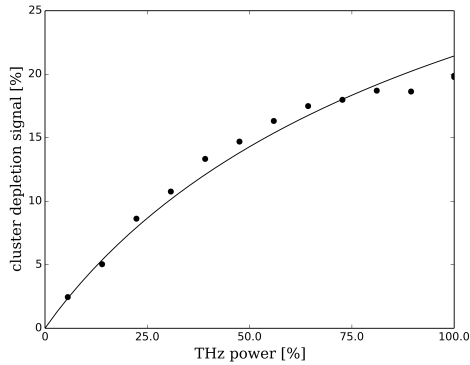
In this section the two models in combination with different measurements are used in order to estimate the ratio between the two different ternary rate-coefficients for the rotational ground state and the first excited state.

The first approach is to use the analytical model to fit the three measured power dependency curves, which were already shown in section 5.3.3.2. For this the parameter a was varied in the model until the simulated power dependency curve fits best to the experimental data. Afterwards the same three measurements will be fitted with the numerical model in the same way. The values used in the models are listed in table 5.19. The helium number density is slightly different for the three measurements. Therefore, the simulations are performed with the corresponding densities. For the two measurements with the unfocussed setup the maximum power in the simulation is $3.5 \cdot 10^{-6} \text{ W}$ and for the measurement with the focussed setup a maximum power of $2 \cdot 10^{-5} \text{ W}$ is used.

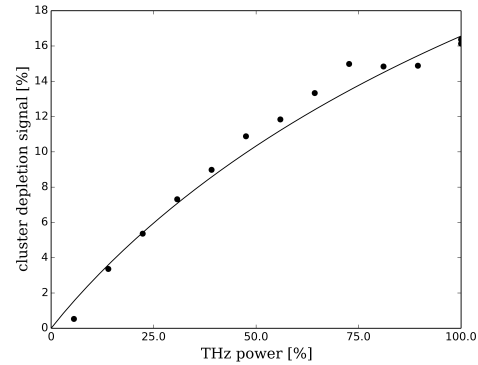
Table 5.19: Parameters for the simulations - estimation of a for CD^+

parameter	value
nominal temperature	4 K
collisional & internal temperature	6.0 K
storage time	600 ms
helium number density	see measurements
max. radiation power	$2 \cdot 10^{-5} \text{ W} / 3.5 \cdot 10^{-6} \text{ W}$
ratio a	variable
rate-coefficients $k_{3_0} / k_{3_1} / k_{32} [\text{cm}^6 \text{ s}^{-1}]$	$9.6 \cdot 10^{-31} / a \cdot 9.6 \cdot 10^{-31} / 2.9 \cdot 10^{-30}$
rate-coefficients $k_{\text{CID}} / k_{\text{CID}2} [\text{cm}^3 \text{ s}^{-1}]$	$6.7 \cdot 10^{-16} / 1.9 \cdot 10^{-15}$
branching ratio p	0.5
collisional rate-coefficients	see table 5.6 and 5.7

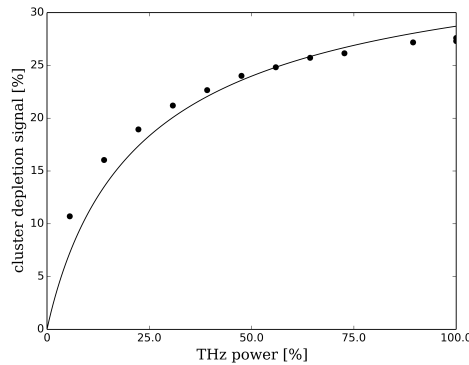
The plots in figures 5.23(a) to 5.23(c) show the best fits obtained by the analytical model. The dots represent the measured cluster depletion signal values and the solid lines are results of the analytical model, performed with the values given in table 5.19.



(a) Fit for CD^+ at $2.94 \cdot 10^{14} \text{ cm}^{-3}$ / $a = 0.31$ / unfocussed



(b) Fit for CD^+ at $4.87 \cdot 10^{14} \text{ cm}^{-3}$ / $a = 0.26$ / unfocussed



(c) Fit for CD^+ at $3.48 \cdot 10^{14} \text{ cm}^{-3}$ / $a = 0.45$ / focussed

Figure 5.23: The three plots show the fits obtained with the analytical model to the measured power dependence curves. In the top row the two measurements with the unfocussed setup are shown and in the bottom row the measurement with the focussed setup is plotted. From these three fits the value for the ratio a is $0.24 \leq a \leq 0.46$. The lower border is determined by the fit for the unfocussed measurement at a helium number density of $4.87 \cdot 10^{14} \text{ cm}^{-3}$, and the upper border by the fit for the measurement with the focussed setup.

The obtained values for a with the analytical model from these three fits are summarized in table 5.20.

Table 5.20: Results for a for CD^+ obtained with the analytical model

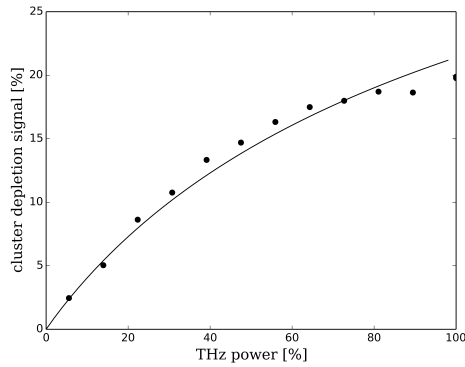
figure	minimum value a	maximum value a
5.23(a)	0.28	0.34
5.23(b)	0.24	0.30
5.23(c)	0.40	0.46

The two values gained from the fits of the unfocussed measurements match within their errors, while the resulting value for a for the focussed setup is higher. The reason

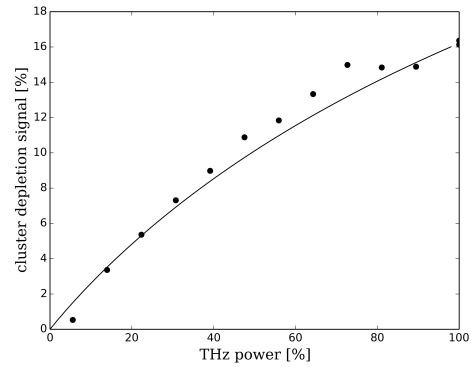
for this is probably a problem with the estimation of the maximum available THz power for the two different setups. If, for example, the maximum power for the unfocussed setup is changed from $3.5 \cdot 10^{-6} \text{ W}$ to $4.5 \cdot 10^{-6} \text{ W}$ the estimated ratios from the two methods match. Overall the estimated value for a from the analytical model with this method is

$$0.24 \leq a \leq 0.46 \quad (5.74)$$

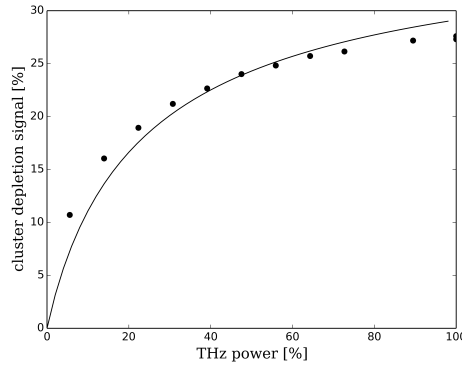
In the next step the same procedure is repeated with the numerical simulation. The results for these fits are shown in the figures 5.24(a) to 5.24(c).



(a) Fit for CD^+ at $2.94 \cdot 10^{14} \text{ cm}^{-3}$ / $a = 0.31$ / unfocussed



(b) Fit for CD^+ at $4.87 \cdot 10^{14} \text{ cm}^{-3}$ / $a = 0.26$ / unfocussed



(c) Fit for CD^+ at $3.48 \cdot 10^{14} \text{ cm}^{-3}$ / $a = 0.43$ / focussed

Figure 5.24: The three plots show the fits obtained with the numerical model to the measured power dependence curves. In the top row the two measurements with the unfocussed setup are shown and in the bottom row the measurement with the focussed setup is plotted. From these three fits the value for the ratio a is $0.24 \leq a \leq 0.46$. The lower border is determined by the fit for the unfocussed measurement at a helium number density of $4.87 \cdot 10^{14} \text{ cm}^{-3}$ and the upper border by the fits for the measurement with the focussed setup.

The derived values for a with the numerical model from the three different fits are summarized in table 5.21.

The calculated values for a for the two unfocussed measurements match with each other. As for the analytical approach the derived value based on the focussed measure-

Table 5.21: Fit results for a for CD⁺ with the numerical model

figure	minimum value a	maximum value a
5.24(a)	0.28	0.33
5.24(b)	0.24	0.29
5.24(c)	0.40	0.46

ment is higher than for the unfocussed measurements. Overall the value for a based on the fits with the numerical simulation is

$$0.24 \leq a \leq 0.46 \quad (5.75)$$

This range for the ratio a is equal to the range determined by the analytical simulation (see equation (5.74)).

One uncertainty in these approaches, besides the available THz power, is that in the analytical model as well as in the numerical model the collisional rate-coefficients for collisions with helium are included. The rate-coefficients are calculated for CH⁺ and not for CD⁺ and in addition, the values have to be extrapolated for the different temperatures. At the end of section 5.3.1 the equation

$$a = \frac{c_1 - c_1 c_3 - s - c_1 s}{c_1 c_3 s + c_1^2 c_3 s + c_1 - c_1 c_3} \quad (5.76)$$

was derived for a , under the assumption that the system is dominated by the radiation, and thus independent of k_{coll} and the maximum cluster depletion signal is observed. Figure 5.20 can be used to estimate the maximum cluster depletion signal, since the observed signal for the last two data points at 90 % and 100 % there is almost no increase in the cluster depletion signal visible. From the plot the maximum signal of ~27-28 % can be estimated. This value for the maximum cluster depletion signal can be inserted in equation 5.76 and by this a value for a can be calculated. With these values for the maximum signal a varies between

$$0.58 \leq a \leq 0.60 \quad (5.77)$$

This range for a , using this approach, does not match with the calculated ranges for a obtained by the previous method.

In the numerical model it is not possible to get rid of the collisional rate-coefficients for the collisions with helium. Thus, the idea to get an approximation for a out of the maximum observed cluster depletion signal is different. The approach is here to vary the collisional rate-coefficients for the collisions with helium by a factor of ± 5 and vary the value for a in a way that the calculated cluster depletion signal is always ~28 %. In table 5.22 the calculated cluster depletion signal are listed for the different combinations of a and k_{coll} .

An interesting fact in table 5.22 is that the calculated cluster depletion signals for a given ratio a is only influenced little if the value for the collisional rate-coefficient with helium is changed from one half to one fifth of the original value. The reason

Table 5.22: Calculated strength of the cluster depletion signal in dependence of the different collisional rate-coefficients for CD^+ and helium used in the simulation and different values of the ratio a between the ternary rate-coefficients of the rotational ground and first excited state. The maximum cluster depletion signal measured under these conditions was $\sim 28\%$. For the values used in the simulation refer to table 5.19.

value for a	$0.2 \cdot k_{\text{coll}}$	$0.5 \cdot k_{\text{coll}}$	$1 \cdot k_{\text{coll}}$	$2 \cdot k_{\text{coll}}$	$5 \cdot k_{\text{coll}}$
0.00	67.9 %	61.8 %	53.7 %	42.6 %	26.3 %
0.20	53.4 %	48.6 %	42.2 %	33.5 %	20.7 %
0.40	39.3 %	35.8 %	31.2 %	24.7 %	15.3 %
0.42	37.9 %	34.6 %	30.1 %	23.9 %	14.8 %
0.44	36.6 %	33.3 %	29.0 %	23.0 %	14.2 %
0.46	35.2 %	32.1 %	27.9 %	22.2 %	13.7 %
0.48	33.8 %	30.8 %	26.8 %	21.3 %	13.2 %
0.50	32.5 %	29.6 %	25.8 %	20.5 %	12.6 %
0.52	31.1 %	28.4 %	24.7 %	19.6 %	12.1 %
0.54	29.8 %	27.1 %	23.6 %	18.8 %	11.6 %
0.56	28.4 %	25.9 %	22.6 %	17.9 %	11.1 %
0.58	27.1 %	24.7 %	21.5 %	17.1 %	10.6 %
0.60	25.8 %	23.5 %	20.4 %	16.2 %	10.0 %
0.62	24.4 %	22.3 %	19.4 %	15.4 %	9.5 %
0.64	23.1 %	21.1 %	18.3 %	14.6 %	9.0 %
0.66	21.8 %	19.9 %	17.3 %	13.7 %	8.5 %
0.68	20.5 %	18.7 %	16.2 %	12.9 %	8.0 %
0.70	19.2 %	17.5 %	15.2 %	12.1 %	7.5 %
0.80	12.7 %	11.6 %	10.1 %	8.0 %	5.0 %

for this is that in this regime the collisions with helium are negligible and the system is dominated by the light. In this case the computed signal (for $a=0.0$) is near to the maximum signal, which is 73.4% for CD^+ (see equation 5.59 in section 5.3.1). Even if the collisional rate-coefficient for helium is changed by another factor of 2 the cluster depletion signal would not change dramatically. So the upper limit for the ratio a obtained by this method is reliable. For increasing the collisional rate-coefficients with helium there is no such barrier. Due to this the lower limit for a is obtained by restricting the variation to a factor of 2, because by varying the collisional rate-coefficients by a factor of 5 the calculated signal for is even for $a = 0.00$ lower than the observed signal in the experiment. With these limits the ratio between the two lowest collisional rate-coefficients for CD^+ is

$$0.40 \leq a \leq 0.58 \quad (5.78)$$

The lower limit obtained by this method is in the same range as for the fitting procedures presented at the beginning of this chapter. The upper limit of $a = 0.58$ is considerably higher than the values obtained by the fitting procedures. Altogether, the limits for a obtained with the last two procedures are higher than the limits calculated by the fitting method.

5.4 Rotational Spectroscopy of HCO^+

5.4.1 Motivation

As a second test-case for the model HCO^+ was chosen. HCO^+ is a rotationally and ro-vibrationally spectroscopically well characterized closed-shell linear molecule ([55], [56], [57]), so the purpose of the measurements was to use this well known system in order to compare the results with the measurements of CD^+ to test the simulation. Another benefit of HCO^+ is that there is state-to-state rotational collisional excitation data for collisions with helium available ([58], [59]). This data is for example needed to run the simulations presented in chapter 5.3. Therefore, HCO^+ is a good test-candidate for the numerical simulation. In this section the experiments on the underlying kinetic experiments are presented. Besides this also measurements of the rotational transition $J=1\leftarrow 0$ at 89.188525 GHz ([56]) are presented and the analytical and numerical model are used to estimate the ratio α for HCO^+ and compare it to CD^+ .

5.4.2 Experimental Setup

As a precursor in the source a mixture of CO, He, and H_2 in the ratio of 1:2:3 was used for the experiments. The source was operated with pressures around $7 \cdot 10^{-6}$ mbar. For generating the HCO^+ ions an electron impact energy of 20 eV was used. The first quadrupole was tuned to select mass 29 u. With these settings and a helium number density of $\sim 1.6 \cdot 10^{14} \text{ cm}^{-3}$ in the trap, around 7000 HCO^+ ions could be stored in the trap at a temperature of 4 K.

For the rotational spectroscopy measurements a storage time of 600 ms was used. Even if the system is not completely at equilibrium (see figure 5.26) this storage time was chosen due to experimental requirements. As a radiation source the Rohde & Schwarz SMF100A synthesizer was used (as for the measurements of CD^+ see subsection 6.1.2). For HCO^+ the synthesizer was used in combination with the VDI AMC 375 high-power multiplier chain at a frequency of 89.188525 GHz. The multiplier chain was directly placed in front of the 0.8 mm thick diamond CVD window from Diamond Materials GmbH. The maximum available power for this setup is $\sim 1 \cdot 10^{-5}$ W. The total power was measured outside the trap with two iris to simulate the diamond window and the bender entrance.

5.4.3 Experimental Data

As for the previous examples, CD^+ and C_3H^+ , first kinetic measurements were performed to investigate the time evolution of the HCO^+ and helium system. First of all a mass spectrum was recorded in order to check if there are competing processes to the cluster formation and how many helium atoms can be attached to the HCO^+ ion under typical conditions. A typical mass spectrum is shown in figure 5.25.

The spectrum was recorded at 4 K, after a storage time of 500 ms, and at a helium number density of $1 \cdot 10^{15} \text{ cm}^{-3}$. The largest peak at mass 29 u is the initially injected HCO^+ . As shown in the mass spectrum easily up to five helium atoms can be attached

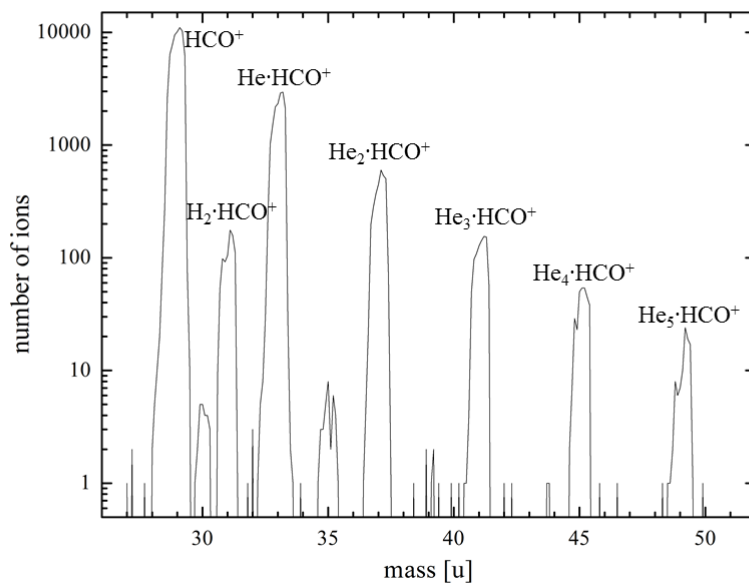
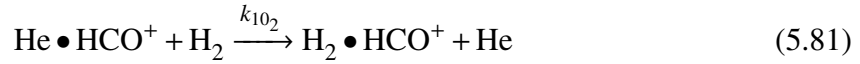
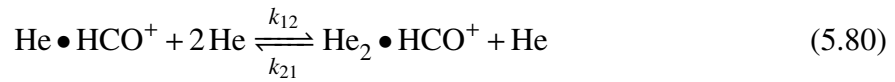
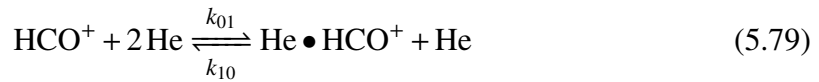


Figure 5.25: Mass scan of trapped HCO^+ ions at 4 K. The ions were stored for 500 ms in a cold helium bath. The helium number density was in this case $1 \cdot 10^{15} \text{ cm}^{-3}$. The HCO^+ peak and the different $\text{He}_n \bullet \text{HCO}^+$ ions correspond to the masses 29 u, 33 u, 37 u, 41 u, 45 u and 49 u. The peak at mass 31 u is $\text{H}_2 \bullet \text{HCO}^+$ due to residual H_2 in the helium gas.

to HCO^+ (~ 20 counts at mass 49 u). Roughly 30% of the HCO^+ ions are converted into cluster ions. Besides the series of the $\text{He}_n \bullet \text{HCO}^+$ cluster ions, there are also mass peaks at 30 u, 31 u, and 35 u visible in the spectrum, that do not belong to the HCO^+ -helium cluster ions. The strongest of these three peaks at mass 31 u belongs to $\text{H}_2 \bullet \text{HCO}^+$. This ion is produced inside the trap due to residual H_2 gas. To reproduce the evolution of the system (see figure 5.26) it is necessary to take the formation of this ion into account. It turned out that the $\text{H}_2 \bullet \text{HCO}^+$ ion is formed out of the first helium cluster by a collision and a switching with a H_2 molecule. So the formation of the $\text{H}_2 \bullet \text{HCO}^+$ ion is another destruction process for the $\text{He} \bullet \text{HCO}^+$ cluster ion in addition to the collision induced dissociation process. The complete system that is used to describe the HCO^+ helium system is ($\text{H}_2 \text{CO}^+$ (mass 30 in figure 5.25) and $\text{He} \bullet \text{H}_2 \bullet \text{HCO}^+$ (mass 35 in figure 5.25) were neglected), therefore:



(5.84)

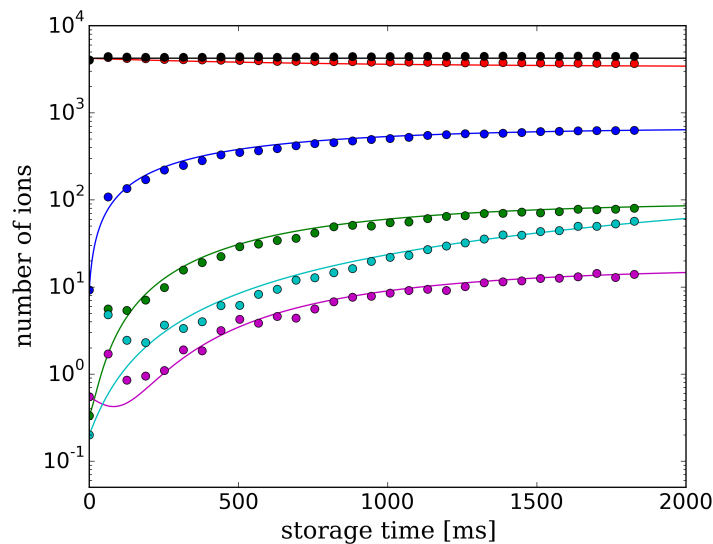


Figure 5.26: Time evolution of the HCO⁺ and He system. The measurement was performed at a helium number density of $4.1 \cdot 10^{14} \text{ cm}^{-3}$ at a nominal temperature of 4 K. The dots represent the different types of measured ions while the solid lines show the output of the corresponding numerical simulations to fit the time evolution. In red the initial HCO⁺ is shown, in blue the He•HCO⁺ cluster ion, in green the He₂•HCO⁺, and in magenta the He₃•HCO⁺. The black data represents the overall number of ions and the cyan data is the H₂•HCO⁺ cluster ion.

For the reaction with H₂ the limitations as in the case of C₃H⁺ are still valid. The reaction is included in the simulation, but since the number density of the H₂ gas is unknown, no rate-coefficients can be derived for this reaction out of the numerical simulations. In the shown example for a time scan in figure 5.26 the maximum storage time was varied between 10 ms and 1900 ms. The helium number density was $4.1 \cdot 10^{14} \text{ cm}^{-3}$ and the nominal trap temperature was 4 K. Since the storage time is long and the increase of the cluster ions in the beginning is not very fast, measurements like this could be used to derive both the ternary rate-coefficients and the collision induced dissociation rate-coefficients. The measurements were performed at different helium number densities between $1.5 \cdot 10^{13} \text{ cm}^{-3}$, and $6.8 \cdot 10^{14} \text{ cm}^{-3}$, and at different nominal temperatures between 4 K, and 12 K. The results for the dependency on the helium number

density of the ternary rate-coefficients is shown in figure 5.27(a). In figure 5.27(b) the corresponding binary rates are plotted as a function of the helium number density. The results for the temperature dependence of the ternary rate-coefficient and of the collision induced dissociation rate-coefficient are shown in figures 5.28(a) and 5.28(b).

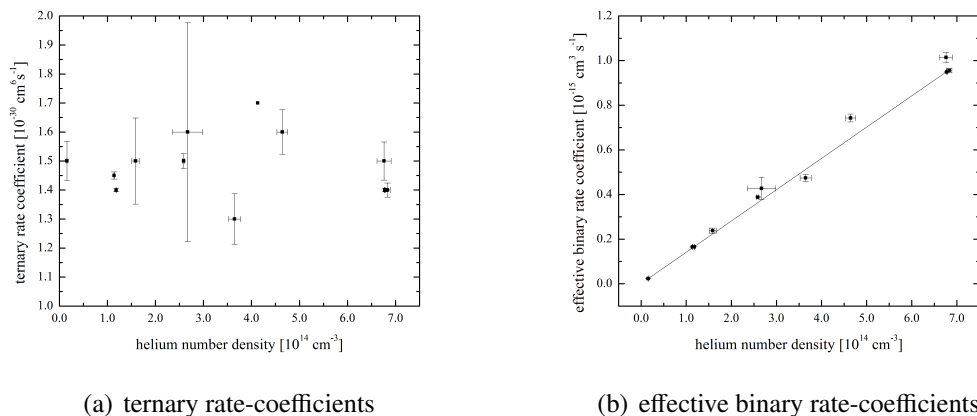


Figure 5.27: Dependence of the helium-cluster formation rate-coefficient on the helium number density. All measurements were performed at 4 K. (a) shows the dependence of the fitted ternary rate-coefficient k_{01} on the helium number density. (b) shows the corresponding effective binary rates for the same measurements.

Figure 5.27(a) reveals that within the error bars no dependence of the ternary rate-coefficient on the helium number density is visible. In figure 5.27(b) the corresponding effective binary rate-coefficients are plotted. These rate-coefficients are calculated from the ternary rate-coefficients by multiplying the values with the helium number density. The solid line shown in the figure is a linear fit to the data and the slope of the linear function is $(1.40 \pm 0.01) \cdot 10^{-30} \text{ cm}^6 \text{ s}^{-1}$, which corresponds to the ternary rate. This value is in a good agreement with the derived values from the numerical simulations shown in figure 5.27(a). The intercept of the linear fit is $(1.2 \pm 1.6) \cdot 10^{-18} \text{ cm}^3 \text{ s}^{-1}$. According to the theory for the three-body ion-molecule reactions discussed in chapter 5.2.1 this value is equal to the radiative rate-coefficient. In this case the value is approximately a factor of 100 smaller than the effective binary rate-coefficient. Therefore, the influence of the radiative processes can be neglected for this system.

In the investigated temperature range from 4 K to 12 K there is no dependency of the ternary rate-coefficient k_{01} on the trap temperature visible. The binary collision induced dissociation rate-coefficient changes in the same temperature range approximately by a factor of two. As discussed for CD^+ in section 5.2.2 the exact calculation of the helium number density for 4 K is difficult due to freeze-out effects of the helium in the trap. Summaries of the obtained values for the ternary rate-coefficients and the collision induced dissociation rate-coefficients at the different temperatures are given in tables 5.23 and 5.24.

The collision induced dissociation rate-coefficient can now again be used to estimate the binding energy of the helium atom in the cluster ion. For this estimation the same approach is used as for CD^+ (see 5.2.2). The first step is to determine the temperature

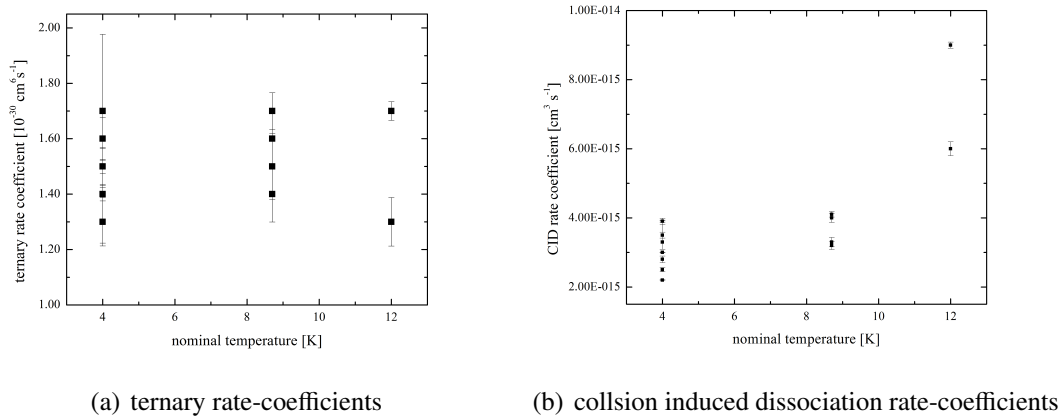


Figure 5.28: Temperature dependence of the ternary rate-coefficient and the collision induced dissociation rate-coefficient for HCO^+ . The figure shows the measured temperature dependence for (a) the ternary rate-coefficients and (b) for the collision induced dissociation rate-coefficients. The nominal trap temperature was varied between 4 K and 12 K.

Table 5.23: Overview of the obtained ternary rate-coefficients for different temperatures for HCO^+ from the numerical simulations. The rate-coefficients are given in $\text{cm}^6 \text{ s}^{-1}$. The values for the nominal temperatures of 4 K, and 8.7 K are averaged values, and therefore the errors are standard deviation errors. For 12 K only one measurement was performed and the errors are the uncertainties from the fit. At 12 K the cluster ion with three helium atoms was not observable.

T [K]	k_{01}	k_{12}	k_{23}
4	$(1.54 \pm 0.09) \cdot 10^{-30}$	$(2.9 \pm 0.2) \cdot 10^{-30}$	$(5.7 \pm 0.5) \cdot 10^{-30}$
8.7	$(1.53 \pm 0.13) \cdot 10^{-30}$	$(3.4 \pm 0.2) \cdot 10^{-30}$	$(7.5 \pm 1.9) \cdot 10^{-30}$
12	$(1.7 \pm 0.2) \cdot 10^{-30}$	$(3.3 \pm 0.3) \cdot 10^{-30}$	—

of the HCO^+ ions. At a nominal trap temperature of 4 K for example we recorded the rotational transition shown in figure 5.29.

By fitting the line with a Gaussian (black line in figure 5.29) two interesting facts turned out. First the signal strength is clearly weaker than for CD^+ . Possible reasons for this are discussed in section 5.4.3.1. Second the value for the FWHM is 1.2 MHz, which is very broad. By using this value the corresponding Doppler temperature is in the order of several thousand Kelvin, which is an unrealistic high value. Hence, one can use again a Voigt profile as for CD^+ (see section 5.1.4) to describe the observed line width. For the calculation the estimated power of $\sim 1 \cdot 10^{-5} \text{ W}$ is used together with an assumed ion temperature of $(15 \pm 2) \text{ K}$ to calculate the corresponding line width, which is $\sim 0.7 \text{ MHz}$. This value is close to the observed line width of 1.2 MHz, so the assumed values seem to be reasonable. For the simulation the Voigt profile is evaluated at the transition frequency.

The assumed ion temperature of $(15 \pm 2) \text{ K}$ at a nominal trap temperature of 4 K is slightly higher as for CD^+ . For the helium in the trap a temperature of 4 K (equal to the nominal trap temperature) is assumed. With these values the translational temperature T for this system is

$$T = (5.3 \pm 0.3) \text{ K}$$

Table 5.24: Overview of the obtained collision induced dissociation rate-coefficients for different temperatures for HCO^+ from the numerical simulations. The rate-coefficients are given in cm^3s^{-1} . The values for the nominal temperatures of 4 K, and 8.7 K are averaged values, and therefore the errors are standard deviation. For 12 K only one measurement was performed and the errors are the uncertainties from the fit. At 12 K the cluster ion with three helium atoms was not observable.

T [K]	k_{10}	k_{21}	k_{32}
4	$(3.3 \pm 0.6) \cdot 10^{-15}$	$(8.1 \pm 1.3) \cdot 10^{-15}$	$(1.3 \pm 0.2) \cdot 10^{-15}$
8.7	$(3.5 \pm 0.4) \cdot 10^{-15}$	$(2.1 \pm 0.3) \cdot 10^{-14}$	$(4 \pm 2) \cdot 10^{-14}$
12	$(9.0 \pm 0.6) \cdot 10^{-15}$	$(2.3 \pm 0.3) \cdot 10^{-14}$	—

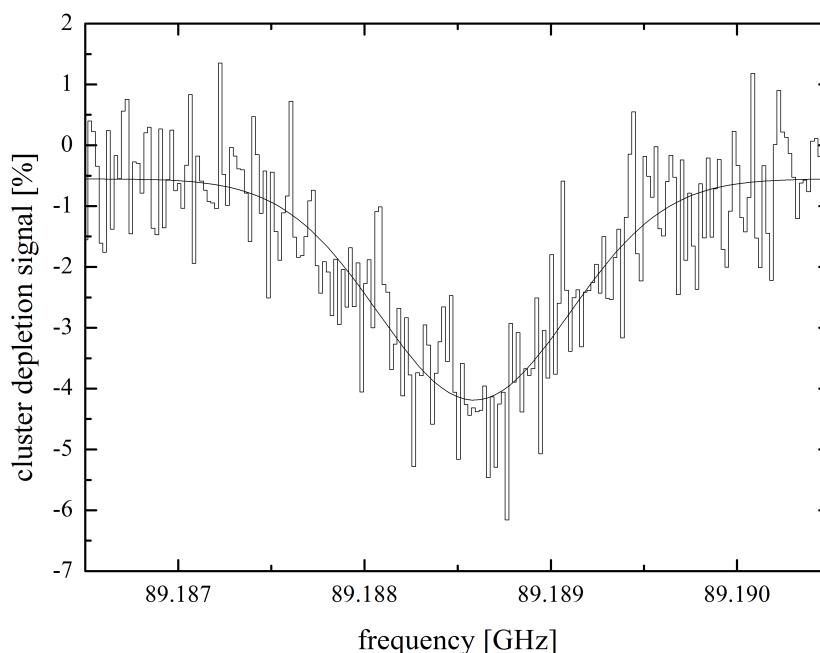


Figure 5.29: Cluster depletion signal of HCO^+ . The figure shows the recorded $J=1 \leftarrow 0$ rotational transition measured with the cluster depletion method. The black histogram shows the signal for 15 iterations. The nominal temperature during the measurement was 4 K and the helium number density was $2.5 \cdot 10^{14} \text{ cm}^{-3}$. In comparison to the observed signals for the CD^+ (see figure 5.7) the signal is weaker. An explanation for this fact is given in section 5.4.3.1.

The averaged collision induced dissociation rate-coefficient for the nominal temperature of 4 K is $(3.3 \pm 0.6) \cdot 10^{-15} \text{ cm}^3\text{s}^{-1}$. With these values the binding energy T_D can be estimated with equation 5.34 to:

$$T_D = (63 \pm 19) \text{ K}$$

for HCO^+ , assuming a Langevin rate-coefficient of $k_L = 4.43 \cdot 10^{-10} \text{ cm}^3 \text{ s}^{-1}$. This value is in the same range as the calculated values for CD^+ and therefore the dissociation energy is again small compared to the values for other molecular ions. Meuwly for example stated that the binding energy D_0 for $\text{He} \bullet \text{HCO}^+$ is $\sim 244 \text{ K}$ for the vibrational ground state ([60]), which is a factor 4 larger than our value. Our calculated value is

limited on the one hand by the estimated value for the temperature of the HCO⁺ ions and on the other hand by the very simple model, which is used to calculate the binding energy.

5.4.3.1 Estimation of the Ratio $a = \frac{k_3(1)}{k_3(0)}$ for HCO⁺

The estimation of the ratio a for HCO⁺ is more difficult than for CD⁺, because not as much data is available due to limited time for the measurements and due to technical reasons. For example for HCO⁺ no power dependency measurements were performed. Therefore, a fitting procedure as described in the first part of section 5.3.3.5 is not possible. Nevertheless, by estimating a maximum value for the observed cluster depletion signal based on the different measurements at different helium number densities, it is possible to use the second method presented in the previous section to derive a rough value for a . In table 5.26 the values used in the simulations for HCO⁺ are summarized and in table 5.25 the collisional rate-coefficients for collision of HCO⁺ and helium are given for a temperature of 10 K ([59]). Since there are only values available for 10 K and it is likely that the collisional rate-coefficients are smaller for lower temperatures (see [59]), the used values are for $k_{JJ'}$ are upper limits.

Table 5.25: Rate-coefficients $k_{JJ'}$ for rotational collisional excitation of HCO⁺ in collision with 4 He between the lowest rotational levels ($J < 3$). The rate-coefficients are given in units of cm³ molecule⁻¹ s⁻¹. The notation a(b) means $a \times 10^{-b}$. Values are taken from [59].

$k_{JJ'}$	10 K
k_{01}	2.200(10)
k_{02}	0.857(10)
k_{03}	0.143(10)
k_{12}	1.152(10)
k_{13}	0.266(10)
k_{23}	0.657(10)

Table 5.26: Parameters for the simulations - estimation of a for CD⁺

parameter	value
Einstein A ₁₀	$4.187 \cdot 10^{-5} \text{ s}^{-1}$
Einstein B ₁₀	$9.545 \cdot 10^{19} \text{ m}^3 \text{ J}^{-1} \text{ s}^{-2}$
Einstein B ₀₁	$2.863 \cdot 10^{20} \text{ m}^3 \text{ J}^{-1} \text{ s}^{-2}$
nominal temperature	4 K
collisional & internal temperature	5.3 K
storage time	600 ms
helium number density	$2.5 \cdot 10^{14} \text{ cm}^{-3}$
radiation power	max. $1 \cdot 10^{-5} \text{ W}$
ratio a	variable
rate-coefficients $k_{3_0} / k_{3_1} / k_{32}$ [cm ⁶ s ⁻¹]	$1.5 \cdot 10^{-30} / a \cdot 1.5 \cdot 10^{-30} / 2.9 \cdot 10^{-30}$
rate-coefficients $k_{\text{CID}} / k_{\text{CID}2}$ [cm ³ s ⁻¹]	$3.3 \cdot 10^{-15} / 8.1 \cdot 10^{-15}$
branching ratio p	0.5
collisional rate-coefficients	see table 5.25

From the measurements with different helium number densities a maximum cluster depletion signal of $4.8 \pm 0.2\%$ can be estimated for HCO^+ . By using the listed parameters in table 5.26 with the analytical (equation 5.72) model a value of

$$0.75 \leq a \leq 0.77 \quad (5.85)$$

for HCO^+ is obtained. The results for varying the collisional rate-coefficients for helium with HCO^+ in the numerical model are summarized in table 5.27.

Table 5.27: Calculated strength of the cluster depletion signal as a function of the different collisional rate-coefficients for HCO^+ and helium used in the simulation and different values of the ratio a between the ternary rate-coefficients of the rotational ground and first excited state. The maximum cluster depletion signal measured under these conditions was $\sim 4.8 \pm 0.2\%$. For the values used in the simulation refer to table 5.26.

value for a	$0.1 \cdot k_{\text{coll}}$	$0.2 \cdot k_{\text{coll}}$	$1 \cdot k_{\text{coll}}$	$5 \cdot k_{\text{coll}}$	$10 \cdot k_{\text{coll}}$
0.00	39.0 %	36.6 %	24.4 %	9.2 %	5.2 %
0.40	15.6 %	14.6 %	9.8 %	3.7 %	2.1 %
0.50	12.1 %	11.4 %	7.6 %	2.9 %	1.6 %
0.60	9.1 %	8.6 %	5.7 %	2.2 %	1.2 %
0.62	8.6 %	8.1 %	5.4 %	2.0 %	1.1 %
0.64	8.1 %	7.6 %	5.1 %	1.9 %	1.1 %
0.66	7.6 %	7.1 %	4.8 %	1.8 %	1.0 %
0.68	7.1 %	6.6 %	4.4 %	1.7 %	0.9 %
0.70	6.6 %	6.2 %	4.1 %	1.6 %	0.9 %
0.80	4.4 %	4.1 %	2.8 %	1.0 %	0.6 %

From the numerical simulation values between

$$0.40 \leq a \leq 0.80 \quad (5.86)$$

are calculated if one allows to vary the values for the collisional rate-coefficients with helium by a factor of 5. This relatively wide range for a matches with the calculated range for a based on the analytical model.

The estimation for the ratio between the ternary rate-coefficients of the two lowest rotational states of HCO^+ is not so exact as for CD^+ . On the one hand the reason for this is that the investigation of HCO^+ is not as detailed as for CD^+ . Thus, the used value for the maximum cluster depletion signal is not so reliable as for CD^+ . On the other hand also the used models in the case of HCO^+ are not as good as for CD^+ . The energetic distance between the rotational levels of HCO^+ is not so wide as for CD^+ . So the assumptions of a two level system for the analytical model is not as justified. The same holds for the numerical model, since one assumption in this model is that the second rotational state does not form any helium cluster ions. In the case of CD^+ these assumptions are not as critical since the numerical calculations show that the second rotational state is quasi not populated (see figure 5.21(c) and 5.21(d)), even at higher temperatures. For HCO^+ this is not the case as shown in figures 5.30(a) and 5.30(b).

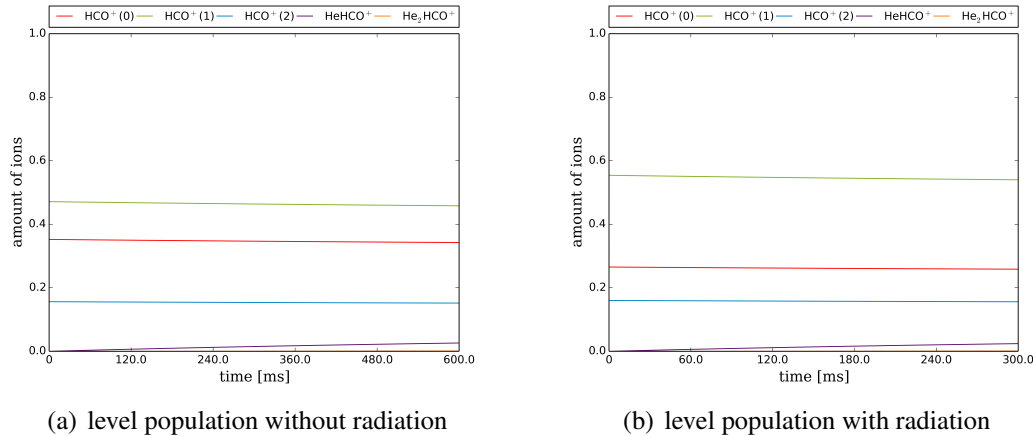


Figure 5.30: Simulated level populations for HCO^+ . The situation is different compared to CD^+ . Due to the smaller energy gap between the rotational level (only 2.975 cm^{-1} between $J=0$ and $J=1$ for HCO^+ compared to 15.123 cm^{-1} for CD^+) the higher rotational levels of HCO^+ are populated even at a nominal trap temperature of 4 K ($J=0$: 34.8 %, $J=1$: 46.7 %, and $J=2$: 15.5 %). Even without light the first rotational level is more populated than the rotational ground state. Due to this the effect of the applied radiation is reduced and this results in a smaller cluster depletion signal.

For HCO^+ the second rotational state is noticeably populated ($J=0$: 34.8 %, $J=1$: 46.7 %, $J=2$: 15.5 %) even at a nominal trap temperature of 4 K (respectively a collisional temperature of 5.3 K). This is one reason for the smaller signal that is obtained for HCO^+ compared to CD^+ , because this fact reduces the amount of ions which is influenced by the light and therefore the maximum signal is reduced. The second reason is that the first rotational level is more populated than the rotational ground state. By this the influence of the applied resonant light is reduced, because the resulting redistribution is not so pronounced. To compare the maximum signal one could switch off the collisions with helium and this would result in a maximum cluster depletion signal (for the limiting case of $a=0$) of $\sim 40 \%$ according to equation 5.59. This is less than for CD^+ and therefore it is reasonable that the observed signal HCO^+ is smaller. This value is also reproduced by the results of the numerical simulation given in table 5.27. In the left column the collisional rate-coefficients are reduced by a factor of 10. Therefore, the collisional rates are in the order of 10^3 s^{-1} , while the rates for the stimulated emission and absorption are in the order of $10^4 - 10^5 \text{ s}^{-1}$. Thus, the system is already dominated by the applied light.

One idea to improve the full numerical model for HCO^+ would be to include cluster formation for higher rotational states. If one implements this it is also necessary to record more data for higher transitions (e.g. $J=2 \leftarrow 1$) to get an idea of the different formation rates for the higher rotational states.

5.4.4 Conclusion & Discussion

It was possible to apply the new developed method for rotational spectroscopy also to HCO^+ . The well known rotational transition $J=1 \leftarrow 0$ at 89.188525 GHz could be measured. In comparison to CD^+ the cluster depletion signal is considerably weaker. According to the model there are two reasons for the smaller cluster depletion signal

of HCO^+ compared to CD^+ . One reason is that even at low temperatures the first rotational state is more populated than the rotational ground state. This reduces the effect of the applied light to the system and thereby the cluster depletion signal is reduced. The second effect is that if higher rotational states are populated the amount of ions, which are affected by the light is reduced. This effect also reduces the observable signal. An additional factor is also the value for a . From the estimations performed in this chapter the value for a is larger for HCO^+ than for CD^+ and this reduces the signal as well.

Beside the rotational transition also the kinetics of HCO^+ and helium at temperatures between 4 K and 12 K could be investigated and rate-coefficients for the ternary rates and the collision induced dissociation rate-coefficients could be determined for the first time. An overview of the results is given in tables 5.23 and 5.23, and in the figures 5.27(a) to 5.28(b).

6

Rotational Spectroscopy of C_3H^+

In this chapter the measurements of $l-C_3H^+$ with the new method, introduced in chapter 5, are presented. The measurement of the four rotational transitions of $l-C_3H^+$ differs from the previously shown measurements of CD^+ and HCO^+ in the sense, that it was the first time that the new method was used to measure unknown pure rotational transitions of an ion.

6.1 C_3H^+

6.1.1 Astronomical Interest

In general small hydrocarbons play an important role in the astrochemistry of the interstellar medium as well as in the circumstellar medium. The proposed formation routes lead to large organic molecules and result finally in the formation of polycyclic aromatic hydrocarbons (PAHs) and carbonaceous dust ([61], [62], [63]). In UV-rich environments like diffuse clouds and photodissociation regions (PDRs), small hydrocarbon molecules are important as tracers to understand the interplay between PAH formation and their photo-destruction ([64]). Small neutral hydrocarbons like C_3H_2 and C_2H are often used as probes for physical and chemical conditions in the interstellar medium ([65], [66]). The observation of reactive carbon containing cations, which are important intermediates in the carbon chemistry ([67], [68]), was limited so far to C^+ and CH^+ (for example [69], [70], [71]). The reason for these limitations were mostly a lack of accurate laboratory data for larger cations.

In 2012 Pety et al. ([2]) observed a series of unidentified rotational emission lines at millimeter-wavelengths toward the Horsehead PDR. These lines were first assigned to the carbocation $l-C_3H^+$. Since in the past no laboratory data was available for $l-C_3H^+$ the identification based on spectroscopic constants resulting from a simultaneous fit of six (and in addition of two tentatively) detected harmonically related rotational lines to a closed shell linear-rotor Hamiltonian. The derived B constant of ~ 11.245 GHz was in a good agreement with the corresponding value for $l-C_3H^+$ from previous theoretical quantum-chemical calculations ([72]). In addition to the originally observed lines, absorption features belonging to the same series of lines have been detected in

the cold, diffuse gas surrounding Sgr B2(N) ([3]), a high mass star forming region, and in diffuse clouds in the line of sight towards the same source ([4]). That the originally supposed $l-C_3H^+$ is the carrier of this line was questioned in this context by Huang et al. ([73]) on the basis of new state-of-the-art high accuracy ab initio calculations. As an alternative for $l-C_3H^+$ Fortenberry et al. supposed the $l-C_3H^-$ anion as a carrier for the lines because of a better match of the calculated spectroscopic constants, in particular D, with high-level ab initio calculations ([74]).

Nevertheless there existed observational evidences against this assignment to the quasi linear and energetically high-lying anion $l-C_3H^-$. The most valid argument was that the Horsehead PDR or the regions towards Sgr B2(N) are extremely rich in neutral and cationic species, but not any other molecular anion has been observed before in this region ([75], [76]). A similar type of argument is that in the prototypical sources for carbon chain anions like the dark cloud TMC-1 or the circumstellar envelope around the late-type star IRC+10216, none of these lines were clearly detected ([4]). Of course these arguments are not very strong since one cannot be sure if the chemistry of formation or destruction of $l-C_3H^-$ is not somewhat different to other carbon containing molecules. Hence, for a clear assignment laboratory data was needed. The first attempt to measure the astronomically observed lines in the laboratory was done by McCarthy and coworkers. They were able to reproduce a pair of the astronomical lines in a Fourier Transform Microwave Spectrometer. Their laboratory data supported the assumption that the astronomical lines belong to the cation $l-C_3H^+$, but the charge of the carrier could not definitely be determined. In this chapter, the unambiguous laboratory measurement of the pure rotational spectrum of $l-C_3H^+$ will be presented by the method of cluster depletion described in chapter 5. Afterwards, our results were confirmed by measurements of McCarthy et al. ([77]) and new theoretical calculations ([78], [79]). In 2015 also new spatially resolved observations of C_3H^+ in the Horsehead PDR were published ([80]).

6.1.2 Experimental Setup

As a precursor gas for producing the $l-C_3H^+$ ions, a mixture of allene (C_3H_4) and helium at a ratio of $\sim 1:2$ was used in the storage ion source (see 2.2). The total pressure in the ion source for these experiments was $\sim 10^{-5}$ mbar. To generate the $l-C_3H^+$ ions, an electron impact energy of 40 eV was used. The first quadrupole operated in mass selective mode. To select mass 37 u, the quadrupole was set to a DC voltage of 33.4 V and a nominal AC voltage of 130 V. The number of C_3H^+ ions stored in the 22-pole ion trap was typically around 30000 at a nominal trap temperature of 4 K together with helium at a number density of 10^{15} cm^{-3} .

For the measurement of the rotational lines, the storage time was set to 100 ms to increase the speed of the measurements, which was possible because the equilibrium was reached on a short timescale. As radiation sources two different narrow-band rubidium-clock referenced microwave synthesizers were employed. To record the two lower transitions $J=1\leftarrow 2$ (44.9 GHz) and $J=2\leftarrow 3$ (67.4 GHz) of $l-C_3H^+$ the Agilent E8257D PSG synthesizer was directly used as a radiation source, whereas for the higher transitions $J=3\leftarrow 4$ and $J=4\leftarrow 5$, a Rhode & Schwarz SMF100A synthesizer in combination with a high-power frequency tripler from Virginia Diodes Inc. (VDI AMC 375) was used to reach the frequencies of 90 GHz and 112 GHz, respectively. In both configurations the

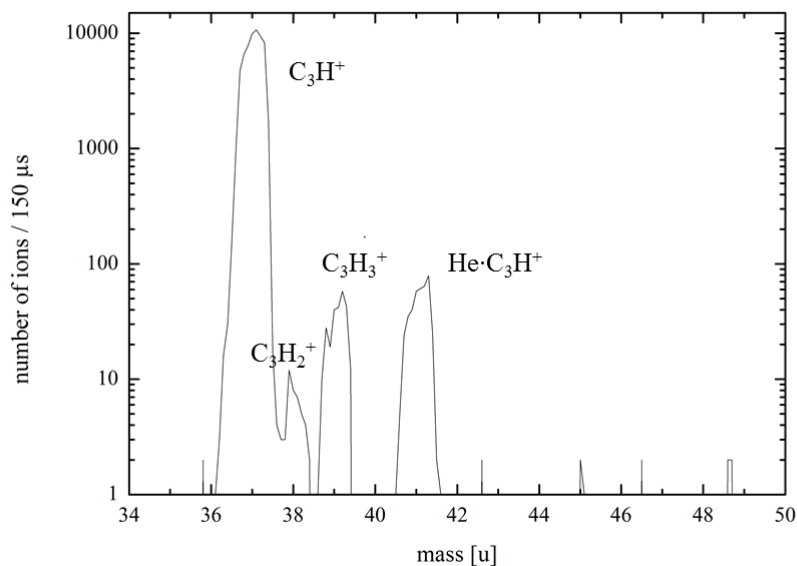


Figure 6.1: Mass scan of trapped C₃H⁺ at 4 K. The ions were stored for 600 ms in a cold helium bath. The helium number density for this measurement was $3.9 \cdot 10^{14} \text{ cm}^{-3}$. The helium attachment equilibrium ratio is in this case only $\sim 1\%$, which is much smaller than for CD⁺ (see figure 5.3).

radiation was directly coupled into the experiment via a conical horn antenna through a 0.8 mm thick CVD diamond window from Diamond Materials GmbH. Since no additional optical focussing elements were used, around 0.1 % of the initial output power of 10 mW was available in the trap region.

6.1.3 Experimental Data & Results

Prior to the recording of the rotational lines of l-C₃H⁺ by employing the new method of cluster depletion (see chapter 5.3.1), the kinetics of the C₃H⁺ and helium system was investigated. First of all it is necessary that a noticeable number of He•C₃H⁺ cluster ions are formed in the 22-pole trap under typical conditions. Figure 6.1 shows the content of the 22-pole trap extracted after a storage time of 600 ms. For this measurement, the C₃H⁺ ions were stored at 4 K together with helium at a number density of $3.9 \cdot 10^{14} \text{ cm}^{-3}$. As the mass scan shows, only $\sim 1\%$ of the C₃H⁺ ions were converted into He•C₃H⁺ cluster ions at equilibrium. In comparison to the CD⁺ and helium system previously investigated (see chapter 5.2.2), this value is rather small and generates some difficulties for the measurement of the rotational transitions of C₃H⁺. A low number of cluster ions is not favorable for a good signal to noise ratio.

The next step is to check the time evolution of the system to clarify if the used storage time is suitable for the observed system. The figures 6.3 and 6.2 show two different time scans for long and short storage times. It becomes obvious that the system is already in an equilibrium state after a relatively short storage time of ~ 100 ms. As a consequence, the storage time for the rotational measurements was set

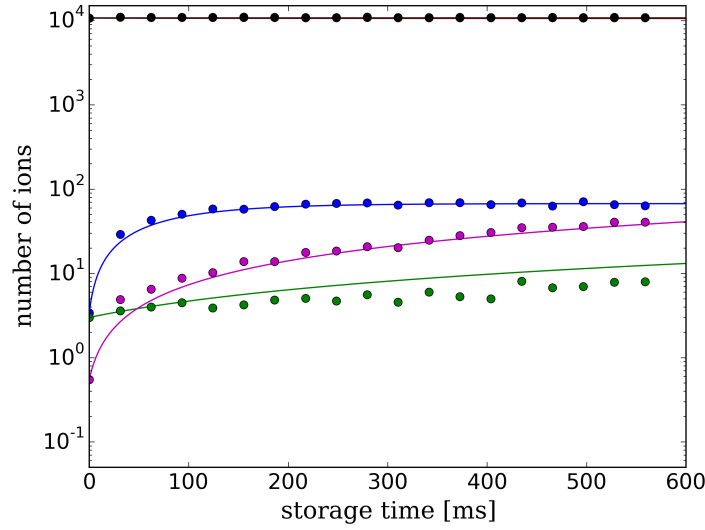
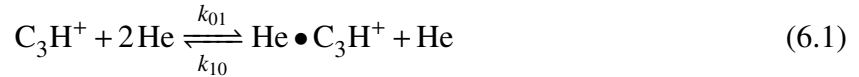


Figure 6.2: Time scan for a long storage time to determine the collision induced dissociation rate-coefficient for the C_3H^+ helium system. The dots represent the measured values for C_3H^+ (black) and $He \bullet C_3H^+$ (blue). In this measurement also the time evolution of the $C_3H_3^+$ (pink) and the $C_3H_2^+$ (green) ions were obtained. The solid lines are the results of the applied numerical simulation. The measurement was performed at a nominal trap temperature of 4 K and a helium number density of $3.9 \cdot 10^{14} \text{ cm}^{-3}$.

to 100 ms, which significantly reduced the time needed per measurement cycle. In addition, it is also interesting to obtain the ternary rate-coefficient and the collision induced dissociation rate-coefficient for this system. Since only one helium atom is observed to attach to the C_3H^+ ions, the system is quite simple to describe.



(6.2)

Besides the attachment of helium, the C_3H^+ ions can also react with residual H_2 gas that is present in the helium gas. An inspection of the recorded mass spectrum reveals that by these reactions also $C_3H_2^+$ and $C_3H_3^+$ are formed in the trap. In order to describe the kinetics of the system properly, the reactions with H_2 are included into the coupled rate equations. However, due to the unknown number density of the residual H_2 gas, it is not possible to calculate reliable values for the rate-coefficients of these reactions in our experiment. Down to a nominal temperature of 10 K the values for the rate-coefficients are known ([81]).

Since the equilibrium for the system of C_3H^+ and helium is reached after a few ten milliseconds, the time scan shown in figure 6.3 was used to determine the ternary rate-coefficient k_{01} for C_3H^+ whereas the measurement shown in figure 6.2 was used to determine the collision induced dissociation rate-coefficient k_{10} . The second measurement was also used to model the reactions with the residual H_2 gas. In both cases the nominal trap temperature was 4 K and the helium number density in the trap was in the order of $\sim 4 \cdot 10^{14} \text{ cm}^{-3}$.

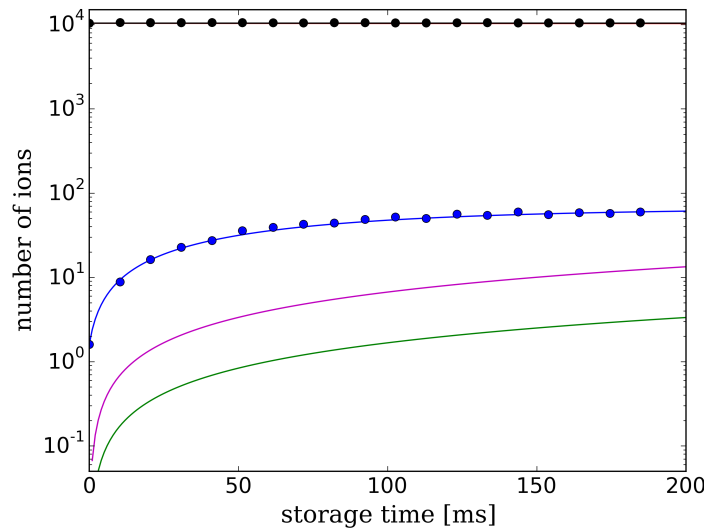


Figure 6.3: Time scan for a short storage time to determine the ternary rate-coefficient for the C₃H⁺ and helium system. The measurement was performed at nominal trap temperature of 4 K and with a helium number density of $3.9 \cdot 10^{14} \text{ cm}^{-3}$. The dots indicate the measured values for C₃H⁺ (red) and He•C₃H⁺ (blue). The solid lines are the results of the applied numerical simulation. In this case, also the C₃H₃⁺ (pink) and the C₃H₂⁺ (green) ions are included in the numerical simulation based on the values obtained from the measurement shown in figure 6.2.

The ternary association and dissociation rate-coefficients for C₃H⁺ and helium at a nominal trap temperature of 4 K are

$$k_{01} = (5.0 \pm 0.3) \cdot 10^{-31} \text{ cm}^6 \text{ s}^{-1} \quad (6.3)$$

$$k_{10} = (3.0 \pm 0.2) \cdot 10^{-14} \text{ cm}^3 \text{ s}^{-1} \quad (6.4)$$

For the measurement of the pure rotational transitions of C₃H⁺, similar experimental conditions as for the kinetic measurements were used. The temperature of the trap was 4 K and the number density was $1 \cdot 10^{15} \text{ cm}^{-3}$. It was possible to measure four pure rotational transitions of C₃H⁺ (J=2←1, J=3←2, J=4←3, J=5←4). A frequency range of 2 MHz centered on the calculated transition frequency based on the spectroscopic constants provided by Pety et al. ([2]) was used for these measurements. Since the observed signals are relatively small and the number of cluster ions is low, it was necessary to measure the signal several hundred times. The averaged signals are shown in figures 6.4(a) - 6.4(d).

To obtain the line center positions and their 1σ uncertainties, a Lorentzian line-shape function was fit to the observed transitions. It is noticeable that the lines are all homogeneously broadened, and the line widths are almost one order of magnitude larger than the corresponding Doppler line widths expected for the low trap temperatures. Referring to section 5.1.4 in the previous chapter one can use the limiting case of a Lorentzian profile (since the lines are obviously broadened) to describe the observed line width. With the estimated power of 1 mW this leads for the J=2←1 transition to an calculated FWHM of $\sim 6 \cdot 10^5 \text{ Hz}$, which is close to the observed FWHM of 4.55

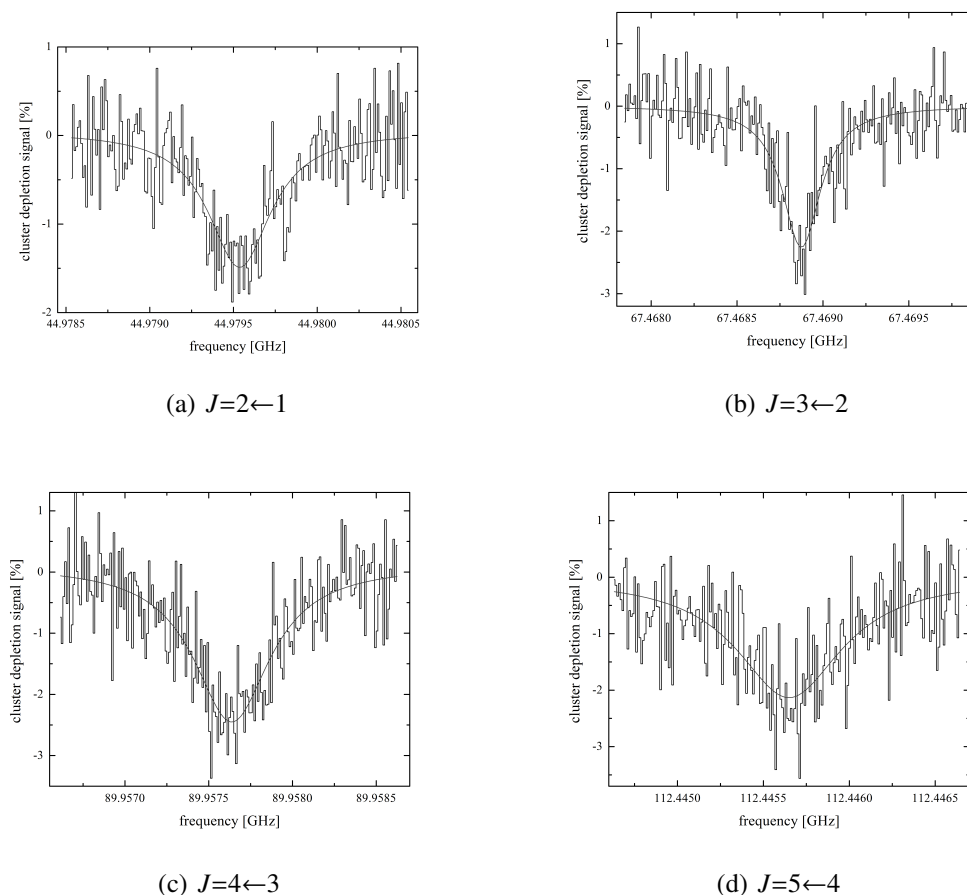


Figure 6.4: Rotational transitions of $l-C_3H^+$. The transitions were measured at 4 K, with a helium number density of $\sim 1 \cdot 10^{15} \text{ cm}^{-3}$. The black histogram shows the normalized change of $He \bullet C_3H^+$ cluster ion as a function of the excitation frequency. The signal was averaged over several hundred iterations. The solid lines are fits of a Lorentzian line-shape function to the data.

$\cdot 10^5 \text{ Hz}$. This is another indication, that the used model for the description of the line width in the model is correct. Despite the broadened lines the relative frequency accuracy of the center frequency is $3 \cdot 10^{-7}$ or better. The obtained rotational transition frequencies are summarized in table 6.1. The frequencies for the $J=1 \leftarrow 2$, $J=3 \leftarrow 4$, and $J=4 \leftarrow 5$ transitions were also observed by McGuire et al. and Pety et al. and the corresponding frequencies are in excellent agreement with the frequencies measured in our laboratory.

In order to allow for a better comparison to the astronomical data, the observed laboratory $l-C_3H^+$ transition frequencies (obtained in course of this thesis) were fit in a least-squares procedure to a linear rotor Hamiltonian ($E(J) = B \cdot J \cdot (J + 1) - D \cdot [J \cdot (J + 1)]^2 + H \cdot [J \cdot (J + 1)]^3$, with J the quantum number of the rotational level) using the spfit/spcat program routines by Pickett ([82]). Two different fits were performed, where the first one (I in table 6.2) only includes the four transition frequencies. The fit reproduces the experimental transition frequencies to an rms value of 0.011 MHz, and the resulting rotational constant B as well as the centrifugal distortion constant D are in excellent agreement with the values obtained from the astronomical lines, taking into account the uncertainty of the source velocity. Since only low J tran-

Table 6.1: Measured rotational transition frequencies of l-C₃H⁺

Transition	Frequency [GHz]	o-c [kHz]
J = 1-2	44.979536(14)	-18
J = 2-3	67.4688744(85)	4
J = 3-4	89.957637(13)	4
J = 4-5	112.445649(20)	-8

Table 6.2: Spectroscopic constants l-C₃H⁺. The values for the spectroscopic constants are given in MHz. Fit I is based only on the four measured rotational lines. Fit II includes the sextic order distortion constant derived from astronomical observations by McGuire et al. The value was kept fixed in the fit. The standard deviation of the last digits is given in parentheses.

Constant	Fit I	Fit II
B	11244.95000(216)	11244.95030(216)
D · 10 ³	7.685(69)	7.709(69)
H · 10 ⁶	—	[0.49]
rms	0.011	0.011

sitions were measured, it is not possible to calculate the sextic centrifugal distortion constant H. Therefore a second fit (II in figure 6.2) was performed, which includes the value obtained from astronomical data by McGuire et al. as a fixed constant.

6.1.4 Discussion & Conclusion

The spectra presented in this chapter were taken from only several thousand mass- and charge-selected ions. By using the first quadrupole as a mass filter tuned to the mass of 37 u, the only possible contamination of the stored C₃H⁺ ions are traces of ¹³C substituted C₃⁺ ions. Their relative abundance compared to the C₃H⁺ ions should be less than 0.5% estimated from the amount of unsubstituted C₃⁺ produced in the storage ion source. The presence of the cyclic isomer c-C₃H⁺ is even less likely. This isomer lies 220 kJ mol⁻¹ higher in energy than the linear C₃H⁺, and it was demonstrated by Savić et al. that the formation of c-C₃H⁺ is efficiently quenched under the typical conditions in the trap ([83]). Even if a few c-C₃H⁺ were present in the trap, their transition frequencies would be very different from the ones for l-C₃H⁺, and it is questionable that they would be observable. The same holds for the rotational transition frequencies of the cluster ion He•C₃H⁺. They will be very different from the ones for C₃H⁺. Therefore, the presented transition frequencies in this chapter belong unambiguously to the l-C₃H⁺ cation. These measurements demonstrate also that it is possible to measure new transitions with the method of cluster depletion (see chapter 5), as long as the line position is approximately known. Due to these measurements it is also evident that the observed lines by Pety et al. ([2]) and McGuire et al. ([3] and [4]) belong to the l-C₃H⁺ cation.

The observed strength of the cluster depletion signals for C₃H⁺ (for every transition of the order of 2%) is clearly smaller than the signal for CD⁺. Anyhow, the fact that there is an observable signal for the higher transitions means of course that the model described in section 5.3.1 is too simple and it has to be extended to more

rotational levels. For the short discussion here effects as collisions with helium will be neglected and it is assumed that the applied power is high enough to completely pump the system, and also all other rotational states are ignored. If one now inspects the rotational transition $J=2-3$ at an assumed collisional temperature of 5 K one can use the model to check if the expected signal for C_3H^+ is smaller than for CD^+ . For this, first the populations of the two involved rotational states have to be calculated. The populations are $J=0$: 10.5 %, $J=1$: 25.4 %, $J=2$: 27.5 %, $J=3$: 20.2 %, $J=4$: 10.8 %, $J=5$: 4.2 %, and $J=6$: 1.2 %. Since one assumes that the system is completely pumped by the applied radiation the level distribution with light is $J=2$: 19.8 % and $J=3$: 27.8 %. This change in the populations is relatively small in comparison to the CD^+ system and by using equation 5.59 from section 5.3.1 the maximum achievable cluster depletion signal for C_3H^+ would be 27.7 %, which is less than the maximum calculated signal for CD^+ . This signal is of course an upper limit, since it is assumed that no cluster ions are formed from all other rotational levels, which is of course not true. So based on this short estimation it is reasonable that the observed signal for C_3H^+ is smaller than for CD^+ .

Conclusion & Outlook

Pure rotational transitions of three different molecular ions (CD^+ , HCO^+ , C_3H^+) have been recorded in a cold 22-pole ion trap instrument in this work. The spectra were recorded with a newly developed technique, which is a subtype of the proven Laser Induced Reactions (LIR) action spectroscopy method. The new method is based on state-selective attachment of helium atoms to stored molecular ions. The development has been made possible by the completion of the new cryogenic ion trap apparatus FELion during this work that was used for these measurements. The FELion experiment itself is described and characterized in the first part of this work.

For the new experimental scheme a simple kinetic description was developed and implemented in an analytical and a numerical model. The two models were used to explain the results obtained under various experimental conditions. For this part mainly the system of CD^+ and helium was used. The second test case for the model was the system of HCO^+ and helium. The experimental finding that the observable signal in the respective rotational ground state transition for HCO^+ is much smaller than for CD^+ could be explained by the model on a basic level. These two ions were chosen for testing the model since the measured transitions were well known.

In the case of the third ion, C_3H^+ , this was not the case. For C_3H^+ it was possible to record four low-lying rotational transitions with the new method. These measurements were used to assign so far not identified astronomically observed rotational lines. The example of C_3H^+ also demonstrates that the new technique allows to record so far unknown rotational transitions if reliable predictions for the transition frequencies are available. The new technique has some advantages compared to absorption experiments with ions in discharge cells. One big advantage is that the new method is mass-selective and the ions are internally cold, which is especially helpful if one wants to record low-lying rotational lines. Another benefit is that only a few thousand ions are needed to record a spectrum.

Based on the simulations and the experimental results for the different ions one can list some conditions which should be fulfilled to apply the new method to so far unknown transitions of an ion. One disadvantage of the method is that the observed signals are often small ($\sim 5\%$ for HCO^+ and below 3% for C_3H^+). Due to this long integration

times are needed before a significant signal to noise ratio can be achieved. Thus, good predictions for the rotational transition are needed in order to reduce the frequency range that has to be scanned. To obtain a good signal to noise ratio it is also favorable if the absolute number of cluster ions is large. In other words the formation of cluster ions is the basic requirement for the new method. As a first step, therefore, the helium attachment and dissociative kinetics has to be investigated in order to verify that a sufficient number of cluster ions are formed. Since it is assumed in the model that the formation of cluster ions is a ternary process in contrast to the binary dissociation of the cluster ion it is helpful to increase the helium number density in the trap to increase the number of cluster ions. There are two limitations for this approach. On the one hand the helium number density is limited due to technical issues and on the other hand it was shown in chapter 5 that the observed line signal decreases with an increasing helium number density due to competing collisional de-excitation.

According to the model the second important factor determining the strength of the signal is the relative population of the involved rotational states. For example for the strong $J=1\leftarrow 0$ transition of CD^+ the population at low temperatures is favorable, since the $J=1$ state is more or less not populated (only 6.2 % compared to 93.8 % in the rotational ground state at a temperature of 5.7 K). Due to this the redistribution effect achieved by the resonant excitation is large and this results in a strong signal. For C_3H^+ in contrast the achievable relative redistribution of the rotational states is less pronounced and this is one reason for the lower signal strength in the model. Another factor which reduces the signal strength is connected to this. If one assumes that a lot of rotational states are populated (which will be the case even at temperatures below 10 K if the splitting between the rotational energies is only of the order of a few cm^{-1} , like for C_3H^+) one always gets a reservoir of ions which are not influenced by resonant excitation of one specific transition (for CD^+ 100 % of the ions are in the two levels which are influenced). This effect also reduces the observable signal. Hence, according to the model it will be more difficult to observe a signal with this method for more complex ions, which have a higher density of states. To a certain extend this effect can be reduced by cooling down the ions, but nevertheless this is a limiting factor. On the other hand the low temperatures needed for the technique can also be a problem for the measurement of higher J transitions, since these states are not sufficiently populated. The strength of the modeled signal also depends on the stimulated absorption and emission rates. These rates have at least to be of the same order as the collisional de-excitation rates for collisions with helium. Due to this it is necessary that the used radiation source provides a sufficient power level. If the corresponding Einstein-coefficients for the transition and the collisional rate-coefficients for the collisions with helium are known, one can calculate the different rates for the system in advance and if the collisional rates are significantly larger than the reachable stimulated rates it is unlikely that one can observe a signal for this transition.

Besides these (maybe) assessable factors there are of course factors influencing the line signal that are not predictable at the moment. One of these factors is the ratio of the ternary rate-coefficients of the involved rotational states. At the moment there is no possibility to estimate this ratio in advance. Due to this it is possible that one could not observe a signal for a transition, although all factors discussed above are fulfilled. One example for this is the CO^+ ion. The CO^+ measurements, which were performed with the new method, but were not shown in this work, reveal an interesting finding.

CO^+ has a $^2\Sigma^+$ electronic ground state leading to a splitting of each rotational level N into a doublet ($J=N \pm 1/2$). The two lowest transitions are the $N_J = 0_{1/2} \leftarrow 1_{1/2}$ transition at 117.692360 GHz and the $N_J = 0_{1/2} \leftarrow 1_{3/2}$ transition at 118.101812 GHz. The $N_J = 0_{1/2} \leftarrow 1_{1/2}$ transition could not be observed under optimal conditions down to a relative signal of 0.05 % (rms), while for the $N_J = 0_{1/2} \leftarrow 1_{3/2}$ transition a clear signal (maximum strength ~ 10 %) was observed. This difference cannot be explained by the expected only slightly different transition rates. This shows on the one hand that even if the conditions are favorable it is possible that one cannot observe a signal. On the other hand it shows that the used model is too simple since no mechanism is included in the model that considers effects like this. So one conclusion from this example is that it is necessary to understand the reasons for the state selective-helium attachment if one wants to make reliable predictions for the observable signal. The example of CO^+ is a strong hint that it is not possible to explain this effect by a kinetic approach but one has to use a quantum mechanical concept, since for these two transitions of CO^+ the energy added to the system and the excitation rates are comparable for both transitions. Therefore, the vanishing of the signal for the $N_J = 0_{1/2} \leftarrow 1_{1/2}$ transition has to be explained by the quantum behavior of the $\text{He}\bullet\text{CO}^+$ complex formation process.

Part III

Appendix

8

Appendix - Design FELion

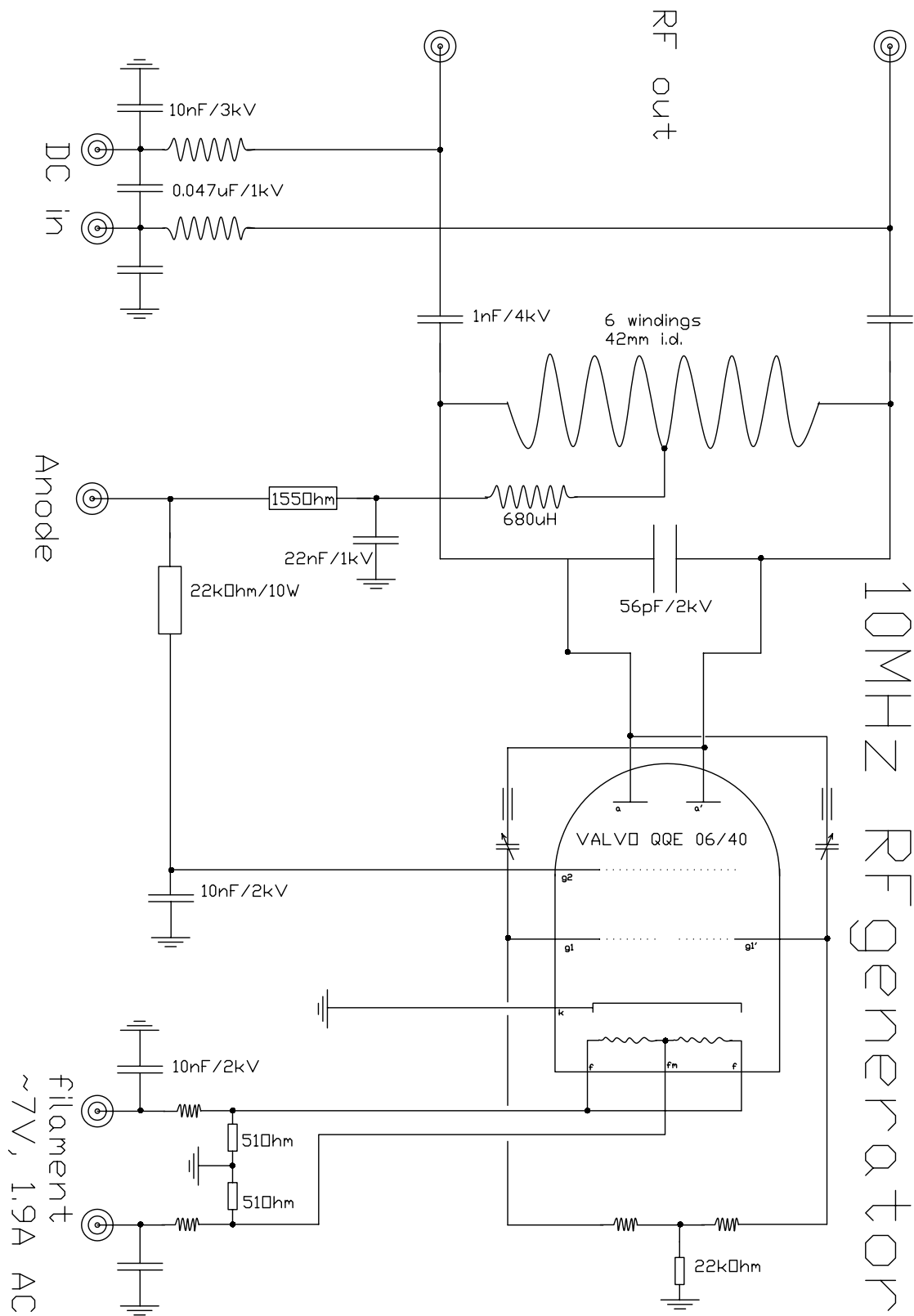


Figure 8.1: Circuit diagram of the 10 MHz RF-generator for the Storage Ion Source.

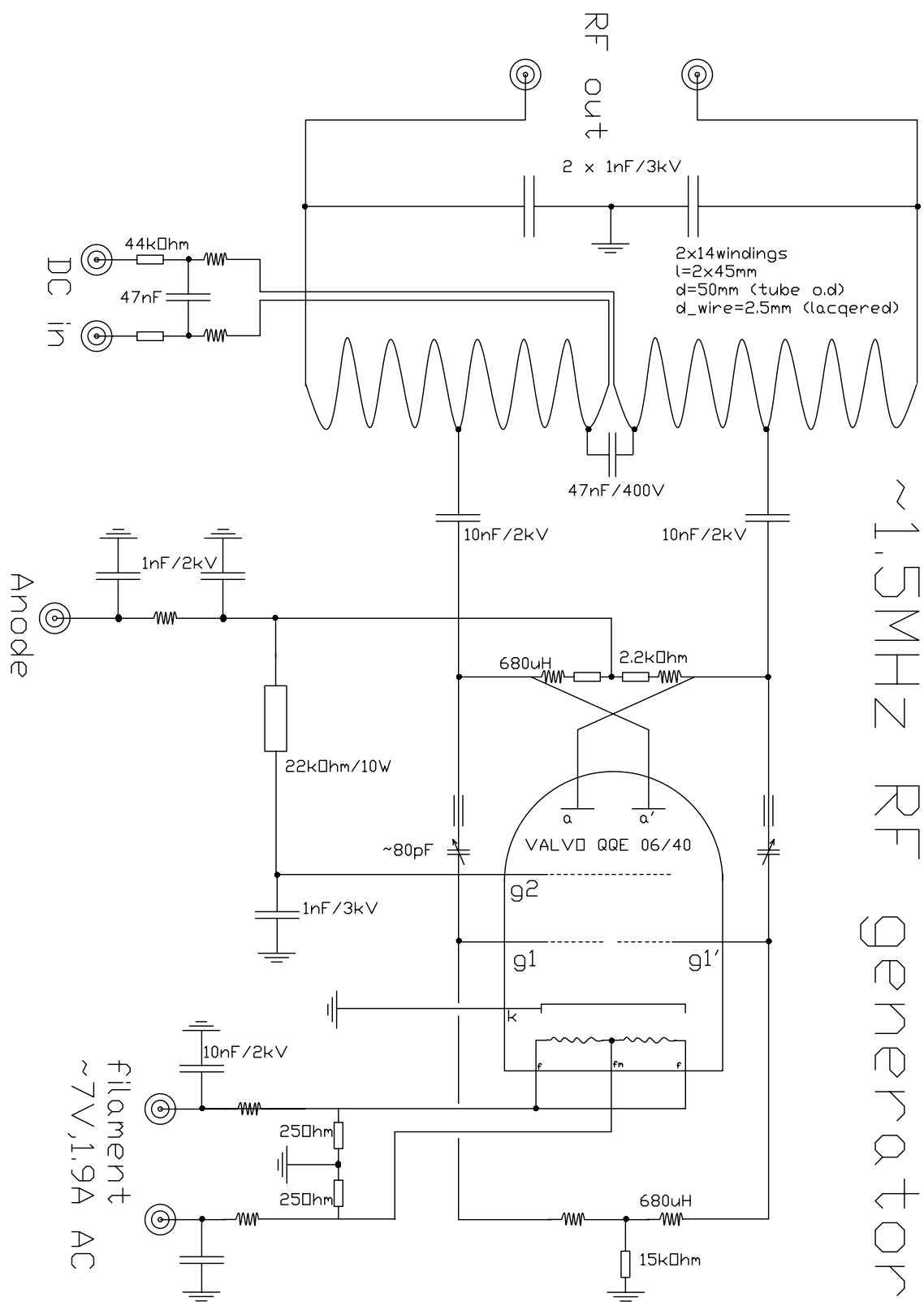


Figure 8.2: Circuit diagram of the 1.5 MHz RF-generator for the first quadrupole mass filter.

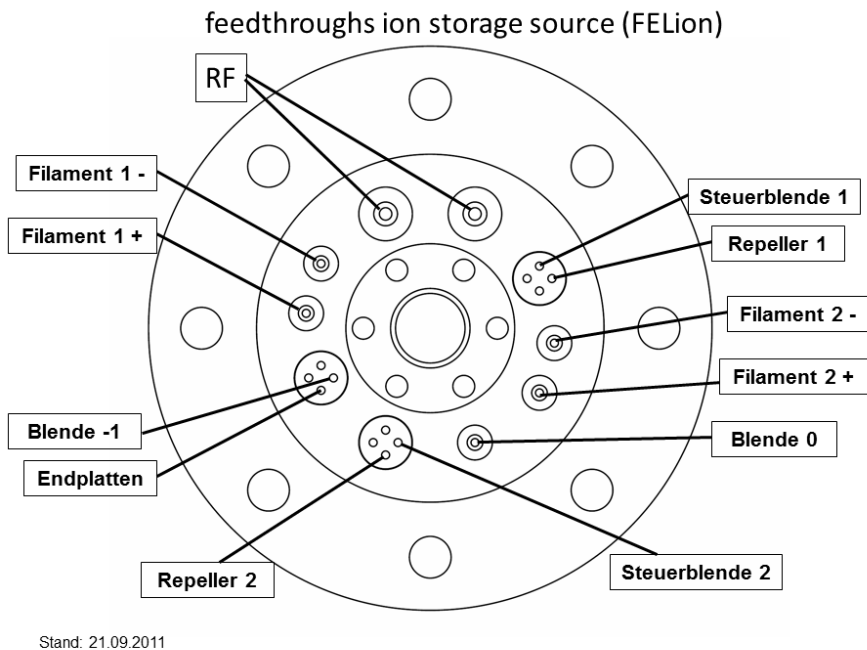


Figure 8.3: Technical drawing of the feedthrough-flange for the SIS. Top view on the layout of the feedthroughs for the Storage Ion Source from outside. All voltages with the same number belong to the same filament, e.g. Filament 1+, Filament 1-, Steuerblende 1, and Repeller 1.

Source-Connection-Box

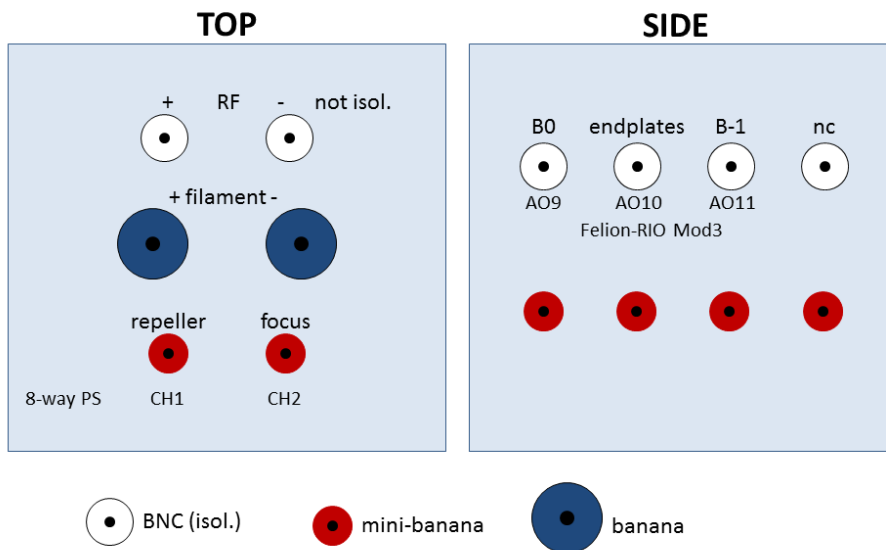


Figure 8.4: Schematic of the Connection Box for the Storage Ion Source.

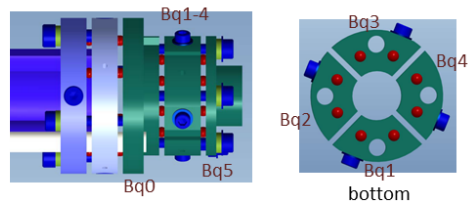
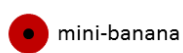
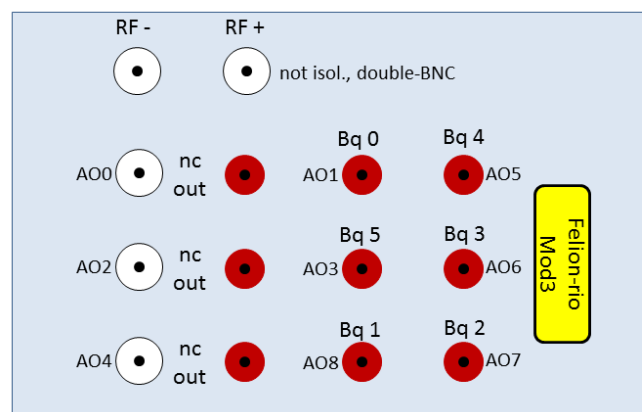


Figure 8.5: 3D-view of the Einzel-lense of the first quadrupole with designations

Quad I Connection Box

SIDE



D-sub 9pol

Figure 8.6: Schematic of the Connection Box for the first quadrupole.

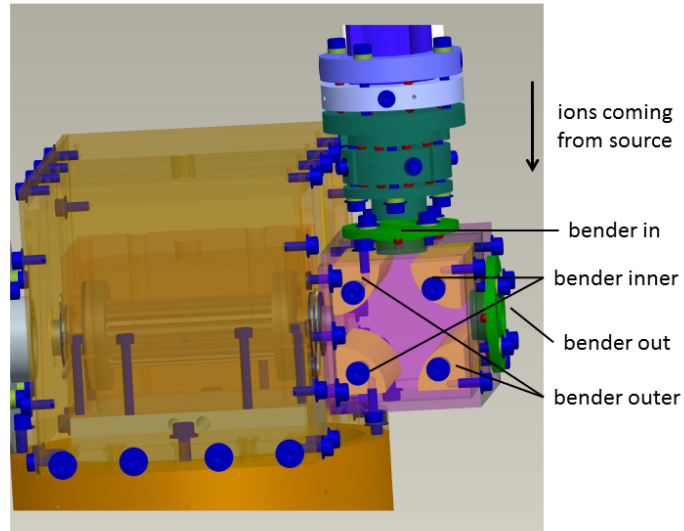


Figure 8.7: Designation of the bender-parts.

feedthroughs 22-pole FELION

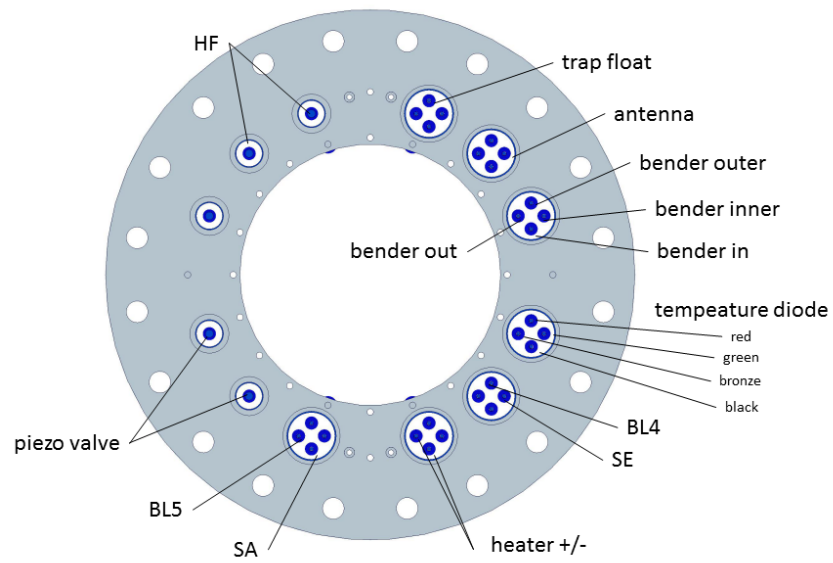


Figure 8.8: Technical drawing of the feedthrough-flange for the 22-pole trap.

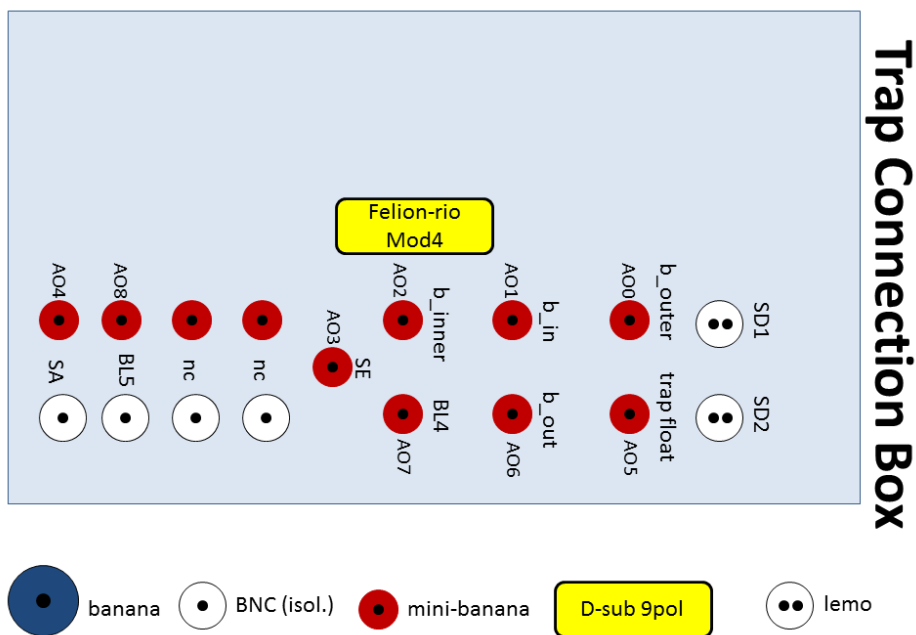


Figure 8.9: Schematic of the Connection Box for the 22-pole trap.

Trap Connection Box

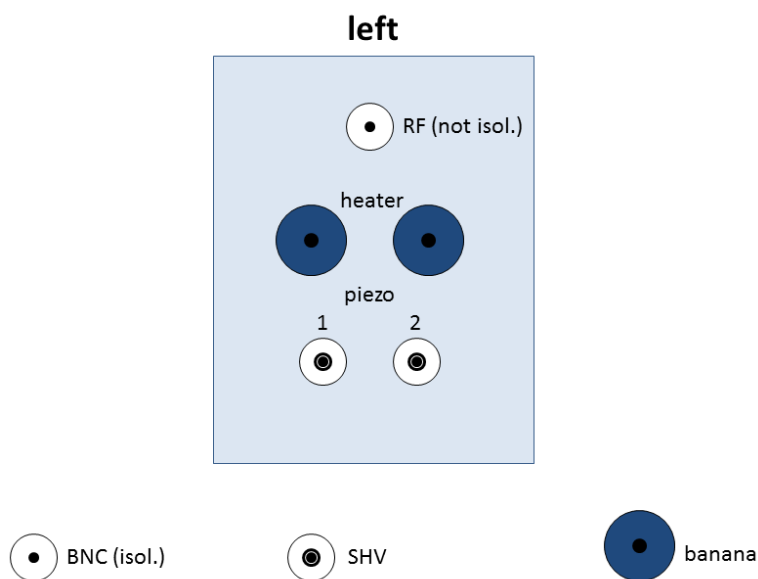


Figure 8.10: Schematic of the Connection Box for the 22-pole trap.

Bibliography

- [1] S. Brünken, L. Kluge, A. Stoffels, O. Asvany, and S. Schlemmer. Laboratory Rotational Spectrum of $l\text{-C}_3\text{H}^+$ and Confirmation of its Astronomical Detection. *ApJL*, 783:L4, 2014.
- [2] J. Pety, P. Gratier, V. Guzmán, et al. The IRAM-30 m line survey of the Horsehead PDR. *Astron. Astrophys.*, 548:A68, 2012.
- [3] B. A. McGuire, P. B. Carroll, R. A. Loomis, et al. A Search for $l\text{-C}_3\text{H}^+$ and $l\text{-C}_3\text{H}$ in Sgr B2(N), Sgr B2(OH), and the Dark Cloud TMC-1. *The Astrophysical Journal*, 774:56, 2013.
- [4] B. A. McGuire, P. B. Carroll, P. Gratier, et al. An Observational Investigation of the Identity of B11244 ($l\text{-C}_3\text{H}^+/\text{C}_3\text{H}^-$). *The Astrophysical Journal*, 783:36, 2014.
- [5] W. Paul, O. Osberghaus, and E. Fischer. Ein Ionenkäfig. *Forsch.Berichte des Wirtschaftsministeriums Nordrhein-Westfalen*, Nr.415:1–42, 1955.
- [6] E. Fischer. Die dreidimensionale Stabilisierung von Ladungsträgern in einem Vierpolfeld. *Zeitschrift für Physik*, 156:1–26, 1959.
- [7] W. Neuhauser, M. Hohenstatt, P. E. Toschek, and H. Dehmelt. Localized visible Ba^+ mono-ion oscillator. *Phys. Rev. A*, 22:1137–1140, 1980.
- [8] D. J. Wineland, J. C. Bergquist, W. M. Itano, J. J. Bollinger, and C. H. Manney. Atomic-Ion Coulomb Clusters in an Ion Trap. *Phys. Rev. Lett.*, 59:2935–2938, 1987.
- [9] T. Rosenband, D. B. Hume, P. O. Schmidt, et al. Frequency Ratio of Al^+ and Hg^+ Single-Ion Optical Clocks; Metrology at the 17th Decimal Place. *Science*, 319:1808–1812, 2008.
- [10] J. Harju, M. Juvela, S. Schlemmer, et al. Detection of 6 K gas in Ophiuchus D. *Astron. Astrophys.*, 482:535–539, 2008.
- [11] D. Gerlich. Inhomogeneous RF fields: A versatile Tool for the Study of processes with Slow Ions. In C.-Y. Ng and M. Baer, editors, *Adv. Chem. Phys.: State-Selected and State-to-State Ion-Molecule Reaction Dynamics*, volume LXXXII, pages 1–176. Wiley, New York, 1992.

- [12] D. Gerlich. Ion-Neutral Collisions in a 22-pole trap at very low energies. *Phys. Scr.*, T59:256–263, 1995.
- [13] O. Asvany, F. Biela, D. Moratschke, J. Krause, and S. Schlemmer. New design of a cryogenic linear RF multipole trap. *Rev. Sci. Instr.*, 81:076102, 2010.
- [14] D. Gerlich and S. Horning. Experimental Investigations of Radiative Association Processes as Related to Interstellar Chemistry. *Chem. Rev.*, 92:1509–1539, 1992.
- [15] D. Gerlich and S. Schlemmer. Deuterium fractionation in gas-phase reactions measured in the laboratory. *Planet. Space Sci.*, 50:1287–1297, 2002.
- [16] W. Paul, B. Lücke, S. Schlemmer, and D. Gerlich. On the dynamics of the reaction of positive hydrogen cluster ions (H_5^+ to H_{23}^+) with para and normal hydrogen at 10K. *J. Mass Spectrom. Ion Processes*, 150:373–387, 1995.
- [17] W. Paul, S. Schlemmer, B. Lücke, and D. Gerlich. Deuteration of positive hydrogen cluster ions H_5^+ to H_{17}^+ at 10 K. *Chem. Phys.*, 209:265–274, 1996.
- [18] O. V. Boyarkin, S. R. Mercier, A. Kamariotis, and T. R. Rizzo. Electronic Spectroscopy of Cold, Protonated Tryptophan and Tyrosine. *J. Am. Chem. Soc.*, 128:2816–2817, 2006.
- [19] J. Grzetic and J. Oomens. Spectroscopic Evidence for an Oxazolone Structure in Anionic b-Type Peptide Fragments. *J. Am. Soc. Mass Spectrom.*, 23:290–300, 2012.
- [20] E. T. White, J. Tang, and T. Oka. CH_5^+ : The Infrared Spectrum Observed. *Science*, 284:135–137, 1999.
- [21] O. Asvany, P. Padma Kumar, B. Redlich, et al. Understanding the Infrared Spectrum of Bare CH_5^+ . *Science*, 309:1219–1222, 2005.
- [22] O. Asvany, K. M. T. Yamada, S. Brünken, A. Potapov, and S. Schlemmer. Experimental ground-state combination differences of CH_5^+ . *Science*, 347:1346–1349, 2015.
- [23] P. Jusko, O. Asvany, A.-C. Wallerstein, S. Brünken, and S. Schlemmer. Two-Photon Rotational Action Spectroscopy of Cold OH^- at 1 ppb Accuracy. *Phys. Rev. Lett.*, 112:253005, 2014.
- [24] R. M. Jones, D. Gerlich, and S. L. Anderson. Simple radio-frequency power source for ion guides and ion traps. *Review of Scientific Instruments*, 68:3357–3362, 1997.
- [25] R. M. Jones and S. L. Anderson. Simplified radio-frequency generator for driving ion guides, traps, and other capacitive loads. *Review of Scientific Instruments*, 71:4335–4337, 2000.
- [26] P. H. Dawson. *Quadrupole Mass Spectrometry and Its Applications*. AIP Press, Woodbury, New York, 1995.

- [27] picture taken from <http://www.pfeiffer-vacuum.com/know-how/mass-spectrometers-and-residual-gas-analysis/introduction-operating-principle/quadrupole-mass-spectrometers-qms/technology.action?chapter=tec4.1.2>.
- [28] H. D. Zeman. Deflection of an ion beam in the twodimensional electrostatic quadrupole field. *Rev. Sci. Instrum.*, 48:1079–1085, 1977.
- [29] P. R. Mahaffy and K. Lai. An electrostatic quadrupole deflector for mass spectrometer applications. *J. Vac. Sci. Technol. A*, 8:3244–3246, 1990.
- [30] L. A. Kluge. Protonen Transfer zwischen H_2 und O_2 - Speicherexperimente bei tiefen Temperaturen. Diploma thesis, University of Cologne, 2011.
- [31] N. R. Daly. Scintillation Type Mass Spectrometer Ion Detector. *Rev. Sci. Instrum.*, 31:264–267, 1960.
- [32] S. Gärtner. Influence of Internal States on Ion-Molecule Reactions in a Temperature Variable 22-Pole Ion Trap. PhD thesis, University of Cologne, 2014.
- [33] S. Fanghänel. Pulshöhenverteilungen eines empfindlichen Ionendetektors. Staatsexamensarbeit, Universität zu Köln, 2012.
- [34] O. Asvany, T. Giesen, B. Redlich, and S. Schlemmer. Experimental determination of the ν_5 cis-bending vibrational frequency in ground state ($X^2\Pi_u$) $C_2H_2^+$ using laser induced reactions. *Phys. Rev. Lett.*, 94:073001, 2005.
- [35] S. Gärtner, J. Krieg, A. Klemann, et al. High-Resolution Spectroscopy of CH_2D^+ in a Cold 22-Pole Trap. *J. Phys. Chem. A*, 117:9975–9984, 2013.
- [36] S. Gärtner, J. Krieg, A. Klemann, O. Asvany, and S. Schlemmer. Rotational Transitions of CH_2D^+ determined by high-resolution IR spectroscopy. *Astron. Astrophys.*, 516:L3, 2010.
- [37] S. Schlemmer, T. Kuhn, E. Lescop, and D. Gerlich. Laser excited N_2^+ in a 22-pole ion trap: experimental studies of rotational relaxation processes. *Int. J. Mass Spectrom.*, 185:589–602, 1999.
- [38] S. Schlemmer, E. Lescop, J. v. Riechthofen, and D. Gerlich. Laser Induced Reactions in a 22-Pole Trap: $C_2H_2^+ + hv_3 + H_2 \rightarrow C_2H_3^+ + H$. *J. Chem. Phys.*, 117:2068–2075, 2002.
- [39] O. Asvany, S. Brünken, L. Kluge, and S. Schlemmer. COLTRAP: a 22-pole ion trapping machine for spectroscopy at 4 K. *Applied Physics B*, 114:203–211, 2014.
- [40] S. Chakrabarty, M. Holz, E. K. Campbell, et al. A Novel Method to Measure Electronic Spectra of Cold Molecular Ions. *J. Phys. Chem. Lett.*, 4:4051–4054, 2013.
- [41] O. Asvany, O. Ricken, H. S. P. Müller, et al. High-Resolution Rotational Spectroscopy in a cold Ion Trap: H_2D^+ and D_2H^+ . *Phys. Rev. Lett.*, 100:233004, 2008.

- [42] T. Amano. The $J = 1 \rightarrow 0$ Transitions of $^{12}\text{CH}^+$, $^{13}\text{CH}^+$, and $^{12}\text{CD}^+$. *ApJL*, 716:L1, 2010.
- [43] G. A. Miller. On the calculation of thermal transpiration. *J. Phys. Chem.*, 67:1359–1361, 1963.
- [44] H. Tanuma, H. Fujimatsu, and N. Kobayashi. Ion mobility measurements and thermal transpiration effects in helium gas at 4.3 K. *J. Chem. Phys.*, 113:1738–1744, 2000.
- [45] T. Takaishi and Y. Sensui. Thermal transpiration effect of hydrogen, rare gases and methane. *Trans. Faraday Soc.*, 59:2503–2514, 1963.
- [46] J. Olivero and R. Longbothum. Empirical fits to the Voigt line width: A brief review. *J. Quant. Spectrosc. Radiat. Transfer*, 17:233 – 236, 1977.
- [47] E. Herbst. A statistical theory of three-body ion molecule reactions. *J. Chem. Phys.*, 70:2201–2204, 1979.
- [48] D. R. Bates. Ion-molecule association. *J. Phys. B*, 12:4135–4146, 1979.
- [49] J. Xie, B. Poirier, and G. I. Gellene. A quantum dynamical study of the $\text{He}^+ + 2\text{He} \rightarrow \text{He}_2^+ + \text{He}$ reaction. *J. Chem. Phys.*, 119:10678–10686, 2003.
- [50] F. Grandinetti. Helium chemistry: a survey of the role of the ionic species. *Int. J. Mass spectrom.*, 237:243 – 267, 2004.
- [51] T. Stoecklin and A. Voronin. Vibrational and rotational energy transfer of CH^+ in collisions with ^4He and ^3He . *EPJ D*, 46:259–265, 2008.
- [52] M. Meuwly and N. J. Wright. The Potential Energy Surface and rovibrational States of He-CH^+ . *J. Phys. Chem. A*, 104:1271–1277, 2000.
- [53] F. Turpin, T. Stoecklin, and A. Voronin. Rotational excitation and de-excitation of CH^+ molecules by ^4He atoms. *Astron. Astrophys.*, 511:A28, 2010.
- [54] H. S. P. Müller, S. Thorwirth, D. A. Roth, and G. Winnewisser. The Cologne Database for Molecular Spectroscopy, CDMS. *Astronomy and Astrophysics*, 370:L49–L52, April 2001.
- [55] T. Amano. The ν_1 fundamental band of HCO^+ by difference frequency laser spectroscopy. *J. of Chem. Phys.*, 79:3595–3595, 1983.
- [56] F. Tinti, L. Bizzocchi, C. Degli Esposti, and L. Dore. Improved Rest Frequencies of HCO^+ at 1 THz. *ApJL*, 669:L113–L116, 2007.
- [57] G. Cazzoli, L. Cludi, G. Buffa, and C. Puzzarini. Precise THz Measurements of HCO^+ , N_2H^+ , and CF^+ for Astrophysical Observations. *ApJS*, 203:11, 2012.
- [58] G. Buffa, L. Dore, F. Tinti, and M. Meuwly. Experimental and Theoretical Study of Helium Broadening and Shift of HCO^+ Rotational Lines. *ChemPhysChem*, 9(15):2237–2244, 2008.

- [59] G. Buffa, L. Dore, and M. Meuwly. State-to-state rotational transition rates of the HCO^+ ion by collisions with helium. *Mon. Not. R. Astron. Soc.*, 397(4):1909–1914, 2009.
- [60] M. Meuwly. The potential energy surface and rovibrational states of He HCO^+ . *J. Chem. Phys.*, 110:4347–4353, 1999.
- [61] R. P. A. Bettens and E. Herbst. The Formation of Large Hydrocarbons and Carbon Clusters in Dense Interstellar Clouds. *The Astrophysical Journal*, 478:585, 1997.
- [62] A. Tielens. Interstellar Polycyclic Aromatic Hydrocarbon Molecules. *Annual Review of Astronomy and Astrophysics*, 46:289–337, 2008.
- [63] S. Cuadrado, J. R. Goicoechea, P. Pilleri, et al. The chemistry and spatial distribution of small hydrocarbons in uv-irradiated molecular clouds: the orion bar pdr^{*,**}. *Astron. Astrophys.*, 575:A82, 2015.
- [64] J. Pety, D. Teyssier, D. Fossé, et al. Are PAHs precursors of small hydrocarbons in photo-dissociation regions? The Horsehead case. *Astron. Astrophys.*, 435:885–899, 2005.
- [65] R. Lucas and H. Liszt. Comparative chemistry of diffuse clouds. I. C_2H and C_3H_2 . *Astron. Astrophys.*, 358:1069–1076, 2000.
- [66] D. Teyssier, D. Fossé, M. Gerin, et al. Carbon budget and carbon chemistry in Photon Dominated Regions. *Astron. Astrophys.*, 417:135–149, 2004.
- [67] B. E. Turner, E. Herbst, and R. Terzieva. The Physics and Chemistry of Small Translucent Molecular Clouds. XIII. The Basic Hydrocarbon Chemistry. *The Astrophysical Journal Supplement Series*, 126:427, 2000.
- [68] V. Wakelam, I. Smith, E. Herbst, et al. Reaction Networks for Interstellar Chemical Modelling: Improvements and Challenges. *Space Science Reviews*, 156:13–72, 2010.
- [69] J. P. Pérez-Beaupuits, H. Wiesemeyer, V. Ossenkopf, et al. The ionized and hot gas in M17 SW: SOFIA/GREAT THz observations of [C II] and ^{12}CO J=13-12. *Astron. Astrophys.*, 542:L13, 2012.
- [70] E. Habart, E. Dartois, A. Abergel, et al. SPIRE spectroscopy of the prototypical Orion Bar photodissociation region. *Astron. Astrophys.*, 518:L116, 2010.
- [71] Z. Nagy, F. F. S. Van der Tak, V. Ossenkopf, et al. The chemistry of ions in the Orion Bar I. - CH^+ , SH^+ , and CF^+ :The effect of high electron density and vibrationally excited H_2 in a warm PDR surface. *Astron. Astrophys.*, 550:A96, 2013.
- [72] S. Ikuta. An ab initio MO study on structures and energetics of C_3H^- , C_3H , and C_3H^+ . *The Journal of Chemical Physics*, 106:4536–4542, 1997.
- [73] X. Huang, R. C. Fortenberry, and T. J. Lee. Spectroscopic Constants and Vibrational Frequencies for l- C_3H^+ and Isotopologues from Highly Accurate Quartic Force Fields: The Detection of l- C_3H^+ in the Horsehead Nebula PDR Questioned. *The Astrophysical Journal Letters*, 768:L25, 2013.

- [74] R. C. Fortenberry, X. Huang, T. D. Crawford, and T. J. Lee. High-accuracy Quartic Force Field Calculations for the Spectroscopic Constants and Vibrational Frequencies of $1^1A'$ l - C_3H^- : A Possible Link to Lines Observed in the Horsehead Nebula Photodissociation Region. *The Astrophysical Journal*, 772:39, 2013.
- [75] M. Agúndez, J. Cernicharo, M. Guélin, et al. Search for anions in molecular sources: C_4H^- detection in L1527. *Astron. Astrophys.*, 478:L19–L22, 2008.
- [76] H. Gupta, C. A. Gottlieb, M. C. McCarthy, and P. Thaddeus. A Survey of C_4H , C_6H , and C_6H^- with the Green Bank Telescope. *Astrophys. J.*, 691:1094–1500, 2009.
- [77] M. C. McCarthy, K. N. Crabtree, M.-A. Martin-Drumel, et al. A Laboratory Study of C_3H^+ and the C_3H Radical in Three New Vibrationally Excited $^2\Sigma$ States Using a Pin-Hole Nozzle Discharge Source. *ApJS*, 217:10, 2015.
- [78] M. Mladenović. The B11244 story: Rovibrational calculations for C_3H^+ and C_3H^- revisited. *J. Chem. Phys.*, 141:224304, 2014.
- [79] P. Botschwina, C. Stein, P. Sebald, B. Schröder, and R. Oswald. Strong Theoretical Support for the Assignment of B11244 to l - C_3H^+ . *Astrophys. J.*, 787:72–76, 2014.
- [80] V. V. Guzmán, J. Pety, J. R. Goicoechea, et al. Spatially Resolved l - C_3H^+ Emission in the Horsehead Photodissociation Region: Further Evidence for a Top-Down Hydrocarbon Chemistry. *ApJL*, 800:L33, 2015.
- [81] A. Sorgenfrei and D. Gerlich. Ion-trap experiments on $C_3H^+ + H_2$: Radiative association vs. hydrogen abstraction. *J. Chem. Phys.*, 124:244303, 2006.
- [82] H. M. Pickett. The Fitting and Prediction of Vibration-Rotation Spectra with Spin Interactions. *J. Molec. Spectroscopy*, 148:371–377, 1991.
- [83] I. Savić and D. Gerlich. Temperature variable ion trap studies of $C_3H_n^+$ with H_2 and HD. *PCCP*, 7:1026–1035, 2005.

Danksagung

An dieser Stelle möchte ich allen danken, die mich während meiner Promotionszeit begleitet und die, in der einen oder anderen Weise, zum Gelingen dieser Arbeit beigetragen haben:

Prof. Dr. Stephan Schlemmer danke ich für die sehr gute Betreuung und für sein großes Interesse auch an den kleinen Details meiner Arbeit. Ebenso möchte ich mich für die vielen interessanten Diskussionen und die lehrreichen Bastel- und Technikstunden im Labor bedanken. Wichtig war für mich auch die sehr gute und lockere, aber stets zielorientierte Arbeitsatmosphäre, die in der Arbeitsgruppe von Prof. Schlemmer immer herrschte.

Prof. Dr. Thomas Michely möchte ich für die bereitwillige Übernahme des Zweitgutachtens danken.

Prof. Dr. Axel Klein danke ich für die Bereitschaft, den Vorsitz in der Disputationsprüfung zu übernehmen.

Dr. Sandra Brünken danke ich für die Übernahme des Prüfungsbesitzes, genauso wie für die unzähligen hilfreichen Diskussionen über die verschiedensten Aspekte meiner Arbeit und die zahlreichen Hilfestellungen und guten Tipps im Labor. Natürlich möchte ich mich ganz besonders für das Korrekturlesen meiner Arbeit bedanken.

Besonders bedanken möchte ich mich bei der gesamten Arbeitsgruppe für die großartige Arbeitsatmosphäre und die Hilfsbereitschaft, wann immer es ein Problem zu lösen galt.

Dr. Monika Koerber danke ich für die lustigen Teepausen, ob nun im Büro oder bei Sonnenschein draußen auf dem Affenfelsen. Dabei erinnere ich mich gerne an die vielen intensiven Diskussionen um die, immer noch ungeklärte Frage, ob denn nun Schweden oder Dänemark das schönere Reiseziel in Skandinavien ist. Darüber hinaus beantwortete Monika mir viele Fragen zu allen möglichen anderen Themen. Schließlich bedanke ich mich bei ihr für das Korrekturlesen meiner Arbeit.

Dr. Sabrina Gärtner möchte ich für die vielen Jahre der guten Büronachbarschaft und für die Lösungen vieler Probleme in Python und GNU-Plot danken - sie hatte immer Zeit, mit mir über alles und jedes zu diskutieren.

Alexander Stoffels danke ich für die gute Zusammenarbeit beim Aufbau und seine Unterstützung bei den Messungen mit FELion und für die lustigen Abende mit dem ein oder anderen alkoholhaltigen Getränk.

Peter Stölzgen und Henning Adams möchte ich für ihre vielfältige Unterstützung im Laufe meiner Doktorarbeit danken. Sei es für die Hilfe bei den unzähligen ProEngineer Fragen, Problemen bei der Konstruktion von Bauteilen und die Geduld dabei, wenn die Konstruktion dann doch zum dritten Mal geändert wurde. Peter danke ich besonders für die Einführung in die Programmierung mit LabView und für seine großartige Hilfe bei der Programmierung der Steuersoftware für FELion.

Bei Hanno Schmiedt und Sven Fanghänel möchte ich mich für die stets interessanten Diskussionen über viele (mehr oder weniger) theoretische Fragestellungen bedanken. Hanno ist hoch anzurechnen, dass er sich als Theoretischer Physiker beim Korrekturlesen durch den experimentellen Teil meiner Arbeit gequält hat.

Dr. Frank Lewen war mir mit seinen vielen Ausführungen zu den THz-Ketten und

-Detektoren, die mir bei der Beantwortung meiner Fragen immer sehr weiter geholfen haben, eine sehr große Hilfe.

Viele lustige Rennradtouren und Gespräche über Sport und Training aller Art mit Dr. Sven Thorwirth sorgten für einen wichtigen Ausgleich zur ansonsten doch sehr kopflastigen Arbeit.

Herzlich möchte ich mich auch bei allen, die im Laufe der Zeit mit mir in Raum 316 gesessen haben, für die stets angenehme und lockere Arbeitsatmosphäre bedanken. Großer Dank gilt auch meinen Laborkollegen Dr. Oskar Asvany und Dr. Pavol Jusko, die immer eine hilfreiche Hand frei hatten und stets zur Verfügung standen, wenn es Probleme zu lösen galt.

Der Feinmechanischen Werkstatt des I. Physikalischen Institutes der Universität zu Köln möchte ich für die stets gute Zusammenarbeit und die vielen sehr konstruktiven Lösungsvorschläge bei Problemen mit dem Bau der neuen Ionenfallen danken.

Ganz besonders bedanken möchte ich mich bei meinen Eltern, die mich zu jeder Zeit im Studium und während der Promotion unterstützt haben und immer für mich da waren.

Auch meinen Freunden, die mich im Laufe der Zeit durch das Studium und die Promotion begleitet haben, danke ich für ihr Verständnis, wenn ich aufgrund von Prüfungen oder Schreibstress einmal weniger Zeit für sie hatte und auch den einen oder anderen Termin absagen musste. Besonders erwähnen möchte ich hier Stefan Schumacher, Semir Smajic, Vera Derya, Imke Keppeler, Florian Zeisbrich, Silke Andree-Labsch, Sven Müller und Carolin Küppersbusch.

Erklärung

Ich versichere, dass ich die von mir vorgelegte Dissertation selbständig angefertigt, die benutzten Quellen und Hilfsmittel vollständig angegeben und die Stellen der Arbeit - einschließlich Tabellen, Karten und Abbildungen -, die anderen Werken im Wortlaut oder dem Sinn nach entnommen sind, in jedem Einzelfall als Entlehnung kenntlich gemacht habe; dass diese Dissertation noch keiner anderen Fakultät oder Universität zur Prüfung vorgelegen hat; dass sie - abgesehen von unten angegebenen Teilpublikationen - noch nicht veröffentlicht worden ist sowie, dass ich eine solche Veröffentlichung vor Abschluss des Promotionsverfahrens nicht vornehmen werde. Die Bestimmungen der Promotionsordnung sind mir bekannt. Die von mir vorgelegte Dissertation ist von Prof. Dr. Stephan Schlemmer betreut worden.

Teilpublikationen

- S. Brünken, L. Kluge, A. Stoffels, O. Asvany, and S. Schlemmer. Laboratory Rotational Spectrum of $l\text{-C}_3\text{H}^+$ and Confirmation of its Astronomical Detection. *ApJL* **783** (2014), L4 (4pp)
- O. Asvany, S. Brünken, L. Kluge, and S. Schlemmer. COLTRAP: a 22-pole ion trapping machine for spectroscopy at 4 K. *Appl. Phys. B* **114** (2014), 203-211

Lebenslauf

Persönliche Angaben

Name: Lars Alexander Kluge
Adresse: Aachener Straße 328
50933 Köln
Geburtsdatum/-ort: 05.04.1986 in Leverkusen
Staatsangehörigkeit: deutsch
Familienstand: ledig

Schulausbildung

1992–1996 Gemeinschaftsgrundschule Dierath in Burscheid
1996–2005 Werner Heisenberg Gymnasium in Leverkusen
Juni 2005 Abitur

Studium

10/2005–10/2007 Grundstudium in Physik an der Universität zu Köln
Vordiplom im Oktober 2007
10/2007–01/2010 Hauptstudium in Physik an der Universität zu Köln
01/2010–04/2011 Diplomarbeit in Experimentalphysik am I. Physikalischen Institut
„Protonen-Transfer zwischen H₂ und O₂ - Speicherexperimente bei tiefen Temperaturen“
Diplom im März 2011
04/2011 Beginn des Promotionsstudiums an der Universität zu Köln

Beschäftigung

04/2009–03/2011 Studentische Hilfskraft am I. Physikalischen Institut der Universität zu Köln
seit 04/2011 Wissenschaftlicher Mitarbeiter am I. Physikalischen Institut der Universität zu Köln

Lehrtätigkeit

04/2009–09/2011 Versuchsbetreuung im Praktikum A der Physik
seit 10/2011 Übungsleiter für Vorlesungen in der Experimentalphysik